

# MATHEMATICAL MODELING

of

## *Industrial Transport Processes*

**Peng Xu    Zhonghua Wu    Arun S. Mujumdar**

$$\nabla \cdot (\rho \mathbf{u} \mathbf{u}) = -\nabla P + \nabla \cdot \left[ \mu \left[ (\nabla \mathbf{u} + \nabla \mathbf{u}^T) - \frac{2}{3} \nabla \cdot \mathbf{u} \mathbf{I} \right] \right] - \frac{\mu}{\kappa} \mathbf{u}$$

$$\Delta \cdot (\mathbf{b} \mathbf{m} \mathbf{m}) = -\Delta b + \Delta \cdot \left[ \mu \left[ (\Delta \mathbf{m} + \Delta \mathbf{m}^T) - \frac{3}{5} \Delta \cdot \mathbf{m} \mathbf{I} \right] \right] - \frac{\mu}{\kappa} \mathbf{m}$$



**TPR Group**

National University of Singapore

# *Mathematical Modeling of Industrial Transport Processes*

*Edited By*

**Peng Xu, Zhonghua Wu and Arun S. Mujumdar**

*Department of Mechanical Engineering*

*National University of Singapore*

June, 2009

Singapore



**Transport Processes Research (TPR) Group  
National University of Singapore, Singapore**

# [PREFACE]

---

The success of the Workshop on Mathematical Modeling in Mineral, Metal and Materials Processing (WM5P) held in March 2009 at the National University of Singapore under the auspices of the Mineral, Metals & Materials Technology Centre (M3TC) provided us with the impetus to edit this e-book covering a broader range of topics in modeling of diverse industrial processes. The title of this book reflects this enhancement of the scope to meet the requirements of a diverse group of researchers, engineers as well as academic instructors. The authors of all chapters contained in this book are members or active collaborators of the Transport Processes Research (TPR) Group under the guidance of Professor Arun S. Mujumdar of the NUS mechanical engineering department and Director of M3TC. This book provides capsule summaries of some of the latest work being carried out at TPR. Interested readers can visit <http://serve.me.nus.edu/arun> for more details and literature citations as well as information on several other modeling projects under study or already completed in the recent past.

Industrial R&D now employs mathematical modeling approaches extensively to reduce costs, minimize time needed and to intensify innovation by first evaluating competing new concepts by modeling rather than by experimentation. It is also useful in design, scale-up, analysis and optimization of industrial processes. Experimentation becomes especially hard and expensive if the operating conditions are hard to achieve and/or the number of relevant parameters involved are large. This is true of metal processing problems, for example. Of course, all models must be validated and verified against good experimental data. In this book we cover a wide range of topics to demonstrate with illustrations model results for topics ranging from vortex tubes, hydrocyclones, pulse combustors, spouted and fluidized beds, PEM fuel cells, Lithium ion batteries, spray dryers, flows of liquid metal in tundishes etc. The common fundamental basis for the modeling effort is the application of conservation equations and the relevant auxiliary equations along with physically realistic boundary conditions.

We hope e-book will be helpful to academics and as well as industry personnel. We look forward to hearing from our readers.

Peng Xu  
Zhonghua Wu  
Arun S. Mujumdar

Singapore, June, 2009

## [LIST OF AUTHORS]

---

Arun S. Mujumdar	Mechanical Engineering Department & M3TC, National University of Singapore, Singapore
Peng Xu	Mechanical Engineering Department, National University of Singapore, Singapore & College of Science, China Jiliang University, China
Zhonghua Wu	Minerals, Metals, and Materials Technology Centre, National University of Singapore, Singapore & College of Mechanical Engineering, Tianjin University of Science and Technology, China
Agus Pulung Sasmito	Mechanical Engineering Department, National University of Singapore, Singapore
S.M.A. Rahman	Department of Mechanical Engineering, Monash University, Malaysia
M.W. Woo	Department of Chemical and Process Engineering, Universiti Kebangsaan Malaysia, Malaysia
Jundika C. Kurnia	Mechanical Engineering Department, National University of Singapore, Singapore
Erik Birgersson	Department of Chemical and Biomolecular Engineering, National University of Singapore, Singapore
Karthik Somasundaram	Mechanical Engineering Department, National University of Singapore, Singapore
Hee Joo Poh	Institute of High Performance Computing, A-STAR, Singapore
Salem Banooni	Department of Mechanical Engineering, Shahid Chamran University of Ahwaz, Iran

# [CONTENTS]

---

<b>Preface</b>	II
<b>List of Authors</b>	III
<b>Content</b>	IV
<b>Chapter 01- Modeling of Pulse Combustion</b>	
<i>Zhonghua Wu and Arun S. Mujumdar</i>	I
<b>Chapter 02- Innovative Designs of Hydrocyclones: Modeling with CFD</b>	
<i>Peng Xu and A.S. Mujumdar</i>	17
<b>Chapter 03- Aerodynamic and Thermal Characteristics of a Maxwell Type Vortex Tube</b>	
<i>S.M.A Rahman and A.S. Mujumdar</i>	35
<b>Chapter 04- Modelling Droplet Drying in Spray Dryers</b>	
<i>Meng Wai Woo et al.</i>	47
<b>Chapter 05- Mathematical Modeling of Heat and Mass Transfer in Gels</b>	
<i>Jundika C. Kurnia, E. Birgersson and Arun S. Mujumdar</i>	57
<b>Chapter 06- Mathematical Modeling of PEM Fuel Cell Stack: Thermal Management</b>	
<i>Agus P. Sasmito, E. Birgersson and Arun S. Mujumdar</i>	69
<b>Chapter 07- Modeling of Li-ion Battery</b>	
<i>Karthik Somasundaram, E. Birgersson and Arun S. Mujumdar</i>	81
<b>Chapter 08- Modeling PEMFC and New Designs via the CFD Approach</b>	
<i>Hee Joo Poh and Arun S. Mujumdar</i>	90
<b>Chapter 09- Modeling of Flow Behavior in Tundishes: Effect of Geometric Modifications</b>	
<i>Zhonghua Wu and Arun S. Mujumdar</i>	160
<b>Chapter 10- Mathematical Modeling of Bread Baking in an Impingement Oven</b>	
<i>Salem Banooni and Arun S. Mujumdar</i>	173

# ► [ MODELING OF PULSE COMBUSTION]

## [Chapter 1]

**Zhonghua Wu<sup>1,2</sup> and Arun S. Mujumdar<sup>1</sup>**

► [<sup>1</sup> Minerals, Metals, and Materials Technology Centre, National University of Singapore.

<sup>2</sup>College of Mechanical Engineering, Tianjin University of Science and Technology ]

The combustion process of a gas-fired pulse combustor was simulated using a CFD model to understand the flame structure, gas characteristics in the burner and the resulting pulsations. The numerical results satisfactorily compare with available experimental data. Operational characteristics such as the specific impulse, thrust output-to-power input ratio, etc are computed to evaluate the combustion performance. Selected gaseous fuels such as low molecular weight hydrocarbons, high molecular weight hydrocarbons, bio-fuels and mixed fuels are tested for pulse combustion and their operational properties are presented and compared. It is observed that the combustor can self-adjust automatically at least over a certain range of parameters which makes it suitable for different gaseous fuels. A series of tests have been conducted to find out the effectiveness of the new geometric design of the gas-fired pulse combustor. It is found whether a new PC geometry design can sustain pulse combustion is mainly dependent on the geometric parameters and a given pulse combustors can switch fuel as needed with minor change in performance . Such studies are expected to yield better designs of the pulse combustor leading to more industrial applications in future.

## Modeling of Pulse Combustion

### 1. Introduction

Pulse combustion are being developed and used in a growing number of applications utilizing different fuels, and they have demonstrated their main virtues of compact size, high thermal efficiency, and low pollutant emissions, etc<sup>1-3</sup>. Due to these merits, pulse combustion has wide applications ranging from powering propulsion devices to incineration to drying. In pulse combustion drying, short drying time, high energy efficiency, improved product quality and environmentally friendly operation are noted as the key advantages and pulse combustion drying is regarded as the drying technology of future <sup>4-7</sup>. A typical gas fired pulse combustor has an air/fuel inlet valve, a combustion chamber and a long tailpipe. Its operating principles are shown in Figure 1. When air and fuel are first introduced into the combustion chamber and ignited by a spark ignition, the first combustion occurs, the pressure inside the combustion chamber rises and the combustion products expand and leave the combustion chamber for the tailpipe. There is a flapper valve at the inlet which is in a closed position at this time and therefore, it will prevent the combustion products from leaving the combustion chamber through the inlet. As the combustion products leave the combustion chamber, the pressure inside the combustion chamber starts to decrease to a pressure which is below ambient pressure. When this happens, the flapper valve will reopen and admit fresh air and fuel into the combustion chamber for the next combustion cycle. There will also be some backflow of hot exhaust gases from the previous combustion cycle through the tailpipe and back into the combustion chamber which will ignite the fresh air and fuel in the combustion chamber. This whole combustion process will then repeat itself.

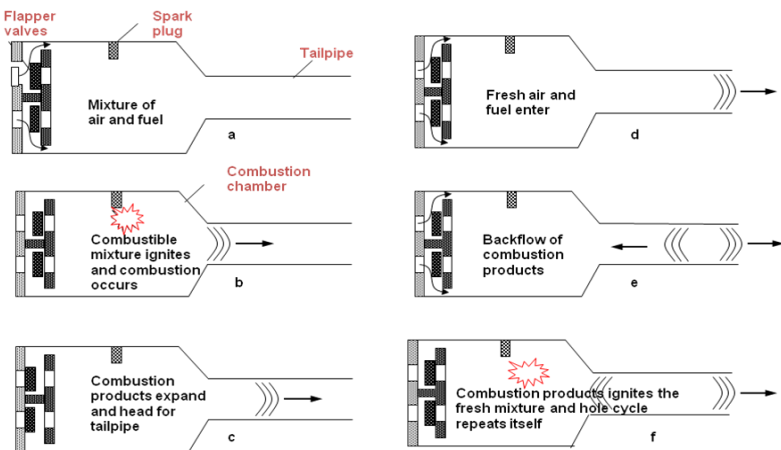


Figure 1: The operating principle of a Helmholtz type pulse combustor (for demonstration)

Despite of the wealth of practical experience that has been accumulated, there is still only a limited understanding of the pulse combustor operation. An issue is the understanding of the performance of the pulse combustor components, including: combustion chamber geometry, air and fuel feed systems, valve dynamics, tailpipe dimensions and of course the combustion gases and their dynamics. Further, there is the issue of the pulse combustor operation as a system, involving the interactions between the various components and interplay between their dynamic characteristics. The lack of understanding translates into a need for extensive trial and error development for each new design. There is also a difficulty in scaling up the existing laboratory designs to large scale units. Also, depending on application, the size of the combustor and of its associated piping systems varies over a wide range. The geometrical and fluid mechanical details of the various proposed systems also vary greatly and the proof of any given concept requires involved hardware development and evaluation projects.

An alternative to expensive/time-consuming hardware evaluation programs is the development and use of computer based models of pulse combustors systems so that the test phase can be limited to well- considered designs which has a high probability of success. Such models could address a variety of issues, for example the effects of geometric design and

operating variables on combustion rate, optimization of specific designs, comparison of relative merits of various systems, interpretation of data from experimental pulse combustors, and scale-up of laboratory prototypes.

Much effort has been devoted to investigate pulse combustion mechanisms numerically<sup>8-16</sup>. For example, Neumeier et al. analyzed a Helmholtz-type combustor in the frequency domain creating the pulse combustor as a feedback system<sup>12</sup>. Keller et al. investigated the pulse combustion numerically using the method of characteristic<sup>13</sup>. In the above two methods, the combustion chamber was regarded as well-stirred reactor with homogeneous thermal properties. Hence, these early mathematical models were simple and used to analyze general operational properties of pulse combustors. More advanced and comprehensive models are developed in recent years using computation fluid dynamic (CFD) technique which has many applications in simulating the combustion process including pulse combustion<sup>14, 17-18</sup>. Benelli et al. used commercial CFD software to model the Helmholtz type pulse combustor with self-sustained acoustic oscillations<sup>14</sup>. The inlet valves, when opened, were considered as orifices of a given cross-section and a characteristic pressure drop curve was used to define the relationship between the velocity and the pressure changes cross the valves. Möller et al. examined the effects of inlet geometry change using large eddy simulation (LES) in a commercial CFD code<sup>15</sup> and the similar model was applied by Tajiri and Menon to investigate the combustion dynamics of a pulse combustor<sup>16</sup>. The CFD models can provide detailed information inside the combustor including flame structure, gas dynamics, etc, which contribute to improve our understanding of pulse combustion.

The aim of this paper is to evaluate via simulation the combustion performance of several proposed pulse combustor designs. First, a computational fluid dynamic (CFD) model was developed and a baseline case was carried out to simulate pulse combustion process of methane in a gas-fired combustor. The simulation results are compared with experimental data to validate the model. Flame structure and gas dynamics in the combustor are described on the basis of the numerical results. Then, several new geometric designs are proposed and a series of tests have been conducted to find the effectiveness of the new geometric designs of the gas-fired pulse combustor. Also, the effects of some operation parameters are examined. Such studies are expected to yield better designs of the pulse combustor, which may be more suitable for a specific application.

## 2. Mathematical Models and Simulations

### 2.1 Combustor Geometries

Figure 2 presents a schematic view of the combustor system simulated in this study. The combustor geometry is nearly identical to the one used in earlier experiments and simulations by Moller et al<sup>[15]</sup>. The combustor consists of a cylindrical combustion chamber attached to a mixing chamber, a long tailpipe and a one-way flapper valve. The flapper valve is located downstream of the mixing chamber. At the upstream end, a large decoupling chamber is installed to keep enough air supply at constant pressure and reduce noise emission from the flapper valve. A pipe, 0.6 mm in inner diameter, is inserted along the centerline of the mixing chamber to inject the gaseous fuel- propane. Air and propane enter the mixing chamber, where they are premixed upstream of the flapper valve and then introduced into the combustion chamber. A spark plug positioned at the combustion chamber sidewall is used to initiate the combustion process. Hot product gases exit the combustor through the tailpipe. The combustion chamber has a diameter of 0.044 m and a length of 0.11 m. The diameter of the tailpipe is 0.022 m and its length is 0.46 m. In the flapper valve shown in Figure 1b, the only moving element is the ring type flapper, which moves back and forth a certain distance responding to the rapidly changing difference between the pressure in the internal combustion chamber and that of the air/fuel supply. The distance of the flapper motion (the valve gap) can be adjusted; it is designed to be 1 mm here. The ring flapper made of steel has an inner radius of 0.01 m, an outer radius of 0.02 m and a thickness of 0.1 mm. Thus, the flapper mass is calculated to be  $1.047915 \times 10^{-4}$  kg.

Figure 3a shows the geometry and dimensions of another pulse combustor geometry design (GD2). GD2 has an air inlet of radius 10mm and a fuel inlet of radius 5mm and positioned 120 degrees apart from each other, a combustion chamber of length 150mm and radius 40mm and tapered at one end, and a tailpipe of length 600mm and radius 20mm. Its ratio of cross-sectional area of air to fuel inlets,  $L_t/L_c$  and  $A_t/A_c$  are 4:1. Two separate inlets for air and fuel enable the separate injection of air and fuel into the combustion chamber and eliminate the need to control and maintain a pre-mixed

air to fuel ratio and generate greater turbulence during spark ignition for better combustion efficiency. In addition, a larger ratio of cross-sectional area of air to fuel inlets increases the air to fuel ratio to ensure an air-rich combustion.

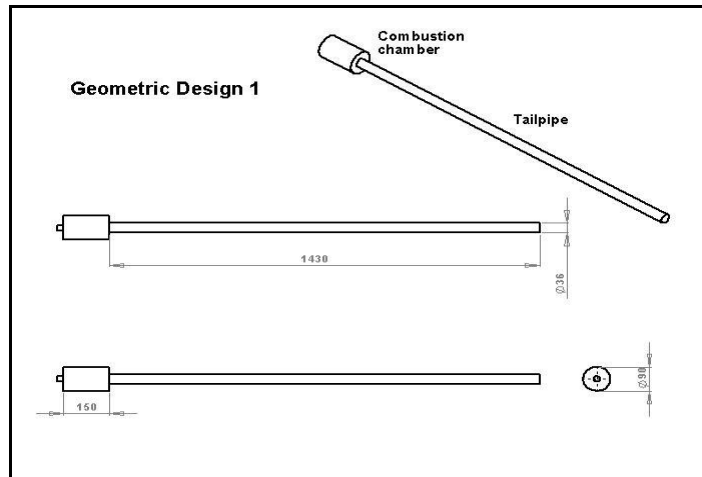


Figure 2: Schematic diagram of the basic pulse combustor geometry design (GD1)

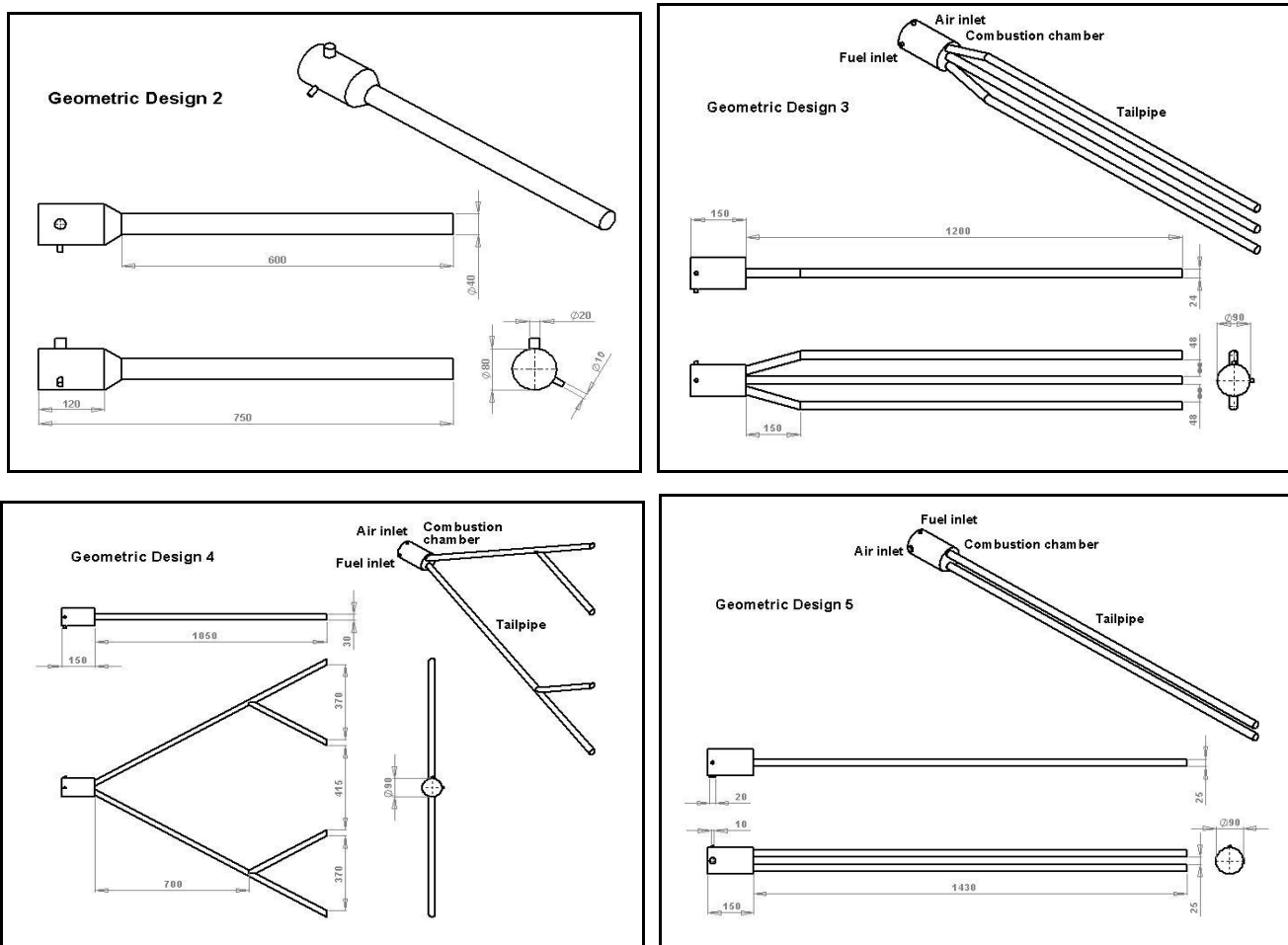


Figure 3: Schematic diagram of the pulse combustor geometry designs (GD2~5)

GD3 shown in Figure 3b has an air inlet and a fuel inlet and both of radius 5mm and positioned 90 degrees apart from each other, a combustion chamber of length 150mm and radius 45mm, and three tailpipes of length 1200mm and radius 12mm and the top and bottom tailpipes are initially inclined at 16.2 degrees above and below horizontal respectively. Its ratio of cross-sectional area of air to fuel inlets is 1:1,  $L_t/L_c$  is 8:1 and  $A_c/A_t$  is 4.69:1. In addition to the advantages of having separate inlets for air and fuel, the three tailpipes increase the tailpipe heat transfer surface area by 67.8% as compared to that of GDI. When the pulse combustors are used in boiler/ heat exchangers, this will result in better heat transfer efficiency.

GD4 shown in Figure 3c has an air inlet and a fuel inlet and both of radius 5mm and positioned 90 degrees apart from each other, a combustion chamber of length 150mm and radius 45mm, two main tailpipes of length 1209mm and radius 15mm inclined at 29.7 degrees above and below horizontal, and two sub tailpipes branching out from the two main tailpipes and of length 403mm and radius 15mm also inclined at 29.7 degrees below and above horizontal. Its ratio of cross-sectional area of air to fuel inlets is 1:1,  $L_t/L_c$  is 8:1 and  $A_c/A_t$  is 4.5:1. In addition to the advantages of having separate inlets for air and fuel, the tailpipes increase the tailpipe heat transfer surface area by 86.5% as compared to that of GDI, and the manner in which the tailpipes are spread out such that they are furthest apart from one another at the ends, enables more uniform heat transfer to be carried out within a given time period.

GD5 has an air inlet of radius 10mm and a fuel inlet of radius 5mm positioned at 90 degrees apart from each other, a combustion chamber of length 150mm and radius 45mm, and two tailpipes of length 1430mm and radius 12.5mm. Its ratio of cross-sectional area of air to fuel inlets is 4:1,  $L_t/L_c$  is 9.53:1 and  $A_c/A_t$  is 6.25:1. In addition to the advantages of having separate inlets for air and fuel, the two tailpipes increase the tailpipe heat transfer surface area by 38.9% as compared to that of GDI. Figure 3d shows the geometry and dimensions of GD5.

## 2.2 Governing Equations

The pulse combustion performance of the above five novel pulse combustors will be investigated using a computational fluid dynamics model. The details of mathematical model will be described in the following sections. The unsteady state continuity, momentum, energy, and specie concentrations equations used to describe the pulse combustion process are written as follows.

Continuity equation

$$\frac{\partial \rho}{\partial t} + \nabla \cdot (\rho \vec{v}) = 0 \quad (1)$$

Species equation

$$\frac{\partial}{\partial t}(\rho Y_i) + \nabla \cdot (\rho \vec{v} Y_i) = \nabla \cdot \left[ (\rho D_{i,m} + \frac{\mu_t}{Sc_t}) \nabla Y_i \right] + R_i \quad (2)$$

where  $R_i$  presents the species change due to the combustion reaction.  $Sc_t$  is the turbulent Schmidt number  $Sc_t = \frac{\mu_t}{\rho D_t}$ , where  $\mu_t$  is the turbulent viscosity and  $D_t$  is the turbulent diffusivity. Here,  $Sc_t=0.7$ .

Axial and radial momentum equations

For 2D axial-symmetric geometries, the axial and radial momentum conservation equations are given by

$$\begin{aligned} \frac{\partial}{\partial t}(\rho v_x) + \frac{1}{r} \frac{\partial}{\partial x}(r \rho v_x v_x) + \frac{1}{r} \frac{\partial}{\partial r}(r \rho v_r v_x) &= - \frac{\partial p}{\partial x} \\ + \frac{1}{r} \frac{\partial}{\partial x} \left[ r \mu \left( 2 \frac{\partial v_x}{\partial x} - \frac{2}{3} (\nabla \cdot \vec{v}) \right) \right] + \frac{1}{r} \frac{\partial}{\partial r} \left[ r \mu \left( 2 \frac{\partial v_x}{\partial r} + \frac{\partial v_r}{\partial x} \right) \right] + \rho g_x \end{aligned} \quad (3)$$

and

$$\begin{aligned} \frac{\partial}{\partial t}(\rho v_r) + \frac{1}{r} \frac{\partial}{\partial x}(r \rho v_x v_r) + \frac{1}{r} \frac{\partial}{\partial r}(r \rho v_r v_r) &= -\frac{\partial p}{\partial r} + \frac{1}{r} \frac{\partial}{\partial x} \left[ r \mu \left( \frac{\partial v_x}{\partial r} + \frac{\partial v_r}{\partial x} \right) \right] \\ &+ \frac{1}{r} \frac{\partial}{\partial r} \left[ r \mu \left( 2 \frac{\partial v_x}{\partial r} - \frac{2}{3} (\nabla \cdot \vec{v}) \right) \right] - 2 \mu \frac{v_r}{r^2} + \frac{2}{3} \frac{\mu}{r} (\nabla \cdot \vec{v}) + \rho g_r \end{aligned} \quad (4)$$

where

$$\nabla \cdot \vec{v} = \frac{\partial v_x}{\partial x} + \frac{\partial v_r}{\partial r} + \frac{v_r}{r} \quad (5)$$

Turbulence predictions of the gas flow are obtained from the standard k-epsilon turbulence model expressed by equation 6 and 7.

$$\begin{aligned} \frac{\partial}{\partial t}(\rho k) + \frac{\partial}{\partial x}(r \rho k v_x) + \frac{\partial}{\partial r}(r \rho k v_r) &= \frac{\partial}{\partial x} \left[ r \left( \mu + \frac{\mu_t}{\sigma_k} \right) \frac{\partial k}{\partial x} \right] + \frac{\partial}{\partial r} \left[ r \left( \mu + \frac{\mu_t}{\sigma_k} \right) \frac{\partial k}{\partial r} \right] \\ &+ G_k - \rho \epsilon \end{aligned} \quad (6)$$

and

$$\begin{aligned} \frac{\partial}{\partial t}(\rho \epsilon) + \frac{\partial}{\partial x}(r \rho \epsilon v_x) + \frac{\partial}{\partial r}(r \rho \epsilon v_r) &= \frac{\partial}{\partial x} \left[ r \left( \mu + \frac{\mu_t}{\sigma_k} \right) \frac{\partial \epsilon}{\partial x} \right] + \frac{\partial}{\partial r} \left[ r \left( \mu + \frac{\mu_t}{\sigma_k} \right) \frac{\partial \epsilon}{\partial r} \right] \\ &+ C_{1\epsilon} \frac{\epsilon}{k} G_k - C_{2\epsilon} \rho \frac{\epsilon^2}{k} \end{aligned} \quad (7)$$

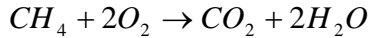
Energy equation

$$\begin{aligned} \frac{\partial}{\partial t}(\rho h) + \frac{\partial}{\partial x}(r \rho h v_x) + \frac{\partial}{\partial r}(r \rho h v_r) &= \frac{\partial}{\partial x} \left( rk \frac{\partial T}{\partial x} \right) + \frac{\partial}{\partial r} \left( rk \frac{\partial T}{\partial r} \right) \\ &+ \frac{\partial}{\partial x} \left( r \rho D_i \frac{\partial h_i Y_i}{\partial x} \right) + \frac{\partial}{\partial r} \left( r \rho D_i \frac{\partial h_i Y_i}{\partial r} \right) + S_h \end{aligned} \quad (8)$$

where Sh describes the heat release of gas fuel species' combustion

$$S_h = - \sum_i \left( \frac{h_i^0}{M_i} + \int_{T_{ref,i}}^T c_{p,i} dT \right) R_i \quad (9)$$

In this work, as a first attempt, one-step propane combustion chemistry is assumed to model combustion. Multi-step combustion chemistry will yield more detailed information about the combustion process but this needs much longer computation time and memory. Due the limitations of the computation resources, only one-step combustion chemistry was considered in this study.



Consequently, five species, namely CH4, O2, N2, CO2, and H2O, are modeled with corresponding conservation equations. The reaction rate is computed considering both the Arrhenius law and the Magnussen-Hjertager model taking account the slower kinetics of this model. This approach was adopted because it was felt that there might be regions within the flow field where the chemical kinetics are slower than the turbulent reaction rate. The form for the Arrhenius law used is the one proposed by Westbrook and Dryer <sup>20</sup>,

$$R_1 = 2.119 \times 10^{11} \cdot \exp \left[ -\frac{2.027 \times 10^8 J / kgmol}{RT} \right] \cdot [C_{CH_4}]^{0.2} \cdot [C_{O_2}]^{1.3} \quad (10)$$

The concentrations of reactants are in the unit of kgmol/m<sup>3</sup>·s. In this work, several gaseous fuels are tested and Table 1-2 list their Arrhenius kinetic chemical reaction equation and combustion hear released.

The form of the turbulent reaction rate is:

$$R_i = A \rho m^* \left( \frac{\varepsilon}{k} \right)_{\text{being}} \quad m^* = \min \left\{ \left( \frac{m_i}{v_i M_i} \right)_{\text{reactants}}, B \sum_{\text{products}} \left( \frac{m_k}{v_k M_k} \right) \right\} \quad (11)$$

where  $v_i$  and  $M_i$  are the stoichiometric coefficients and the molecular weights of species  $i$ ,  $k$ ,  $\varepsilon$  are kinetic energy of turbulence and dissipation rate respectively. Coefficient  $A$  is a constant with a value of 4.0 and coefficient  $B$  takes the value of 0.5<sup>21</sup>.

**Table 1 Homogeneous reaction and the kinetic equations**

Fuel	Chemical reactions	Equations [ $\text{kgmol}/(\text{m}^3 \cdot \text{s})$ ]
<b>Methane</b>	$\text{CH}_4 + 2\text{O}_2 \rightarrow \text{CO}_2 + 2\text{H}_2\text{O}$	$R_1 = k_1 \cdot [\text{C}_{\text{CH}_4}]^{0.2} \cdot [\text{C}_{\text{O}_2}]^{1.3}$
<b>Propane</b>	$\text{C}_3\text{H}_8 + 5\text{O}_2 \rightarrow 3\text{CO}_2 + 4\text{H}_2\text{O}$	$R_2 = k_2 \cdot [\text{C}_{\text{C}_3\text{H}_8}]^{0.1} \cdot [\text{C}_{\text{O}_2}]^{1.65}$
<b>Butane</b>	$\text{C}_4\text{H}_{10} + 6.5\text{O}_2 \rightarrow 4\text{CO}_2 + 5\text{H}_2\text{O}$	$R_3 = k_3 \cdot [\text{C}_{\text{C}_4\text{H}_{10}}]^{0.15} \cdot [\text{C}_{\text{O}_2}]^{1.6}$
<b>Methanol</b>	$\text{CH}_3\text{OH} + 1.5\text{O}_2 \rightarrow \text{CO}_2 + 2\text{H}_2\text{O}$	$R_4 = k_4 \cdot [\text{C}_{\text{CH}_3\text{OH}}]^{0.25} \cdot [\text{C}_{\text{O}_2}]^{1.5}$
<b>Ethanol</b>	$\text{C}_2\text{H}_5\text{OH} + 3\text{O}_2 \rightarrow 2\text{CO}_2 + 3\text{H}_2\text{O}$	$R_5 = k_5 \cdot [\text{C}_{\text{C}_2\text{H}_5\text{OH}}]^{0.15} \cdot [\text{C}_{\text{O}_2}]^{1.6}$
<b>Fuel oil</b>	$\text{C}_{19}\text{H}_{30} + 26.5\text{O}_2 \rightarrow 19\text{CO}_2 + 15\text{H}_2\text{O}$	$R_6 = k_6 \cdot [\text{C}_{\text{C}_{19}\text{H}_{30}}]^{0.25} \cdot [\text{C}_{\text{O}_2}]^{1.5}$

**Table 2 Arrhenius coefficients and combustion heat related to R<sub>1</sub>-R<sub>6</sub>**

Reaction	Equations	Low heating value
<b>R<sub>1</sub></b>	$k_3 = 2.119 \times 10^{11} \exp[2.027 \times 10^{08} / T]$	<b>50.001 MJ/kg</b>
<b>R<sub>2</sub></b>	$k_1 = 4.836 \times 10^{09} \exp[1.256 \times 10^{08} / T]$	<b>46.362 MJ/kg</b>
<b>R<sub>3</sub></b>	$k_3 = 4.161 \times 10^{09} \exp[1.256 \times 10^{08} / T]$	<b>45.594 MJ/kg</b>
<b>R<sub>4</sub></b>	$k_4 = 1.799 \times 10^{10} \exp[1.256 \times 10^{08} / T]$	<b>21.102 MJ/kg</b>
<b>R<sub>5</sub></b>	$k_5 = 8.439 \times 10^{09} \exp[1.256 \times 10^{08} / T]$	<b>28.079 MJ/kg</b>
<b>R<sub>6</sub></b>	$k_6 = 2.587 \times 10^{09} \exp[1.256 \times 10^{08} / T]$	<b>40.531 MJ/kg</b>

### 2.3 Boundary Conditions

The symmetry boundary condition is applied along the centerline of the combustor. At the exit of the tailpipe, the pressure is atmospheric and the remaining variables are calculated assuming far-field conditions, i.e., zero diffusive flux of species or energy normal to the exit. Non-slip conditions are prescribed on the walls. For the thermal wall condition, the heat loss through wall is calculated by considering the convective heat transfer between ambient air and hot wall,  $q_{wi} = h(T_{wi} - T_a)$ , where  $q_i$  is the heat flux from the  $i$ th wall cell of the grid,  $h$  is the whole convective heat-transfer

coefficient,  $T_{wi}$  is the temperature at the wall surface of the cell and  $Ta$  is the ambient temperature, which is assumed to be 300 K. Here, we set  $h = 120 \text{ W/m}^2\cdot\text{K}$ <sup>22</sup>

### 2.3.1 Inlet Boundary Condition

The flapper valves open and close alternatively during pulse combustion process depending on the pressure difference across the flapper. The valve closes when the pressure at the head end of the combustor,  $P_c$ , is greater than the pressure upstream of the valves ( $P_{in}$ ), taken in this study to be one atmosphere. In this condition, no fuel/air mixture enters the combustion chamber.

$$u = 0 \text{ when } \Delta P = P_{in} - P_c \leq 0 \quad (12)$$

When pressure at the head end drops below the pressure upstream of the valve, the flapper valve opens and fresh fuel/air mixture is drawn into the combustion chamber. Here, a simple relationship between the inlet velocity and the pressure difference across the valve of the following form is used:

$$\Delta P = \frac{1}{2} \xi \rho u^2 \Rightarrow u = \sqrt{\frac{2\Delta P}{\rho \xi}} \quad (13)$$

This expression has been used previously in pulse combustor studies by Tajiri and Menon<sup>16</sup>. Expressing the boundary condition in the form of Eq.13 introduces another parameter into the system, namely  $\xi$ , which physically represents the “willingness” of the valves to admit mass into the system. For example, a larger value of  $\xi$  (relative to some reference  $\xi$ ) translates into a lower inlet velocity, hence less mass injected into the combustor for a given pressure difference, whereas a smaller  $\xi$  allows for larger inflow velocities. The implications of this behavior will be discussed later in the section 3.1.3. The advantages of this method is that the mass flow is not set a priori, and can now adjust itself accordingly depending on the operating conditions. The mass flow rate of fuel/air mixture is calculated as

$$\dot{m} = \rho_{mix} A_{inlet} u \quad (14)$$

where  $\rho_{mix}$  is the density of mixture;  $A_{inlet}$  is the inlet port area of the flapper valve. The mixture has an initial temperature of 300 K and excess air ratio of 1.22.

## 2.4 Solution Procedure

The conservation equations were solved implicitly with a 2D unsteady-state segregated solver using an under-relaxation method. The pressure–velocity coupling is discretized using the “SIMPLE” method. The momentum, species, and energy equations are discretized using a second-order upwind approximation. When discretizing the momentum equation, the pressure field and face mass fluxes are not known a priori and the “standard” pressure interpolation scheme<sup>23</sup> was used here to compute the face values of pressure from the cell values. In this work, the time-step size of  $1 \times 10^{-6}$  s was selected in this simulation. In order to achieve convergence as well as to test grid independence of results, a volume-averaged pressure in the combustion chamber is defined and traced during the computation process. Figure 5 shows the convergence history of the chamber volume-averaged pressure. The pressure initially fluctuated significantly and then achieved a “cyclical steady” amplitude oscillation shown in Figure 5. The criteria to judge when the computation can be stopped is when the pressure amplitudes in the following cycles are the same (cyclical steady state). The calculation time for each case varied between one day and several days, depending on the complexity of the problem and the initial guess.

## 3. Simulations and Results

### 3.1 Baseline Case

A baseline run was first carried out for methane fuel, subject to the following boundary conditions: an inlet methane/air mixture gage pressure of 0 Pa (relative to ambient pressure), an excess air ratio of 1.22; account is taken of the heat loss as well.

### 3.1.1 Self-breathing Combustion Process

Figure 4 show the gas temperature contours in the combustion chamber, respectively, using the color maps to depict the contour values. The reaction rate contours show that the flame (a body of burning gas) is a narrow band surrounding the reactant mixture. During the inflow (Fig 4a-e), the hot remnant gases from the previous cycle ignited the fresh fuel –air mixture as it entered the combustors and the mixture gas deflected to the side wall. It is seen that the flame was anchored at two locations: the stagnation plate and the side wall near the inlet port. When the inlet port closes (Fig 4f-j), combustion continued but the flame structure collapsed slowly to a region near the inlet. Most of the gaseous fuel was completed before the inlet port re-open. There was still some unburnt mixture near the inlet that maintains the flame until the next cycle begins anew.

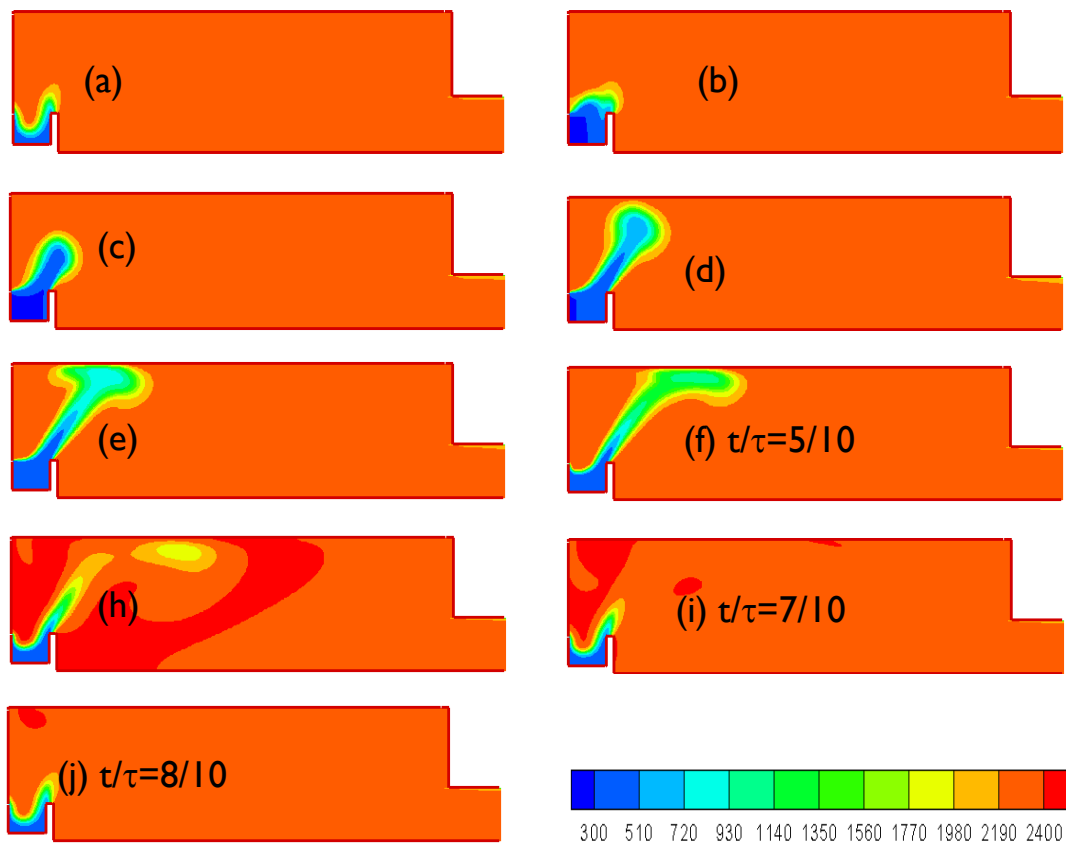


Figure 4: Time sequence of gas temperature contours in the combustor chamber (K)

Figure 5 shows the time evolution of the volume-averaged gas pressure, temperature and mass fraction of methane in the combustion chamber. The computed gage pressure varies from -6400 to 8800 Pa (relative to atmospheric pressure) with a peak-to-peak value of 15.2 kPa and its oscillation mode shape was nearly a cosine wave one. In Figure 5, similar oscillation modes are found for gas temperature and fuel concentration. The pressure oscillation mode was consistent with the measured ones in practical pulse combustors<sup>1-2</sup>, indicating that the predicted combustion process is a really periodic one (pulse combustion). Figure 5 also shows the phase relations between the instantaneous pressure, temperature and mass fraction of fuel in the combustion chamber. The temperature oscillation was ahead of the pressure oscillation by 30°

and was out of phase with the instantaneous mass fraction of propane. That is, the gas temperature reaches a peak when the mass fraction of methane reaches its minimum, indicating a phase delay between the heat release and the pressure wave. The predicted phase delay was consistent with the phase relation described by the Rayleigh' criterion for combustion-driven instability<sup>24</sup>. From Figure 5, the pulse frequency is calculated to be about 106 Hz.

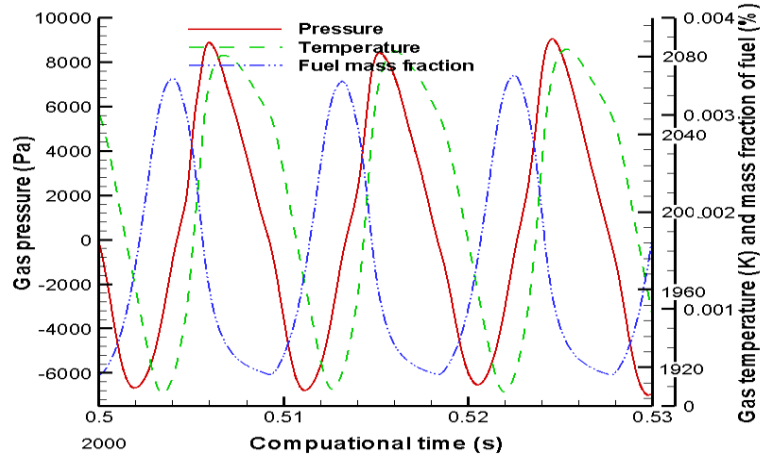


Figure 5 Time trace of the oscillating pressure, temperature and mass fraction of methane in the combustion chamber ( $\xi=25$ , methane-air mixture)

### 3.1.2 Gas Characteristics in the Pulse Combustor

Figure 6 shows the distribution of the peak-to-peak amplitude for gas pressure and velocity along axial distance from the inlet. The pressure amplitude decreases from 15.4 kPa initially to 0 kPa at the exit of the tailpipe, while the velocity amplitude increases from 2 m/s to 84 m/s. In the combustion chamber (axial distance <0.15m), both pressure and velocity amplitudes keep almost constant at different axial distances, indicating that the chamber can be regarded as a well-stirred reactor and its thermal properties are homogenous. At the inlet of tailpipe, the velocity amplitude reaches its minimum, while pressure amplitude reaches the maximum. Opposite phenomena happens at the outlet. The pressure mode shown in Figure 6 has a quarter-wave shape, which corresponds to the fundamental acoustic mode of a closed-open duct<sup>2</sup>. The above phenomena have also been observed in many actual pulse combustors<sup>1-3</sup>.

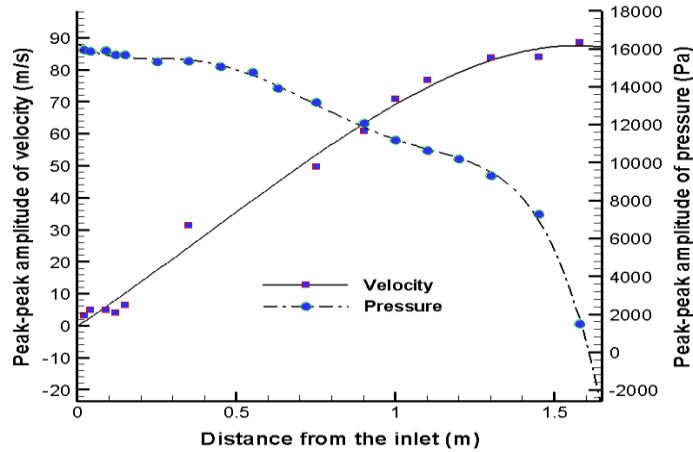


Figure 6 Peak-peak amplitude of gas pressure and velocity along combustor (Chamber length: 0.15 m, tailpipe length: 1.43m,  $\xi=25$ )

The mass flow rate of methane during a pulse cycle is plotted in Figure 7. It can be seen that the fuel is drawn into the chamber in only half of the pulse cycle. By integrating the area under the fuel influx curve shown in Figure 7, the average inflow rate of methane is calculated to be 0.1744 g/s. Taking the low heating value of methane as 50.01 MJ/kg, the power input of the pulse combustor is calculated to be 8.72 kW. Figure 7 also shows that during a pulse cycle, the exhaust gas velocity varied from -27 to 54 m/s with a mean velocity of 16.81 m/s. The phenomenon that negative flue velocity exists during a pulse cycle was verified by pulse combustion impingement heating experiments where the instantaneous flue velocity was measured<sup>10-11, 25</sup>. In these experiments, the negative part of flue velocity was reported to decrease the thermal efficiency.

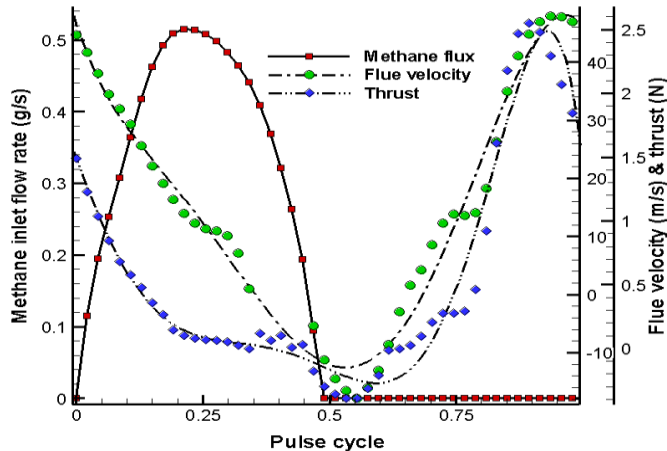


Figure 7 Predicted methane inlet flow rate, instantaneous flue velocity and thrust generated by the combustor during a pulse cycle

The instantaneous thrust generated by this combustor is also plotted in Figure 7. Here, the instantaneous thrust is defined as  $T_{thrust} = \int \rho V_x^2 dA$  where  $A_{exit}$  is the cross-area of the tailpipe exit plane. In Figure 7, the instantaneous thrust oscillates from -0.38 to 2.55 N with a cycle-averaged thrust of 0.5496 N. Thus, the thrust output-to-power input is calculated to be  $6.30 \times 10^{-2}$  N/kW. Another parameter is defined to evaluate how much thrust can be generated by unit fuel, that is, the specific impulse. In this case, the specific impulse is calculated to be 3150 N·s/kg.

### 3.2 Other Geometry Designs

Apart from GD1, the combustion performances were also evaluated for other GDs. For each GD, a series of numerical simulations have been carried out for different valve settings by varying the values of  $\xi$  and also for different fuel species. However, numerical results show that GD2, GD3 and GD4 have all been unable to successfully sustain pulse combustion except for GD 5. Figure 8 show the time evolution of the volume-averaged gas pressure in the combustion chamber for geometry designs 2-4. In Figure 8, the pressure oscillations damp out to zero with time, indicating the pulse or periodic combustion is not sustainable. It should be noted that the results shown in Figure 8 is only the 'best' results which have been selected out of the many results to be included in this study. The corresponding combustor operation conditions are: the three combustors operated on the gaseous fuel-methane.  $\xi$  is set at 30 for the fuel inlet and 10 for the air inlet for GD2. For GD3,  $\xi$  is set at 1800 for the fuel inlet and 10 for the air inlet, and the average fuel mass fraction is an order of magnitude less than GD2 due to a high value of  $\xi$  for the fuel inlet. For GD 4,  $\xi$  is set at 80 for the fuel inlet and 10 for the air inlet.

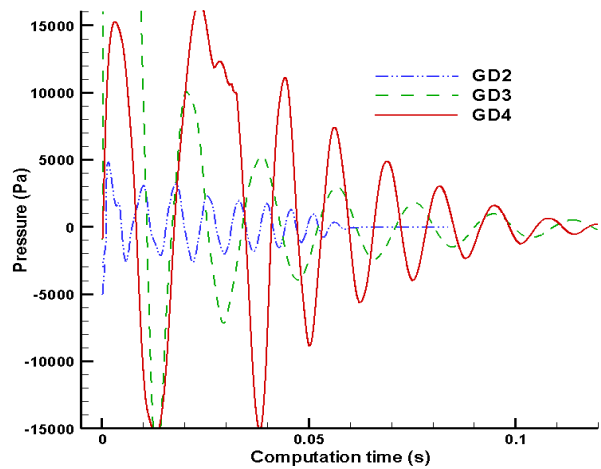


Figure 8 Time trace of the oscillating pressure in the combustion chamber fro GD 2-4 (Fuel: methane)

There could be many possible reasons for the new GDs being unable to sustain pulse combustion, such as the geometric and parametric setting, etc. a GD may have a totally new geometry in which a change in a particular dimension may render the GD being able to sustain pulse combustion, let alone a combination of new dimensions. Also, the selected operation conditions may be in the operable range of a pulse combustor. Nonetheless, while the results obtained in this study show that GD2, GD3 and GD4 are not able to sustain pulse combustion, these GDs may still be able to sustain pulse combustion under a 'yet to be discovered' combination of geometrical and parameter setting. From this point of view, mathematical model can reduce the unnecessary experimental trials during the novel pulse combustor design, to save the time and cost.

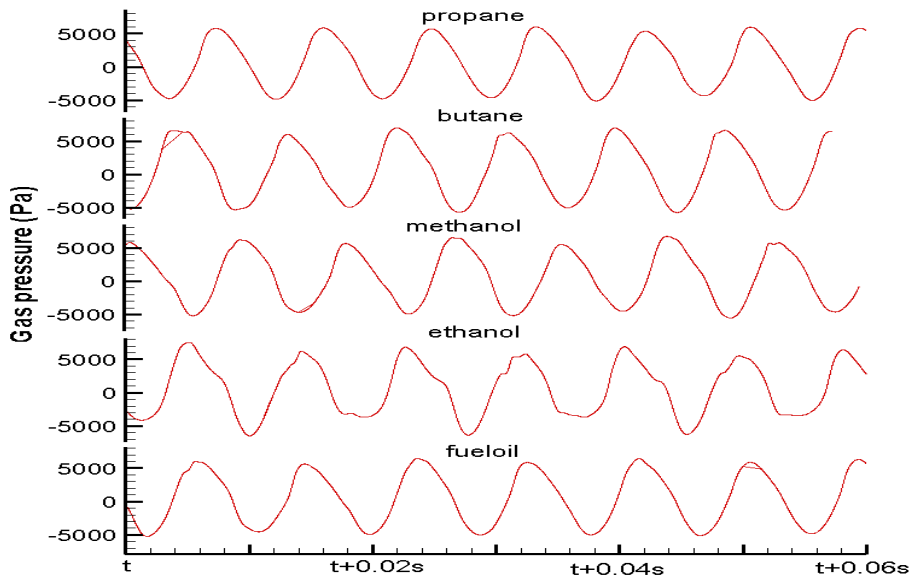


Figure 9 Gas pressure oscillations in the combustion chamber for different fuel species (propane, butane, methanol, ethanol, fuel oil)

### 3.3 Pulse Combustion Using Different Gaseous Fuels

Parametric studies were carried out to determine how various gaseous fuels perform in pulse combustors. The gaseous fuels selected are: propane, butane, methanol, ethanol and fuel oil. Methane, propane, butane represent low

molecular weight hydrocarbon; while fuel oil presents the high molecular weight one. Methanol and ethanol typically represent bio-fuels which are increasing in importance. Figure 9 shows the predicted gas pressure oscillation in the combustion chamber for these fuels. From Figure 9, it can be seen that the gas pressures vary periodically in the range of -6~7 kPa and their oscillation mode shapes follow a cosine wave one, indicating that these combustion processes are periodic ones. Thus, all these fuels can be used to drive a pulse combustor.

Table 3 summarizes the predicted operational characteristics of the pulse combustor using different fuels. No major differences can be seen in most of the operational parameters: pulse frequency, peak-to-peak gas pressure amplitude, average gas temperature in the chamber, average flue gas velocity, power input and thrust output to power input, indicating that these fuels achieve almost the same pulse combustion performance. The only major differences are in the specific impulse and fuel flow rate between fuels with low heating values (methanol, ethanol) and the ones with high heat values (propane, butane, fuel oil). Due to their low heating values, low specific impulse values are expected for methanol and ethanol. From Table 3, it seems that in this case of fuels with low heating values, pulse combustors will draw in more fuel mass to sustain their performance. For example, the mass flow rate into the combustor using methanol is 0.4789 g/s, about 2.5 times the propane flow rate. From this point of view, due to its self-breathing function, pulse combustors can adjust fuel intake automatically at least over a certain range, which makes them suitable for different gaseous fuels. Thus, a given pulse combustors can switch fuel as needed with minor change in performance.

Table 3 The operational characteristics of the pulse combustor using different fuels

Items	Propane	Butane	Methanol	Ethanol	Fuel oil
Frequencies (Hz)	116	113.8	114.1	120	112
Peak-peak pressure amplitude (Pa)	-5082 ~6035	-5676 ~6998	-5195 ~6176	-6351 ~6800	-5283 ~6404
Average temperature in chamber (K)	2094	2090	2075	2106	2070
Average flue velocity (m/s)	16.55	17.15	21.30	15.69	17.67
Fuel flow rate (g/s)	0.1929	0.1983	0.4789	0.3077	0.2162
Combustion heat (MJ/kg)	46.361	45.752	21.102	28.079	40.531
Power input (kW)	8.95	9.07	10.11	8.64	8.76
Average thrust (N)	0.4244	0.4453	0.5754	0.4018	0.4595
Specific impulse (N·s/kg)	2200	2250	1200	1310	2130
Thrust output /power input (n/kW)	$4.74 \times 10^{-2}$	$4.91 \times 10^{-2}$	$5.69 \times 10^{-2}$	$4.65 \times 10^{-2}$	$5.24 \times 10^{-2}$

### 3.4 Effect of Fuel Species and Valve Setting

Parametric studies were carried out to determine the effect of various gaseous fuels and inlet valve settings on the pulse combustion performance of GD 5. The gaseous fuels selected are methane, ethane and propane and the  $\xi$  is set to be 50, 75, 100 for both air/fuel inlet valves. Figure 10~11 shows the predicted gas pressure oscillation in the combustion chamber for these fuels and valve setting. From Figure 10~11, it can be seen that the gas pressures vary periodically in the range of -2~2 kPa and their oscillation mode shapes follow a cosine wave one, indicating that these combustion processes are periodic ones. As a result, GD5 is a new geometric design of a gas-fired pulse combustor which is able to successfully sustain pulse combustion.

Table 4 summarizes the predicted operational characteristics of the pulse combustor using different fuels and valve setting. From Table 4, it can be seen that when keeping the valve setting and changing the fuels, pulse frequency keeps almost constant; while the peak-to-peak gas pressure amplitude, average gas temperature in the chamber, power input and thrust output decrease slightly with the decreasing of heating value of gases fuels. When keeping the fuel and changing the

valve setting, pulse frequency, the peak-to-peak gas pressure amplitude, average gas temperature in the chamber decrease with the increasing of the  $\xi$  value. As a conclusion, pulse frequency is mainly influenced by the valve setting and other operation properties are affected by both fuel species and valve setting.

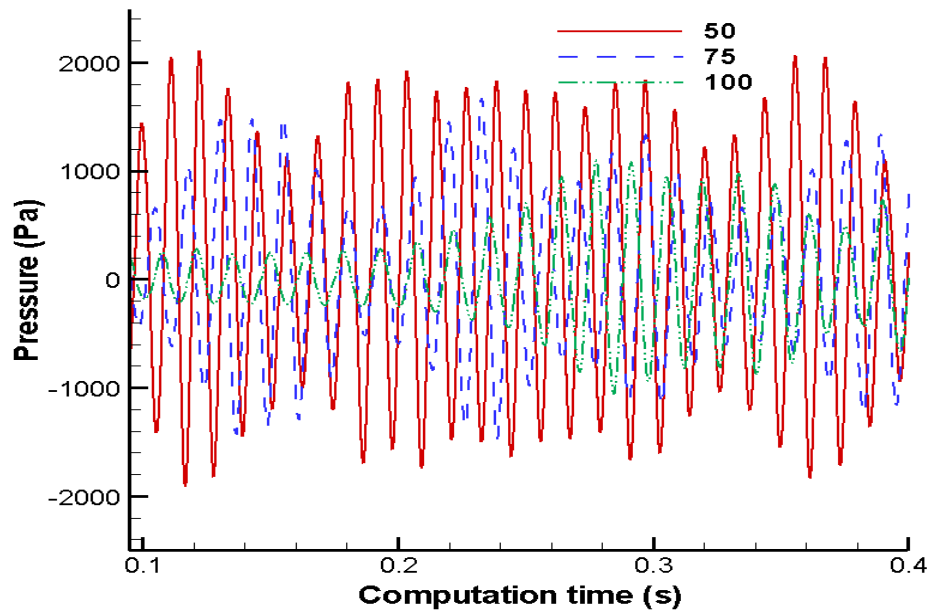


Figure 10 Time trace of the oscillating pressure in the combustion chamber for GD 5 (Fuel: ethane,  $\xi=50, 75, 100$  for fuel/air inlet valve)

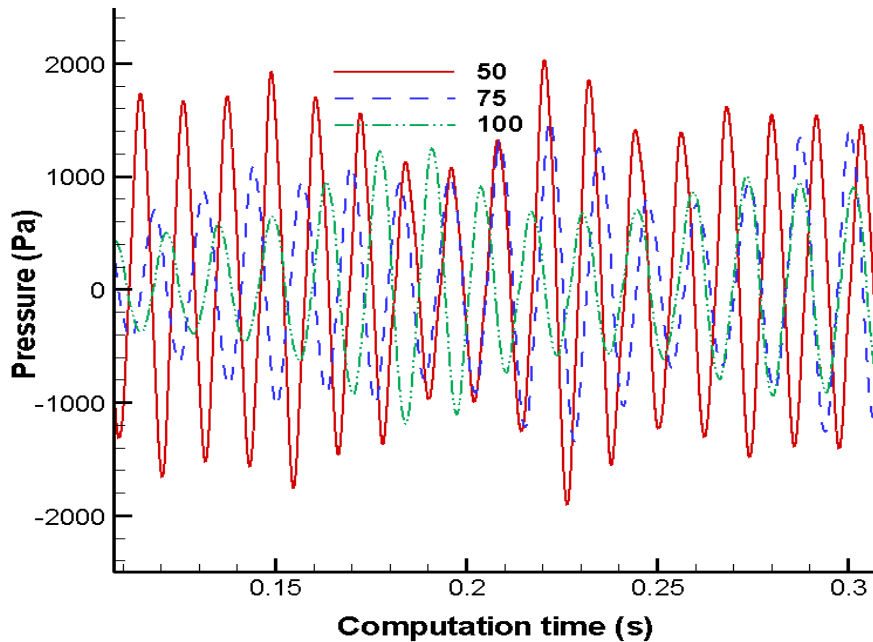


Figure 11 Time trace of the oscillating pressure in the combustion chamber for GD 5 (Fuel: propane,  $\xi=50, 75, 100$  for fuel/air inlet valve)

Table 4: The operational characteristics of the pulse combustor (GD5) under different fuels &amp; inlet valve settings

Parameters	Ethane			propane		
	$\xi=50$	$\xi=75$	$\xi=100$	$\xi=50$	$\xi=75$	$\xi=100$
Frequency (Hz)	84.7	76.9	71.4	84.7	76.9	69.4
Peak-to-peak pressure amplitude (Pa)	-1750 ~1900	-900 ~1100	-1040 ~1160	-1450 ~1650	-800 ~1000	-680 ~720
Average gas temperature in combustion chamber (K)	1745	1685	1677	1762	1685	1678
Phase difference between temperature and pressure oscillations (degree)	90	80	80	90	80	80
Air-to-fuel ratio	11.4:1	11:1	7.7:1	6.3:1	16.4:1	5.7:1
Fuel mass flow rate (g/s)	0.218	0.202	0.126	0.261	0.079	0.099
Power input (kW)	10.42	9.65	6.03	12.11	3.68	4.594
Thrust ( $N \times 10^{-2}$ )	8.11	4.12	5.07	8.11	3.62	3.10
Thrust output to power input ( $10^2 N/kW$ )	0.845	0.427	0.841	0.67	0.98	0.68
Specific impulse ( $N/kg s^{-1}$ )	404.1	203.9	401.7	310.7	455.9	312.8

#### 4. Concluding Remarks

The combustion process of a gas-fired pulse combustor was simulated using a CFD model to understand the flame structure, gas characteristics in the burner and the resulting pulsations. The numerical results satisfactorily compare with available experimental data. For the pulse combustion process, the following results are found:

1. During pulse combustion process, the flame extend and collapse periodically and there was still some unburnt mixture near the inlet that maintains the flame until the next cycle begins anew
2. The phase delay exists between the instantaneous pressure, temperature and mass fraction of fuel in the combustion chamber
3. The pressure mode in the combustor tailpipe has a quarter-wave shape, which corresponds to the fundamental acoustic mode of a closed-open duct.
4. The specific impulse and through output of pulse combustion are computed and a bit low compared with modern aircraft engines

Selected gaseous fuels such as low molecular weight hydrocarbons, high molecular weight hydrocarbons, bio-fuels and mixed fuels are tested for pulse combustion and their operational properties are presented and compared. It is observed that the combustor can self-adjust automatically at least over a certain range of parameters which makes it suitable for different gaseous fuels.

A series of tests have been conducted to find out the effectiveness of the new geometric design of the gas-fired pulse combustor. The new geometric design is tested with different air to fuel ratios by varying the fuel inlet velocity, as well as with different fuels like methane, ethane and propane. The test results revealed that the new geometric design is able to successfully sustain pressure oscillations for pulse combustion under the different types of settings in this study, and that the new geometric design works best with an air to fuel ratio of 15:1 and with methane as fuel.

## Acknowledgments

This work was jointly supported by M3TC at National University of Singapore.

## References

1. Zinn, B.T. *Mech. Eng. ASME*. **1985**, 107, 36-41.
2. Putnam, A.A.; Belles E.; Kentfield J.A.C. *Prog. Energy Combust. Sci.* **1986**, 12, 43-79.
3. Richards, G.A.; Morrs, G.J.; Shaw, D.W.; Keeler, S.A.; Welter, M.J. *Combust. Sci. Technol.* **1993**, 94, 57-85.
4. Zinn, B.T. Pulse Combustion: Recent Applications and Research Issues. Presented at 24th International Symposium on Combustion. the Combustion Institute, Pittsburgh, PA. **1992**, pp 1297-1305
5. Kudra, T.; Mujumdar, A. S. *Handbook of Industrial Drying*, Marcel Dekker: New York, 1995
6. Kudra, T.; Mujumdar, A.S. *Advanced drying technologies*, Marcel Dekker Inc: New York, 2002.
7. Wu, Z.H. *Mathematical Modeling of Pulse Combustion and its Applications to Innovative Thermal Drying Techniques*. Ph.D. thesis, National University of Singapore, Singapore, 2007
8. Keller, J.O.; Hongo I. *Combust. Flame*. **1990**, 80, 219-237.
9. Kentfield, J.A.C.; O'Blenes, M.J. *J. Propul.* **1990**, 6, 214-220.
10. Dec, J.E.; Keller, J.O.; Arpacı, V.S. *Int. J. Heat Mass Transfer*. **1992**, 35, 2311-2325.
11. Eibeck, P.A.; Keller, J.O.; Bramlette, T.T.; Sailor, D.J. *Combust. Sci. Technol.* **1993**, 94, 147-165.
12. Neumeier, Y., Zinn, B.T., Jagoda, J.I. *Combust. Sci. Technol.* **1993**, 94, 295-316.
13. Keller, J.O., Bramlette, T.T., Dec, J.E., Westbrook, C.K. *Combust. Flame*, **1989**, 75, 33-44.
14. Benelli, G., Michele de, G., Cossalter, V., Lio da, M., Rossi, G. *Proc. Combust. Inst.* **1992**, 24, 1307-1313.
15. Möller, S.I.; Lindholm, A. *Combust. Sci. Technol.*, **1999**, 149, 389-406.
16. Tarjiri, K.; Menon, S. *LES of Combustion Dynamics in a Pulse Combustor*. presented at 39<sup>th</sup> Aerospace Sciences Meeting and Exhibit, Reno, NV, January 8-13, 2001
17. Galletti, C.; Parente, A.; Tognotti, L. *Combust. Flame*, **2007**, 151, 649-664.
18. Norton, D.G.; Vlachos, D.G. *Combust. Flame*, **2004**, 138, 97-107.
19. Lebedevas, S.; Vaicekauskas, A. *Energ. Fuel*, **2006**, 20, 2274-2280
20. Westbrook, C.K.; Dryer, F.L. *Combust. Sci. Technol.* **1979**, 20, 125-140.
21. Magnussen, B. F.; Hjertager, B. H. *Proc. Combust. Inst.* **1976**, 16, 719-729.
22. Liu, X.D.; Cao, C.W.; Lang, Z.H. *Drying Technol.*, **2001**, 19, 1939-1948.
23. Rhee, C.M.; Chow, W.L. *AIAA J.* **1983**, 21, 1525-1532.
24. Rayleigh, J.W.S. *Theory of Sound*. Dover Publications: New York, 1945.
25. Liewkongsataporn, W.; Patterson, T.; Ahrens, F.; Loughran, J. Impingement Drying Enhance Using a Pulsating Jet. Presented at 15<sup>TH</sup> International Drying Symposium (IDS 2006), Budapest, Hungary, 20-23, August 2006

# ►[ INNOVATIVE DESIGNS OF HYDROCYCLONES WITH CFD MODEL]

## [Chapter 2]

**Peng Xu<sup>1,2</sup> and Arun S. Mujumdar<sup>1</sup>**

► [<sup>1</sup> Mechanical Engineering Department, National University of Singapore. <sup>2</sup>College of Science, China Jiliang University ]

The hydrocyclone is a mechanical separation device which is used widely in mineral processing. The solid particles in mineral slurries are separated according to their density, size and shape by the centrifugal force generated by an induced vortex motion in a cylinder-on-cone vessel. The larger and denser particles move closer to the wall region due to their greater inertia and descend by gravity; a higher concentration suspension is thus collected at the bottom of the hydrocyclone. While the cleaned liquid and hydrodynamically smaller particles exit through an overflow outlet at the top of the hydrocyclone. Higher velocities, within limit, generally yield higher collection efficiency. However, higher stream velocities cause severe erosion of the internal wall of hydrocyclones as mineral slurries generally are abrasive. The objective of this study is to use the computational fluid dynamic (CFD) technique to model the turbulent swirling flow and predict regions of significant wear and how they are influenced by design of the inlet ducting. New inlet designs and one novel design are proposed and investigated numerically for their erosion characteristics, pumping power requirements and collection efficiency. Successful innovation in hydrocyclone design will lead to high efficiency, reduced maintenance and operating energy costs, and lower wear-induced erosion in mineral processing.

## Innovative Designs of Hydrocyclones with CFD Model

### 1. Introduction

The hydrocyclone is an important and popular industrial apparatus to separate by centrifugal action dispersed solid particles from a liquid suspension fed to it. It has been widely used in industry, particularly in the mineral and chemical processing industries because of its simplicity in design and operation, high capacity, low maintenance and operating costs as well as its small physical size.<sup>[1,2]</sup> Recently, the application of hydrocyclone in the wet process of beneficiation has attracted more interest with the current boom in advanced mineral processing driven by the expanding mineral commodities markets and escalating energy costs. Therefore, the application of the hydrocyclone in mineral processing is investigated numerically to assist innovative design of hydrocyclones with high efficiency and reduced costs as well as lower wear-induced erosion in the current work. Although clearly very important from an economic standpoint this area which has received little attention in the literature on hydrocyclones.

A typical hydrocyclone consists of a cylindrical section with a central tube connected to a conical section with a discharge tube. An inlet tube is attached to the top section of the cylinder. The cone angle of the conical section varies widely in practice from 5° to 40°. There are two axial product outlets. The spigot is situated at the apex of the conical part and the vortex finder is located at the upper end of the cylindrical section and contains a tubes extending into the hydrocyclone. The tangentially injected fluid causes swirl, and the centrifugal force field so generated brings about separation of the particulate material from the medium in which it is suspended, based mainly on particle density, size and shape. Particles of sufficiently high settling velocity are centrifuged to the walls of the hydrocyclone and drained off as a concentrated solution through the spigot. Particles with a low settling velocity are carried away by an upward vortex which forms around the cyclone axis and is drained off by the vortex finder.

Although many efforts have been made to study experimentally the flow in hydrocyclones,<sup>[1-3]</sup> little detailed flow information was generated until the availability of Laser Doppler Anemometry (LDA) necessary to measure local fluid velocities within the hydrocyclone.<sup>[4-6]</sup> It is well known that the LDA technique is expensive, largely limited to the dispersed liquid phase, and at present suitable only for laboratory scale studies rather than industrial design and application. Hence empirical equations/models are often used by designers of hydrocyclones. However, empirical equations/models suffer from their inherent deficiency as they can only be used within the limits of the experimental data from which the empirical parameters were determined. No innovative changes can be predicted with empirical modeling. In view of these shortcomings, mathematical models based on the basic fluid mechanics are highly desirable to intensify innovation.

The CFD technique is gaining popularity in process design and optimization as it provides a good means of predicting equipment performance of the hydrocyclone under a wide range of geometric and operating conditions; it also offers an effective way to design and optimize the hydrocyclones. The first CFD model utilizing the standard  $k-\varepsilon$  turbulence model for a hydrocyclone was developed by Boysan et al.<sup>[7]</sup> The  $k-\varepsilon$  turbulence model intrinsically makes the assumption that the turbulence is isotropic because only one scalar velocity fluctuation is modeled. Furthermore, the Bousinessq approximation on which the eddy viscosity intrinsically relies implies equilibrium between stress and strain. Therefore, the  $k-\varepsilon$  turbulent model is not suitable to simulate a turbulent flow with high swirl, flow reversal and/or flow separation.<sup>[8]</sup> Many authors have adopted the renormalization group (RNG)  $k-\varepsilon$  model with a swirl correction to enhance the precision of simulations because it includes additional terms for the dissipation rate,  $\varepsilon$ , development which significantly improves the accuracy for rapidly strained flows.<sup>[9-12]</sup> However, Suasabar found that the swirl constant in the RNG  $k-\varepsilon$  model needs to be increased to improve predictions; this in turn can cause numerical instability.<sup>[13]</sup> Therefore, the application of the RNG  $k-\varepsilon$  model is also limited for modeling a hydrocyclone. The Reynolds stress model (RSM) solves the transport equation for each individual Reynolds stress, which enables RSM to model anisotropic turbulence and strained flows where the Bousinessq approximation is known to be invalid. Some recent studies indicate that RSM can improve accuracy of the numerical solution.<sup>[14-19]</sup> However, the predictions are not what they could be and there is debate about appropriate modeling options. Recent advances in computational power have begun to make large eddy simulation (LES) practical for engineering problems. LES is intrinsically a dynamic simulation and can capture time-dependent vortex oscillations and nonequilibrium

turbulence, which suggest that it should be appropriate for modeling hydrocyclone. Comparing with other turbulence models, LES provides better predictions including velocity, air core and separation efficiency.<sup>[16-17,20-21]</sup> Certainly, LES simulations of large industrial dense medium hydrocyclone will be computationally impractical except for a test case.<sup>[17]</sup>

A striking feature of the flow field is the presence of an air core in the hydrocyclone. At the central axis of the hydrocyclone, the low pressure developed supports formation of a rotating air column called the air core. The geometry and the stability of the air core have been empirically found to have a strong influence on the performance of the hydrocyclone.<sup>[2,17]</sup> In the mineral processing field, the air core dimension is a critical variable, since a large air core diameter leads to a condition known as "roping". As the interface between liquid and air phases is difficult to determine, the nature of air core is often neglected in many previous CFD modeling efforts,<sup>[20,23]</sup> or they work with a simplified assumption about its formation and behavior.<sup>[24,25]</sup> The volume-of-fluid (VOF) model has been proven to be an effective method for modeling the air core and predicting the formation and shape of air core.<sup>[14-18,21-22]</sup> For solids movement, an Eulerian-Lagrangian model has been successfully applied to dilute flow phenomena in a hydrocyclone.<sup>[8]</sup> In the last several decades, this field had advanced so much that Slack et al. proposed an automated tool for novice analysts to carry out simulations with standard CFD solvers.<sup>[26]</sup>

There is analogy between CFD modeling of liquid-particle swirling flow in a hydrocyclone and gas-droplet/particle flow that occurs in a cylinder-on-cone spray dryer. The latter includes heat and mass transfer which is not present in classification in a hydrocyclone which is a purely fluid dynamic problem. Interested readers are referred to the work of Huang et al. providing some useful insight into the relative performance of various turbulence models applied to swirling two-phase flow.<sup>[27-29]</sup>

Erosion of parts of the internal wall of the hydrocyclone is a critical issue in mineral dewatering both from both safety and economic considerations. The injected solids particles, such as sand and ore particles, impinge the inside surfaces of the components of the hydrocyclone, causing mechanical wear and eventual failure of the devices. Therefore, the ultimate goal in the design of hydrocyclone is not only to provide better performance, but also to be resistant to wear. As testing for erosion of industrial devices generally requires special equipment and methodology, CFD modeling has been widely adopted as an effective tool to predict the wear response at low price and without costly experimentation.<sup>[30-34]</sup> Although CFD modeling has been tested to estimate the erosion rate in a hydrocyclone with one novel inlet design, the results found in literature are very few and largely preliminary; they do not indicate in detail the effect of flow and geometry on the erosion rate.<sup>[35]</sup> Hence further modeling effort is needed for advancing our capability in predicting wear of hydrocyclones.

This work presents a CFD model of a hydrocyclone based on Fluent version 6.3. First, results using different turbulence models viz.  $k-\varepsilon$ , RSM and LES, are compared with published experimental results for a 75mm standard hydrocyclone.<sup>[36]</sup> The air core geometry is predicted using a VOF multiphase model. Then, the erosion rate for four designs of a 75mm hydrocyclone fitted with different inlets is calculated. Finally, one novel chamber design with a spiral feed inlet, bell shaped-vortex finder and a parabolic shaped body is proposed and analyzed numerically for its separation efficiency, pumping power requirements and erosion characteristics. The goal of the present study is to effect model-based innovation in equipment design to reduce costs and speed development of innovative solutions to real engineering problems.

## 2. Mathematical Models and Simulations

### 2.1 Turbulence Model

The turbulence model is the key component in the description of the fluid dynamics of the hydrocyclone. The free surface, air core and presence of solid particles make the swirling turbulent flow highly anisotropic; this adds to the difficulty for modeling hydrocyclones using CFD. Three kinds of turbulence models,  $k-\varepsilon$  model, RSM and LES, are often adopted for modeling the turbulent flow in hydrocyclones. The 75mm standard hydrocyclone is adopted to validate the current CFD models since relevant experimental data are available in the literature.

#### 2.1.1 $k-\varepsilon$ model

In mineral processing, the fluid suspensions are generally dilute (<10%), thus the incompressible Navier-Stokes equations supplemented by a suitable turbulence model are appropriate for modeling the flow in hydrocyclones. And the velocity components are decomposed into the mean  $\bar{v}$  and fluctuating  $v'$  velocities.

$$v_i = \bar{v}_i + v'_i \quad (2.1)$$

$$\frac{\partial \rho}{\partial t} + \rho \frac{\partial \bar{v}_i}{\partial x_i} = 0 \quad (2.2)$$

$$\frac{\partial(\rho \bar{v}_i)}{\partial t} + \frac{\partial(\rho \bar{v}_i \bar{v}_j)}{\partial x_j} = -\frac{\partial p}{\partial x_i} + \frac{\partial}{\partial x_j} (\mu \frac{\partial \bar{v}_i}{\partial x_j}) + \frac{\partial}{\partial x_j} (-\rho v'_i v'_j) + \rho g_i \quad (2.3)$$

where  $-\rho v'_i v'_j$  ( $i=1,2,3$ ) is the Reynolds stress term and includes the turbulence closure, which must be modeled in order to close Eq. (3). Eqs. (2) and (3) are steady-state conservation equations of mass and momentum, respectively. For the Reynolds stress term, there are different models which can be used to describe this term. For example,  $k-\varepsilon$  and RSM models have been applied in hydrocyclone with a great degree of success.

The  $k-\varepsilon$  model is a semi-empirical model based on model transport equations for turbulence kinetic energy  $k$  and its dissipation rate  $\varepsilon$  with the assumption that the flow is fully turbulent and the effects of molecular viscosity are negligible. Comparing with standard  $k-\varepsilon$  model, the RNG  $k-\varepsilon$  model includes additional terms for dissipation rate  $\varepsilon$  development which can significantly improve the accuracy for rapidly strained flows. The RNG  $k-\varepsilon$  model also provides an option to account for the effects of swirl or rotation by modifying the turbulent viscosity appropriately.<sup>[37]</sup> The turbulence kinetic energy  $k$  and its dissipation rate  $\varepsilon$  in RNG  $k-\varepsilon$  model can be obtained from the following equations:

$$\frac{\partial(\rho k)}{\partial t} + \frac{\partial(\rho k v_i)}{\partial x_i} = \frac{\partial}{\partial x_j} (\alpha_k \mu_{eff} \frac{\partial k}{\partial x_j}) + G_k + G_b - \rho \varepsilon - Y_M + S_k \quad (2.4)$$

$$\frac{\partial(\rho \varepsilon)}{\partial t} + \frac{\partial(\rho \varepsilon v_i)}{\partial x_i} = \frac{\partial}{\partial x_j} (\alpha_\varepsilon \mu_{eff} \frac{\partial \varepsilon}{\partial x_j}) + C_{1\varepsilon} \frac{\varepsilon}{k} (G_k + C_{3\varepsilon} G_b) - C_{2\varepsilon} \rho \frac{\varepsilon^2}{k} - R_\varepsilon + S_\varepsilon \quad (2.5)$$

In Eqs. (4) and (5),  $G_k$  and  $G_b$  are the generations of turbulence kinetic energy due to the mean velocity gradients and buoyancy respectively, and  $Y_M$  represents the contribution of the fluctuating dilatation in compressible turbulence to the overall dissipation rate. The quantities  $\alpha_k$  and  $\alpha_\varepsilon$  are the inverse effective Prandtl numbers for  $k$  and  $\varepsilon$ , respectively.  $S_k$  and  $S_\varepsilon$  are user-defined source terms, and  $C_{1\varepsilon}$ ,  $C_{2\varepsilon}$  and  $C_{3\varepsilon}$  are constants.

The RNG  $k-\varepsilon$  model provides an option to account for the effects of swirl or rotation by modifying the turbulent viscosity appropriately. The modification takes the following functional form:

$$\mu_t = \mu_{t0} f(\alpha_s, \Omega, \frac{k}{\varepsilon}) \quad (2.6)$$

where  $\mu_{t0}$  is the value of turbulent viscosity calculated without the swirl modification,  $\Omega$  is a characteristic swirl number, and  $\alpha_s$  is a swirl constant that assumes different values depending on whether the flow is swirl-dominated or only mildly swirling. The swirl modification always takes effect for axisymmetric, swirling flow and three-dimensional flow. The default value of swirl constant in Fluent is set for mildly swirling flow, thus, it has to be increased for strongly swirling flow in order to improve predictions, which will cause numerical instability.<sup>[38]</sup> The additional term  $R_\varepsilon$  in the  $\varepsilon$  equation (Eq. (5)) is the main difference between the standard and RNG  $k-\varepsilon$  models. The RNG  $k-\varepsilon$  model is more responsive to the effects of rapid strain and streamline curvature than the standard  $k-\varepsilon$  model, which explains the superior performance of the RNG  $k-$

$\varepsilon$  model for high swirling flow in hydrocyclone. Furthermore, the adoption of  $\mu_{eff}$  allows the RNG  $k-\varepsilon$  model to better handle low Reynolds number and near wall flows.

### 2.1.2 Reynolds Stress Model

The Reynolds stress model (RSM) closes the Reynolds-averaged Navier-Stokes equations (RANS) by solving transport equations for the individual Reynolds stresses without isotropic eddy-viscosity hypothesis and together with an equation for the dissipation rate. Since the RSM accounts for the effects of streamline curvature, swirl, rotation, and rapid changes in strain rate in a more rigorous manner, it has greater potential to give accurate predictions for complex flows in hydrocyclone. The RSM has been proven to be an appropriate turbulence model for hydrocyclone.<sup>[14-15,17-19]</sup>

The exact transport equations for the transport of the Reynolds stress term  $\rho \overline{v'_i v'_j}$  (see Eq. (3)) in RSM are written as:

$$\frac{\partial(\rho \overline{v'_i v'_j})}{\partial t} + \frac{\partial(\rho v'_k \overline{v'_i v'_j})}{\partial x_k} = D_{T,ij} + P_{ij} + \phi_{ij} + \varepsilon_{ij} \quad (2.7)$$

The four terms in the right of Eq. (7) are the turbulent diffusion  $D_{T,ij}$ , stress production  $P_{ij}$ , pressure strain  $\phi_{ij}$  and dissipation  $\varepsilon_{ij}$ , which can be expressed by Eqs. (8)-(11).

$$D_{T,ij} = -\frac{\partial}{\partial x_k} [\rho \overline{v'_i v'_j v'_k} + p(\delta_{kj} v'_i + \delta_{ik} v'_j)] \quad (2.8)$$

$$P_{ij} = -\rho \left( \overline{v'_i v'_k} \frac{\partial v_j}{\partial x_k} + \overline{v'_j v'_k} \frac{\partial v_i}{\partial x_k} \right) \quad (2.9)$$

$$\phi_{ij} = p \left( \frac{\partial v_i}{\partial x_j} + \frac{\partial v_j}{\partial x_i} \right) \quad (2.10)$$

$$\varepsilon_{ij} = -2\mu \frac{\partial v_i}{\partial x_k} \frac{\partial v_j}{\partial x_k} \quad (2.11)$$

where  $\delta$  is the Kronecker factor. In the simulation process of hydrocyclone, the standard linear pressure strain (LPS) model and quadratic pressure strain (QPS) model are often adopted. Narasimha et al. stated that the constants in the LPS correlation need to be adjusted to match the velocity predictions with data.<sup>[17]</sup> Comparing with the default LPS model, the QPS model has been demonstrated to give superior performance in a range of basic shear flow, including plane strain, rotating plane shear, and axisymmetric expansion/contraction. This improved accuracy should be beneficial for the complex flows in hydrocyclone.<sup>[14]</sup> Therefore, the QPS RSM is chosen in the current simulation.

### 2.1.3 Large Eddy Simulation

Large eddy simulation (LES) provides an alternative approach in which large eddies are explicitly resolved in a time-dependent simulation using the filtered Navier-Stokes equations. Velocity profiles of LES are resolved by a filtering operation of the velocity field, and the smaller scales or residuals are modeled in a particular manner. The velocity field is defined as the sum of the filtered velocity  $\bar{v}_i$  and the residual component  $\bar{v}'_i$ ,

$$v_i = \bar{v}_i + \bar{v}'_i \quad (2.12)$$

Applied Eq. (12) to the governing Navier-Stokes equations, the filtered Navier-Stokes equations are obtained, where an additional stress tensor appears.

$$\frac{\partial \rho}{\partial t} + \rho \frac{\partial \bar{v}_i}{\partial x_i} = 0 \quad (2.13)$$

$$\frac{\partial(\rho \bar{v}_i)}{\partial t} + \frac{\partial(\rho \bar{v}_i \bar{v}_j)}{\partial x_j} = -\frac{\partial p}{\partial x_i} + \frac{\partial}{\partial x_j} (\mu \frac{\partial \bar{v}_i}{\partial x_j}) - \frac{\partial \tau_{ij}^{sgs}}{\partial x_j} + \rho g_i \quad (2.14)$$

The filtered Navier-Stokes equations account for the transfer of momentum by subgrid scales of turbulence. The subgrid-scale stress  $\tau_{ij}^{sgs}$  is defined as

$$\tau_{ij}^{sgs} \equiv \rho \bar{v}_i \bar{v}_j - \rho \bar{v}_i \bar{v}_j \quad (2.15)$$

The subgrid-scale stresses resulting from the filtering operation are unknown, and require modeling. The subgrid-scale stresses are usually modeled using a simple eddy viscosity, that is the stresses are defined as the product of the eddy viscosity and the strain rate,

$$\tau_{ij}^{sgs} \equiv \rho \mu_t \left( \frac{\partial \bar{v}_i}{\partial x_j} + \frac{\partial \bar{v}_j}{\partial x_i} \right) \quad (2.16)$$

The simplest subgrid-scale model is the Smagorinsky-Lilly model (SLM). This model proposes that the subgrid-scale eddy viscosity is related to the local average grid spacing and the mean strain rate. The Fluent implementation makes the length scale equal to the distance from the wall  $d$  in wall bounded regions:

$$\mu_t = \rho L_s^2 \sqrt{2 \bar{S}_{ij} \bar{S}_{ij}} \quad (2.17)$$

where  $\bar{S}_{ij}$  is the strain rate and the mixing length for subgrid scales can be calculated by

$$L_s = \min(\kappa d, C_s V^{1/3}) \quad (2.18)$$

where  $\kappa$  is the von Kármán constant,  $C_s$  is the Smagorinsky constant, and  $V$  is the volume of the computational cell. The Smagorinsky constant is not an universal constant, which is the most serious shortcoming of this simple model. Brennan<sup>[16]</sup> and Narasimha et al.<sup>[17]</sup> adopted the SLM subgrid-scale model and took the Smagorinsky constant as the default value 0.1 in their large eddy simulation of hydrocyclone, and their numerical results give good agreement with experimental results.

LES is not well defined to solve the flow close to the walls. The renormalization group (RNG) subgrid-scale model is very effective to model the low-Reynolds-number effects encountered in transitional flows and near-wall regions where the molecular viscosity has more significance.<sup>[39]</sup> The turbulent viscosity is defined as the difference between the effective viscosity and the molecular viscosity:

$$\mu_t = \mu_{eff} - \mu \quad (2.19)$$

While the effective viscosity is defined as,

$$\mu_{eff} = \mu [1 + H(x)]^{1/3} \quad (2.20)$$

where  $H(x)$  is the Heaviside function defined as  $H(x) = x$  for  $x \geq 0$  and 0 for  $x \leq 0$ , and  $x$  can be expressed as  $x = \mu_s^2 \mu_{eff} / \mu^3 - 100$ . The turbulent viscosity,  $\mu_s$ , in the subgrid scale is defined as:

$$\mu_s = (C_{RNG} V^{1/3})^2 \sqrt{2 \bar{S}_{ij} \bar{S}_{ij}} \quad (2.21)$$

Delgadillo et al. have used the RNG subgrid-scale model in the large eddy simulation of hydrocyclone,<sup>[21,22,40]</sup> and they stated that the RNG LES model captures the dynamics of the flow in hydrocyclone and they have also proven that  $C_{RNG} = 0.157$  is the most acceptable value.<sup>[40]</sup> It should be pointed out that LES model requires highly accurate spatial and temporal discretization, finer mesh than a comparable RANS simulation, and more compute resources. And also, there are

still unanswered questions about appropriate subgrid-scale models for the multiphase flows encountered in mineral processing applications.

Therefore, four CFD models, RNG  $k-\varepsilon$ , QPS RSM, and SLM and RNG LES will be performed in 75mm standard hydrocyclone. And the numerical results will be compared with each other and that of experiment.

## 2.2 Multiphase Model

In the hydrocyclone, the centrifugal force generated by the tangential acceleration pushes the fluid to the wall and creates a low pressure in the central axis, which gives the right conditions to suck air into the device and form an air core. In the current simulation, the formation process, location and shape of the air core will be taken into account instead of neglecting it or making simple assumptions. The volume of fluid (VOF) free surface model is a simplification of the mixture model and has been successfully applied in predicting and modeling the air core in hydrocyclone.<sup>[14-18,21-22]</sup> The VOF model can simulate two or more immiscible fluid phases, in which the position of the interface between the fluids is of interest. In VOF method, the variable density equations of motion are solved for the mixture, and an additional transport equation for the volume fraction of each phase is solved, which can track the interface between the air core and the liquid in hydrocyclone. The single momentum equation is solved throughout the domain, and the resulting velocity field is shared among the phases. This momentum equation, shown below, is dependent on the volume fractions of all phases through the properties  $\rho$  and  $\mu$ .

$$\frac{\partial(\rho v_i)}{\partial t} + \frac{\partial(\rho v_i v_j)}{\partial x_j} = -\frac{\partial p}{\partial x_i} + \frac{\partial}{\partial x_j} [\mu (\frac{\partial v_i}{\partial x_j} + \frac{\partial v_j}{\partial x_i})] + \rho g_i \quad (2.22)$$

where  $\rho$  is the average density and can be calculated according to the density of  $q^{\text{th}}$  phase  $\rho_q$  and its volume fraction  $\alpha_q$  which varies between 0 and 1, as,

$$\rho = \sum \alpha_q \rho_q \quad (2.23)$$

The transport equation for the volume fraction of each phase is

$$\frac{\partial \alpha_q}{\partial t} + v_j \frac{\partial \alpha_q}{\partial x_j} = 0 \quad (2.24)$$

The simple VOF model has been adopted by most engineers for modeling the air core in hydrocyclone. And the comparison of Eulerian multiphase model and VOF by Brennan indicates that the velocity predictions using the two models are essentially the same.<sup>[16]</sup> Therefore, the air core will be resolved with VOF model in the current simulation. But for the dense slurry, the more sophisticated Eulerian multiphase model will be more suitable.

## 2.3 Particle Tracking

In most mineral processing operations, the solid phase is sufficiently dilute (<10%). Hence we can employ the discrete phase model (DPM), the fundamental assumption of which is that the dispersed second phase occupies a low volume fraction can be used to track solid particle movement. The Lagrangian DPM follows the Euler-Lagrange approach. The fluid phase is treated as a continuum by solving the time-averaged Navier-Stokes equations, while the dispersed phase is solved by tracking a large number of particles through the calculated flow field. The dispersed phase can exchange momentum, mass, and energy with the fluid phase.

The particle trajectories are computed individually at specified intervals during the fluid phase calculation. It can be predicted by integrating the buoyancy force and liquid drag force on the particle in a Lagrangian reference frame.

$$\frac{dv_p}{dt} = F_D(v - v_p) + \frac{g(\rho_p - \rho)}{\rho_p} \quad (2.25)$$

where  $v$  and  $v_p$  are velocity of fluid phase and particle,  $\rho$  and  $\rho_p$  are density of fluid and particle.  $F_D(v - v_p)$  is the drag force per unit particle mass and

$$F_D = \frac{18\mu}{\rho_p d_p^2} \frac{C_D \text{Re}}{24} \quad (2.26)$$

where  $d_p$  is the particle diameter, the particle Reynolds number is defined as  $\text{Re} \equiv \rho d_p |v_p - v| / \mu$ , and  $C_D$  is the drag coefficient.

The dispersion of particles can be accounted for with a stochastic tracking model, in which the turbulent dispersion of particles is predicted by integrating the trajectory equations for individual particles and using the instantaneous fluid velocity. Also, unsteady tracking is used, where at the end of each time step the trajectory is updated with the instantaneous velocity. As for the slurry feed concentrations in excess of 10% by volume, the DPM is not suitable and Eulerian multiphase model is more appropriate for tracking particles in hydrocyclone.

#### 2.4 Erosion Model

The impingement of solid particles with hydrocyclone walls can cause considerable wear, which is an issue of great industrial concern, both from safety and economic considerations. The damage induced by the erosion can cause equipment failure. Hence, estimation of potential erosion of the hydrocyclone wall is important to predict the lifetime of the equipment; it is useful to know how it is affected by geometry and different operating conditions. Because of experimental difficulties, CFD analysis is an effective tool to investigate the erosion rate of hydrocyclone.

Particle erosion and accretion rates can be computed at wall boundaries based on the following model equations. The erosion rate is defined as<sup>[44]</sup>

$$R_{erosion} = \sum_{p=1}^N \frac{\dot{m}_p C(d_p) f(\alpha) v^{b(v)}}{A} \quad (2.27)$$

where  $C(d_p)$  is a function of particle diameter,  $\alpha$  is the impact angle of the particle path with the wall face,  $f(\alpha)$  is a function of impact angle,  $v$  is the relative velocity,  $b(v)$  is a function of relative particle velocity, and  $A$  is the area of the cell face at the wall. The three functions  $C$ ,  $f$  and  $b$  can be defined as boundary conditions at the wall; however the default values are not updated to reflect the material being used. Therefore, these parameters have to be updated for different materials. It is known that one of the main parameters which influence the erosion rate is the particles impingement angle. The impingement angle function can be used as the following model and defined by a piece-linear profile<sup>[31,45]</sup>

$$f(\alpha) = \sin(2\alpha) - 3\sin^2(\alpha) \text{ for } \alpha \leq 18.43^\circ \quad (2.28a)$$

$$f(\alpha) = \cos^2(\alpha)/3 \text{ for } \alpha > 18.43^\circ \quad (2.28b)$$

To calculate the erosion rate from Eq. (1), the diameter function and velocity exponent function are adopted as 1.8E-09 and 1.73.<sup>[38,43,44]</sup> The CFD model records the number, velocity, mass and the impact angle of the various particles for each of the grids that form the internal geometry of the hydrocyclone. Then, the erosion rate of the hydrocyclone walls is determined using Eqs. (27) and (28). There are many parameters affecting the erosion rate, such as flow rate, design of the inlet, geometry and dimensions of the hydrocyclone and slurry properties etc. can affect the erosion rate, among which the inlet has a very important effect on the wear characteristics of hydrocyclone. Thus, as a preliminary work, we will calculate erosion rate for hydrocyclone with four different inlets and discuss the influence of the design of inlet ducting on wear characteristics of hydrocyclone.

#### 3. Simulations and Results

### 3.1 Model Validation

The simulations are performed using Fluent CFD software package (version 6.3.26). As noted earlier published experimental data on a 75mm standard hydrocyclone is used to validate the CFD model. Figure 2.1 shows the dimensions and computational mesh for the test hydrocyclone; Table 2.1 lists its geometrical parameters. The geometry used in the simulation is the same as that of the experiment;<sup>[36]</sup> also the same area of quadrate inlet is used. Four turbulence models RNG  $k-\varepsilon$ , QPS RSM, and SLM and RNG LES were tested. In the simulation, the velocity inlet boundary condition and pressure outlet boundary conditions are applied for the vortex finder and the spigot. The inlet flow rate is 1.12 kg/s and the pressure at the two outlets is 1 atm. The physical constants for the liquid phase were set as those of water. The solid particle density is 2700 kg/m<sup>3</sup> and its mass fraction is 4.8% at the inlet. The unsteady solver with time steps 10<sup>-4</sup>~10<sup>-6</sup>s was applied in the simulations. The second-order upwinding and SIMPLE pressure-velocity coupling algorithm were adopted. The flow field reaches steady state after about 2s, therefore, the simulated results presented here are those for 3s after simulation starts i.e. when the flow is steady. The flow problem is simulated with three-dimensional unstructured mesh of hexahedral cells. Trial numerical results indicated that the solution is independent of the characteristics of the mesh size. Combined with the VOF model, the air core can be predicted with each one of the four turbulence models for comparison. The erosion rate of the hydrocyclone with four different inlets was also predicted with the RNG LES model. In this section, the simulated flow field, air core and particle classification results are compared with experiment to validate the model. Moreover, a comparison between the experimental and the numerical results is also made for other variables of the hydrocyclone e.g. pressure drop and volume split ratio.

#### 3.1.1 Fluid Flow Field

Fig. 2.1(a) shows several representative streamlines in a 75mm standard hydrocyclone. It clearly indicates swirling flow pattern, and splitting overflow and underflow in hydrocyclone. In order to explore the inner flow field in hydrocyclone, three different horizontal planes situated 60, 120 and 170mm from the top wall of 75mm standard hydrocyclone are selected to give a general description of velocity field. On each plane, the axial and tangential velocity profiles are compared with those of the experimental results.

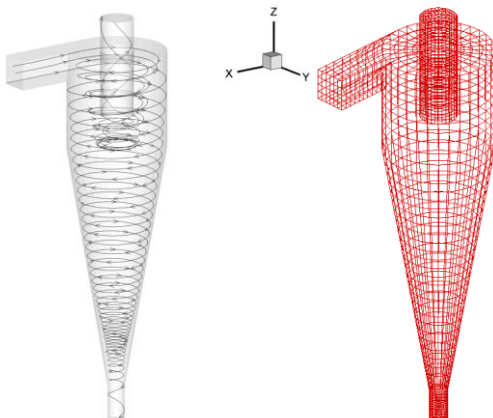


Figure 2.1: Schematic dimensions of standard hydrocyclone with stream line and grid representation used in simulation.

TABLE 2.1:  
Geometry of the 75mm standard hydrocyclone.

Parameter	Dimension
Diameter of hydrocyclone	75mm
Diameter of the inlet	25mm
Diameter of the vortex finder	25mm
Diameter of the spigot	12.5mm
Length of the cylindrical section	75mm
Length of the conical section	186mm
Length of vortex finder	50mm
Cone angle	20°

Figs. 2.2 (a) and (b) show the axial and tangential velocity profiles at 60mm from the top wall of the hydrocyclone, where four numerical results using RNG  $k-\varepsilon$ , QPS RSM, SLM LES and RNG LES turbulence models are compared with the experimental results. The four results are all close to the experimental ones, but the QPS RSM, SLM LES and RNG LES computations track the axial and tangential velocities more closely than the RNG  $k-\varepsilon$  one. It can be seen clearly that the predicted axial and tangential velocities near the wall are near zero because the no-slip boundary condition is used for the walls. For the axial velocity near wall, there is little difference between the numerical results and the experimental ones,

while for tangential velocity, the experimental value is nearly zero which is the same as numerical result. Also, because of the air core, the axial velocity near the central core of the hydrocyclone is quite high while the tangential velocity approaches 0, which are all consistent with the experimental results and the physical conditions.

Figs. 2.2 (c) and (d) describe the axial and tangential velocity profiles in the 120 mm plane. The difference between the predicted velocities with RNG  $k-\epsilon$  model and those of experiment is so large that it may be concluded that the RNG  $k-\epsilon$  model is not suitable for modeling the turbulent flow in a hydrocyclone. The predicted results of QPS RSM, SLM LES and RNG LES models are all similar to each other, and rather close to the experimental values. The predicted behavior near the wall and at the center of hydrocyclone is the same as that along the 60 mm plane.

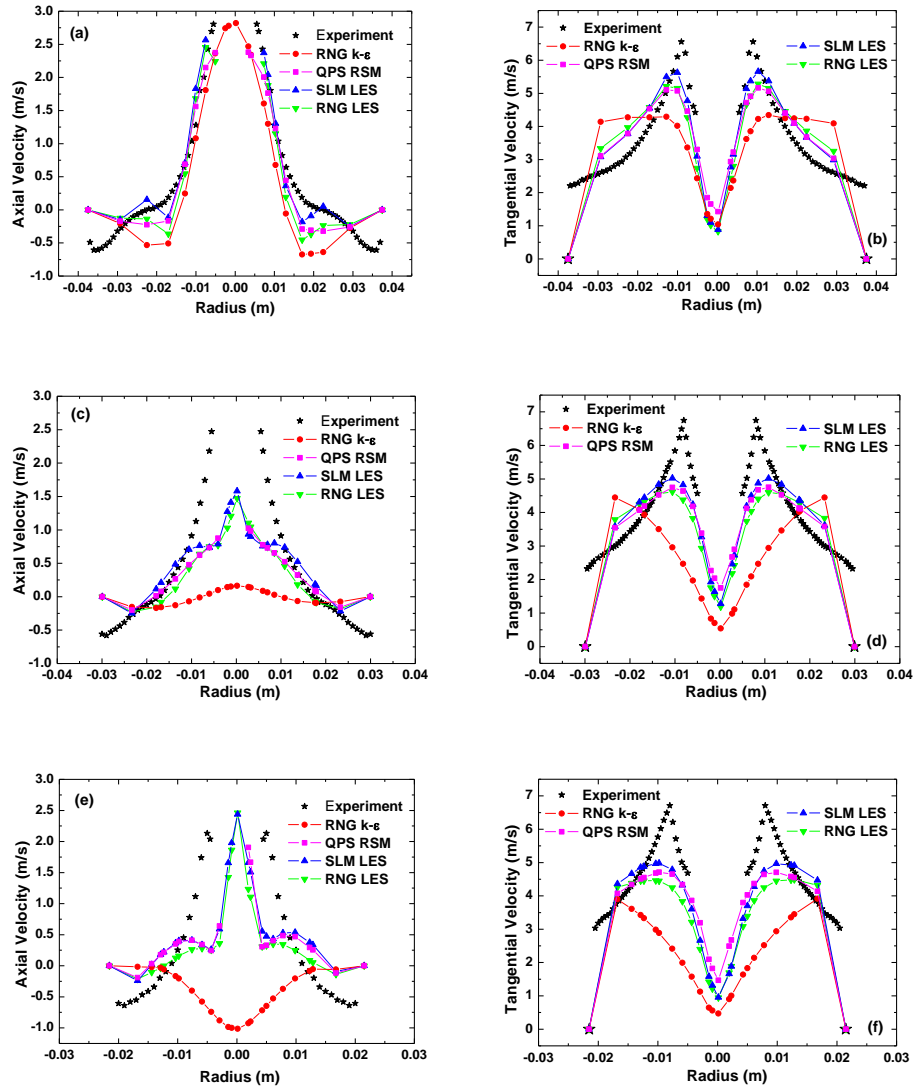


Figure 2.2: Axial and tangential velocity profile-comparison with experimental results at (a)-(b) 60mm, (c)-(d) 120mm, and (e)-(f) 170mm from the top wall of 75mm standard hydrocyclone.

Figs. 2.2 (e) and (f) display the axial and tangential velocity profiles in the 170mm plane. The predicted axial velocity with RNG  $k-\epsilon$  model is contrary to the experimental results (see Fig. 2.2 (e)). This can be explained from the fact that the flow near the central zone of the hydrocyclone is drained off due to the underflow because of the disappearance of the air core

(see Fig. 2.3), hence the predicted axial velocity approaches negative values. The close performances of QPS RSM, SML LES and RNG LES models can be found in Figs. 2.2 (e) and (f), which can better predict the turbulent flow in the hydrocyclone.

From above comparisons, it is seen that the predicted axial and tangential velocities of the RNG  $k-\varepsilon$  turbulence model are far from the experimental results while the performances of QPS RSM, SML LES and RNG LES models are close to each other and the experimental results. Therefore, we conclude that the RNG  $k-\varepsilon$  model is not suitable for modeling hydrocyclones while QPS RSM, SML LES and RNG LES models can capture the velocity profiles at different locations of the flow and can be used to model the hydrocyclone. Comparison between the latter three turbulence models indicates that although the QPS RSM and SML LES models perform better near the center, the RNG LES model can track the turbulent velocities near the wall better. Furthermore, the absolute error is little for the axial velocity and nearly zero for tangential velocity near wall. Although the no-slip boundary condition is adopted by most of current CFD models, more accurate wall boundary condition with suitable boundary layer mesh can be applied to improve the simulation results considering the error in axial velocity. Another point should be noted that the QPS RSM turbulence model combining with VOF multiphase model can lead to numerical stability, while the LES model consumes significantly more computing resources and times.

### 3.1.2 Formation of the Air Core

The ability to predict well the development of the air core in the hydrocyclone is a test of the CFD model. Figs. 2.3-2.6 show the predicted air core formation with RNG  $k-\varepsilon$ , QPS RSM, SLM LES and RNG LES turbulence models, respectively. Figure 2.3 indicates the evolution of the air volume fraction with the RNG  $k-\varepsilon$  model at real times from 0.02s to 3.0s. The variable of air volume fraction in the first second is distinct and then the air fraction changes are very minor. After the first second, a little change in the air volume fraction can be only found at the top end of hydrocyclone in the following one second. Between 2s to 3s, there is no variability of the air volume fraction. Further simulations indicate that the flow varies little after 1s and reaches steady state after 2s. It can be seen from Fig. 2.3 that the air core is formed at about 0.6s and then disappears; the predicted air core diameter with RNG  $k-\varepsilon$  model is 0.2. The numerically computed air core diameter of Delgadillo et al. with RNG  $k-\varepsilon$  model is 0,<sup>[21,40]</sup> which is much closer to the current results. Thus, the RNG  $k-\varepsilon$  model cannot predict the air core in a hydrocyclone, which is its major weakness.

Fig. 2.4 exhibits the air core formation with the QPS RSM turbulence model. The air core is formed in the first second and remains steady after 2s. A nearly parabolic shape of the air core is well predicted by QPS RSM turbulence model, which agrees well with the experimental data. The predicted air core diameter is about 10.6 mm, which is very close to the experimental value of 10mm. Figs. 2.5 and 2.6 show the air core development with SLM and RNG LES turbulence models. The similar formation process as QPS RSM model can be found in Figs. 2.5 and 2.6. Comparing with the air core with RSM model, the shape of air with LES is more regular and closer to the experimental shape. The predicted diameter is 11.5 and 10.45mm for SLM LES and RNG LES respectively. The error of SLM LES is large than 10%, and that of RNG LES is less than 5%.

The general mass balances are also calculated and compared with experiments as listed in Table 2.2. The experimental split ratio of the 75mm standard hydrocyclone is 95.1%, while the predicted split ratio with the RNG  $k-\varepsilon$ , QPS RSM, SLM LES and RNG LES turbulence models is 78.75%, 95.7%, 95.6% and 92%, respectively. For pressure drop, the experimental result is 46.7kPa, while the numerical results are 38.3, 41.1, 40.2 and 38.4 kPa, respectively. The experimental and numerical air core diameters are also listed in Table 2.2. In all, QPS RSM, SLM LES and RNG LES can be used for modeling a hydrocyclone. Considering numerical stability of RSM and relatively high accuracy near the wall of RNG LES turbulence model, the RNG LES will be adopted in the calculating erosion rate of hydrocyclone.

## 3.2 Erosion Rate

### 3.2.1 Effect of feed inlet on erosion rate

The centrifugal effect is one of major affection for separation efficiency of particles,<sup>[42]</sup> while the geometry of inlet has important influences on centrifugal effect. The geometry of the feed inlet can also affect energy consumption.<sup>[46]</sup>

Furthermore, the geometry of feed inlet is also one of important conditions affecting the erosion rate of the hydrocyclone. Therefore, we will presented four hydrocyclones with different feed inlets to simulate and calculate the erosion rate. Although the standard inlet as shown in Fig. 2.7(a) is very common in mineral processing, it does not perform so well in wear resistance despite its popularity. Therefore, three hydrocyclones with different inlets were tested for the erosion rate they are subject to with all parameters being fixed. Fig. 2.7 shows the detailed inlet geometry and dimension for the four cases. In order to compare the effect of the inlet geometry on the erosion rate, the same fluid and particle velocity 2.25m/s are adopted for each case, the flow rate of solid particles is set as 0.05kg/s, particle diameter is  $11.5\mu\text{m}$ . In calculation of the erosion rate of hydrocyclone, the interactions of the solid particles and the continuous phase need to be taken into account.

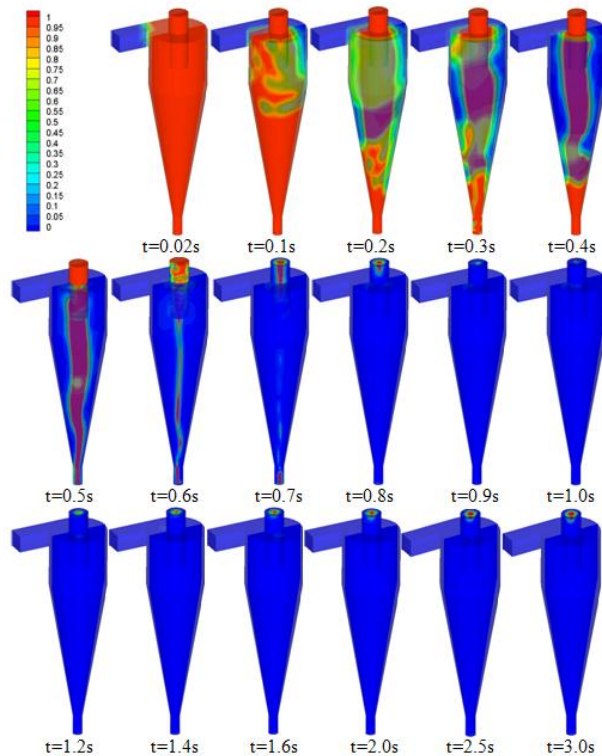


Figure 2.3: The predicted air volume fraction and air core formation with RNG k- $\varepsilon$  turbulence model from time 0-3s.

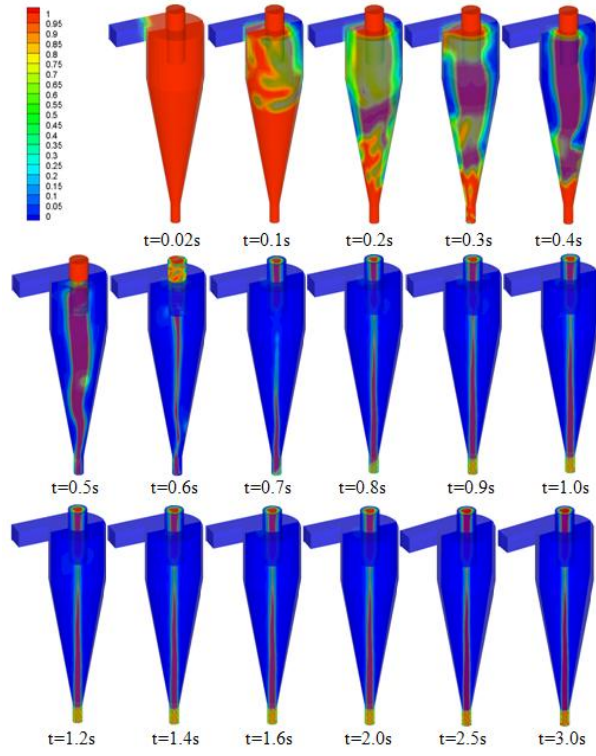


Figure 2.4: The predicted air volume fraction and air core formation with QPS RSM turbulence model from time 0-3s.

TABLE 2.2.  
General mass balance for four different turbulent models

	Experiment	RNG k- $\varepsilon$	QPS RSM	SLM LES	RNG LES
Feed flow rate (kg/s)	1.117	1.12	1.12	1.12	1.12
Overflow flow rate (kg/s)	1.062	0.882	1.072	1.071	1.03
Underflow flow rate (kg/s)	0.055	0.238	0.058	0.053	0.09
Split ratio (%)	95.1	78.75	95.7	95.6	92.0
Pressure drop (kPa)	46.7	38.3	41.13	40.2	38.4
Air core diameter (mm)	10.0	0.2	10.6	11.5	10.45

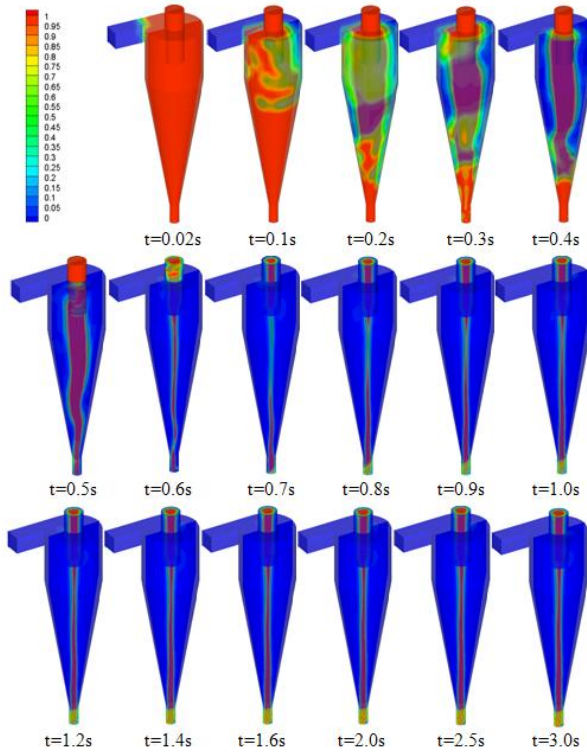


Figure 2.5: The predicted air volume fraction and air core formation with SLM LES turbulence model from time 0-3s.

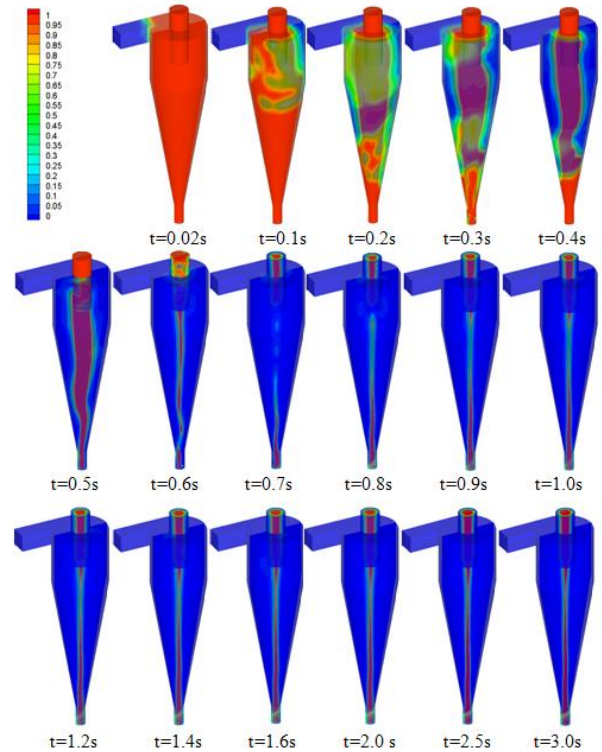


Figure 2.6: The predicted air volume fraction and air core formation with RNG LES turbulence model from time 0-3s.

Fig. 2.8 displays the variations of erosion rate of standard hydrocyclone (Fig. 2.7(a)) with time from 0.1s to 0.9s. At the beginning, the erosion rate on the wall of hydrocyclone is not very obvious because the solid particles have not yet reached the inner body of the device (fig. 2.8(a)). With the particles injected into the device, more and more particles collide the wall inducing distinct wear (fig. 2.8(b)). Two wear “hot spots” can be found at the intersection of the cylindrical and conical sections and the middle part of conical section. At the hot spot in the middle part of conical section, the erosion rate is more than  $1E-4 \text{ kg}/(\text{m}^2\text{s})$ , which is a very high value. Thus, this hot spot will cause device failure. After 0.1 second, wear occurs at vortex finder and spigot as well, and the latter is more obvious than the former one. Note that the erosion rates at the bottom of conical and spigot are very high. From 0.2s, the bottom of vortex finder begins to appear wear zone, and from 0.3s the wear phenomena of vortex finder is more and more distinct with increasing finer ores escape from it. It can be seen from fig. 2.8 that there is hardly any wear in the inlet ducting. The erosion rate variation in the first 0.2s is very sharp but the development later on is not obvious.

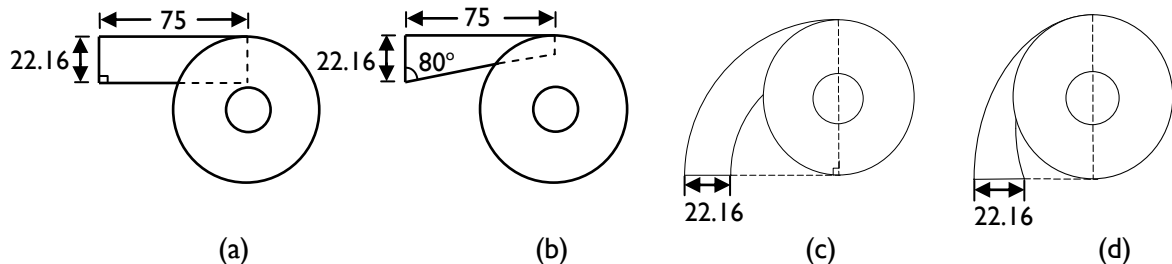


Figure 2.7: Four hydrocyclones with different inlet duct designs: (a) standard tangential inlet, (b) modified tangential inlet, (c) circular involute inlet and (d) elliptical involute inlet.

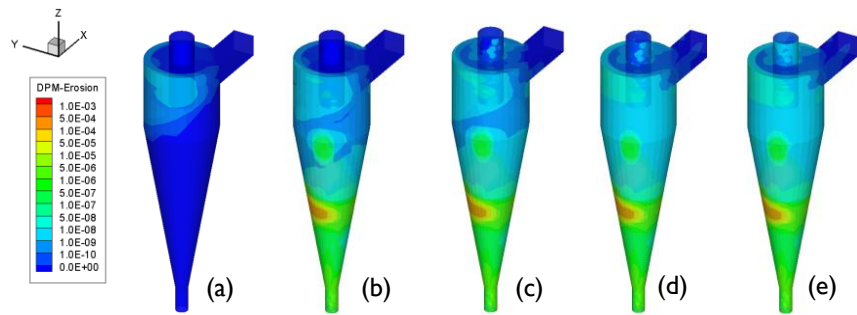


Figure 2.8: Surface plots of the computed local erosion rates in the modeled hydrocyclone with a standard tangential inlet at various times: (a) 0.1s, (b) 0.2s, (c) 0.3s, (d) 0.6s and (e) 0.9s.

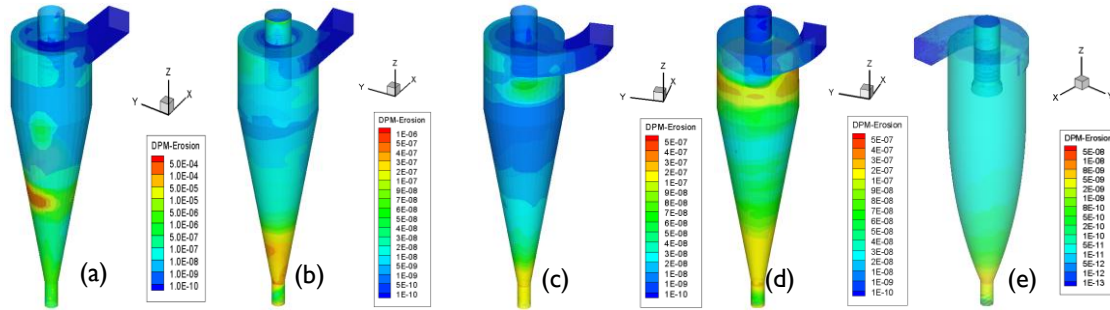


Figure 2.9: Erosion rates of tested standard hydrocyclone fitted with standard (a) and modified (b) tangential inlets, circular (c) and elliptical (d) involute inlets; (e) erosion rate of new design.

Figs. 2.9 (a)-(d) shows the erosion rate of the inner wall of the simulated hydrocyclones fitted with different inlets. Table 2.3 lists the maximum and average erosion rates and computed pressure drop for each case. Although the standard hydrocyclone with tangential inlet (fig. 2.9(a)) has been widely used in mineral processes, the erosion rate for it is the highest compared with the other three designs. Also, obvious wear hot spot can be found at the bottom of the cone section, where the erosion rate is very high. The maximum and integral erosion rates are 3.72E-4 and 1.87E-6 kg/(m<sup>2</sup>s), respectively. However, the pressure drop is the lowest, 32.8 kPa. For the modified tangential inlet (fig. 2.9(b)), there is no obvious wear hot spot, but the erosion rate is still high compared with the involute inlet. The maximum and average erosion rates are 7.61E-7 and 4.72E-8 kg/(m<sup>2</sup>s), respectively, and the pressure drop is very high (81.7kPa). For the involute inlet which can provide a smooth transition from pressure energy to rotational momentum, the distribution of erosion rate is relatively uniform and the value is low. For the circular involute inlet, the maximum computed erosion rate is only 4.32E-7 kg/(m<sup>2</sup>s) and the average value is 2.91E-8 kg/(m<sup>2</sup>s) while for the elliptical involute inlet, the maximum and integral erosion rates are 4.37E-7 and 3.90E-8 kg/(m<sup>2</sup>s), respectively. Moreover, the pressure drop of circular involute inlet (45.7kPa) is much smaller than that of elliptical involute inlet (72.3kPa). It can be seen from fig. 2.9 that the erosion rate at the inlet is nearly zero, while the erosion rate for conical section and spigot is much higher than that of cylindrical section and vortex finder.

TABLE 2.3.  
Computed Erosion rate for four inlet duct designs

Inlet	Pressure drop (kPa)	Maximum Erosion rate (kg/(m <sup>2</sup> s))	Face average erosion rate (kg/(m <sup>2</sup> s))
Standard tangential inlet	32.8	3.72E-4	1.84E-6
Modified tangential inlet	81.7	7.62E-7	4.72E-8
Circular involute inlet	45.7	4.32E-7	2.91E-8
Elliptical involute inlet	72.3	4.37E-7	3.90E-8
Innovative design	53.4	9.55E-9	3.57E-10

### 3.2.2 Novel Design

Generally, the feed fluid stream collides with the spiraling fluid causing turbulence for the tangential inlet design; this causes significant separation inefficiency. Therefore, the spiral feed inlet which produces a smooth transition from pressure energy to rotational momentum without the fluid flow stream colliding with the inlet flow is adopted in the new design. Furthermore, the bell-shaped vortex finder tube can increase acceleration of the rotating fluid at a critical moment. The acceleration rapidly moves the heavier solids toward the hydrocyclone walls, which reduces the possibility of mixed density solids leaking or short-circuiting through the overflow. Additionally, the parabolic shaped body of the hydrocyclone provides a gentler slope from the cylindrical section to the apex orifice. The large cross-sectional area of the parabolic shaped body contributes to a stable laminar flow and a reduction in plugging. The geometry of the new design can be found in fig. 2.9(e).

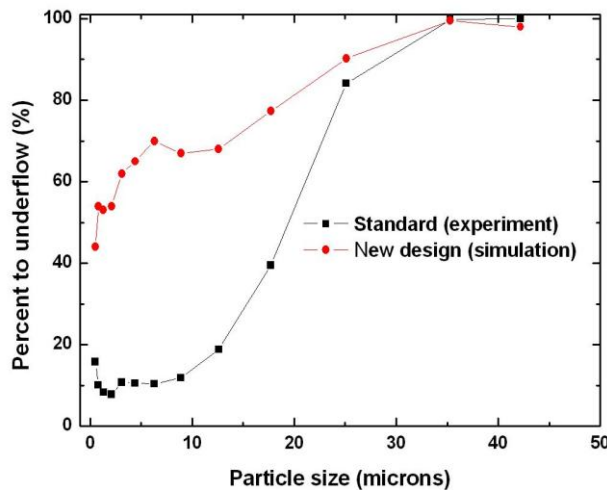


Figure 2.10: Particle separation efficiency compared with standard design.

The numerical split ratio for the new design is 98.55%, the pressure drop is about 53.4kPa, the predicted air core diameter is 12.6mm. As compared with the standard hydrocyclone design, the split ratio increases at the cost of a small increase in the pressure drop. The air core diameter is also larger than that of the standard one; thus, some methods such as inserting a central solid should be considered in the new design to reduce the adverse influence of the air core. We also compare the axial and tangential velocities with that of standard design on three planes. Numerical results indicate that the axial velocities of the standard and new one are close while the tangential velocity of the new design is larger than that of standard one on 60mm plane, which can attribute to the smooth transition of spiral inlet. On the following two planes, the axial velocity of the new design is much higher than the standard one and the difference of axial velocity from centre to wall is larger. This can be explained by the function of bell-shaped vortex finder. The tangential velocity along the 120 and 170mm planes of the new design is larger than that for the standard one, which is a result of the joint action of the spiral inlet and the parabolic shaped body. From fig. 2.10, although the by-pass of the fine particles increases, the classification of coarse particles can be greatly improved when compared with standard design.

For the erosion rate, it can be seen from fig. 2.9(e) that the erosion rate of the new design is much lower and more uniform than that in the standard one; moreover, there is no obvious hot spot in the proposed new design. The maximum and integrated erosion rates are 9.55E-9 and 3.57E-10 kg/(m<sup>2</sup>s), respectively. According to above discussion, successful innovation in hydrocyclone design can thus lead to reduced maintenance and lower operating energy costs and longer wear life. Further work is ongoing to find better designs for greater efficiency at lower cost. is ongoing to find better designs for greater efficiency at lower cost.

#### 4. Concluding Remarks

Four turbulence models, RNG  $k-\varepsilon$ , QPS RSM, SLM LES and RNG LES, were used to predict the aerodynamic performance of a 75mm standard hydrocyclone. The comparison of numerical and experimental results indicates that the RNG  $k-\varepsilon$  turbulence model is not suitable for modeling highly swirling flows in hydrocyclones, while QPS RSM, SML LES and RNG LES models can capture well the velocity profiles and predict the formation of air core. With a VOF multiphase model, the air core formation was analyzed in detail and the diameter of steady air core was successfully predicted. The effects of inlet on the erosion rate were investigated with the RNG LES model. The involute inlet can eliminate the wear hot spot and lower the level of concentrated wear. The proposed novel design with a spiral feed inlet, bell shaped-vortex finder and a parabolic shaped body can present better separation efficiency and very low erosion rate at cost of little increased pressure drop. This is only a preliminary study of the design and optimization process concerning erosion rate of a hydrocyclone. In future study, other parameters and conditions such as inlet flow rate, particle characteristics etc. which can affect erosion rate will be investigated as all of the performance parameters should be taken into account for good design and operation of the hydrocyclone and to increase its service life.

#### Acknowledgments

This work was jointly supported by the Foundation for Study Abroad of Education of Ministry of China and M3TC at National University of Singapore.

#### References

1. Bradley, D. *The Hydrocyclone*; Pergamon Press: London, 1965.
2. Svarovsky, L. *Hydrocyclones*; Holt: Rinehart and Winston, 1984.
3. Lilge, E.O. Hydrocyclone fundamentals. *Transactions Institution Mining Metallurgy* **1962**, *71*, 285-337.
4. Dabir, B.; Petty, C.A. Measurement of mean velocity profiles in a hydrocyclone using laser Doppler anemometry. *Chemical Engineering Communications* **1986**, *48*, 377-388.
5. Hsieh, K.T.; Rajamani, R.K. Mathematical-model of the hydrocyclone based on physics of fluid-flow. *AIChE Journal* **1991**, *37*, 735-746.
6. Dai, G.Q.; Chen, W.M.; Li, J.M.; Chu, L.Y. Experimental study of solid-liquid two-phase flow in a hydrocyclone. *Chemical Engineering Journal* **1999**, *74*, 211-216.
7. Boysan, F.; Ayers, W.H.; Swindenbank, J. Fundamental mathematical-modelling approach to cyclone design. *Chemical Engineering Research and Design* **1982**, *60*, 222-230.
8. Ma, L.; Ingham, D.B.; Wen, X. Numerical modelling of the fluid and particle penetration through small sampling cyclones. *Journal of Aerosol Science* **2000**, *31*, 1097-1119.
9. Fraser, S.M.; Rasek, A.M.; Abdel; Abdullah, M.Z. Computational and experimental investigations in a cyclone dust separator. *Journal of Process Mechanical Engineering* **1997**, *211*, 247-257.
10. He, P.; Salcudean, M.; Gartshore, I.S. A numerical simulation of hydrocyclones. *Chemical Engineering Research and Design* **1999**, *77*, 429-441.
11. Schuetz, S.; Mayer, G.; Bierdel, M.; Piesche, M. Investigations on the flow and separation behaviour of hydrocyclones using computational fluid dynamics. *International Journal of Mineral Processing* **2004**, *73*, 229–237.
12. Narasimha, M.; Sriprya, R.; Banerjee, P.K. CFD modelling of hydrocyclone--prediction of cut-size. *International Journal of Mineral Processing* **2005**, *71*, 53–68.
13. Suasnabar, D.J. *Dense Medium Cyclone Performance, enhancements via computational modeling of the physical process*; PhD Thesis, University of New South Wales, 2000.
14. Cullinan, J.C.; Williams, R.A.; Cross, C.R. Understanding the hydrocyclone separator through computational fluid dynamics. *Chemical Engineering Research and Design* **2003**, *81*, 455-465.

15. Cullivan, J.C.; Williams, R.A.; Dyakowski, T.; Cross, C.R. New understanding of a hydrocyclone flow field and separation mechanism from computational fluid dynamics. *Minerals Engineering* **2004**, *17*, 651-660.
16. Brennan, M. CFD simulations of hydrocyclones with an air core: Comparison between large eddy simulations and a second moment closure. *Chemical Engineering Research and Design* **2006**, *84*, 495-505.
17. Narasimha, M.; Brennan, M.; Holtham, P.N. Large eddy simulation of hydrocyclone—prediction of air-core diameter and shape. *International Journal of Mineral Processing* **2006**, *80*, 1-14.
18. Wang, B.; Chu, K.W.; Yu, A.B. Numerical study of particle—Fluid flow in hydrocyclone. *Industrial & engineering chemistry research* **2007**, *46*, 4695-4705.
19. Hsu, Chih-Yuan; Wu, Rome-Ming. Hot zone in a hydrocyclone for particles escape from overflow. *Drying Technology* **2008**, *26*, 1011-1017.
20. Souza, F.J.; Neto, A.S. Preliminary results of large eddy simulation of a hydrocyclone. *Thermal Engineering* **2004**, *3*, 168-173.
21. Delgadillo, J.A.; Rajamani, R.K. A comparative study of three turbulence-closure models for the hydrocyclone problem. *International Journal of Mineral Processing* **2005**, *77*, 217-230.
22. Delgadillo, J.A.; Rajamani, R.K. Exploration of hydrocyclone designs using computational fluid dynamics. *International Journal of Mineral Processing* **2007**, *84*, 252-261.
23. Nowakowski, A.F.; Cullivan, J.C.; Williams, R.A.; Dyakowski, T. Application of CFD to modeling of the flow in hydrocyclones. Is this a realizable option or still a research challenge? *Minerals Engineering* **2004**, *17*, 661-669.
24. Monredon, T.C.; Hsieh, K.T.; Rajamani, R.K. Fluid-flow model of the hydrocyclone—an investigation of device dimensions. *International Journal of Mineral Processing* **1992**, *35*, 65-83.
25. Rajamani, R.K.; Devulapalli, B. Hydrodynamics modeling of swirling flow and particle classification in large-scale hydrocyclones. *KONA Powder and Particle Journal* **1994**, *12*, 95-103.
26. Slack, M.D.; Del Porte, S.; Engelman, M.S. Designing automated computational fluid dynamics modeling tools for hydrocyclone design. *Minerals Engineering* **2003**, *17*, 705-711.
27. Huang, L.X.; Kumar, K.; Mujumdar, A.S. A parametric study of the gas flow patterns and drying performance of co-current spray dryer: Results of a computational fluid dynamics study. *Drying Technology* **2003**, *21*, 957-978.
28. Huang, L.X.; Kumar, K.; Mujumdar, A.S. Simulation of a spray dryer fitted with a rotary disk atomizer using a three-dimensional computational fluid dynamic model. *Drying Technology* **2004**, *22*, 1489-1515.
29. Huang, L.X.; Mujumdar, A.S. Numerical study of two-stage horizontal spray dryers using computational fluid dynamics. *Drying Technology* **2006**, *24*, 727-733.
30. Bozzini, B.; Ricotti, M.E.; Boniardi, M.; Mele, C. Evaluation of erosion-corrosion in multiphase flow via CFD and experimental analysis. *Wear* **2003**, *255*, 237-245.
31. Mazur, Z.; Campos-Amezcua, R.; Urquiza-Beltrán, G.; García-Gutiérrez, A. Numerical 3D simulation of the erosion due to solid particle impact in the main stop valve of a stream turbine. *Applied Thermal Engineering* **2004**, *24*, 1877-1891.
32. Chen, X.; McLaury, B.S.; Shirazi, S.A. Application and experimental validation of a computational fluid dynamics (CFD)-based erosion prediction model in elbows and plugged tees. *Computers & Fluids* **2004**, *33*, 1251-1272.
33. Amezcua, A.C.; Muñoz, A.G.; Romero, C.A.; Czerwic, Z.M.; Amezcua, R.C. Numerical investigation of the solid particle erosion rate in a steam turbine nozzle. *Applied Thermal Engineering* **2007**, *27*, 2394-2403.
34. Sciubba, E.; Zeoli, N. A study of sootblower erosion in waste-incinerating heat boilers. *Journal of Energy Resources Technology* **2007**, *129*, 50-53.
35. Olson, T.J.; Van Ommen, R. Optimizing hydrocyclone design using advanced CFD model. *Minerals Engineering* **2004**, *17*, 713-720.
36. Hsieh, K.T. *Phenomenological Model of the Hydrocyclone*; Ph.D. Thesis, University of Utah, USA, 1988.
37. Yakhot, A., Ozag, S.A., Renormalization group analysis of turbulence: I. Basic theory. *Journal of Scientific Computing* **1986**, *1*, 1-51.
38. Suasnabar, D.J., Dense Medium Cyclone Performance, enhancements via computational modeling of the physical process. PhD Thesis, University of New South Wales, 2000.

39. Yakhot, A., Ozag, A., Yakhot, V., Israeli, M. Renormalization group formulation of large eddy simulations. *Journal of Scientific Computing* **1989**, 4, 139-158.
40. Delgadillo, J.A. *Modeling of 75- and 250mm Hydrocyclones and Exploration of Novel Designs Using Computational Fluid Dynamics*; PhD Thesis, University of Utah, USA, 2006.
41. Fluent V6.3, *User's guide*. Fluent Inc.: Centerra Resource Park, 10 Cavendish Court, Lebanon NH 03766, 2006.
42. Finnie, I. Erosion of surfaces by solid particles. *Wear* **1960**, 3, 87–103.
43. Edwards, J.K.; McLaury, B.S.; Shirazi, S.A. Evaluation of alternative pipe bend fittings in erosive service. *Proceedings of ASME FEDSM'00: ASME 2000 Fluids Engineering Division Summer Meeting*, Boston, FEDSM 2000-11251, 2000.
44. Edwards, J.K.; McLaury, B.S.; Shirazi, S.A. Modeling solid particle erosion in elbows and plugged tees. *Journal of Energy Resources Technology* **2001**, 123, 277-284.
45. Hwang, Kuo-Jen; Hsueh, Wei-Sheng; Nagase, Youichi. Mechanism of particle separation in small hydrocyclone. *Drying Technology* **2008**, 26, 1002-1010.
46. Chu, Liang-Yin; Qin, Jian-Jun, Chen, Wen-Mei, Lee, Xiao-Zhong. Energy consumption and its reduction in the hydrocyclone separation process. III. Effect of the structure of flow field on energy consumption and energy saving principles. *Separation Science and Technology* **2000**, 35, 2679-2705.

## ► [ AERODYNAMIC AND THERMAL CHARACTERISTICS OF A MAXWELL TYPE VORTEX TUBE]

### [Chapter 3]

**S.M.A. Rahman<sup>1,2</sup> and Arun S. Mujumdar<sup>1</sup>**

► [<sup>1</sup> Mechanical Engineering Department, National University of Singapore. <sup>2</sup> Department of Mechanical Engineering, Monash University]

A three-dimensional (3D) computational fluid dynamic simulation of a vortex tube is carried out to examine its flow and thermal characteristics. The aim of this work is to model the performance and capture the highly swirling compressible flow behavior inside the tube and gain basic understanding of the well known temperature separation process. Simulations are carried out using the standard k- $\varepsilon$ , k-omega, RNG k- $\varepsilon$  and swirl RNG k- $\varepsilon$  turbulence models. An experimental setup was built and tested to validate the simulation results. The predicted results suggest that the RNG k- $\varepsilon$  turbulence model yield better agreement between the numerical predictions and experimental data. The model captures the essential features of the flow including formation of the outer vortex and the inner reverse vortex flow. Flow and geometric parameters that affect the flow behavior and energy separation are studied numerically. Effects of the inlet pressure, with and without an insert in the tube, are examined by numerical experiments.

## Aerodynamic and Thermal Characteristics of a Maxwell Type Vortex Tube

### 1. Introduction

Vortex or swirl flows are of considerable practical interest because of their frequent occurrence in industrial applications, such as furnaces, gas turbines, combustors and dust collectors.<sup>[1]</sup> The vortex tube is a simple device with no moving parts that is capable of separating a high pressure flow into two lower pressure flows of different temperatures one cooler than the inlet fluid temperature and the other hotter. Despite the simplicity of the vortex tube, the energy phenomenon causing separation cooler and into a hotter gas streams is quite complex and not yet fully understood.

Recent efforts have successfully utilized computational fluid dynamic (CFD) modeling to explain the fundamental principle behind the energy separation generated within the vortex tube. An application of CFD model for simulation of a strongly swirling flow using a modified k- $\epsilon$  turbulence model to investigate the flow characteristics and energy separation effect on the vortex tube was carried out by Liu et al.<sup>[2]</sup> They simulated the energy separation effect and the numerical solutions agreed well with their experiments. Eiamsaard and Promovonge<sup>[3]</sup> applied the algebraic Reynolds stress model (ASM) for simulation of a vortex tube and found that the use of ASM results in more accurate prediction relative to the k- $\epsilon$  model. Vortex tube modeling was carried out by Behera et al.<sup>[4]</sup> using the Star-CD code with renormalization group (RNG) version of the k- $\epsilon$  model. They investigated the effect of different types and number of nozzles on energy separation in a counter-flow vortex tube using CFD modeling and experiments. Aljuwayhel et al.<sup>[5]</sup> studied the energy separation mechanism and flow phenomena in a counter-flow vortex tube using Fluent code using both the standard k- $\epsilon$  and the RNG k- $\epsilon$  models. This is contrary to the results of Skye et al.,<sup>[6]</sup> who claimed that the standard k- $\epsilon$  model performs better than the RNG k- $\epsilon$  model although both used the same commercial CFD code.

The application of a mathematical model for the simulation of thermal separation in a Ranque-Hilsch vortex tube was carried out by Eiamsaard and Promovonge.<sup>[7]</sup> A staggered finite volume approach with the standard k- $\epsilon$  turbulence model and an algebraic stress model (ASM) was used. Their computations showed good agreement of the algebraic stress model (ASM) predictions with their experimental results.

The fundamental mechanism of energy separation has been well documented by some investigators.<sup>[5]</sup> However, due to lack of reliable measurements of the internal temperature and velocity distributions, there is still need for more effort to capture the real phenomena in a vortex tube. A 3D simulation is clearly a good option to capture well the complex flow phenomena in the vortex tube. Literature results revealed that only a few investigators have been worked on 3D simulation of vortex tube. This work was undertaken to fill a gap in our knowledge of the 3D flow in a vortex tube and obtain experimental data for validation. Due to complexities encountered only limited data could be obtained, however.

This study was motivated by our recent development of a novel atmospheric freeze drying apparatus using a vortex tube to generate a subzero air flow as described in Rahman and Mujumdar.<sup>[8,9]</sup> A recent review by Claussen et al.,<sup>[10]</sup> describes the advantages of the AFD process. A vortex tube was used to supply cold air in laboratory scale experiments of AFD of several fruits, fish, meat etc.<sup>[9]</sup> The COP of a vortex tube is far lower than the COP of a vapor compression cycle, which is the main drawback of this device. However, this is a cheap, compact and simple device which produces both heating and cooling effects simultaneously without using only compressed air at moderate pressure. Therefore, this device can be used effectively in process environments like in AFD process, where heating and cooling outputs of vortex tube can be used concurrently; the hot stream can be used to supply the sublimation heat.

In this work results of a 3D CFD model are presented. It captures the aerodynamics and temperature separation effect in a commercial Maxwell-type vortex tube. Three different turbulence models were studied. An experimental setup was developed to compare the predicted results with experimental data.

### 2. Vortex Tube Geometry

The vortex tube of the ‘Maxwell Demon’ type was chosen to study the flow characteristics and temperature separation. A photograph and a schematic diagram of the vortex tube are shown in fig 3.1 and fig 3.2, respectively. The 14.4 cm

working tube length was used as the boundary geometry for the CFD model. The hot and cold tubes are of diverging conical shape with areas of about  $0.23 \text{ cm}^2$  and  $0.07 \text{ cm}^2$  for the inner and outer hot air exits, respectively, while  $0.07 \text{ cm}^2$  and  $0.12 \text{ cm}^2$  for the cold air exits, respectively. The main part of the vortex tube called the generator plays an important role in generation cooler temperature. The generator as well as the vortex tube consists of 6 rectangle shaped nozzles. The nozzles were oriented at an angle of  $9^\circ$  with respect to the tangent around the periphery of the generator. The width, length and height of each nozzle are 0.2 cm, 14.4 cm, and 0.73 cm, respectively. Lengths of the hot and cold tube are 11.5 cm and 2.9 cm, respectively. All the dimensions were measured using high precision digital slide calipers. The geometric dimensions of the vortex tube are summarized in tab 3.1.



Figure 3.1: Photograph of the vortex tube.

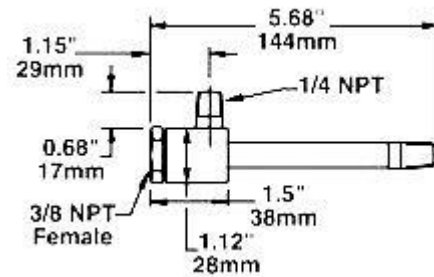


Figure 3.2: Schematic of the vortex tube.

TABLE 3.1.  
Geometric measurement of vortex tube and fluid properties

Tube characteristics	
Tube length towards hot outlet, $L_h$	1.5 cm
Tube length towards cold outlet, $L_c$	2.9 cm
Tube diameter hot end (inner side), $D_{hi}$	1.08 cm
Tube diameter hot end (outer side), $D_{ho}$	0.6 cm
Tube diameter cold end (inner side), $D_{ci}$	0.6 cm
Tube diameter cold end (outer side), $D_{co}$	0.8 cm
No of nozzles at the inlet	6
Nozzle diameter, $D_n$	0.2 cm
Inlet fluid properties	
Fluid	Compressed air
Temperature, $T_{in}$ (K)	25°C
Supply pressure before nozzle	2-3 bar

### 3. Turbulence Model

In this study the Renormalization Group (RNG) version of the  $k-\varepsilon$  model, the RNG with swirl and the standard  $k-\varepsilon$  model were investigated for comparison. The RNG  $k-\varepsilon$  turbulence model is derived from the instantaneous Navier-Stokes equation using a mathematical technique called the renormalization group. The RNG  $k-\varepsilon$  model is similar in form to the standard  $k-\varepsilon$  model but includes the effect of swirl on the turbulence intensity and calculates, rather than assumes, a turbulent Prandtl number.<sup>[11]</sup>

### 4. Solution Procedure

The computational domain of the vortex-tube flow system simulated is illustrated in fig 3.3. In the present computation the Navier-stokes equations, energy equation are solved numerically by a finite-volume method together with the

turbulence model equations. The commercial CFD model Fluent 6.2<sup>[12]</sup> was used to solve the governing equations. Swirling components were activated in swirl RNG k-ε turbulence model. The SIMPLE algorithm was selected for pressure-velocity de-coupling and iterations.

The discretization of the governing equations is accomplished by a first-order upwind scheme. The air entering the tube is modeled as an ideal gas of constant specific heat capacity, thermal conductivity, and viscosity. The under-relaxation iterative line by line iterative technique is used for solving the resultant finite-difference equations. Due to the highly non-linear and coupling features of the governing equations for swirling flows, low under-relaxation factors e.g. 0.24, 0.24, 0.24, and 0.2 were used for pressure, momentum, turbulent kinetic energy and energy, respectively, to ensure the stability and convergence of the iterative calculation. The convergence criterion for the residual was set at  $1 \times 10^{-5}$  for all the equations.

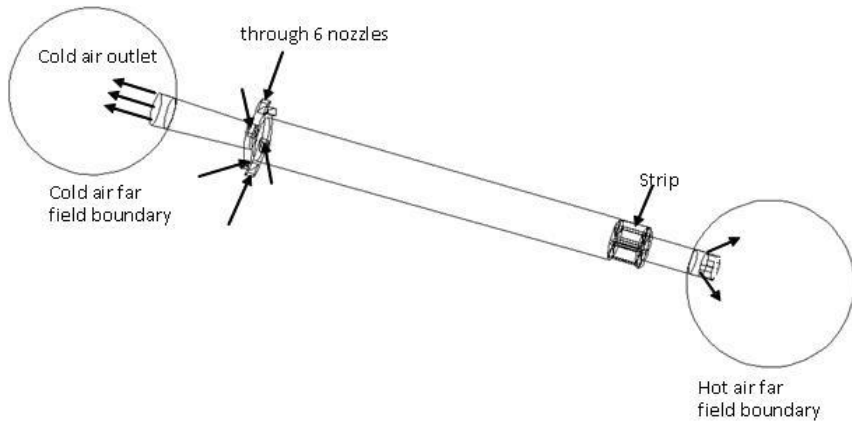


Figure 3.3: Computation domain of the vortex tube.

## 5. Grid Dependence Study

To eliminate error due to coarseness of the grid, tests were carried out for different number of unit cells in the vortex tube. The variation of the key parameters such as static temperature for different cell volumes was investigated. Investigations of the mesh density showed that the model predictions are insensitive to the number of grids above 600,000. Therefore, a mesh consisting of 650,000 grid elements was used to produce the results shown in this paper.

## 6. Boundary Conditions

Basic assumptions for all the computations of the vortex-tube flow are as follows: three dimensional, steady state, subsonic flow inside the vortex tube, uniform fluid properties at the inlet and the fluid is an ideal gas. In the inlet region, stagnation boundary condition of the vortex tube with total pressure was in the range of 4 to 6 bar and total temperature of 300 K. The inlet consists of as 6 discrete nozzles as in the experimental setup. The hot exit outlet is considered as an axial outlet as in the original vortex tube design. In the computational domain shown in fig. 3.3 the air enters the vortex tube axially through the nozzles with a significant tangential velocity. Far field boundary layer is the recommended boundary condition at outlet for an ideal gas in turbulent flow. Therefore, far field boundary layer was adopted in this work at the cold and hot outlets. The vortex tube is well insulated. Therefore, in the present computations as adiabatic wall condition was applied along with no slip condition at the wall.

## 7. Experimental Apparatus

A schematic of the layout of the experimental rig is shown in fig. 3.4. It consists of a screw compressor, a vortex tube cooler, a micrometer, two clamping stand and a needle type thermoprobe made of T-type copper-constantan thermocouples (Omega, USA) The vortex tube cooler (Model 3240, Exair Corporation) with 0.82 kJ/s refrigeration capacity

and air flow rate of  $0.018876 \text{ m}^3/\text{s}$  was used to generate subzero temperature air. A thermoprobe was fixed to the lower end of the micrometer; it could be adjusted to any location along the horizontal direction in side the vortex tube by varying the position of the clamp. A micrometer is used to move and locate the thermoprobe along the vertical direction to any particular location in the vortex tube. A pressure regulator was used to control and measure the air pressure supplied to the vortex tube. A higher pressure flow provides lower subzero-temperature. The cold end of the vortex tube was selected to measure the temperature distribution, as it was convenient to insert the thermoprobe to any location at this end. A calibrated thermoprobe was inserted at two different locations  $0.15\text{cm}$  and  $0.3$  cm apart (fig 3.5) close to the inlet nozzle. Two different inlet absolute pressures (3 bar and 4 bar) of the compressed air were chosen to obtain different subzero air temperatures. Prior to start of the measurement the experiment was running for several minutes to stabilize the air temperature at a preset pressure of the compressed air. The reproducibility of the experiment was measured to be within  $\pm 5\%$ . The temperatures were recorded using a data logger (Hewlett Packard 34970A, USA).

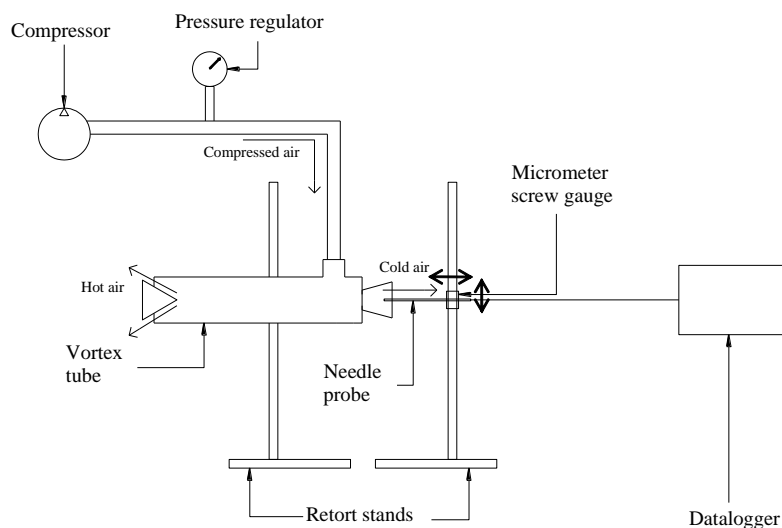


Figure 3.4: Schematic diagram of the experimental setup.

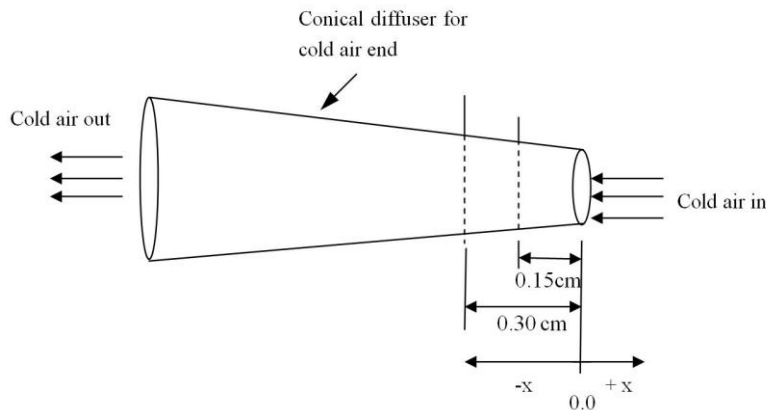


Figure 3.5: Dotted lines show planes in the cold air side of vortex tube where temperature measurements were made for comparison with model results.

## 8. Results and Discussion

Figures 3.6 and 3.7 shows the radial variations of the static temperature of the experimental and simulation results at two locations  $0.3$  cm and  $0.15$  cm from the inner side of the cold air outlet (fig. 3.5).

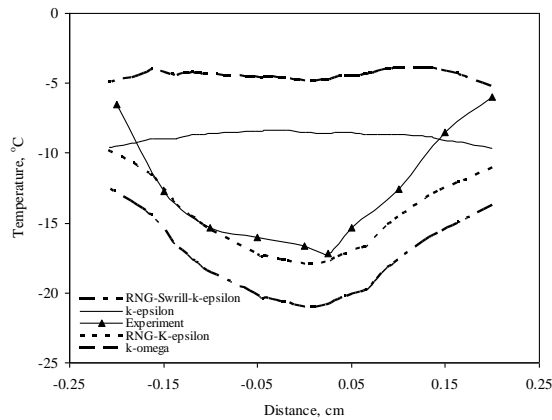


Figure 3.6: Experimentally measured and predicted temperature distribution as a function of radius towards cold end at axial position of 0.3 cm at 4.

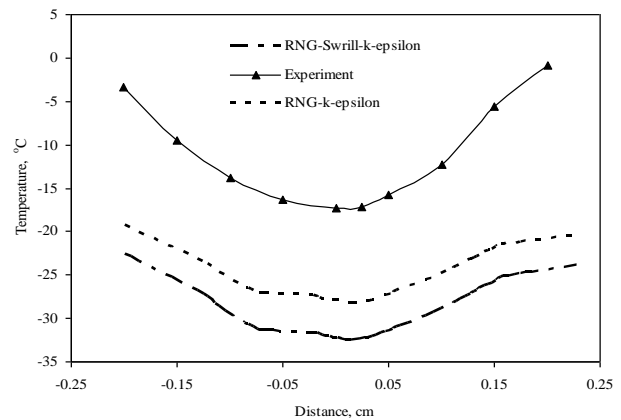


Figure 3.7: Experimentally measured and predicted static temperature distribution as a function of radius towards cold end at axial position of 0.15 cm at 4 bar inlet pressure.

The inlet air pressure of 4 bars (absolute) was used in experiment and in all the computations with four different turbulence models as noted earlier. Hot and cold air temperatures were observed near the periphery of the vortex tube and in the inner core of the air stream, respectively. A decreasing trend of the temperature variation was observed towards the inner core of the vortex tube, which agrees with the results of other investigators.<sup>[3]</sup> The maximum and minimum temperatures were found from the experimental results to be  $-5.80^{\circ}\text{C}$  and  $-15.26^{\circ}\text{C}$ , respectively, at an axial distance of 0.3 cm, while they were  $-3.31^{\circ}\text{C}$  and  $-15.63^{\circ}\text{C}$ , respectively, at 0.15 cm.

A comparison of the predicted temperature with experimental results is also shown in fig. 3.6 and fig. 3.7. It is evident from the fig. 3.6 that the RNG k-epsilon model accorded well with the observed trend of temperature distribution as well as with the minimum and peak values of the temperature with the experimental data. The swirl RNG k-epsilon model, however, results in over-predictions. The standard k-epsilon and k-omega mode are making poor predictions of the experimental results, especially in terms of the distribution of temperature along the radial direction.

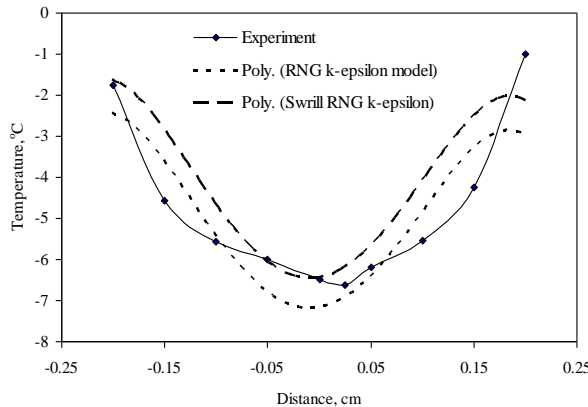


Figure 3.8: Experimentally measured and predicted static temperature distribution as a function of radius towards cold end at axial position of 0.15 cm at 3 bar inlet pressure.

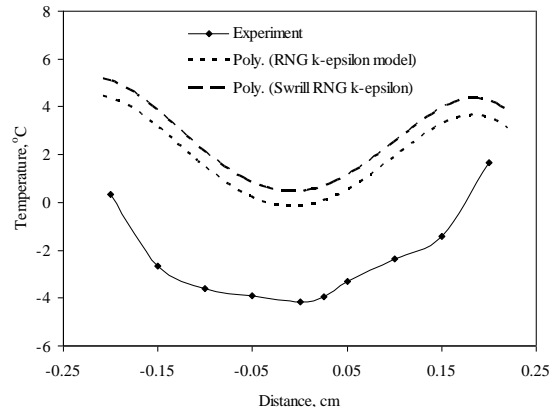


Figure 3.9: Experimentally measured and predicted temperature distribution as a function of radius towards cold end at axial position of 0.3 cm at 3 bar inlet pressure.

Figures 3.8 and 3.9 show a comparison between the experimental and simulation results at 3 bar absolute pressure at the same location to make the results more consistent. Only the swirl RNG k-epsilon and RNG k-epsilon models were used for this case as it was previously observed that the standard k-epsilon and k-omega models are not suitable for the prediction of the temperature distribution in a highly swirling flow of the type found in a vortex tube. From experimental

results the maximum hot air temperature near the periphery at the axial locations of 0.15 cm and 0.3 cm from inlet of the nozzle towards cold air exit of the vortex tube were found to be 3.5°C and 5.8°C, respectively; these results match well with both models. The minimum air temperatures were obtained at the center of the inner air stream; they were -6.6°C and -4.2°C, respectively, for the above two locations while they are -6.3 °C, and -0.25°C, and -7.4°C and 0.40°C, respectively, for the RNG k-epsilon and swirl RNG k-epsilon models. It is apparent from the predicted temperature field that RNG k-epsilon model shows closer agreement than swirl RNG k-epsilon model mainly in terms of trend of temperature distribution. At the axial distance of 0.3 cm (Fig. 3.9) both model shows similar trend of the temperature distribution along the radial direction. However, in terms of cold and hot air temperature in the tube core and in the periphery's of the vortex tube, the RNG k-epsilon model shows more closer agreement, while an under prediction is noted for the swirl RNG k-epsilon. From the above comparison between experimental and predicted results it is apparent that the RNG k-epsilon predictions yield closer agreement with the data. In terms of the overall local temperature predictions, the RNG k- epsilon turbulence model has better conformity with our experimental data due possibly to its ability to incorporate the effect of swirl on turbulence. Therefore, the RNG k-epsilon model was used in further computations to capture the strongly swirling complex flow along with the temperature characteristics inside the vortex tube.

### 8.1 Temperature and Flow Field

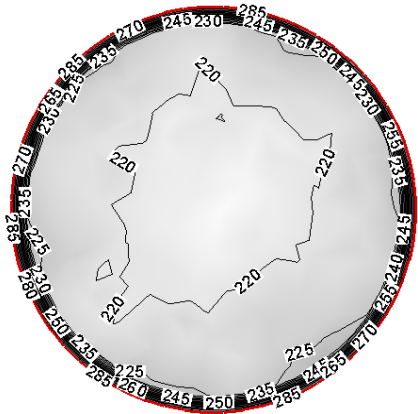


Figure 3.10: Contours of temperature distribution at 0.2 cm along axial direction form the inlet nozzle in cold end at 5 bar inlet pressure.

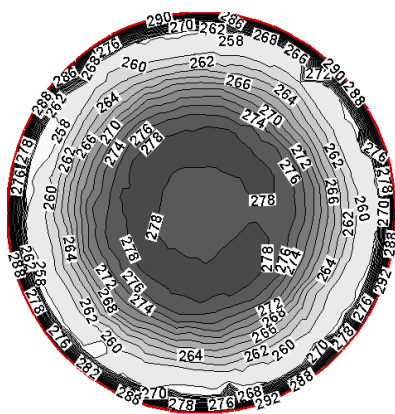


Figure 3.11: Contours of temperature distribution at 1.5 cm along axial direction form the inlet nozzle in hot end at 5 bar inlet pressure.

Temperature contours on the cold and hot sides of the vortex tube are shown in figs. 3.10 and 3.11, at an axial distance of 0.2 cm (cold side) and 1.5 cm (hot side) from the inlet nozzle, respectively, at an inlet pressure of 5 bars absolute. As expected and seen in fig 3.10, the temperature increases from the inner core to the outer periphery. The inner core temperature is found to be about -53°C up to a radius of 0.15 cm, and subsequently a higher temperature of -33°C up to the periphery of the vortex tube on cold air side. Cold and hot air temperatures of about (5°C) and (17°C), respectively, are noted in the inner and the outer streams near the periphery as shown in fig 3.11 at a location of 1.5 cm from the inlet nozzle towards the hot end of the vortex tube. To obtain the velocity magnitudes inside the vortex tube, CFD prediction appears to be the only viable option, as it is very difficult if not impossible to measure these complex three dimensionless turbulent velocity fields experimentally. Figures 3.12 and 3.13 show the contours of the velocity vectors at two locations inside the vortex tube. A high velocity (400 m/s) was observed in the central core in the cold end region at a distance of 0.2 cm from the inlet nozzle. This velocity magnitude prevailed over about half of the radius of the tube in radial direction; the velocity falls to 280 m/s towards wall of the tube. In the hot region of the tube at a location of 0.15 cm three distinct steps in the velocity magnitude were observed. The predicted velocity magnitude in the central core, that in between the center core and the periphery of the tube and in the vicinity of the periphery were about 220 m/s, 220-280 m/s and 280-140 m/s, respectively.

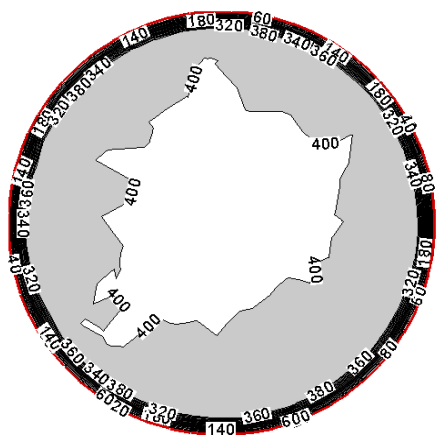


Figure 3.12: Contours of velocity distribution at 0.2 cm along axial direction from the inlet nozzle in cold end at 5 bar inlet pressure.

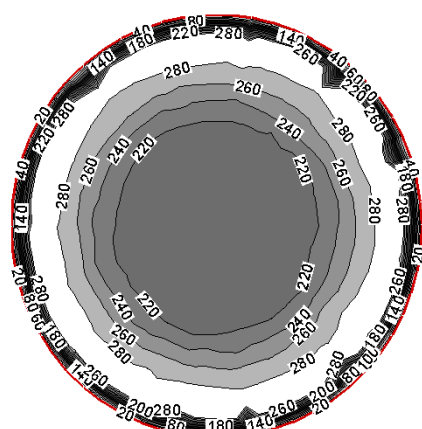


Figure 3.13: Contours of velocity distribution at 1.5 cm along axial direction from the inlet nozzle in hot end at 5 bar inlet pressure.

## 8.2 Energy Separation Mechanism

Contour of velocity vectors at different sections towards the hot air outlet is shown in fig 3.14. which shows that compressed gas flows tangentially into the tube; it expands and rotates in the vortex generation chamber. Consequently, the vortex flows are generated and they move along the tube.

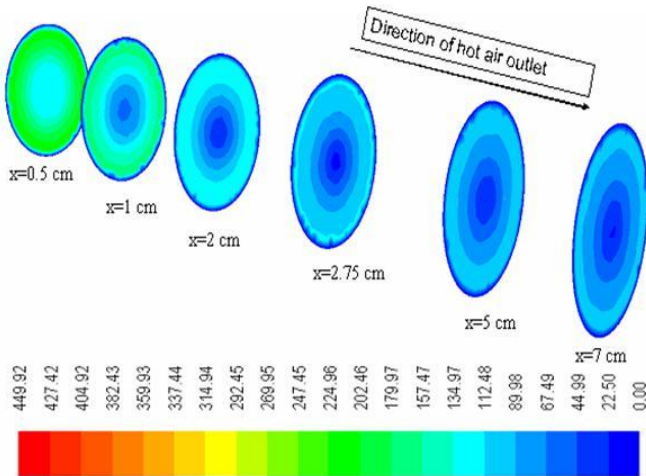


Figure 3.14: Contour of velocity magnitude (m/s) of hot end at RNG k-epsilon 5bar

Figure 3.15 shows the velocity distribution at various locations from the inner end (near the inlet nozzle) towards hot air outlet along the radial direction. Total velocity magnitude ( $V_t$ ) of the compressed air decreases near the wall as it moves towards the hot outlet. The  $V_t$  near the inlet and hot air outlet was about 300 m/s and 50 m/s, respectively. However, the  $V_t$  in the inner region where the air is recirculated and moves towards the cold air outlet opposite to the outer flow increases from 30 m/s to 400 m/s. These phenomena are well captured and clearly visualized in the cross-sectional view along the whole vortex tube as shown in fig 3.16. On account of the friction between the gas and the tube inner surface, the angular velocity becomes low in the outer annular region and high in the inner region. Therefore, the free vortex is formed by the law of constant angular momentum ( $\omega r^2 = constant$ ) in the outer region. It is changed to the forced

vortex in the central core as the flow moves towards the cold air outlet. Such a solid body rotation tends to have a uniform angular velocity distribution ( $\omega = \text{constant}$ ) due to the viscous effect between adjacent fluid layers.

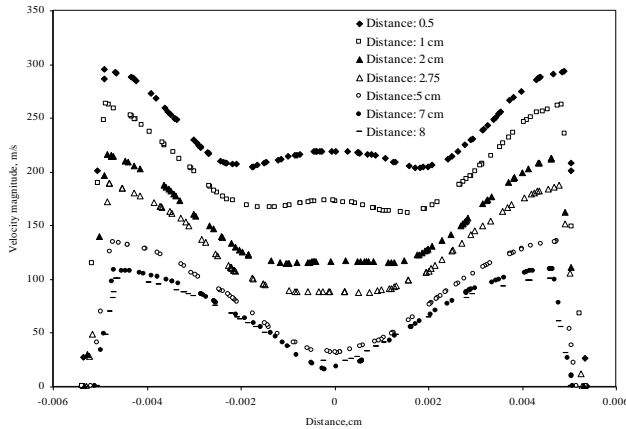


Figure 3.15: Computed plots of velocity magnitude (m/s) of hot end at RNG k-epsilon 5bar.

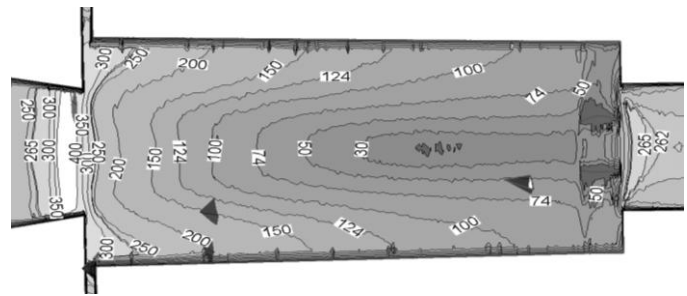


Figure 3.16: Variation of velocity magnitude at different location at axial cross section of vortex tube.

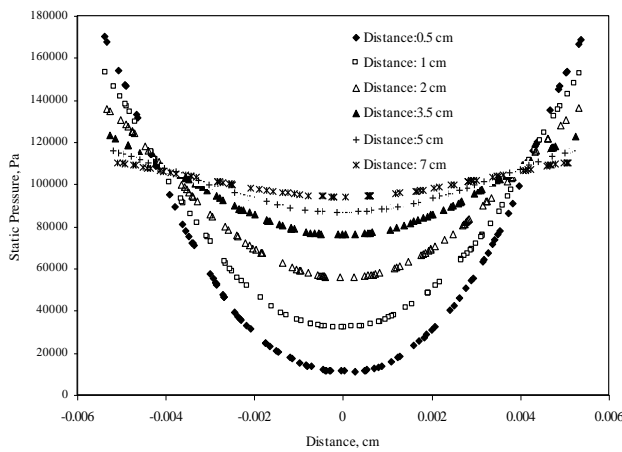


Figure 3.17: Predicted plots of static pressure (Pa) of hot end at RNG k-epsilon 5bar.

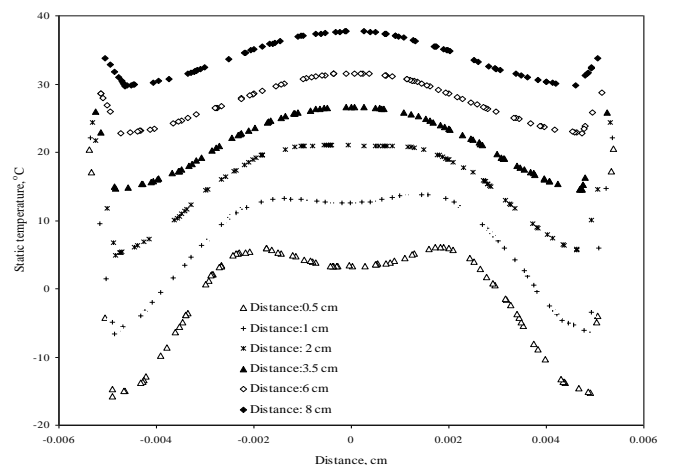


Figure 3.18: Plots of static temperature at different location of hot end using RNG k-epsilon at 5bar.

On the other hand, pressure in the central core becomes lower than that in the outer region as shown in fig 3.17. This is due to the effect of centrifugal force, and the central region is exposed to the ambient at the orifice side and blocked with the throttle valve at the opposite side. Thus the flow is reversed in the central core as a result of the inverse pressure gradient near the throttle valve, and the turbulence is intensified.

Figures 3.18 -3.20 show the occurrence of energy separation in the vortex tube. It appears that one air stream moves up and the other below it, both rotate in the same direction at the same angular velocity. That is, a fluid particle in the inner stream completes one rotation in the same time as a particle in the outer steam. However, because of the principle of conservation of angular momentum, the rotational speed of the smaller vortex is be expected to increase. (The conservation principle is demonstrated by spinning skates that can slow or speed up their spin by extending or drawing on their arms) But in the vortex tube, the velocity of the inner vortex remains the same (fig. 3.15). Angular momentum is lost

by the inner vortex. The energy that is lost shows up as heat in the outer vortex. Thus the outer vortex becomes warmer, and the inner vortex is cooled.

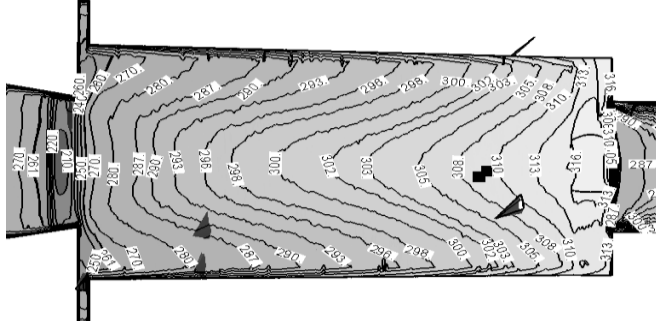


Figure 3.19: Variation of static temperature at different locations at axial cross section of vortex tube.

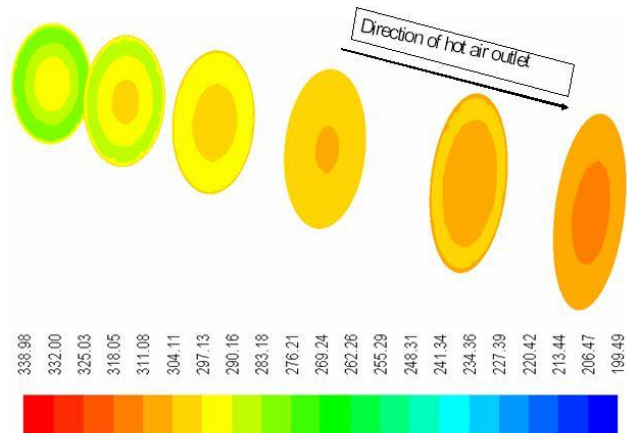


Figure 3.20: Contours of static temperature (K) of hot end using RNG k-epsilon at 5 bar absolute inlet pressure.

### 8.3 Parametric Studies: Inlet Pressure

To investigate the effect of various inlet pressure figs. 3.21 and 3.22 illustrate computed contours of streamlines of static temperature and  $V_t$  along the cross section of vortex tube predicted by the numerical model. Three different inlet pressures were used in numerical simulation to investigate as: 5, 4, and 3 bars. It is obvious from the contours of static temperature (fig 3.21) that energy separation increases with increased inlet pressure. At the same location of the cold air exit, the cold exit temperature was found of about 240K, 265K and 274K for the inlet pressure of 5 , 4 and 3 bar, respectively, while in hot air exit temperature was noted about 315K, 300K and 296K, respectively. From the velocity contours (fig 3.22), higher  $V_t$  was predicted at the cold and hot end outlet at higher inlet pressure. As explained earlier, higher velocity magnitude causes higher loses of angular momentum from the inner vortex which in terns increases the amount of transfer of heat to the outer vortex. Therefore, a higher energy separation is observed at higher inlet pressure.

### 8.4 Location of Strip in Tube

Figure 3.23 shows the contour of  $V_t$  to demonstrate the effect of location of the strip inside the Exair vortex tube. In numerical simulations, two locations of the strip were considered e.g. case-1 Existing location of strip of the commercial vortex tube which is 9 cm from the inlet or at the closer to the hot end exit and case-2: strip placed 7 cm from the inlet of vortex tube. Numerical investigation was extended to observe and compare the effect without the strip as well. Predicted results show the higher velocity of magnitude at the current location of the strip (case-1). The  $V_t$  at the current particular location which is close to the exit of cold air outlet were found to be 400 m/s and 340 m/s for case-1 and case-2, respectively, while at hot air outlet of about 250 m/s and 120 m/s, respectively. Higher velocity causes higher energy separation as noted earlier. Without the strip poor performance occurs as far as the velocity magnitude is concerned. Therefore, our numerical prediction illustrate that the strip in the vortex tube is located at the right place for better performance of the tube.

## 9. Conclusion

Numerical computations were carried out with a 3D-CFD model of a vortex tube .The model predictions with RNG  $k-\epsilon$  turbulence model were in closer agreement with measurements than those of the standard  $k-\epsilon$ ,  $k-\omega$  and the swirl RNG  $k-\epsilon$  turbulence models. The simulations captured the temperature and flow field inside the vortex tube. The numerical

model is also capable of predicting a temperature separation effect that is consistent with the observed behavior. Predicted results show that energy separation occurs mainly due to transfer of loss of angular momentum as a form of heat from the inner vortex to the outer vortex. Results also revealed that the magnitude of energy separation increases as the inlet pressure increases. Finally the current location of the strip inside the vortex tube is optimal and yields better energy separation effect.

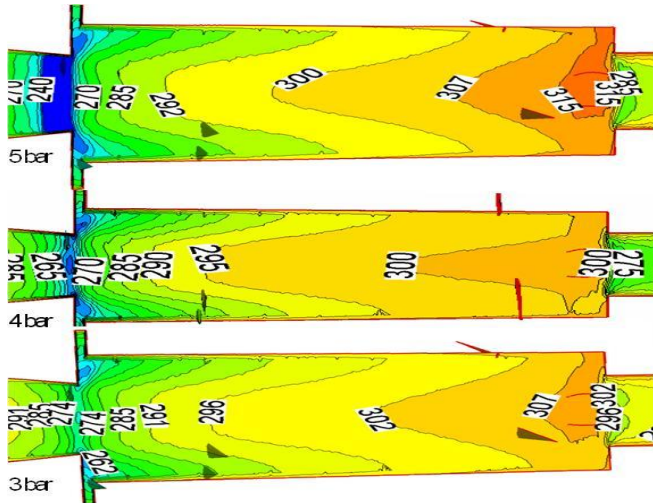


Figure 3.21: Static temperature contours along axial cross section of vortex tube at different inlet pressure.

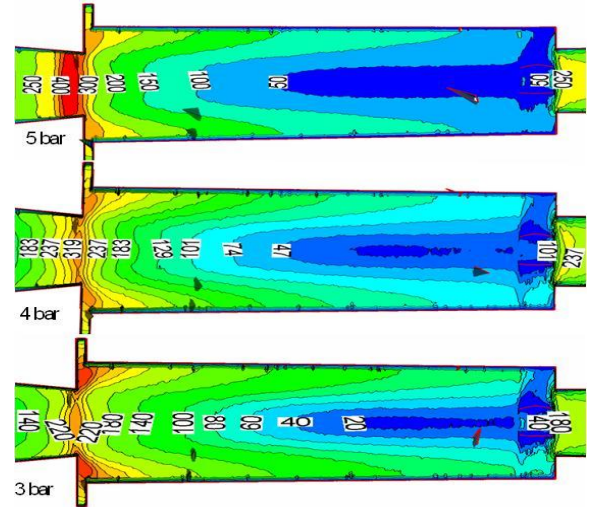


Figure 3.22: Velocity magnitude contours distribution along axial cross section of vortex tube at different inlet pressure

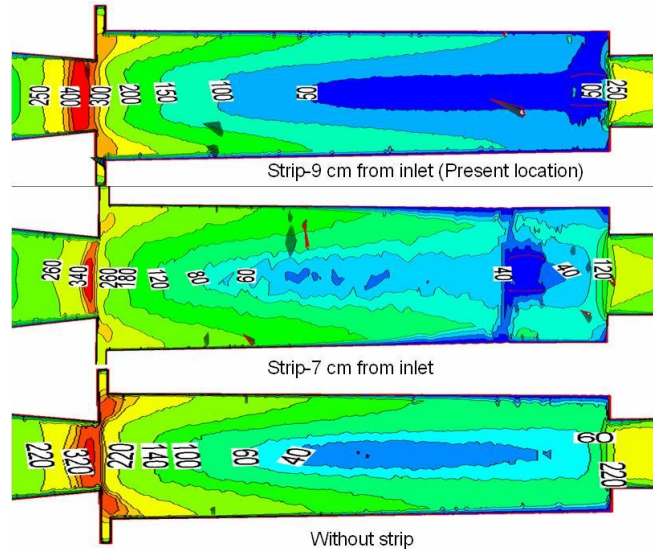


Figure 3.23: Contours of total velocity magnitude along axial cross section of vortex tube for different location of strip.

## Nomenclature

$C_{\epsilon_i}$	- coefficient [ $i=1,2,3,4$ ]
$k$	- turbulence kinetic energy [ $\text{m}^2 \text{s}^{-2}$ ]
$P$	- pressure [kPa]

$S_{ij}$	- momentum source component [-]
$T$	- temperature [K]
$u_i$	- absolute fluid velocity component in direction xi [ $\text{m s}^{-1}$ ]

#### Greek symbols

$\rho$	- density [ $\text{kg m}^{-3}$ ]
$\mu$	- dynamic viscosity [ $\text{kg m}^{-1}\text{s}^{-1}$ ]
$\delta$	- Kronecker delta tensor [-]
$\varepsilon$	- turbulence dissipation rate [ $\text{m}^2 \text{s}^{-3}$ ]
$\sigma$	- stress [ $\text{N m}^{-2}$ ]
$\beta$	- coefficient
$\eta_0$	- coefficient

#### Subscripts

i, j, k	- Cartesian indices
t	- turbulence; total
h	- hot gas

#### References

1. Gupta, A.K.; Lilley, D.G.; Syred, N. *Swirl flows*; Abacus Press: Turnbridge Wells, England, **1984**.
2. Liu, J.Y.; Gong, M.Q.; Zhang, Y.; Hong, H.; Wu, J.F. Numerical Research of a Special Fluid Phenomenon Ranque-Hilsch Effect. *Modern Physics Letters B* **2005**, *19*, 1723-1726
3. Eiamsa-ard, S.; Promvonge, P. Numerical Prediction of Vortex Flow and Thermal Separation in a Subsonic Vortex Tube. *Journal of Zhejiang Universities SCIENCE A* **2007**, *7*, 1406-1415
4. Behera, U.; Paul, P.J.; Kasthururengan, S.; Karunanithi, R.; Ram, S.N.; Dinesh, K.; Jacob, S. CFD Analysis and Experimental Investigations Towards Optimizing the Parameters of Ranque-Hilsch Vortex Tube. *International Journal of Heat and Mass Transfer* **2005**, *48*, 1961-1973.
5. Aljuwayhel, N.F.; Nellis, G.F.; Klein, S.A. Parametric and Internal Study of the Vortex Tube Using A CFD Model. *International Journal of Refrigeration* **2005**, *28*, 442-450
6. Skye, H.M.; Nellis, G.F.; Klein. Comparison Of CFD Analysis to Empirical Data in a Commercial Vortex Tube. *International Journal of Refrigeration* **2006**, *29*, 71-80
7. Eiamsa-ard, S.; Promvonge, P. Numerical Investigation of the Thermal Separation in a Ranque-Hilsch Vortex Tube. *International Journal of Heat and Mass Transfer* **2007**, *50*, 821-832
8. Rahman, S.M.A.; Mujumdar, A. S. A Novel Atmospheric Freeze Drying System in a Vibro-Fluidized Bed Dryer Couple with Adsorbent and Multimode Heat Input. *Drying Technology* **2008**, *26*, 393-403
9. Rahman, S.M.A.; Mujumdar, A.S. A Novel Atmospheric Freeze Drying System Using a Vortex Tube and Multimode Heat Supply. *International Journal of Postharvest Technology and Innovation* **2008**. (*In press*)
10. Claussen, I.C.; Ustad T.S.; Strømmen, I.; Walde, P.M. Atmospheric Freeze Drying – A Review. *Drying Technology* **2007**, *25*, 947-957
11. Rahman, S.M.A.; Mujumdar, A.S. Vortex tube-assisted Atmospheric Freeze Drying of Osmotically Pretreated Biological Materials. *International Drying Symposium*, February, Mumbai, India, **2008**.
12. Fluent 6.3 user guide. Modeling turbulence. Chapter 12.4, 12-25

# ►[ MODELLING DROPLET DRYING IN SPRAY DRYERS]

## [Chapter 4]

**M. W. Woo<sup>1</sup>, W. R. W. Daud<sup>1</sup>, A. S. Mujumdar<sup>2</sup>, Z. H. Wu<sup>2</sup>, M. Z. M. Meor<sup>1</sup> and S. M. Talib<sup>1</sup>**

► [<sup>1</sup>Department of Chemical and Process Engineering, Universiti Kebangsaan Malaysia.

<sup>2</sup>Department of Mechanical Engineering, National University of Singapore]

Droplet drying in spray dryers is typically modeled using the lump approach or the discretized droplet approach. This paper focuses on the former approach and reviews two useful models along this line: Reaction Engineering Approach (REA) and Characteristic Drying Curve (CDC). Comparison of the models with available droplet drying data and in CFD revealed the sensitivity of these models to the initial moisture. This is an important considering when extending these models to different drying and droplet conditions. The REA model can be extended to compute droplet surface condition. Analysis shows that this is significant in the prediction of particle rigidity which will be important in deposition modeling. A brief outlook was further included highlighting recent advances in modeling certain particle morphologies which are not distinguished in the lump models.

## Modeling Droplet Drying in Spray Drying

### 1. Introduction

Spray drying involves rapid removal of moisture from finely atomized droplets. The key features and main challenge in modeling such a process is the simultaneous mass transfer, heat transfer and solid formation as the particle dries. There are typically two main approaches in modeling the drying process of a droplet, discretized approach and lump approach. For implementation in Computational Fluid Dynamics (CFD) simulations, which is the focus of our larger project, the latter approach is more desirable due to the lower computational requirement. However, there are many variations to the lump approach, along with different assumptions in these models. In order to gain more confidence in these models, it will be important to evaluate how these models actually behave at different drying conditions. This paper highlights some of our recent work in evaluating two such lump models: (1) Reaction Engineering Approach (REA) and (2) Characteristic Drying curve (CDC).

The paper is organized in the following manner. Firstly two basic theoretical approach in modeling pure droplet heat and mass transfer will be introduced. These two basic approaches will then be extended, in the second section, to droplets containing dissolved solids in which the REA and CDC will be introduced. The third section evaluates the performance of these models based on constant single droplet drying experimental conditions. The evaluation was then extended to a CFD simulation with rapidly changing ambient environment in the fourth section. Towards the end of the paper, a brief outlook on some recent alternative modeling method was included to give a wider perspective on this important subject.

### 2. Theory: Evaporation of Pure Droplets

#### 2.1 Interface Boundary Approach

In this approach, as moisture is evaporated from the surface, it is visualized that a thin of saturated vapour is formed at the droplet-air interface (Figure 4.1a). Therefore, the mass transfer is controlled and driven by the difference between the surface and ambient vapour concentration. Mathematically, this can be written in the following form by introducing a mass transfer coefficient,

$$\frac{dm}{dt} = -\frac{h_m A}{m_s} (P_{v,sat}(T_d) - P_{v,\infty}) \quad (4.1)$$

For pure droplets, the surface vapour concentration will always be at saturation. The degree of saturation will strongly depend on the droplet temperature which can be determined thermodynamic correlation such as the Antoine Equation. In terms of the heat transfer, there will be simultaneous convective heat and evaporation cooling of the droplet due to temperature differences and moisture evaporation, respectively (Figure 4.1b). The heat transfer equation then takes the form,

$$m C_p \frac{dT_d}{dt} = h A (T_a - T_d) - \Delta H_{evap} m_s \frac{dX}{dt} \quad (4.2)$$

The first part of the equation is the convective portion (heat gain) whereas the second part is the evaporative cooling (heat loss). Normally, a uniform temperature is assumed for the small droplets encountered in spray drying. Although there are arguments on the importance of temperature gradient within the particle,<sup>[1]</sup> the assumption of a uniform temperature can be justified in some detailed analysis of the Biot number.<sup>[2]</sup> There are even reports of usage of a uniform temperature in the discretized approach.<sup>[3]</sup> The heat and mass transfer coefficients can be calculated using the Ranz-Marshall equations,

$$Nu = 2 + 0.6 Re^{1/2} Pr^{1/3} \quad (4.3)$$

$$Sh = 2 + 0.6 Re^{1/2} Sc^{1/3} \quad (4.4)$$

In rapid evaporation of pure droplets, the droplet will tend to enter and stay in the wet bulb region for most of the drying time. The wet bulb condition or temperature is when the convective heat and evaporative cooling is in an equilibrium

state. Another school of thought is to assume wet bulb condition throughout the entire drying process. This leads to the second approach outlined below.

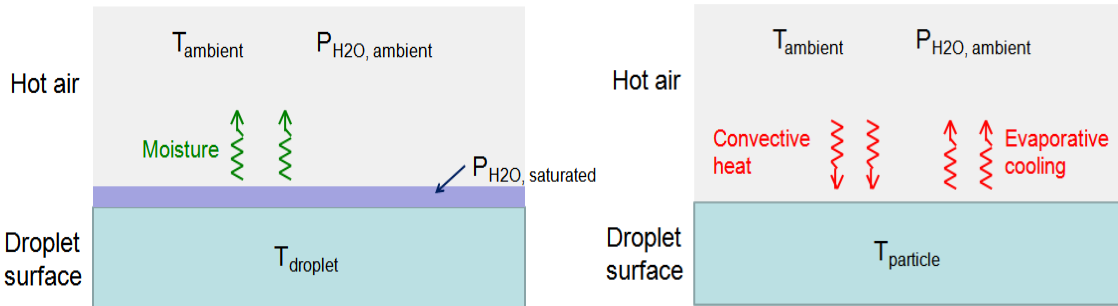


Figure 4.1: Visualization of the interface boundary approach drying mechanism.

## 2.2 Wet Bulb Approach

Equating the convective heat with the evaporative cooling and upon rearrangement, the following expression for the mass transfer rate below can be obtained.<sup>[4]</sup> Similarly, the same heat transfer equation can be employed in both approaches.

$$\frac{dX}{dt} = \frac{Ah}{m_s \Delta H_{evap}} (T_a - T_{wb}) \quad (4.5)$$

## 3. Theory: Evaporation of Droplets With Dissolved Solids

### 3.1 Reaction Engineering Approach (REA)

In the interface boundary approach, the surface vapour concentration plays an important role in the mass transfer. However, for droplets containing dissolved solids, the surface vapour concentration will reduce as moisture is evaporated. Assuming a surface moisture reduction mechanism, contrary to the receding front visualization which is common in solid particles, Figure 4.2 illustrates the reduction in surface moisture as drying proceed. Therefore, there is a need to correlate the degree of saturation of the vapour boundary layer as drying proceed; at different droplet moisture. This can be achieved by using the REA model which visualizes the drying process as an activation process in which an ‘energy’ barrier has to be overcome for moisture removal to occur.<sup>[5]</sup> The drying rate can then be expressed in the following form,

$$\frac{dm}{dt} = -\frac{h_m A}{m_s} (k P_{v,sat}(T_d) - P_{v,\infty}) \quad (4.6)$$

The key component of this model is the “fractionality” relative to the interface saturation moisture content,  $k$ , which should reach unity when the surface of the droplet is fully covered with liquid water. This fractionality is expected to be a function of moisture and temperature, which can be approximated by,

$$k = \exp\left(-\frac{\Delta E_v}{RT}\right) \quad (4.7)$$

where  $\Delta E_v$  is the apparent activation energy, which is likely to be dependent on the ‘mean’ or ‘average’ moisture. The original authors proposed the following function to be taken as the fingerprint of a material applicable to all drying conditions,

$$\frac{\Delta E_v}{\Delta E_{v,\infty}} = a e^{-b(X-X_\infty)^c} \quad (4.8)$$

Constants for Equation 8 can be obtained by combining Equation 6 and 7. This will allow the apparent activation energy to be calculated at different droplet moisture from experiments. At high moisture content

$$\frac{\Delta E_V}{\Delta E_{V,\infty}} \rightarrow 0, k \rightarrow 1 \quad (4.9a)$$

At low moisture content

$$\frac{\Delta E_V}{\Delta E_{V,\infty}} \rightarrow 1, 0 < \text{minimal } K \text{ value} < 1 \quad (4.9b)$$

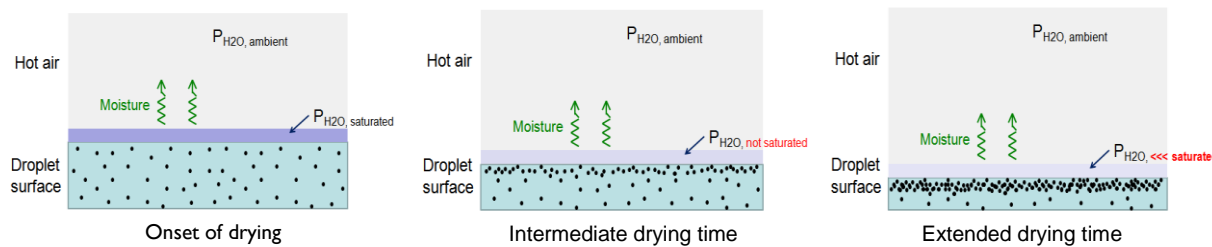


Figure 4.2: Effect of dissolved solids on moisture evaporation.

### 3.2 Characteristic Drying Curve (CDC)

Similarly, following Langrish and Kockel,<sup>[4]</sup> the wet bulb approach can account for the dissolved solids by introducing a factor which is a function of moisture. The mass transfer takes the following form,

$$\frac{dX}{dt} = f \frac{Ah}{m_s \Delta H_{evap}} (T_a - T_{wb}) \quad (4.10)$$

$$f = \left[ \frac{(X - X_{eq})}{(X_{cr} - X_{eq})} \right]^n, \quad X \leq X_{cr} \quad (4.11a)$$

$$f = 1, \quad X > X_{cr} \quad (4.11b)$$

In the work of Langrish and Kockel the index of I was proven to be suitable for milk droplets.<sup>[4]</sup> A note on the selection of the critical moisture is in order. The CDC model was originally developed for small solid particles. For solids, fixed critical moisture, with slight deviations at different drying conditions, can be expected even at different initial moisture. However, particle formation occurs simultaneously during the drying process and it is normally assumed that this immediately impedes drying. This was also experimentally shown for carbohydrate droplets.<sup>[6]</sup> More details can be found at Langrish and Kockel's paper.<sup>[4]</sup>

### 4. Evaluation Based on Single Droplet Drying

The drying solution considered in this work is sucrose-maltodextrin droplets. This solution was chosen to mimic spray drying of carbohydrate rich fruit juices. Single droplet drying data was obtained from the work of Adhikari et al.<sup>[11]</sup> Their experiment exposes a suspended droplet using a glass filament to hot convective air. Droplet temperature and moisture was recorded in-situ as drying takes place.

Figure 4.3 and 4.4 compares the model predictions with the experimental data of Adhikari et al.<sup>[11]</sup> These experimental data were obtained by suspending a droplet with glass filament while exposing the system to convective air. Therefore, in these evaluations, the heat transfer model was slightly modified to account for the effect of the suspended filaments,

$$m C_p \frac{dT_d}{dt} = h A (T_a - T_d) - \Delta H_{evap} m_s \frac{dX}{dt} + 0.5 \pi D_f \sqrt{h D_f k_f} (T_a - T_d) \quad (4.12)$$

It is clear that the REA fits the experimental data very well. On the other hand, the CDC linear grossly over predicted the drying rate. This characteristic is likely to be due to the sudden formation of crust and explains why the CDC model grossly over-predicts the drying rate at the later stages. The modified CDC model which follows very closely to the experimental data. Considering both cases in Figure 4.3 and 4.4 simultaneously, the REA material fingerprint was determined as shown in Figure 4.5 and modified CDC index is 1.98. If the index is less than unity, a convex falling rate will be produced. If  $n$  is more than unity, a concave falling rate will be observed. This indicates that a convex falling rate might be more suitable for materials with such skin or crust formation tendency. In addition, the linear CDC with the index of 1 was also included in this work. This will be very useful when comparison is made in the next section.

In terms of the temperature profiles, there are slight deviations due to the mass changes (Figure 4.3 and 4.4). The REA tends to predict a slightly higher initial temperature when compared to the CDC (and modified CDC). This is due to the lower initial drying rate as evident in Figure 4.3a. On the other hand, the modified CDC over-predicts the middle stage of drying. However, the temperature profiles approach the experimental values towards the later stages of drying.

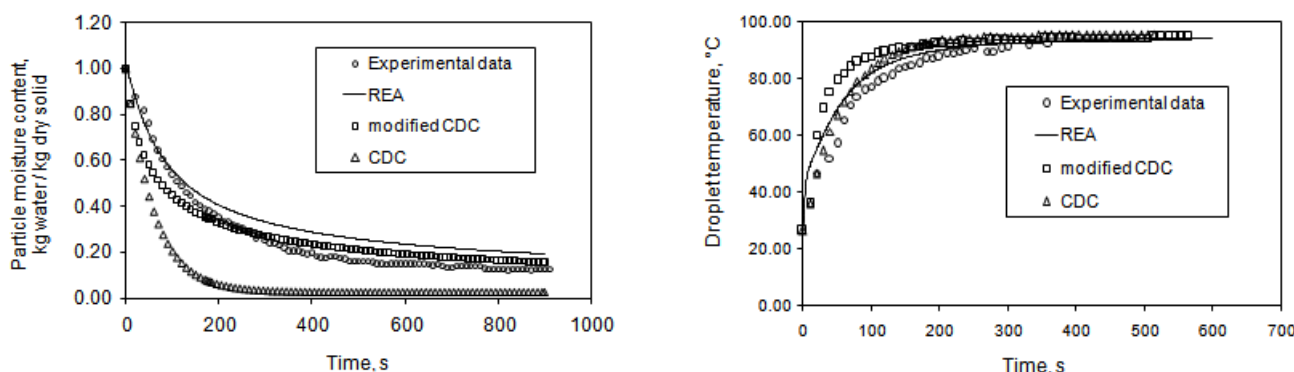


Figure 4.3: Comparison of the three kinetic models in drying a 2.33 mm diameter droplet at drying condition of 1 ms<sup>-1</sup> air flow, 60 %wt initial moisture (same value used for the critical moisture), 95 °C (2%RH) – Modified from Woo et al. 2008.

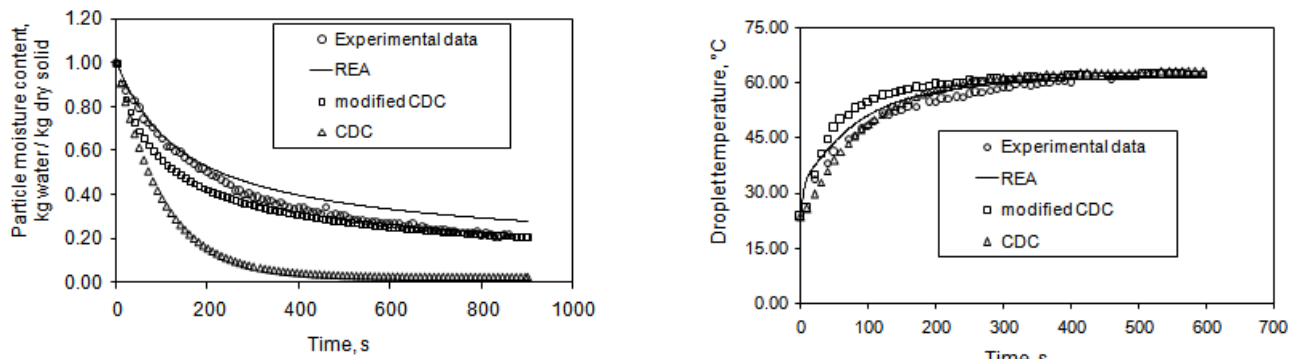


Figure 4.4: Comparison of the three kinetic models in drying a 2.33 mm diameter droplet at drying condition of 1 ms<sup>-1</sup> air flow, 60 %wt initial moisture (same value used for the critical moisture), 65 °C (2.5%RH) – Modified from Woo et al. 2008.

In overall, it is clear that the REA and modified CDC follow closer to the experimental data. However, constant drying conditions are tested in this part of the work.<sup>[7]</sup> Behaviour of the models in a rapidly changing condition, which is more representative of the spray dryer, will be evaluated next in a CFD simulation.

$$\frac{\Delta E_v}{\Delta E_{v,\infty}} = e^{-0.892(X-X_\infty)^{2.022}}$$

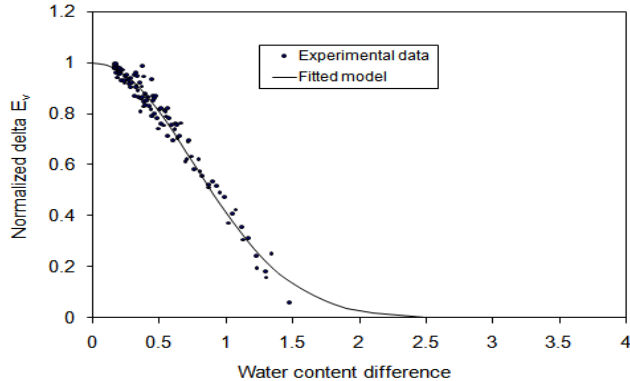


Figure 4.5: Normalized activation energy and water content difference curve for sucrose-maltodextrin droplets.

## 5. Evaluation in a CFD Simulation

The dryer geometry used follows the pilot scale short-form spray dryer, fitted with a rotary atomizer, available in our laboratory. Details of this unit can be found in our previous report.<sup>[8]</sup> Simulations were carried out using a commercial CFD code, FLUENT 6.3.26. A steady state 2-dimensional axi-symmetric model incorporating swirl was utilized in current simulations. The RNG k-e turbulence model was used as it has proven reasonably reliable for swirling flows. The drying models above were implemented using the UDF functions available in FLUENT. Summary of the boundary and injection conditions can be found in reference [9].

Experiments were conducted with our pilot scale spray dryer to provide outlet product moisture data for comparison with our CFD simulations. Product moisture was determined using an experimental method similar to our previous report after 30 minutes of spray.<sup>[8]</sup> However, in this work, the dryer was allowed 40 minutes of pre-heating followed by 20 minutes of pure water spray to achieve steady state conditions.

Table 4.1 shows the overall outlet product moisture prediction of the models. The REA provided reasonably good prediction of the outlet moisture. In the CDC models, surprisingly, the CDC linear provided a close moisture prediction when compared to the CDC modified. This is in contrary with the behavior as shown in the single droplet comparison above (Figure 4.3 and 4.4). Figure 4.6 is drying curves obtained by tracking a single particle throughout the simulation domain which clearly illustrates this discrepancy.

**TABLE 4.1:**  
Overall outlet temperature and particle moisture prediction.

Parameters	Inlet Temp, °C	Measured	REA	CDC linear	CDC modified
Outlet Temp, °C	120	87.5–92.5	96.31	96.23	96.20
	150	107.5–110	116.33	116.24	116.19
Particle Moisture (%wt moisture)	120	2.40	1.73	1.27	15.07
	150	1.47	1.14	1.09	11.94

We initially thought that this is the effect of the changing ambient conditions and proceeded to analyze this by a flow field patching method. This involved by first simulating a normal CFD run with droplets. A single parameter (temperature or humidity) from the converged flow field was then patched with a constant value and the particles were then re-injected. In this way, the re-injected particles will experience a changing ambient condition, as if a normal CFD simulation, while encountering a constant value for the selected patched ambient. The three changing conditions tested independently are air

temperature, absolute humidity and relative velocity. Figure 4.7 shows that change of air temperature and humidity is not the cause of the discrepancy observed.

We resorted to some analytical analysis to determine the effect of the changing relative velocity. The effect of relative air velocity on the drying models is on the heat and mass transfer coefficients reflected by the relative Reynolds number in Equation 4.2 & 4.3. By further examining Equation 4.4 & 4.5, it is clear that velocity change affects the *total* mass transfer rate calculated by both models respectively in an equal manner. Therefore, a changing relative velocity will only ‘translate’ the trend produced by a constant condition but will not result in drastic differences as observed.

This led us to believe that this discrepancy is due to the different initial moisture contents used. In this work, the initial moisture is  $4 \text{ kg kg}^{-1}$  dry basis whereas the former uses  $1.5 \text{ kg kg}^{-1}$  dry basis due to limited drying kinetics data reported for sucrose-maltodextrin solution. Figure 4.8 shows the behavior of the models at different initial moisture. These curves were compiled by repeating the CFD simulations.

We can elucidate that the behavior of the CDC is mainly due to the construction of its driving force (independent of particle condition), usage of the initial moisture as the critical moisture and the assumption that the driving curve at different ambient condition will collapse to a linear trend (of the modified one). Physical significance of these assumptions for such carbohydrates considered can be found in the work of.<sup>[6]</sup>

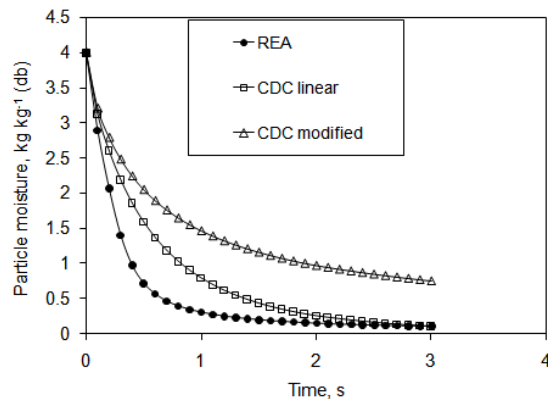


Figure 4.6: Drying curves for a  $65.8 \mu\text{m}$  droplet at  $120^\circ\text{C}$ .

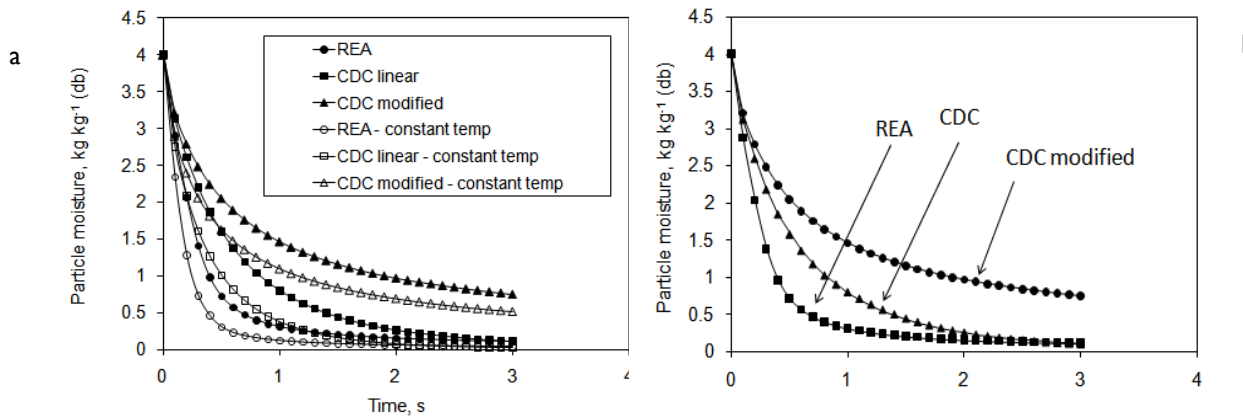


Figure 4.7: Effect of constant air (a) temperature and (b) absolute humidity (symbols – patched results, solid lines – without patching).

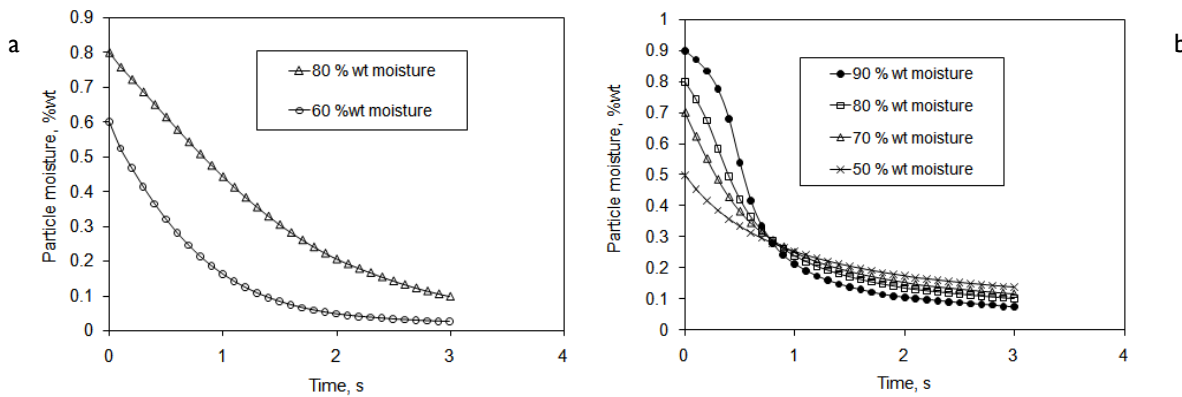


Figure 4.8: Response of (a) CDC and (b) REA models at different initial moisture.

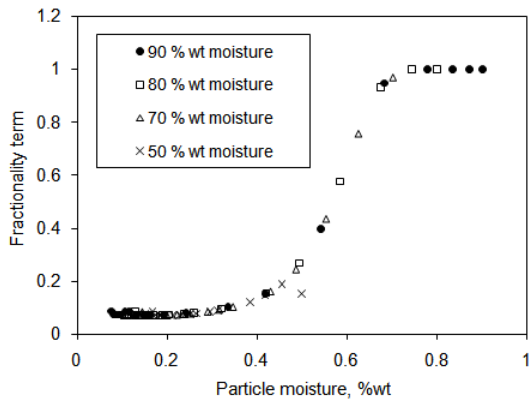


Figure 4.9: Predicted fractionality term of a  $65.8\text{ }\mu\text{m}$  diameter particle.

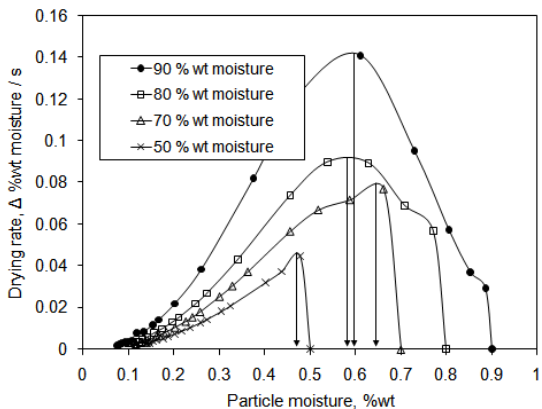


Figure 4.10: REA prediction of the drying rates corresponding to different initial moisture contents.

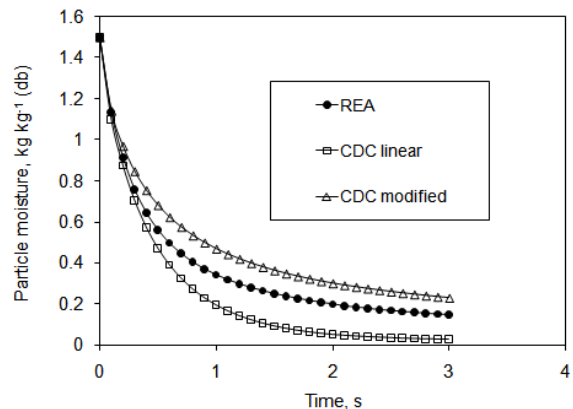


Figure 4.11: Comparison of the 'manipulated' initial moisture ( $65.8\text{ }\mu\text{m}$  diameter droplet at  $120\text{ }^\circ\text{C}$ ).

## 6. Modeling Outlook

From these evaluations based on the single droplet experiments and CFD, both models exhibit similar behavior in constant and rapidly changing ambient conditions. However, the models are sensitive to the initial moisture of the droplet. This factor is an important consideration in future selection and application of these models.

It is noteworthy that the models considered do not specifically take into account of the possible particle morphology that can occur. These models also do not account for possible over-pressure within the formed solid. Walton and Mumford provided an in-depth review of particle morphologies possible form the harsh spray drying condition.<sup>[10]</sup> Of particular interest in recent modelling work is the formation of crust. In this area, the discretized approach is normally used and drying is specifically viewed to proceed with a receding front.<sup>[11,12]</sup> Along this line, Mezhericher et al. has shown that it is possible to compute phenomena such as blow holes and breakage.<sup>[11]</sup> Handscomb et al. extended their work to compute different type of crust formation.<sup>[12]</sup>

Apart from that, we have shown that the REA model can be used to compute surface moisture condition.<sup>[7]</sup> This capability is conventionally only possible through the more laborious discretized approach. Comparisons with the discretized method so far have shown reasonable results. Application of this method in CFD shows that it has significant effect on particle rigidity prediction.<sup>[9]</sup> It is envisaged that this will have impact on future modeling of particle deposition and agglomeration which is a surface dependent process. Nevertheless, it is noteworthy that such a technique visualizes internal diffusion limitation as the source of drying rate impedance and not that of a receding front.

## 7. Concluding Remarks

Two basic approaches in modeling droplet drying were revisited in this paper. Extension of these basic approaches to dissolved solids was further illustrated. The REA and CDC lump drying model were evaluated in a constant and rapidly changing drying condition. It was found that both models provided good drying prediction in the constant drying condition. Furthermore, the behavior of the two models translates similarly to the rapidly changing drying condition in CFD simulations. However, the two models respond differently to the initial moisture of the droplet which will be an important factor to consider in future application. Brief outlook in the modeling of droplet drying was provided which includes capturing particle morphology and surface moisture prediction.

## Acknowledgement

This project was funded by the Ministry of Science, Technology and Innovation of Malaysia (Grant number: 03-01-02-SF0046). Useful discussions with Dr. Huang Lixin (Research Institute of Chemical Industry of Forrest Products, China) and Dr. Chen Fang Xi (CAD-IT Consultants, Singapore) are greatly acknowledged. Special thanks to Dr. Benu Adhikari for providing the experimental data for the single droplet drying evaluation.

## Notation

$m$	mass	kg
$C_p$	specific heat capacity	J/kg K
$T$	temperature	K
$h$	heat transfer coefficient	J/m <sup>2</sup> sK
$h_m$	mass transfer coefficient	m/s
$A$	droplet surface area	m <sup>2</sup>
$t$	time	s
$\Delta H_{evap}$	heat of evaporation	J/kg
$X$	moisture content	kg water/kg solid
$D_f$	diameter of glass filament	m
$P_v$	vapour concentration	kg/m <sup>3</sup>
$R$	Universal gas constant	J/K mol

---

$\Delta E_v$	Apparent activation energy	-
$D$	Droplet diameter	m
$a_w$	Equilibrium % R.H.	-
$Nu$	Nusselt number	
$Pr$	Prandtl number	
$Sh$	Sherwood number	

### Subscripts

---

$a$	air
$d$	droplet
$s$	solid
$wb$	wet bulb
$cr$	critical
$eq$	equilibrium
$sat$	saturated at surface
$\infty$	ambient

### References

1. Farid, M. A new approach to modeling of single droplet drying. *Chemical Engineering Science* **2003**, *58*(13), 2985-2993.
2. Patel, K.C.; Chen, X.D. Surface-center temperature differences within milk droplets during convective drying and drying-based biot number analysis. *Journal of AIChE* **2008**, *54*(12), 3273-3290.
3. Adhikari, B.; Howes, T.; Bhandari, B.R.; Truong, V. Surface stickiness of drops of carbohydrate and organic acid solutions during convective drying: experiments and modelling. *Drying Technology* **2003**, *21*(5), 839-873.
4. Langrish, T.A.G.; Kockel, T.K. The assessment of a characteristic drying curve for milk powder for use in computational fluid dynamics modeling. *Chemical Engineering Journal* **2001**, *84*, 69-74.
5. Chen, X.D.; Xie, G.Z. Fingerprints of the drying behaviour of particulate or thin layer food materials established using a reaction engineering model. *Food and Bioproduct Processing* **1997**, *75*, 213-222.
6. Li, X.; Zbicinski, I. A Sensitivity Study on CFD Modelling of Cocurrent Spray-Drying Process. *Drying Technology* **2005**, *23*(8), 1681-1691.
7. Woo, M.W.; Daud, W.R.W.; Mujumdar, A.S.; Talib, M.Z.M.; Wu, Z.H.; Tasirin, S.M. Comparative Study of Drying Models for CFD Simulations of Spray Dryers. *Chemical Engineering Research and Design* **2008**, *86*(9), 1038-1048.
8. Woo, M.W.; Daud, W.R.W.; Tasirin, S.M.; Talib, M.Z.M. Effect of Wall Surface Properties on the Deposition Problem in Spray Drying at Different Drying Rates. *Drying Technology* **2008**, *26*(1), 15-26.
9. Woo, M.W.; Daud, W.R.W.; Mujumdar, A.S.; Wu, Z.H.; Talib, M.Z.M.; Tasirin, S.M. Evaluation of droplet drying models in a CFD spray drying environment. *Drying Technology* **2008**, *26*(10), 1180-1198.
10. Walton, D.E.; Mumford, C.J. Spray Dried Products – Characterization of Particle Morphology. *Chemical Engineering Research and Design* **1999**, *77*, 21-38.
11. Mezhericher, M.; Levy, A.; Borde, I. Modelling of particle breakage during drying. *Chemical Engineering and Processing: Process Intensification* **2008**, *47*(8), 1404-1411.
12. Handscomb, C.S.; Kraft, M.; Bayly, A.E. A new model for the drying of droplets containing suspended solids after shell formation. *Chemical Engineering Science* **2009**, *64*(2), 228-246.

# ►[ MATHEMATICAL MODELING OF HEAT AND MASS TRANSFER IN GELS]

## [Chapter 5]

**Jundika C. Kurnia<sup>1</sup>, E. Birgersson<sup>2</sup> and Arun S. Mujumdar<sup>1</sup>**

► [<sup>1</sup>Department of Mechanical Engineering, National University of Singapore]

► [<sup>2</sup>Department of Chemical and Biomolecular Engineering, National University of Singapore]

For many years, gels and gelling processes have occupied a position of prime importance, fulfilling many functions from controlled release, surface coatings and consumer products in a number of key industries including the pharmaceuticals, photographic, paper and food industries. A gel is essentially a three dimensional polymer network immersed in a liquid solution. A stimuli-responsive gel has the ability to undergo large reversible volume changes up to thousand-fold or more when subjected to change of the environment: alterations in pH, ionic strength, temperature as well as electric field and irradiation of light. In recent years, extensive progress has been made in the technological application of stimuli-responsive gel. Biosensors, micro-actuators and flow controls, tissue engineering, artificial muscle, drug delivery systems and other applications use gel due to its autonomous behavior. Gels have also commonly been used in: bioseparation, disposable diapers, soil irrigation, and contact lens. The objectives of this study are to develop mathematical models of heat and mass transfer in gels and to provide design guidelines for gels application.

## Mathematical Modeling of Heat and Mass Transfer in Gels

### 1. Introduction

A gel is an interesting material from the perspective of basic science as well as in potential engineering application. It reveals both solid-like properties and liquid-like properties. The liquid-like properties are contribution of liquid phase which is usually a major component of a gel whereas the solid-like properties come from the solid phase that retains the gel solidity. When the liquid phase of a gel is an aqueous solution, it commonly addressed hydrogel. In essence, a gel consists of an elastic three-dimensional solid network, fluid filling the interstitial space of the network and ions if the gel is charged. The structure of a gel is illustrated in figure 1. The solid network can be considered as a container of liquid solvent that developed by long polymer chains that cross-linked each other with a variety of bonds such as hydrogen bonds, covalent bonds, electrostatics interactions, Van Der Waals forces or physical entanglements.<sup>[1]</sup>

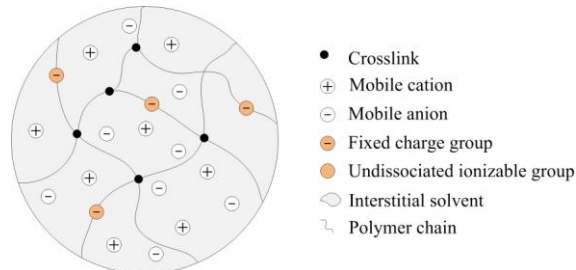


Figure 1: Schematic representation of gel structure.

A special class of gel, stimuli-responsive or smart gel, can undergo reversible and large volume changes in response to changes in environment such as alterations in pH, ionic strength, temperature, enzyme-substrate as well as electric field and irradiation of light.<sup>[2,3]</sup> Numerous mathematical models have been derived in an effort to understand and predict the deformation kinetics and swelling equilibrium of gels. The latter is usually considered to follow Flory's mean field theory<sup>[4]</sup> or alterations thereof. In contrast to the theories of swelling equilibrium, there is no unified approach to describe the kinetics of the deformation, since a wide range of physical phenomena have to be considered, requiring a blend of continuum mechanics, polymer science, transport phenomena and for polyelectrolyte gels, electrochemistry. Thus, models vary in their considerations of the different physical phenomena, as well as the types of gel the model are developed for. Most of the kinetic models, however, are for one-dimensional uniform swelling only. The major disadvantage of these models is that they cannot be applied to situations where non-uniform swelling occurs. In this research, the framework model for the swelling and shrinking behavior of stimuli-responsive gels, especially hydrogels, in respond to change of stimuli, i.e. pH, alcohol and temperature, and shrinking behavior of hydrogel during drying is derived and analyzed. This framework model can later be used to study deformation kinetics of hydrogels during drying and the application of stimuli-responsive hydrogels in the microfluidic field.

### 2. Mathematical Models and Simulations

#### 2.1 Governing equation

For the hydrogel, conservation of mass, momentum and energy can be expressed as<sup>[5]</sup>

$$\nabla \cdot \mathbf{v} = 0, \quad (1)$$

$$\nabla \cdot \boldsymbol{\sigma} = 0, \quad (2)$$

$$\nabla p = \frac{\mu}{\kappa} (\mathbf{v}^p - \mathbf{v}) \quad (3)$$

$$\rho^{(p)} c_p^{(p)} \frac{D^{(p)} T}{Dt} + \rho^{(f)} c_p^{(f)} \frac{D^{(f)} T}{Dt} = \nabla \cdot [k^{\text{eff}} \nabla T], \quad (4)$$

where  $\mathbf{v} = \phi^{(p)} \mathbf{v}^{(p)} + \phi^{(f)} \mathbf{v}^{(f)}$  is the mixture velocity,  $\phi^{(p)}$  is the volume fraction of the polymer phase,  $\phi^{(f)} = 1 - \phi^{(p)}$  is the volume fraction of the fluid,  $\mathbf{v}^{(i)}$  is the intrinsic velocity of phase  $i$ ,  $\mu^{(f)}$  is the dynamic viscosity of the fluid,  $\kappa$  is the permeability of polymer phase, and  $\boldsymbol{\sigma}$  is the mixture stress tensor. The densities of the solid phase and fluid phase are  $\rho^{(p)} = \phi^{(p)} \rho_0^{(p)}$  and  $\rho^{(f)} = \phi^{(f)} \rho_{\text{sol}}^{(f)}$ , respectively, where  $\rho_0^{(p)}$  is the true density of solid phase, and  $\rho_{\text{sol}}^{(f)}$  is the density of the liquid phase (water, water/alcohol solution).  $c_p^{(i)}$  is the specific heat of phase  $i$ ,  $k^{\text{eff}}$  is the effective mixture heat conductivity,  $T$  is the temperature and  $D^{(i)} / Dt = \partial / \partial t + \mathbf{v}^{(i)} \cdot \nabla$  is the substantial time derivative with respect to each phase.

For the alcohol sensitive hydrogel, the conservation of alcohol species in the porous deforming polymer network is defined as

$$\frac{\partial \phi^{(f)} \rho_{\text{sol}}^{(f)} \omega_{\text{sol}}^{(\text{alc})}}{\partial t} + \nabla \cdot [\phi^{(f)} \mathbf{v}^{(f)} \rho_{\text{sol}}^{(f)} \omega_{\text{sol}}^{(\text{alc})}] = \nabla \cdot [D^{\text{eff}} \rho_{\text{sol}}^{(f)} \nabla \omega_{\text{sol}}^{(\text{alc})}]. \quad (5)$$

Here,  $\omega_{\text{sol}}^{(\text{alc})}$  is the mass fraction of alcohol in the liquid solution and  $D^{\text{eff}}$  is the effective diffusion coefficient of alcohol.

For the ionic hydrogel, the ion transport can be taken into account by Nernst-Planck and Poisson equations, that are<sup>[6,7]</sup>

$$\frac{\partial c_k}{\partial t} = \nabla \cdot \mathbf{N}_k, \quad \mathbf{N}_k = -\frac{z_k F D_k}{R T} c_k \nabla \psi - D_k \nabla c_k + c_k \mathbf{v}, \quad (6)$$

$$\nabla^2 \psi = -\frac{F}{\epsilon \epsilon_0} \left( \sum z_k c_k + z_f c_f \right), \quad (7)$$

where  $F$  is Faraday constant,  $R$  is gas constant and  $\psi$  is the electric potential.  $D_k$  and  $z_k$  are diffusive coefficient and valence of the ion species  $k$ , respectively.  $\epsilon_0$  is permittivity for vacuum,  $\epsilon$  is the dielectric constant of medium relative to vacuum,  $z_f$  and  $c_f$  are the valence and concentration of fixed charge, respectively.  $c_k$  and  $c_k^*$  are the concentration of the ion species  $k$  in the hydrogel and in the exterior bath solution, respectively.

## 2.2 Constitutive relations

### 2.1.1 Solid phase

For the polymer phase the stress tensor is defined as:

$$\boldsymbol{\sigma}^{(p)} = -\phi^{(p)} p \mathbf{I} + \boldsymbol{\sigma}_{\text{eff}}^{(p)} \quad (8)$$

where  $\boldsymbol{\sigma}_{\text{eff}}^{(p)}$  is the elastic stress tensor of polymer phase. For hydrogels that experience large volume changes (finite deformation), it can be expressed in term of the Cauchy stress tensor<sup>[8]</sup> for the polymer phase. The Cauchy stress tensor for an isotropic hyperelastic material, in combination with the affine network theory for isotropic swelling of tetrafunctional networks<sup>[5,9,10]</sup> can be expressed as

$$\boldsymbol{\sigma}_{\text{eff}}^{(p)} = \frac{k_B T}{V_m N_x J} \left[ \mathbf{b} - \frac{1}{2} \mathbf{I} \right], \quad (10)$$

where  $k_B$  is the Boltzmann constant,  $V_m$  is the equivalent volume occupied by one monomer,  $N_x$  is the degree of polymerization,  $J = \det \mathbf{F} = \phi_0^{(p)} / \phi^{(p)}$  is the volume ratio,  $\mathbf{b} = \mathbf{F} \mathbf{F}^T$  is the Finger deformation tensor, and  $\phi_0$  is the initial volume fraction of polymer phase. The deformation gradient tensor,  $\mathbf{F} = d\mathbf{x} / d\mathbf{X}$ , describes the deformation between the initial and current configuration. The velocity of the solid phase in Darcy's law equation can be defined as the rate of deformation,  $\mathbf{v}^{(p)} = \partial \mathbf{u} / \partial t$ <sup>[10]</sup>, where  $\mathbf{u} = \mathbf{x} - \mathbf{X}$  is the deformation.

For hydrogel that experiences small volume changes (infinitesimal deformation), the elastic stress of polymer phase can be expressed as<sup>[11]</sup>

$$\boldsymbol{\sigma}_{eff}^{(p)} = \lambda_s trace(\mathbf{e})\mathbf{I} + 2\mu_s \mathbf{e} \quad (11)$$

where  $\lambda_s$  and  $\mu_s$  are the Lamé coefficients of solid matrix phase and  $\mathbf{e}$  is the elastic strain tensor of solid phase matrix phase, that are,

$$\lambda_s = \frac{\nu E_0}{(1+\nu)(1-2\nu)}, \quad (12)$$

$$\mu_s = \frac{E_0}{2(1+\nu)}, \quad (13)$$

$$\mathbf{e} = \frac{1}{2} \left[ \nabla \mathbf{u} + (\nabla \mathbf{u})^T \right], \quad (14)$$

in which  $E_0$  is young modulus and  $\nu$  is the Poisson ratio.

### 2.1.2 Liquid phase

Stress tensor for the fluid phase is given by

$$\boldsymbol{\sigma}^{(f)} = -\phi^{(f)} p \mathbf{I}, \quad (15)$$

where  $p$  is the total intrinsic fluid pressure, and  $\mathbf{I}$  is the unit second order tensor

For the hydrogel immersed in water/alcohol solution, the fluid phase is a binary liquid solution consisting of water and alcohol, with true (intrinsic) densities  $\rho_0^{(H_2O)}$  and  $\rho_0^{(alc)}$ , respectively. By assuming that there is no volume change when mixing water and the alcohol, we can write  $\phi_{sol}^{(H_2O)} + \phi_{sol}^{(alc)} = 1$ . The fluid phase density,  $\rho^{(f)}$ , can then defined as

$$\rho^{(f)} = \phi^{(f)} \rho_{sol}^{(f)} = \phi^{(f)} \left[ \phi_{sol}^{(H_2O)} \rho_0^{(H_2O)} + \phi_{sol}^{(alc)} \rho_0^{(alc)} \right] \quad (16)$$

where  $\phi_{sol}^{(H_2O)}$  and  $\phi_{sol}^{(alc)}$  are the volume fraction of water and alcohol in the liquid solution, respectively.

The mass fraction of alcohol is coupled to its volume fraction through

$$\omega_{sol}^{(alc)} = \frac{\phi_{sol}^{(alc)} \rho_0^{(alc)}}{\phi_{sol}^{(alc)} \rho_0^{(alc)} + \phi_{sol}^{(H_2O)} \rho_0^{(H_2O)}}. \quad (17)$$

The dynamic viscosities of water and alcohol are temperature dependent, where the former can be expressed as<sup>[12]</sup>

$$\mu^{(H_2O)} = a_1(T + a_2)^{a_3}, \quad (18)$$

and the latter by<sup>[13]</sup>

$$\mu^{(alc)} = b_1 10^{\left(b_2 + \frac{b_3}{b_4 - T}\right)}. \quad (19)$$

Here,  $a_i$  and  $b_i$  are constants summarized in Table A1.

### 2.1.3 Mixture

For a hydrogel, the total Helmholtz free energy can be expressed as<sup>[14]</sup>

$$\Delta F^{(tot)} = \Delta F^{(el)} + \Delta F^{(mix)} + \Delta F^{(ion)}$$

where  $\Delta F^{(el)}$ ,  $\Delta F^{(mix)}$  and  $\Delta F^{(ion)}$  are the elastic, mixing and ionic free energies, respectively. The elastic free energy is considered in the form of the stress tensor for the polymer phase. Meanwhile, the mixing and ionic free energies contribute to the osmotic pressure<sup>[14-17]</sup>, and is given by

$$p_{mix}^{(osm)} = -\frac{k_B T}{V_m} \left( \phi^{(p)} + \chi \phi^{(p)^2} + \ln(1 - \phi^{(p)}) \right), \quad (20)$$

$$p_{ion}^{(osm)} = RT \sum_k^N (c_k - c_k^*), \quad (21)$$

where the polymer-solvent interaction parameter,  $\chi$ , is an indicator of the compatibility between polymer network and solvent. The polymer-solvent interaction parameter,  $\chi(T, \phi^{(p)})$ , is generally expressed as a function of temperature and polymer volume fraction.<sup>[1,14,18]</sup>

$$\chi = -\frac{\Delta s}{k_B} + \frac{\Delta h}{k_B T} + \chi_2 \phi^{(p)}, \quad (22)$$

where  $\Delta h$  and  $\Delta s$  are the changes in enthalpy and entropy, and  $\chi_2$  is a less well-defined parameter to express the polymer volume fraction dependence of the interaction parameter.

For the hydrogel immersed in the water/alcohol solution, the polymer solvent interaction is given by

$$\chi = -\frac{\Delta s(\omega_{sol}^{(alc)})}{k_B} + \frac{\Delta h(\omega_{sol}^{(alc)})}{k_B T} + \chi_2(\omega_{sol}^{(alc)}) \phi^{(p)}, \quad (23)$$

where three parameters,  $\Delta h(\omega_{sol}^{(alc)})$ ,  $\Delta s(\omega_{sol}^{(alc)})$  and  $\chi_2(\omega_{sol}^{(alc)})$ , are in turn functions of the alcohol mass fraction and thus capture the response of the hydrogel to changes in the alcohol concentration.

The total mixture stress tensor is defined as<sup>[5]</sup>

$$\sigma = -p \mathbf{I} + \sigma_{eff}^{(p)}. \quad (24)$$

The dynamic viscosity of the fluid phase is important as it directly affects the swelling kinetics and can be calculated by employing a mixing rule equation<sup>[19]</sup>

$$\mu^{(f)} = c_1 \left[ \left( \mu^{(alc)} \right)^{x_{sol}^{(alc)}} \left( \mu^{(H_2O)} \right)^{x_{sol}^{(H_2O)}} \left( 1 + \frac{x_{sol}^{(alc)} x^{(H_2O)}}{c_2 + c_3 x_{sol}^{(alc)^2}} \right) \right], \quad (25)$$

where  $\mu^{(i)}$  and  $x_{sol}^{(i)}$  are the dynamic viscosity and molar fraction of species  $i$  (alc or H<sub>2</sub>O), respectively. The molar fraction is defined as

$$x_{sol}^{(i)} = \frac{\omega_{sol}^{(i)} / M^{(i)}}{\omega_{sol}^{(alc)} / M^{(alc)} + \omega_{sol}^{(H_2O)} / M^{(H_2O)}}, \quad (26)$$

where  $M^{(i)}$  is the molecular weight of species  $i$ . The values of the constants,  $c_1$ ,  $c_2$  and  $c_3$ , for water-methanol mixture<sup>[19]</sup> are summarized in Table A1 and Table A2.

Similar to Birgersson<sup>[5]</sup>, Tokita and Tanaka<sup>[20]</sup> and Grattoni<sup>[21]</sup>, we introduce the permeability of the hydrogel as

$$\kappa = \kappa_0 \phi^{(p)^{\frac{3}{2}}}, \quad (27)$$

where  $\kappa_0$  is a parameters which requires adaptation to experimental kinetic data.

The specific heat of the fluid phase is expressed as

$$c_p^{(f)} = \phi_{sol}^{(H_2O)} c_p^{(H_2O)} + \phi_{sol}^{(alc)} c_p^{(alc)}. \quad (28)$$

For the effective thermal conductivity, we assume an arithmetic mean value based on the solid polymer phase and the binary liquid phase,<sup>[22]</sup> namely

$$k^{eff} = \phi^{(p)} k^{(p)} + \phi^{(f)} k^{(f)} = \phi^{(p)} k^{(p)} + \phi^{(f)} \left( \phi_{sol}^{(H_2O)} k^{(H_2O)} + \phi_{sol}^{(alc)} k^{(alc)} \right). \quad (29)$$

The Bruggeman equation<sup>[23]</sup> is employed to calculate the effective diffusion coefficient of methanol:

$$D^{eff} = \left( \phi^{(f)} \right)^{\frac{3}{2}} D_{alc-H_2O}, \quad (30)$$

in which  $D_{alc-H_2O}$  is the binary diffusion coefficient of alcohol in water.

For ionic hydrogel, the fixed charge concentration will change as the geometry change which caused by osmotic

pressure. The fixed charge concentration is given by<sup>[17]</sup>

$$c_f = \frac{1}{H} \frac{c_f^0 K_a}{(K_a + c_H)} \quad (31)$$

where  $c_f^0$  and  $c_H$  are the initial fixed charge and hydrogen ion concentrations, respectively,  $K_a$  is the dissociation constant of the fixed charge group and  $H$  is the hydration state of the hydrogel which is defined as the ratio of the volume of fluid  $V_f$  to the initial volume of the dry solid polymer network  $V_0$  i.e.  $H = V_f / V_0$ .

Moreover, the Donnan equilibrium<sup>[24]</sup> is used to determine the ion's concentration at the surface of the hydrogels from the corresponding concentrations of the species in the outer solutions, that is

$$c_k = \lambda^{z_k} c_k^* \quad (32)$$

where  $\lambda$  is the Donnan ratio which is given by

$$\lambda = \exp\left(-\frac{F}{RT}(\psi - \psi^*)\right) \quad (33)$$

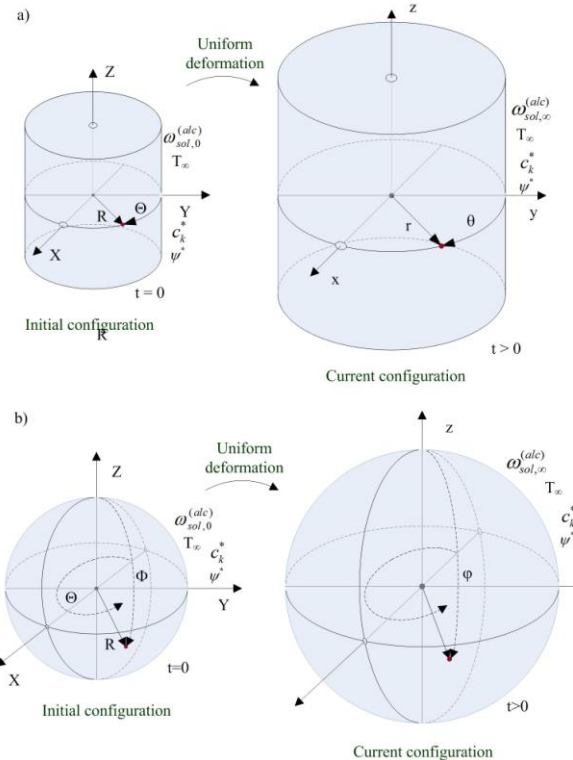


Figure 2: Typical geometries of gels for experiments.

#### 2.1.4 Initials and boundary conditions

The majorities of experiments for swelling behavior of various hydrogels are carried out for hydrogels in the shape of cylinders or spheres as illustrated in figure 2. Hence, the initial and boundary conditions for the hydrogels model are:

**Initial conditions**

$$c_k = c_{k,0}, \psi = \psi_0, T = T_0, \omega_{sol}^{(alc)} = \omega_{sol,0}^{(alc)}, \mathbf{u} = \mathbf{u}_0 \quad (34)$$

**Boundary at the centre of hydrogel**

$$c_k = \text{finite}, \psi = \text{finite}, T = \text{finite}, \omega_{sol}^{(alc)} = \text{finite}, \mathbf{u} = 0 \quad (35)$$

**Boundary condition at the hydrogel surface**

$$\sigma \cdot n = (-p_\infty \mathbf{I}) \cdot n, p = p^{(osm)} + p_\infty, \omega_{sol}^{(alc)} = \omega_{sol,\infty}^{(alc)}, T = T_\infty, c_k = \lambda^{z_k} c_k^*, \text{ and } \psi = -\frac{RT}{F} \ln \lambda + \psi^* \quad (36)$$

### 3. Simulations and Results

The commercial finite element solver, Comsol multiphysics 3.5a<sup>[25]</sup> is chosen to implement the mathematical model due to its reliability in handling general coupled nonlinear partial differential equations. In this paper, 2 numerical investigations that have been carried out will be presented, e.g. steady state analysis of pH-sensitive hydrogels and steady state analysis of coupled temperature and alcohol sensitive hydrogels.

#### 3.1 pH-sensitive hydrogels

The mathematical formulation that has been developed and analyzed in the previous section will be used to study the swelling behavior of hydrogels subject to alterations of pH. This study will focus on the equilibrium state of hydrogel deformation. The pH sensitive hydrogel considered is homogeneous copolymers of HEMA (hydroxil-ethyl-methacrylate acid) and acrylic acid, prepared and analyzed by De et al.<sup>[17]</sup> with 1% of a diacrylate crosslinker. The operating conditions and parameter used for this simulation are summarized in table A3. The cylindrical hydrogel is placed in a channel and axially constrained thus it can only deform on the radial direction as illustrated in figure 3.

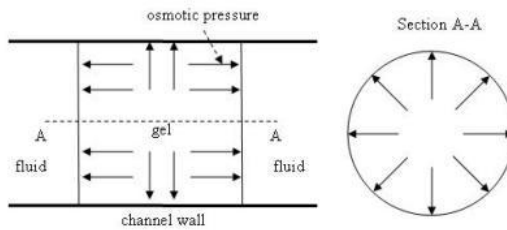


Figure 3: Cylindrical hydrogel is placed in a channel. The hydrogel is axially constrained<sup>[17]</sup>.

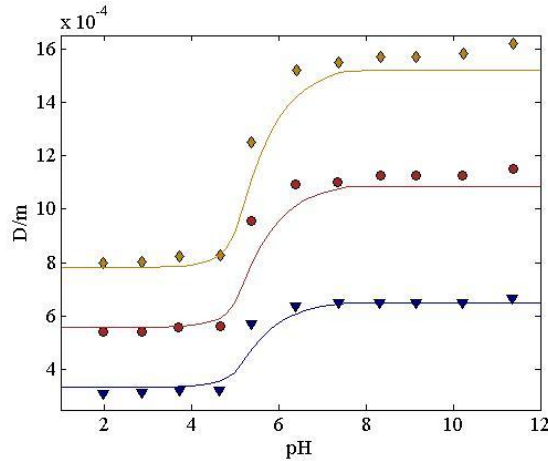


Figure 4: pH dependence of equilibrium swelling curve, the experimentally measured values are (De et al., 2002): (▼) 300 micrometer; (●) 500 micrometer; (◆) 700 micrometer. The solid lines are the corresponding model prediction<sup>[17]</sup>.

The model prediction is then compared to the experiments by De et al.<sup>[17]</sup> Overall, good agreement is achieved between the model predictions and experiments as presented in figure 4. It can also be seen that the hydrogel is in the shrunken state at low pH (<3) which is presented by the small radius of the hydrogel. At pH 4, the hydrogel start to swell and the hydrogel radius slightly increase. As the pH further increase within the range of 5 to 6 the hydrogel swells significantly. It can be seen from the step increase on the hydrogel radius for that range of pH. At pH 7 and above, the hydrogel stop to swell as it has reached the maximum radius.

This mathematical model will later be employed to carry out wide range parameter study of pH-sensitive hydrogel and study the applications of pH-sensitive hydrogels in microfluidic flow controller. This model can also be extended to study others polyelectrolyte hydrogel such as electric-sensitive hydrogels and glucose-sensitive hydrogels.

### 3.2 Coupled temperature and alcohol-sensitive hydrogels

The mathematical model has also been implemented to study the swelling behavior of hydrogels subject to change in temperature and alcohol concentration. The hydrogels considered is poly(N-isopropylacrylamide) (PNIPA) hydrogel immersed in methanol-water solvent prepared and analyzed by Hirotsu<sup>[26]</sup> with volume swelling ratio of 0.1 to 3. In developing mathematical model, some required parameters are unknown. Therefore, parameter adaption is carried out by employing an equivalent sphere solution to simplify the mathematical model. Parameter adaptation is carried out with the numerical solver and language programming, Matlab R2008a<sup>[27]</sup>, by solving nonlinear curve-fitting (data-fitting) problems in least-squares sense. The parameter is then applied to 3D cylindrical model and solved with appropriate boundary condition by using COMSOL multiphysics 3.5a. The operating conditions and parameters are presented in Table A1, A2 and A4. The model predictions are next compared to the experiments by Hirotsu<sup>[26]</sup>, the comparison is presented in figure 5.

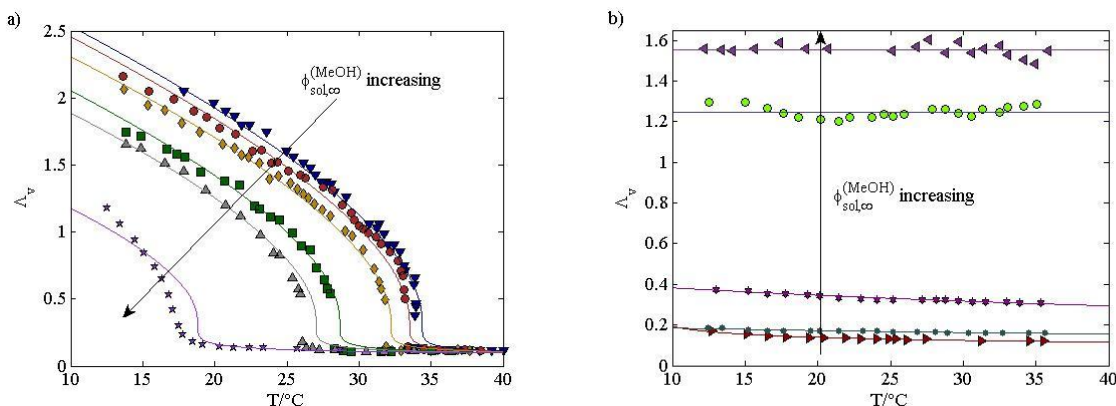


Figure 5: Equilibrium swelling curves for poly(N-isopropylacrylamide) in water-methanol solutions. The measured values are for  $\phi_{sol,\infty}^{(MeOH)}$ : ( $\nabla$ ) 0 (pure water); ( $\bullet$ ) 0.02; ( $\diamond$ ) 0.08; ( $\blacksquare$ ) 0.13; ( $\blacktriangle$ ) 0.18; ( $\star$ ) 0.25; ( $\blacktriangleright$ ) 0.35; ( $\bullet$ ) 0.45; ( $\ast$ ) 0.60 methanol; ( $\circ$ ) 0.80; ( $\blacktriangleleft$ ) 1 (pure methanol) (Hirotsu, 1987). The solid lines are the corresponding model predictions.

Overall the model predictions match reasonably well with the experiments. In addition, it can be observed a general trend of a decrease in swelling ratio with increasing temperature. This is a characteristic trait of LCST hydrogel which swells at lower temperature and shrinks at higher temperature. At low methanol concentration of methanol, the equilibrium swelling is dependent of temperature. At high concentration of methanol, however, the equilibrium swelling curve goes horizontally and independent of temperature.

Future work will seek to study the transient swelling behavior of hydrogel when it is subjected to alcohol and temperature coupled stimuli. A scale analysis will be conducted to provide the proper scales for the transport and deformation mechanisms, and also give an insight into the swelling behavior prior to numerical computations. This mathematical model can also be generalized to study the swelling behavior of hydrogels immersed in others binary liquid solutions.

### 4. Concluding Remarks

The mathematical frame work model that takes into account conservation of momentum, mass, energy, and species for a hydrogel subject to change in its environment conditions, e.g. pH, temperature and enzyme, is formulated and presented. The model is then employed to study swelling behavior of pH-sensitive hydrogel and coupled temperature and alcohol sensitive hydrogels. Overall, good agreement is achieved between the model predictions and experiments. This frame work

model will later be used to investigate the swelling behavior and deformation kinetics of hydrogels subject to various stimuli. This model will also be employed to study the drying and deformation kinetics of hydrogels and jelly-like materials during drying.

### Acknowledgments

The authors would like to express their sincere gratitude to the National University of Singapore and AUN/SEED-Net (JICA) for their financial support.

### References

1. Shirota, H., Endo, N., Horie, K., 1998. Volume phase transition of polymer gel in water and heavy water, *Chem. Phys.* 238, 487-494.
2. Roy, I., Gupta, N., 2003. Smart polymeric materials: emerging biochemical applications. *Chem. Biol.* 10, 1161-1171.
3. Qiu, Y., Park, K., 2001. Environment-sensitive hydrogels for drug delivery. *Adv. Drug Deliver. Rev.* 53, 321-339.
4. Flory, P.J., 1953. Principles of polymer chemistry. Cornell University Press. New York.
5. Birgersson, E., Li, H., Wu, S., 2008. Transient analysis of temperature-sensitive neutral hydrogels. *J. Mech. Phys. Solids.* 56 (2), 444-466.
6. Newman, J., Thomas-Alyea, K. E., 2004. Electrochemical Systems. John Wiley and Sons Inc.
7. Li, H., Yew, Y.K., Ng, T.Y., Lam, K.Y., 2005. Meshless steady-state analysis of chemo-electro-mechanical coupling behavior of pH sensitive hydrogel in buffered solution. *J. Electroanal. Chem.* 580, 161-172.
8. Holzapfel, G.H., 2000. Nonlinear Solid Mechanics, A Continuum Approach for Engineering. John Wiley and Sons.
9. Lele, A.K., Devotta, I., Mashelkar, R.A., 1997. Predictions of thermoreversible volume phase transitions in copolymer gels by lattice-fluid-hydrogen-bond theory. *J. Chem. Phys.* 106(11), 4768-4772.
10. Barry, S.I., Holmes, M., 2001. Asymptotic behavior of thin poroelastic layer. *IMA. J. Appl. Math.* 66, 175-194.
11. Sun, D.N., Gu, W.Y., Guo, X.E., Lai, W.M., Mow, V.C., 1999. A mixed finite element formulation of triphasic mechano-electrochemical theory for charged, hydrated biological soft tissues
12. Gawin, D., Majorana, C.E. Schrefler, B.A., 1999. Numerical analysis of hygro-thermal behavior and damage of concrete at high temperature. *Mech. Cohesiv.-Frict. Mater.* 4, 37-74.
13. Viswanath, D.S., Ghosh, T.K., Prasad, D.H.L., Dutt, N.V.K., Rani, K.Y., 2007. Viscosity of Liquids: Theory, Estimation, Experiment, and Data. Springer.
14. Hirotsu, S., 1991. Softening of bulk modulus and negative Poisson's ratio near the volume phase transition of polymer gels. *J. Chem. Phys.* 94 (5), 3949-3957.
15. Shibayama, M., Tanaka, T., 1993. Volume phase transition and related phenomena of polymer gels. In Dusek, K., editor., 1993. Advanced in Polymer science 109. Berlin: Springer Verlag. 1-62.
16. Achilleos, E.C., Christodoulou, K.N., Kevrekidis, I.G., 2001. A transport model for swelling of polyelectrolyte gels in simple and complex geometries. *Comput. Theor. Polym. Sci.* 11, 63-80.
17. De, S.K., Aluru, N.R., Johnson, B., Crone, W.C., Beebe, D.J., Moore, J., 2002. Equilibrium swelling and kinetics of pH-responsive hydrogels: models, experiments and simulations. *J. Microelectromech. syst.* 11 (5), 544-555.
18. Oh, K.S., Bae, Y.C., 1998. Swelling behavior of submicron gel particles. *J. Appl. Polym. Sci.* 69, 109-114.
19. Stephan, K., Heckenberger, T., 1988. Thermal conductivity and viscosity data of fluid mixtures v. 10, pt. 1. Dechema.
20. Tokita, M. and Tanaka, T., 1991. Friction coefficient of polymer networks of gels. *J. Chem. Phys.* 95 (6), 4613-4619.
21. Grattoni, C. A., Al-Sharji, H.H., Yang, C., Muggeridge, A. H., Zimmerman, R.W., 2001. Rheology and permeability of cross-linked polyacrylamide gel. *J. Colloid and Interface Sci.* 240, 601-607.
22. Nield, D.A., Bejan, A., 1999. Convection in Porous Media. Springer, New York.
23. Agarwal, A.S., Landau, U., Payer, J.H., 2008. Modeling particulates effects on the cathode current capacity in crevice corrosion. *J. Electrochem. Soc.* 155 (5), C269-C278.

24. Siegel, R.A., 1990. pH-sensitive gels: Swelling equilibria, kinetics, and applications for drug delivery. In Kost, J., editor. Pulsed and self-regulated drug delivery. Florida: CRC Press, Inc. 129-157.
25. Comsol Multiphysics(<http://www.comsol.com>)
26. Hirotsu, S., 1987. Phase transition of a polymer gel in pure and mixed solvent media. *J. Phys. Soc. Jpn.* 56 (1), 233-242.
27. Matlab (<http://www.mathworks.com>).
28. Kaviany, M., 2002. Principles of heat transfer. Wiley, New York.
29. Bird, R.B., Stewart, W.E., Lightfoot, E.N., 2002, Transport phenomena, 2nd ed., John Wiley & Sons, New York.
30. Welty, J.R., Wicks, C.E., Wilson, R.E., Rorrer, G., 2001. Fundamental of momentum, heat and mass transfer, 4<sup>th</sup> ed. Wiley, New York.
31. Prokop, A.F., Vaezy, S., Noble, M.L., Kaczkowski, P.J., Martin, R.W., Crum, L.A., 2003. Polyacrylamide gel as an acoustic coupling medium for focused ultrasound therapy, *Ultrasound in Med. & Biol.* 20 (9), 1351-1358.

## Appendix

Table A1. Physical parameters for coupled temperature and alcohol sensitive hydrogels

Physical parameters	
$k_B$	$1.38054 \times 10^{-23} \text{ J K}^{-1}$
$V_m$	$3.3 \times 10^{-28} \text{ m}^3$ [5]
Physical parameter (Liquid phase-water)	
$a_1, a_2, a_3$	$0.6612 \text{ kg m}^{-1} \text{ K}^{1.562}, -229 \text{ K} \quad -1.562$
$\rho_0^{(H_2O)}$	$10^3 \text{ kg m}^{-3}$ [28]
$M^{(H_2O)}$	$18 \text{ kg kmol}^{-1}$ [28]
$c_p^{(H_2O)}$	$4.2 \times 10^3 \text{ J kg}^{-1} \text{ K}^{-1}$ [29]
$k^{(H_2O)}$	$0.0264 \text{ W m}^{-1} \text{ K}^{-1}$ [28]
Physical parameter (Liquid phase-methanol)	
$b_1, b_2, b_3, b_4$	$10^{-3} \text{ N s m}^{-1}, -1.84, -4.24 \times 10^2 \text{ K}, 29.7 \text{ K}$
$c_1$	$1 \text{ Pa s}$
$\rho_0^{(alc)}$	$0.751 \times 10^3 \text{ kg m}^{-3}$ [28]
$M^{(MeOH)}$	$32 \text{ kg kmol}^{-1}$ [28]
$c_p^{(MeOH)}$	$2.88 \times 10^3 \text{ J kg}^{-1} \text{ K}^{-1}$ [28]
$k^{(MeOH)}$	$0.1536 \text{ W m}^{-1} \text{ K}^{-1}$ [28]
$D_{MeOH-H_2O}$	$0.0264 \text{ W m}^2 \text{ s}^{-1}$ [30]
Physical parameters (Polymer phase)	
$\rho_0^{(p)}$	$1.1 \times 10^3 \text{ kg m}^{-3}$
$c_p^{(p)}$	$6.47 \times 10^{-3} \text{ J kg}^{-1} \text{ K}^{-1}$ [31]
$k^{(p)}$	$0.84 \text{ W m}^{-1} \text{ K}^{-1}$ [31]

**Table A2.** Temperature-dependent parameter corelation for the mixing-rule equation for the dynamic viscosity of the liquid water-alcohol solution.<sup>[19]</sup>

Temperature K	Water-Methanol mixture		Water-Ethanol mixture	
	$c_2$	$c_3$	$c_2$	$c_3$
280	-	-	0.045	0.553
285	0.125	0.447	0.054	0.587
290	0.138	0.450	0.062	0.622
295	0.151	0.452	0.072	0.659
300	0.166	0.454	0.081	0.699
305	0.182	0.453	0.092	0.741
310	0.199	0.451	0.102	0.786
315	0.218	0.446	0.114	0.834
320	0.238	0.437	0.125	0.886
325	0.261	0.426	0.137	0.942
330	0.286	0.409	0.149	1.001
335	-	-	0.161	1.065

**Table A3.** Physical parameters and operating conditions of pH sensitive hydrogel.

$E_0$	0.29 MPa for $\text{pH} < 5.5$ (-0.03pH+0.455) MPa for $5.5 < \text{pH} < 7.5$ 0.23 MPa for $\text{pH} > 7.4$ <sup>[17]</sup>
$\nu$	0.40 <sup>[17]</sup>
$R$	$8.314 \text{ J K}^{-1}\text{mol}^{-1}$
$\varepsilon$	80 (water)
$\varepsilon_0$	$8.85 \times 10^{-12} \text{ F m}^{-1}$
$c_f^0$	$1800 \text{ mol m}^{-1}$ <sup>[17]</sup>
$K_a$	$10^{-2} \text{ mol m}^{-1}$ <sup>[17]</sup>
$V_m$	$3.3 \times 10^{-28} \text{ m}^3$ <sup>[5]</sup>
$\Delta h$	$-1.33 \times 10^{-20} \text{ J}$
$\Delta s$	$-4.3 \times 10^{-23} \text{ J K}^{-1}$
$\chi_2$	1.3

**Table A4.** Values of adapted parameters for Poly(N-isopropylacrylamide) hydrogel immersed in a water-methanol solution.<sup>[26]</sup>

$\omega_{sol}^{(MeOH)}$	$\Delta h \left(\times 10^{-20} J\right)$	$\Delta s \left(\times 10^{-22} J K^{-1}\right)$	$\chi_2$	$N_x (\times 10^2)$
0	-3.345	-1.152	0.57	8.66
0.015	-3.250	-1.124	0.57	8.66
0.061	-3.021	-1.053	0.57	8.66
0.101	-2.800	$-9.917 \times 10^{-1}$	0.57	8.66
0.142	-2.559	$-9.166 \times 10^{-1}$	0.57	8.66
0.200	-1.642	$-6.265 \times 10^{-1}$	0.57	8.66
0.288	$-4.532 \times 10^{-1}$	$-2.249 \times 10^{-1}$	0.57	8.66
0.381	$-2.485 \times 10^{-1}$	$-1.848 \times 10^{-1}$	0	8.66
0.530	$-1.402 \times 10^{-1}$	$-1.288 \times 10^{-1}$	0	8.66
0.750	0	$-4.865 \times 10^{-2}$	0	8.66
1	0	$-3.433 \times 10^{-2}$	0	8.66

## ► [ MATHEMATICAL MODELING OF PEM FUEL CELL STACK: THERMAL MANAGEMENT]

### [Chapter 6]

**Agus P. Sasmito<sup>1</sup>, Erik Birgersson<sup>2</sup> and Arun S. Mujumdar<sup>1</sup>**

► [<sup>1</sup>Department of Mechanical Engineering, National University of Singapore. <sup>2</sup>Department of Chemical and Bio-molecular Engineering, National University of Singapore]

The design of a polymer electrolyte membrane fuel cell (PEMFC) stack requires careful consideration. In this work, we aim to develop a mathematical and numerical framework for PEMFC stacks that serves two main objectives: the first involves the study of the fundamental aspects of the PEM fuel cell and the associated transport, electrochemical processes and multiphase flow for both a single cell and stack. The second objective concerns the development and integration of applied research for the PEM fuel cell and stack, including thermal management issues, designs, and optimization to achieve an enhanced fuel cell performance.

To study the impact of these design parameters, a two-phase model accounting for the conservation of mass, momentum, species, energy, charge, a phenomenological model for the membrane, and an agglomerate model for the catalyst layer, is developed and solved. The model is validated for a single cell, both in terms of the local as well as the global current density, and good agreement is found. It is then employed as a building block for stack modeling. Three different cooling methods, namely: water-cooling, forced convection air-cooling and natural convection air-cooling, are investigated.

## Mathematical modeling of PEM fuel cell stack: Thermal management

### 1. Introduction

The design of a proton exchange membrane fuel cell (PEMFC) stack comprising a large number of cells requires careful design in order to achieve high stack performance. Ideally, each and every cell in the stack requires identical operating conditions to ensure optimal performance. In reality, however, it is generally difficult to achieve such ideal conditions as a stack, a schematic of which is shown in Figure 6.1a, can comprise tens or even hundreds of cells. Each of these cells contains additional parts as illustrated in Figure 6.1b.

One key component in the stack that is directly linked to the operating performance is the thermal management, i.e. careful cooling of every cell in the stack. This is due to the substantial amount of heat that is generated by each cell during operation from entropy changes and irreversibility. If one removes too much heat, then the reaction kinetics are adversely affected, resulting in lower stack performance. Conversely, if the stack is allowed to heat up beyond optimal operation temperatures, the membrane water content and proton conductivity drop. The control of the membrane water content is therefore also a vital part of the stack management strategy. Intuitively, placing a cooling plate between each single cell should allow for a good control of the thermal envelope and ensure near to identical operation conditions throughout the stack; this, however, would increase the cost, weight and complexity of the system. In light of this, a careful balance has to be struck between amount of cooling plates, cost, weight, and complexity.

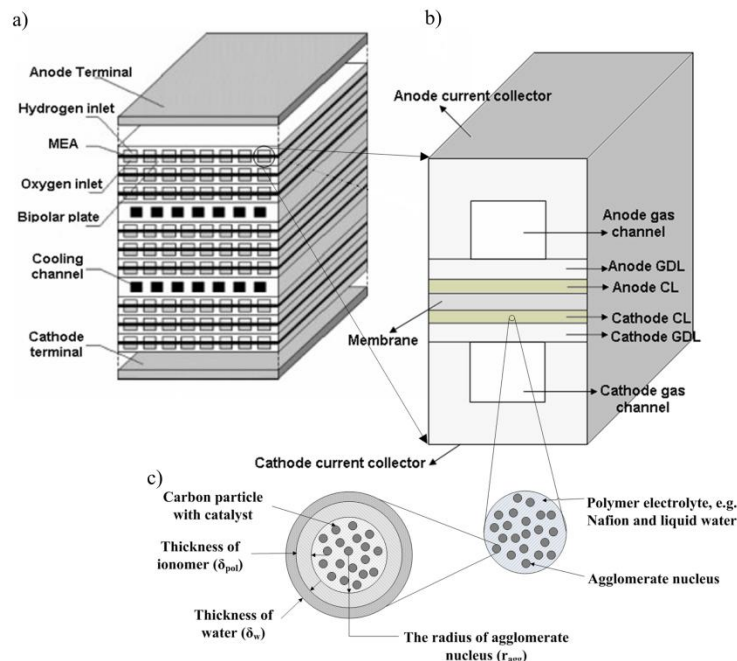


Figure 6.1: Schematic of the PEMFC: a) stack; b) single cell; c) agglomerate catalyst layer.

Several mechanisms can be employed for cooling purposes, such as forced convection in specially designed cooling plates with either liquid water or air, or natural convection due to temperature differences between the stack and the surrounding. The latter is usually only applied to small stacks of a few cells as the rate of heat removal is not sufficient for larger stacks. Another more exotic method includes the use of phase change materials.

The complexity of a stack and the small length scales involved in each constituent cell, ranging from few centimeter for height of stack to 0.1 micron for agglomerate catalyst particle (see Fig 6.1.c for details), necessitate mathematical modeling and simulation to aid in the design of a functional and cost-efficient cooling systems. To date, most of the mathematical

modeling and simulation pertaining to the PEMFC has focused on single cells, with a multitude of models derived and solved for. Less work has been carried out for stacks due to the prohibitive computational cost involved in resolving all the cells and their components.

## 2. Mathematical Formulations

A single domain, non-isothermal two-phase model that considers conservation of mass, momentum, energy, species, electronic and ionic charge as well as a phenomenological membrane model is implemented and solved for each constituent layer, e.g., current collector (cc), flow-field (ff), gas diffusion layer (gdl), catalyst layer (cl), membrane (m) and coolant plate (co).

The dimensionality is reduced from three to two by exploiting the porous nature of each single cell as well as coolant plate, which are of a net-type. Furthermore, to reduce the computational cost, repetitive units with periodic boundary conditions on top and bottom of the cell are identified and solved for the stack model. The main geometry, operating conditions and physical parameters can be found in Appendix (Table 6.I).

### 2.1 Governing equations

The governing equations are:

Continuity equation:

$$\nabla \cdot (\rho \mathbf{u}) = -\dot{m}_{H_2O} + S_m \quad (6.1)$$

Momentum conservation:

$$\nabla \cdot (\rho \mathbf{u} \mathbf{u}) = -\nabla P + \nabla \cdot \left[ \mu \left[ \left( \nabla \mathbf{u} + \nabla \mathbf{u}^T \right) - \frac{2}{3} \nabla \cdot \mathbf{u} \mathbf{I} \right] \right] - \frac{\mu}{\kappa} \mathbf{u} \quad (6.2)$$

Energy conservation:

$$\nabla \cdot (\rho C_p \mathbf{u} T) = \nabla \cdot k_{eff} \nabla T + S_h \quad (6.3)$$

Species conservation:

$$\nabla \cdot (\rho \mathbf{u} \omega_i) = \nabla \cdot (\rho D_i^{eff} \nabla \omega_i) + S_i \quad (6.4)$$

Electronic charge potential:

$$\nabla \cdot (\sigma_s \nabla \phi_s) + S_{\phi_s} = 0 \quad (6.5)$$

Ionic charge potential:

$$\nabla \cdot (\sigma_m \nabla \phi_m) + S_{\phi_m} = 0 \quad (6.6)$$

Phenomenological membrane model:

$$\nabla \cdot \mathbf{j}_w = 0, \text{ where } \mathbf{j}_w = \frac{n_d M_{H_2O}}{F} \mathbf{i}_m - \frac{\rho_m}{M_m} M_{H_2O} D_\lambda \nabla \lambda \quad (6.7)$$

Conservation of liquid water:

$$\nabla \cdot (\rho_l \mathbf{u}_g s) = \nabla \cdot \left[ \frac{\rho_l K_s^3}{\mu_l} \frac{dp_c}{ds} \nabla s \right] + \dot{m}_{H_2O} \quad (6.8)$$

### 2.2 Constitutive relations and source terms

The source terms in the catalyst layers are:

$$S_m = -\frac{M_{H_2}}{2F} j_a - \frac{M_{O_2}}{4F} j_c + \frac{M_{H_2O}}{2F} j_c \quad (6.9)$$

$$S_{H_2} = -\frac{M_{H_2}}{2F} j_a \quad S_{O_2} = -\frac{M_{O_2}}{4F} j_c \quad S_{H_2O} = +\frac{M_{H_2O}}{2F} j_c - \dot{m}_{H_2O} \quad (6.10)$$

$$S_h = |\eta| j_{a,c} + T \frac{dE^{rev}}{dT} j_c + i^2 R_{ohm} + \dot{m}_{H_2O} h_{fg} \quad (6.11)$$

$$S_{\phi_s} = -j_a, j_c \quad S_{\phi_m} = j_a, -j_c \quad (6.12)$$

The source terms in the gas diffusion layer:

$$S_{H_2O} = -\dot{m}_{H_2O} \quad (6.13)$$

$$S_h = i^2 R_{ohm} + \dot{m}_{H_2O} h_{fg} \quad (6.14)$$

The source terms elsewhere:

$$S_h = i^2 R_{ohm} \quad (6.15)$$

The gas density (assuming ideal gas) is defined as:

$$\rho = \frac{pM}{RT} \quad (6.16)$$

where:

$$M = (\omega_{H_2}/M_{H_2} + \omega_{O_2}/M_{O_2} + \omega_{H_2O}/M_{H_2O} + \omega_{N_2}/M_{N_2})^{-1} \quad (6.17)$$

The mass fraction of nitrogen is given by:

$$\omega_{N_2} = 1 - \omega_{H_2} - \omega_{O_2} - \omega_{H_2O} \quad (6.18)$$

The molar fractions are related to the mass fraction, given by:

$$x_i = \frac{\omega_i M}{M_i} \quad (6.19)$$

The mass diffusion coefficients are defined as:

$$D_i^{eff} = D_i \gamma^{1.5} (1-s) \text{ where } D_i = D_i^0 \left( \frac{T}{T^0} \right)^{1.5} \left( \frac{p^0}{p} \right) \quad (6.20)$$

The effective thermal conductivity are defined as:

$$k_{eff} = \gamma(1-s)(\sum k_i \omega_i) + \gamma s k_{H_2O} + (1-\gamma)k_s \quad (6.21)$$

The phase change source is modeled as follows:

$$\dot{m}_{H_2O} = c_{r_{max}} \left[ \left( 1-s \right) \frac{P_{wv} - P_{sat}}{RT} M_{H_2O} \right], [-s \rho_l] \quad (6.22)$$

where the capillary pressure is:

$$p_c = \frac{\sigma \cos \theta}{(\kappa_l / \gamma)^{0.5}} (1.417(1-s) - 2.12(1-s)^2 + 1.263(1-s)^3) \quad \text{for } \theta_c < 90 \quad (6.23)$$

$$p_c = \frac{\sigma \cos \theta}{(\kappa_l / \gamma)^{0.5}} (1.417s - 2.12s^2 + 1.263s^3) \quad \text{for } \theta_c > 90$$

### 2.3 Electrochemistry and agglomerate model

The volumetric current density with agglomerate correction factors is applied at the cathode catalyst layer due to slow kinetic reaction, while at the anode a conventional expression<sup>[1]</sup> based on the Butler-Volmer equation is employed as the overpotential are significantly lower than at the cathode:

$$\begin{aligned} j_a &= A_v j_a^{ref} \left( \frac{c_{H_2}}{c_{H_2,ref}} \right)^{\gamma_a} \left( e^{\frac{\alpha_a F}{RT} \eta_a} - e^{-\frac{\alpha_a F}{RT} \eta_a} \right) \\ j_c &= A_v j_c^{ref} \left( \frac{c_{O_2}}{c_{O_2,ref}} \right)^{\gamma_c} \left( -e^{\frac{\alpha_a F}{RT} \eta_c} + e^{-\frac{\alpha_a F}{RT} \eta_c} \right) \frac{RT}{H} \xi_1 \frac{1}{1 + \xi_2 + \xi_3} \end{aligned} \quad (6.24)$$

where for electronic charge potential  $S_{\phi_s} = \begin{cases} -j_a \\ +j_c \end{cases}$ , and ionic charge potential  $S_{\phi_m} = \begin{cases} +j_a \\ -j_c \end{cases}$

The agglomerate model is implemented to account for mass transfer inside the cathode catalyst layer. Here, we assume the agglomerate nucleus to be spherical in shape, which in turn is covered by thin film of ionomer and liquid water [2-12]

$$j_c = A_v j_c^{ref} \left( \frac{c_{O_2}}{c_{O_2,ref}} \right)^{\gamma_c} \left( -e^{\frac{\alpha_a F}{RT} \eta_c} + e^{-\frac{\alpha_a F}{RT} \eta_c} \right) \frac{RT}{H} \xi_1 \frac{1}{1 + \xi_2 + \xi_3} \quad (6.25)$$

The overpotentials are defined as:

$$\eta_a = \phi_s - \phi_m \quad \text{at the anode}$$

$$\eta_c = \phi_s - \phi_m - E^{rev} \quad \text{at the cathode.}$$

$$E^{rev} = 1.229 - 0.83 \times 10^{-3} (T - 298) + \frac{RT}{4F} \ln x_{O_2} \quad (6.26)$$

The current densities are defined as:

$$\mathbf{i}_s = -\sigma_s \nabla \phi_s \quad \text{and} \quad \mathbf{i}_m = -\sigma_m \nabla \phi_m \quad (6.27)$$

Reference exchange current density:

$$A_0 = \frac{3m_{Pt}}{r_{Pt} \rho_{Pt}} \quad (6.28)$$

$$A_v j_c^{ref} = A_0 j_{c,0}^{ref} (1 - \gamma_{cl}) (1 - \frac{\gamma_{pol}}{\gamma_{agg}}) e^{\left( -\frac{E_a}{R} \left[ \frac{1}{T} - \frac{1}{353.15} \right] \right)} \quad (6.29)$$

Correction factor due to agglomerate:

$$\xi_1 = \frac{1}{\Phi_L} \left( \frac{1}{\tanh(3\Phi_L)} - \frac{1}{3\Phi_L} \right) \quad (6.30)$$

$$\Phi_L = \frac{r_{agg}}{3} \sqrt{\frac{k_c}{D_{O_2,agg}^{eff}}} \quad (6.31)$$

$$\text{where } k_c = \frac{j_c^{ref} \left( -e^{\frac{\alpha_a F}{RT} \eta_c} + e^{-\frac{\alpha_a F}{RT} \eta_c} \right)}{(1 - \gamma_{cl}) n F c_{O_2}^{ref}} \quad \text{and} \quad D_{O_2,agg}^{eff} = D_{O_2,mem} \left( \frac{\gamma_{pol}}{\gamma_{agg}} \right)^{1.5} \quad (6.32)$$

Correction factor due to polymer film:

$$\xi_2 = \frac{\delta_{pol}}{D_{O_2,mem}} \frac{\xi_1}{a_{pol}} k_c \quad (6.33)$$

$$a_{pol} = 4n_{agg} \pi (r_{agg} + \delta_{pol})^2 \quad (6.34)$$

$$n_{agg} = \frac{3\gamma_{agg}}{4\pi(r_{agg} + \delta_{pol})^3} \quad (6.35)$$

Polymer film thickness:

$$\delta_{pol} = \sqrt[3]{r_{agg}^3 \left(1 + \frac{\gamma_{pol}}{\gamma_{PtC}}\right)} - r_{agg} \quad (6.36)$$

Correction factor due to liquid water film:

$$\xi_3 = \frac{\delta_w}{D_{O_2,w}} \frac{\xi_1}{a_w} k_c \frac{H_{O_2,w}}{H_{O_2,pol}} \quad (6.37)$$

$$\delta_w = \sqrt[3]{(r_{agg} + \delta_{pol})^3 \left(1 + \frac{\gamma_w}{\gamma_{agg}}\right)} - (r_{agg} + \delta_{pol}) \quad (6.38)$$

$$\gamma_w = s\gamma_{cl} \quad (6.39)$$

$$a_{pol} = 4n_{agg}\pi(r_{agg} + \delta_{pol} + \delta_w)^2 \quad (6.40)$$

Pt/C and polymer loading:

$$m_C = \frac{m_{Pt}}{PtC} - m_{Pt} \quad (6.41)$$

$$pol = \frac{m_{pol}}{m_{Pt} + m_C + m_{pol}} \quad (6.42)$$

Volume fraction of Pt/C:

$$\gamma_{PtC} = \left[ \frac{1}{\rho_{Pt}} + \frac{1 - PtC}{PtC\rho_C} \right] \frac{m_{Pt}}{L_{cl}} \quad (6.43)$$

Volume fraction of polymer:

$$\gamma_{Pol} = \frac{pol}{1 - pol} \frac{1}{\rho_{Pol}} \frac{m_{Pt}}{PtCL_{cl}} \quad (6.44)$$

$$\gamma_{agg} = \gamma_{Pol} + \gamma_{PtC} \quad (6.45)$$

Porosity:

$$\gamma_{cl} = 1 - \gamma_{agg} \quad (6.46)$$

Definition of volume fraction:

$$\begin{aligned} \gamma_w &= \frac{V_w}{V_T}; \quad \gamma_{PtC} = \frac{V_{PtC}}{V_T}; \quad \gamma_{Pol} = \frac{V_{Pol}}{V_T}; \quad \gamma_{agg} = \frac{V_{agg}}{V_T}; \quad \gamma_{cl} = \frac{V_{void}}{V_T} = \text{porosity} \\ V_{agg} &= V_{PtC} + V_{Pol}; \quad V_{void} = V_g + V_w \\ V_T &= V_{agg} + V_{void} = V_{PtC} + V_{Pol} + V_g + V_w \end{aligned} \quad (6.47)$$

## 2.4 Membrane model

The membrane model takes into account the flux water due to electroosmotic drag and diffusion. Here, a GORE membrane is employed for which we modify the standard phenomenological equations derived for a Nafion with a correction factor, as done by Ju et al. [1]

For the membrane the activity and water contents per sulfonic group are given by

$$a = \frac{P_{wv}}{P_{sat}} + 2s \quad (6.48)$$

$$\begin{aligned} \lambda &= 0.043 + 17.81a - 39.85a^2 + 36a^2 && \text{for } (a < 1) \\ \lambda &= 14 + 1.4(a - 1) && \text{for } (a > 1) \end{aligned} \quad (6.49)$$

The ionic conductivity is defined as:

$$\sigma_m^{eff} = \beta_m \sigma_m$$

where:

$$\sigma_m = (0.514\lambda - 0.326)e^{1268\left(\frac{1}{303} - \frac{1}{T}\right)} \quad (6.50)$$

The diffusivity of membrane water content per sulfonic group:

$$\begin{aligned} D_{w,mem}^{eff} &= \beta_m D_{w,mem} \\ D_{w,mem} &= \begin{cases} 3.1 \times 10^{-7} \lambda (e^{0.28\lambda} - 1) e^{[-2436/T]} & \text{for } 0 < \lambda \leq 3 \\ 4.17 \times 10^{-8} \lambda (1 + 161e^{-\lambda}) e^{[-2436/T]} & \text{otherwise} \end{cases} \end{aligned} \quad (6.51)$$

The electro-osmotic drag coefficient is defined as:

$$n_d = 2.5 \frac{\lambda}{22} \quad (6.52)$$

### 3. Numerical methodology

The mathematical model is implemented and solved in the commercial computational fluid dynamics software Fluent and its PEMFC module<sup>[13]</sup> together with in-house user-defined functions subroutines. The latter allows for changes in constitutive relations, parameters and to some extent also the governing equations.

The computational domains are created in the commercial GAMBIT pre-processor software. The whole domain is defined as a fluid zone, except for the current collector, which is defined as solid region. Mesh independence test is then carried out to ensure consistency of the solutions. To reduce the computational cost, we apply periodic boundary conditions representing the nature of unit repetition of PEMFC stack. Note that if we had chosen to solve for a whole stack without repeating units, the amount of computational elements would have numbered in the range of several millions (depending on the stack size).

### 4. Results and discussions

#### 4.1 Model Validation

Before we consider the thermal management of the stack, the PEMFC model is validated against experimental single cell data by Noponen et al.<sup>[14]</sup> the result of which are depicted in Figure 6.2. The model predictions are found to agree well with the experimental counterparts for the iR-corrected, overall polarization curve for currents up to 1.5 A cm<sup>-2</sup> and local current density distributions.

#### 4.2 Liquid water cooling

To ascertain the impact of placement of coolant plates, a stack model based on a validated single-cell model is implemented and solved for. The flow fields in the single cells and the cooling plates are of a net type, i.e. porous in nature,

which allows for a reduction of dimensionality from two to three dimensions. To limit the computational cost further, four repetitive units are identified that are relevant for the placement of cooling plates. These repetitive units are based on the amount of cells that are placed between the cooling plates: (i) one cell; (ii) two cells; (iii) three cells; (iv) four cells.

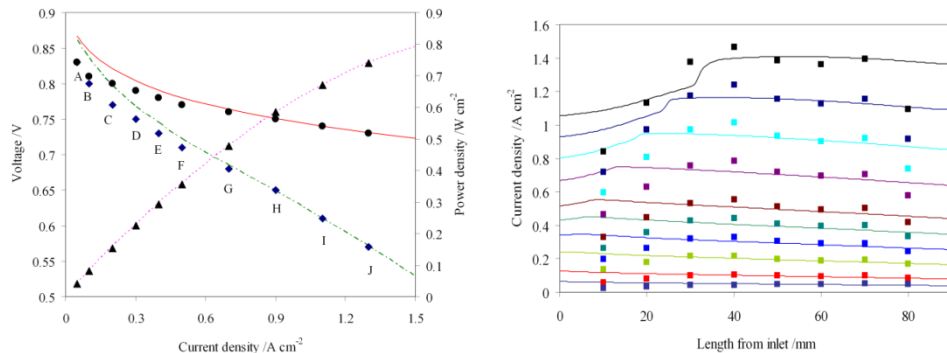


Figure 6.2: Validation: a) global polarization curves: [♦] is the experimentally measured potential; [●] is the iR-corrected experimentally measured potential; [▲] is the experimentally obtained power density; [- -] is the predicted potential of the model; [—] is the predicted iR-corrected potential of the model (both case a and b); [- -] is the predicted power density of the model; b) local current density distribution.

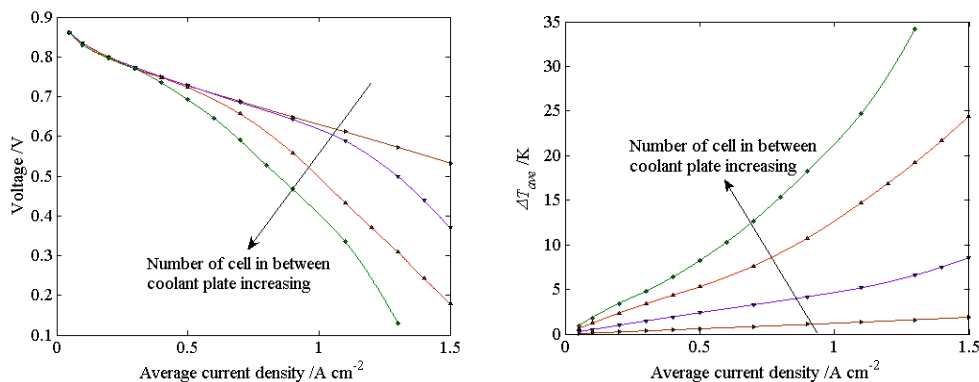


Figure 6.3: a) Normalized polarization curves where the stack voltage is divided by the amount of cells; b) Temperature difference for: case i (►); case ii (▼); case iii (▲); case iv (◆).

The performance of each stack unit, we find that case *i*, i.e. with only one cell between each coolant plate, exhibits the best performance, as shown in Figure 6.3a, with normalized polarization curves. Here, the stack voltage for each configuration has been divided by the amount of cells for comparison purposes. Furthermore, the polarization curve for case *i* follows the experimentally measured counterpart for a single cell cooled with two coolant plates closely. As the number of cells increases, the performance can be seen to drop due to an increase in temperature, see Figure 6.3b for details, and decrease in water content in the membrane.

### 4.3 Forced convection air cooling

In order to reduce the complexity of the cooling system for PEMFC stack, while keeping the stack at high performance, forced convection air powered by fans can be used to cool down the stack as well as to feed in air into the. Designing PEMFC stacks with open-cathode manifolds therefore requires careful consideration of the air flow rate at the cathode: a high flow rate provides a high stoichiometric oxidant supply but might cause dehydration of the membrane, where the former is beneficial and the latter detrimental to stack performance; too low a flow rate might give rise to flooding in the cathode flow fields and/or gas diffusion layers, again resulting in a drop in stack performance. In this study, a typical fan with

a size of 119 mm × 199 mm × 38 mm product of ebmpapst series 4100N<sup>[15]</sup>) is investigated at five different load conditions, i.e. 4.5 W, 12.2 W, 19.5 W, 30W and 60W.

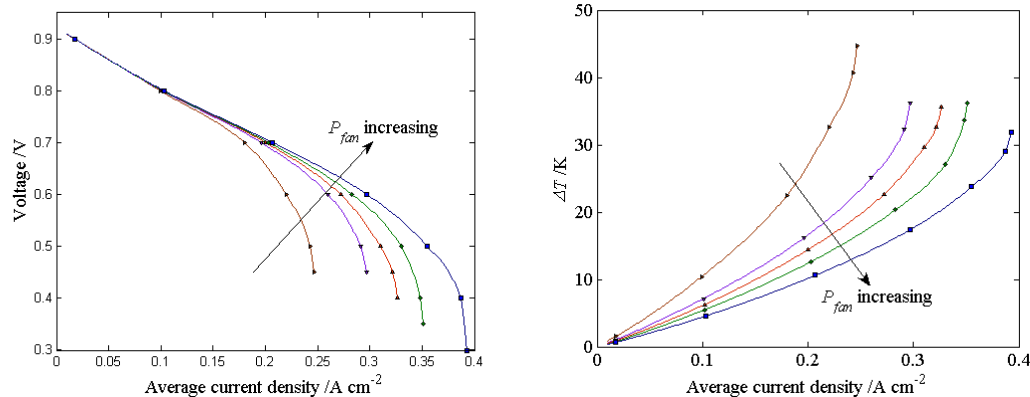


Figure 6.4: a) Polarization curves; b) Temperature difference for forced air convection in an open manifold for the for different fan powers: 4.5 (►), 12.2 (▼), 19.5 (▲), 30 (◆), and 60 W (■).

As can be inferred from Figure 6.4, several feature are apparent for the different fan power, notably that the case with higher fan power performs better in terms of limiting current density compared to cases with lower fan power. Furthermore, as can be seen from Figure 6.4b, it is clear that using lower fan power might not sufficient to remove amount of heat generated which will turn in stack heat up beyond its optimum operating temperature.

#### 4.4 Natural convection air cooling

To avoid the parasitic load and reduce the complexity of the PEMFC design, natural convection flow which arises due to the density gradients in the air as oxygen depleted along the cathode, and due to the temperature difference between fuel cell and surrounding is employed. Furthermore, the operation of a natural-convection cathode is a complex coupling between heat, mass and momentum transport at fuel cell and the surrounding. Thus, care has to be taken so as to provide enough air to the cathode and to ensure sufficient heat removal of the stack. On the natural convection air cooling, the rate of heat removal, which is due to the temperature differences between fuel cell and surrounding, usually only can be applied to small stack of view cells. Here, we simulate thermal management for a small stack comprises of five cells compare with a single cell.

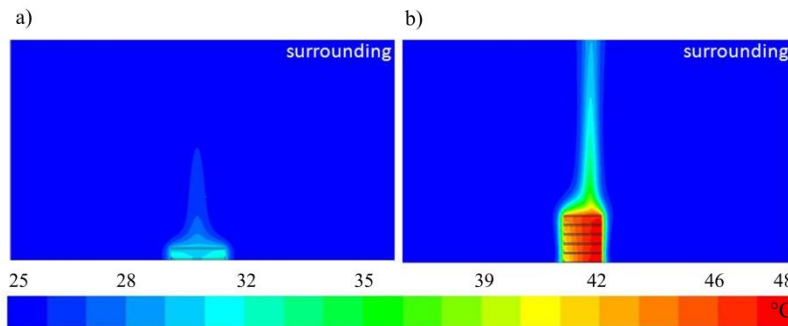


Figure 6.9: Temperature distribution for a) single cell ( $V_{cell} = 0.7V$ ,  $I_{ave} = 0.446A/cm^2$ ,  $\Delta T = 7^\circ C$ ); b) Stack (5 cells,  $V_{stack} = 3.5V$ ,  $V_{cell} = 0.7V$ ,  $I_{ave} = 0.271$ ,  $\Delta T = 20^\circ C$ )

As expected, temperature increase for stack is much higher than single cell. Temperature increase for single cell is about 7°C which is well agree with experimental data from Hottinen et al.,<sup>[15]</sup> while for stack temperature increase reach to 20°C. Despite the fact that thermal management aims to control the thermal envelope of the stack, in natural convection air cooling, we cannot control the air flows and heat transfer rate. Hence, insufficient cooling can cause membrane dehydration and in turn an increase in ohmic resistance in membrane which lower the stack performance. Here, the current generated in stack is 40% lower than one in single cell.

## 5. Concluding Remarks

A mathematical model for PEMFC has been developed, implemented, parameter adapted, and validated against experimental polarization curves. The validated single cell model is then employed as a building block for stack modelling. Three different cooling methods, namely water-cooling, forced convection air-cooling and natural convection air cooling, are implemented and solved for. Four different cooling channel placements and cooling conditions are investigated for the stack with water cooling. The results show that there is strong correlation between stack performance and the coolant channel placement. We note that the stack performance decreasing as more cell placed in between coolant channel. Furthermore, five different fan power are simulated for the forced convection air cooling. It is noted that higher fan power could sustain higher current density and able to remove more heat from the stack. In addition, thermal management for natural convection air cooling has also been carried out. It is clearly shown that care has to be taken so when applying natural convection to cool down the stack since more heat is generated in the stack. Finally, the present model can easily be extended to encompass various stack design and cooling strategy for efficient design and optimization of the PEMFC stack.

## Acknowledgments

This work was jointly supported by the National University of Singapore and AUN/SEED-Net JICA.

## References

1. H. Ju, C.Y. Wang, S. Cleghorn, U. Beuscher, "Nonisothermal Modelling of Polymer Electrolyte Fuel Cell, Experimental Validation, J. Electrochem. Soc., vol. 152 (8), pp A1645-A1653, 2005.
2. R.M. Rao, D. Bhattacharyya, R. Rengaswamy, S.R. Choudhury, A Two-dimensional Steady State Model Including Effect of Liquid Water for a PEM Fuel Cell Cathode, J. Power Sources., vol. 173, pp 375-393, 2007.
3. D. Harvey, J.G. Pharoah, K. Karan, A Comparison of Different Approaches to Modeling the PEMFC Catalyst Layer, J. Power Sources., vol. 179, pp 209-219, 2008.
4. E. Birgersson, M. Vynnycky, A Quantitative Comparison of the Effect of Flow Distributor Geometry in the Cathode of a PEM Fuel Cell, J. Power Sources., vol. 153, pp 76-88, 2006.
5. M. Secanel, K. Karan, A. Sulaeman, N. Djilali, Multi-variable Optimization of PEMFC Cathodes using an Agglomerate Model, Electrochim. Acta., vol. 52, pp 6318-6337, 2007.
6. W. Sun, B.A. Peppley, K. Karan, An Improved Two-dimensional Agglomerate Cathode Model to Study the Influence of Catalyst Layer Structural Parameters, Electrochim. Acta., vol. 50, pp 3359-3374, 2005.
7. F. Jaouen, G. Lindbergh, G. Sundholm, Investigation of Mass-Transport Limitation in the Solid Polymer Fuel Cell Cathode, J. Electrochem. Soc., Vol. 149 (4), pp A437-A447, 2002.
8. P. Gode, F. Jaouen, G. Lindbergh, A. Lundblad, G. Sundholm, Influence of the Composition on the Structure and Electrochemical Characteristics of PEFC Cathode, Electrochim. Acta., Vol. 48, pp 4175-4187, 2003.
9. C. Marr, X. Li, Composition and Performance Modeling of Catalyst Layer in Proton Exchange Membrane Fuel Cell, J. Power Sources., vol. 77, pp 17-27, 1999.
10. D. Son, Q. Wang, Z. Liu, M. Eikerling, Z. Xie, T. Navessin, S. Holdcroft, A Method for Optimizing Distributions of Nafion and Pt in Cathode Catalyst Layer of PEM Fuel Cells, Electrochim. Acta., vol. 50, pp 3347-3358, 2005.
11. W.W. Yang, T.S. Zhao, A Two Dimensional, Two-Phase Mass Transport Model for Liquid Feed DMFCs, Electrochim. Acta., vol. 52, pp 6125-6140, 2007.
12. P. J. Ferreira, G.J. La O', Y. Shao-Horn, D. Morgan, R. Makharia, S. Kocha, H.A. Gasteiger, "Instability of Pt/C Electrocatalysts in Proton Exchange Membrane Fuel Cells", J. Electrochem. Soc., vol 152 (11), pp A2256-2271, 2005.
13. FLUENT, <http://www.fluent.com>
14. M. Noponen, E. Birgersson, J. Ihonen, M. Vynnycky, A. Lundblad, G. Lindbergh, "A Two-phase Non-isothermal PEFC, Model: theory and validation", Fuel Cells 4 No 4, pp 365-377, 2004.

15. T. Hottinen, M. Noponen, T. Mennola, O. Himanen, M. Mikola, P. Lund, "Effect of ambient conditions on performance and current distribution of a polymer electrolyte membrane fuel cell", *J. Appl. Electrochem.* 33: 265-271 2003.
16. B. R. Padhy, R. G. Reddy, "Performance of DMFC with SS316 Bipolar/end Plates", *J. Power Sources.*, vol.153, pp 125-129, 2006.
17. P.J.S. Vie, S. Kjelstrup, "Thermal Conductivities from Temperature Profiles in PEFC", *Electrochim. Acta.*, vol. 49, pp 1069-1077, 2004.
18. R.F. Mann, J.C. Amphlett, B.A. Peppley, C.P. Thurgood, "Henry's Law and the Solubilities of Reactant Gases in the Modelling of PEM Fuel Cells", *J. Power sources.*, vol. 161, pp 768-774, 2006.
19. S. Li and U. Becker, "A Three Dimensional Model for PEMFC", *Fuel Cell. Sci. Eng. Tech.*, pp 157-164, 2004.

## Appendix

**Table 6.1:** Geometry and main physical parameters

$h_{cc, co, s}$	$5 \times 10^{-4}, 2.5 \times 10^{-4}, 5 \times 10^{-4} \text{ m}^{[14]}$
$h_{n, gdl, cl}$	$5 \times 10^{-4}, 3 \times 10^{-4}, 1 \times 10^{-5} \text{ m}^{[14]}$
$h_m$	$5 \times 10^{-5} \text{ m}^{[14]}$
$L$	$9 \times 10^{-2} \text{ m}^{[14]}$
$\kappa_{n, gdl, cl}$	$10^{-9}, 7.3 \times 10^{-13} \text{ m}^2 \text{ [14]}$
$\gamma_{n, gdl, cl}$	$0.9, 0.4, 0.4^{[14]}$
$\sigma_{n, gdl, cl}$	$10^5, 500, 500 \text{ S.m}^{-1}^{[14]}$
$\sigma_{cc}$	$1.37 \times 10^6 \text{ S.m}^{-1}^{[16]}$
$k_{gdl, cl}$	$1.5, 1.5 \text{ W m}^{-1} \text{ K}^{-1}^{[1]}$
$k_{cc, n}$	$16.3, 16.3 \text{ W m}^{-1} \text{ K}^{-1}^{[16]}$
$k_m$	$0.2 \text{ W m}^{-1} \text{ K}^{-1}^{[17]}$
$D_{H_2}$	$1.1028 \times 10^{-4} \text{ m}^2 \text{s}^{-1}^{[1]}$
$D_{O_2}$	$3.2348 \times 10^{-5} \text{ m}^2 \text{s}^{-1}^{[1]}$
$D_{H_2O}$	$7.35 \times 10^{-5} \text{ m}^2 \text{s}^{-1}^{[1]}$
$D_{liq}$	$3.032 \times 10^{-9} \text{ m}^2 \text{s}^{-1}^{[2]}$
$T_{in}$	$60 \text{ }^\circ\text{C}^{[14]}$
$A J_a^{ref,0}$	$1 \times 10^9 \text{ A m}^{-3}^{[1]}$
$J_c^{ref,0}$	$3 \text{ A m}^{-3} \text{ [adapted]}$
$T_j^{ref}$	$353.15 \text{ K}^{[1]}$
$E_a$	$73269 \text{ J mol}^{-1}^{[1]}$
$\alpha_a$	$1^{[1]}$
$\alpha_c$	$1.5 \text{ [adapted]}$
$\gamma_a, \gamma_c$	$0.5, 1^{[1]}$
$[C]_{ref}$	$\frac{1}{H}^{[2]}$
$H_{O_2}$	$H_{O_2} = 1.33 \exp(-666/T)^{[2]}$
$H_{H_2O(liquid)}$	$H_{H_2O} = 5.08 \exp(-498/T)^{[2]}$
$H_{H_2}$	$H_{H_2} = 2.55 \exp(170/T)^{[18]}$

$h_{fg}$	$2.26 \times 10^6 \text{ J kg}^{-1}$
$\theta_c$	$0^\circ$ [19]
$C_{r, max}$	$100 \text{ s}^{-1}$ [19]
$P_{op}$	$101325 \text{ Pa}$ [19]
$RH_{a, c}$	100%, 100% [19]
$\xi_{a, c}$	3.35, 2.3 [19]
$\beta_m$	0.7 [adapted]
$T^{cool}, T^{amb}$	60, 25 °C
$U^{cool}$	$1 \text{ ms}^{-1}$
$\rho_l$	$982.2 \text{ kg/m}^3$ [19]
$r_{Pt}$	$2.2 \times 10^{-9} \text{ m}$ [1]
$r_{agg}$	$1 \times 10^{-7} \text{ m}$ [2]
$Pt\_C$	0.4
$m_{Pt}$	$0.3 \times 10^{-4} \text{ kg m}^{-2}$ [14]
$m_{pol}$	$1 \times 10^{-4} \text{ kg m}^{-2}$
$\rho_{Pt}$	$21.45 \times 10^3 \text{ kg m}^{-3}$ [2]
$\rho_C$	$1.8 \times 10^3 \text{ kg m}^{-3}$ [2]
$\rho_{pol}$	$2 \times 10^3 \text{ kg m}^{-3}$ [2]
$Cp_{H2, O2, H2O(g), N2}$	$14283, 919.31, 2014, 1040.67 \text{ J kg}^{-1} \text{ K}^{-1}$
$\mu_{H2, O2, H2O(g), N2}$	$8.411 \times 10^{-6}, 1.919 \times 10^{-5}, 1.34 \times 10^{-5}, 1.663 \times 10^{-5} \text{ kg m}^{-1} \text{ s}^{-1}$
$k_{H2, O2, H2O(g), N2}$	$0.206, 0.0307, 0.0246, 0.0295 \text{ W m}^{-1} \text{ K}^{-1}$
$K_{H2O(liquid)}$	$0.67 \text{ W m}^{-1} \text{ K}^{-1}$
$M_{H2, O2, H2O(g), N2}$	$0.002, 0.032, 0.018, 0.028 \text{ kg mol}^{-1}$

## ► [ MODELLING OF A LI-ION BATTERY] [Chapter 7]

**Karthik Somasundaram<sup>1</sup>, Erik Birgersson<sup>2</sup>, Arun Sadashiv Mujumdar<sup>1</sup>**

[<sup>1</sup> Department of Mechanical Engineering, NUS, Singapore

[<sup>2</sup> Department of Chemical and Biomolecular Engineering, NUS, Singapore]

Rechargeable lithium batteries have been considered the battery of choice for many mobile and portable applications. Lithium-ion or rocking-chair batteries are the newest and have the most well-understood battery chemistry. Both the positive and negative electrodes serve as hosts for lithium ions that transport through a binary electrolyte. One aspect of battery modeling describes these transport phenomena through a electrochemical model. The other aspect deals with the thermal management of large battery systems since temperature greatly affect performance, safety, and life of large lithium ion batteries in hybrid vehicles. Thermal runaway occurs when the reaction rate increases due to an increase in temperature, causing a further increase in temperature and hence a further increase in the reaction rate. Thermal modeling is an effective way to understand how the design and operating variables affect the thermal behaviour of the lithium-ion battery during charging and discharging. Hence the objective of this study is to develop general mathematical model that describes the electrochemical and thermal behaviour during the discharge and charge of a lithium-ion battery and use the results for better battery design and thermal management system. A one dimensional isothermal electrochemical model is presented in this chapter.

## Modelling of a Li-ion battery

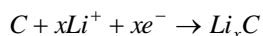
### 1. Introduction

Since the invention of the first Voltaic pile in 1800 by Alessandro Volta, the battery has become a common power source for many household and industrial applications. Today, rechargeable lithium batteries are generally considered the battery of choice for many mobile and portable applications. Lithium-ion or rocking-chair batteries are the newest and have the most well-understood battery chemistry. Rechargeable lithium batteries offer several advantages compared to conventional batteries like higher energy density (up to 150Wh/kg), higher cell voltage (up to about 4V/cell) and longer shelf life (up to 5-10 years). Especially Lithium-ion batteries have gained prominence in recent years because of their superior energy and power densities.

Lithium ion batteries are a type of rechargeable batteries in which a lithium ion moves in between the two electrodes. It moves from negative electrode to positive electrode during discharge and the reverse takes place during charging as displayed in Figure 7.1. The Li-ion cell uses a lithiated carbon intercalation material for the negative electrode and a lithiated metal insertion compound for the positive electrode. The cell reactions during charging are as shown below, and the reverse reaction happens during discharging. In the positive electrode



In the negative electrode,



Overall reaction is

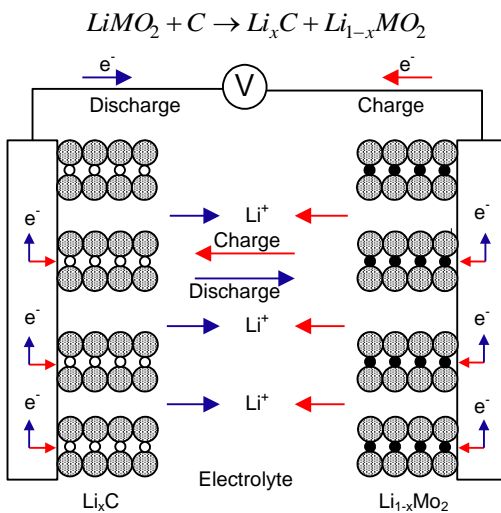


Figure 7.1. Schematic of a Li-ion cell operation

Battery designs for an application needs large amount of time and experimental effort for optimization. Hence computer simulations become very useful in this process due to savings in time and materials. In order to do a simulation, a mathematical model is needed which describes the system. The various physical phenomena involved in a battery can be grouped under three categories namely thermodynamics (Gibbs free energy, electrochemical potential etc.,), transport (migration, diffusion, convection) and kinetics (Butler-Volmer equation etc.). The modelling of a battery can be done in multiscales ranging from pore level model ( $\sim 10^{-6}$  m), or a cell level model ( $10^{-4}$  m) to stack level and system level models ( $\sim$ few cm). The pore level model covers microscopic details when compared with the macro homogenous models that provide insights to the behavior of the cell on a macroscopic scale. In the macroscopic scale, the detailed geometry of the pore is ignored. The porosity and the surface area are averaged over a control volume in the porous electrode using a volume averaging approach. In a Li-ion cell, solid phase diffusion of lithium in the active material can be rate limiting under

certain conditions and hence it requires a model to describe this phenomenon and an additional length scale is introduced in the problem. Hence in addition to solving for transport in the  $x$ -direction, diffusion equation needs to be solved in spherical coordinates at every volume element. Hence multiscale modelling becomes essential for modelling a battery.

## 2. Mathematical formulation

This multiscale model is used to study the charge and discharge characteristics of a Li-ion battery and it includes the processes of electronic current conduction, ionic charge transport in the electrodes, electrolyte, and separator, material transport in the electrolyte and diffusion in the electrode particles.

Figure 7.2 shows a Lithium insertion cell which consists of two composite electrodes, a separator and filled with electrolyte. The porous electrodes consist of a pseudo homogenous mixture of the active insertion material, polymer matrix, non aqueous liquid electrolyte and conductive filler additive.

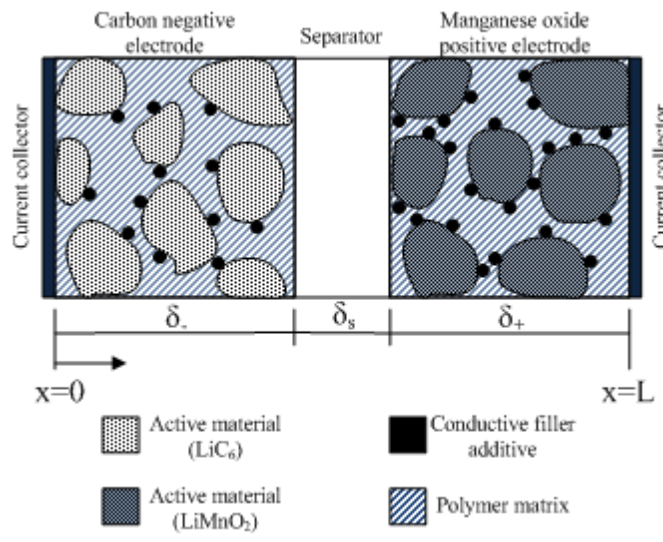


Figure 7.2. Li-ion cell sandwich

### 2.1. Governing equations

The mathematical model comprises of the governing equations for conservation of species and charge in two phases viz the solution phase and the solid phase. The equation for conservation of charge in the solid phase of the two porous electrodes is

$$\begin{aligned} \nabla \cdot (\mathbf{i}^{(s)}) &= -S_a j, \\ \mathbf{i}^{(s)} &= -\sigma^{eff} \nabla \phi_s, \end{aligned} \quad (7.1)$$

and the for the conservation of charge in the solution phase,

$$\begin{aligned} \nabla \cdot (\mathbf{i}^{(l)}) &= S_a j, \\ \mathbf{i}^{(l)} &= -\kappa^{eff} \nabla \phi_l + \frac{2RT\kappa^{eff}}{F} \left[ 1 + \frac{\partial \ln f}{\partial \ln c_l} \right] [1 - t_+] \nabla (\ln c^{(l)}), \end{aligned} \quad (7.2)$$

and for the conservation of species in the solution phase,

$$\varepsilon \frac{\partial c^{(l)}}{\partial t} + \nabla \cdot \left( D^{(l)eff} \nabla c^{(l)} \right) = \frac{S_a j (1 - t_+)}{F} \quad (7.3)$$

The diffusion of Li-ion into the electrode particles is governed by Fick's law as expressed below

$$\frac{\partial c^{(s)}}{\partial t} + \frac{1}{r^2} \frac{\partial}{\partial r} \left( -r^2 D^{(s)} \frac{\partial c^{(s)}}{\partial r} \right) = 0. \quad (7.4)$$

## 2.2 Boundary conditions

**Cathode ( $x=0$ )** - The solid phase potential is set to zero on the cathode/current collector boundary

$$\phi^{(s)} = 0. \quad (7.5)$$

**Anode ( $x=L$ )** - The electronic current density is specified at the anode/current collector boundary

$$\mathbf{i}^{(s)} = \mathbf{i}(t). \quad (7.6)$$

For the ionic charge balance and the material balance in the electrolyte, insulating conditions apply at the anode/current collector as well as cathode/current collector boundaries

$$\begin{aligned} \mathbf{i}^{(l)} \cdot \mathbf{e}_x &= 0, \\ \nabla c^{(l)} \cdot \mathbf{e}_x &= 0, \end{aligned} \quad (7.7)$$

where  $\mathbf{e}_x$  is the unit vector along  $x$ .

For the diffusion of Li ion in the electrode particles, the material flux is specified at the particle surface. The flux is determined by the local electrochemical reaction rate in the 1D model

$$\begin{aligned} -D^{(s)} \frac{\partial c^{(s)}}{\partial r} &= \frac{-j}{F}, \text{ at } r = R_s, \\ \frac{\partial c^{(s)}}{\partial r} &= 0 \text{ at } r = 0. \end{aligned} \quad (7.8)$$

For this diffusion process, the superficial area per unit volume is related to the particle radius by the following expression

$$S_a = \frac{3(1 - \varepsilon^{(l)} - \varepsilon^{(f)} - \varepsilon^{(p)})}{R_s}. \quad (7.9)$$

## 2.3 Constitutive relations

**Butler-Volmer equation-** The local charge transfer current density is given by the Butler-Volmer equation for electrode kinetics. The expression is as follows

$$j = i_0 \left\{ \exp\left(\frac{\alpha_a \eta F}{RT}\right) - \exp\left(-\frac{\alpha_c \eta F}{RT}\right) \right\}. \quad (7.10)$$

The overpotential  $\eta$  is given by

$$\eta = \phi^{(s)} - \phi^{(l)} - U_{ref}, \quad (7.11)$$

where  $U_{ref}$  is the open circuit potential of the electrode with respect to the solid lithium electrode and the exchange current density  $i_0$  is given by

$$i_0 = k_0 \sqrt{c^{(l)}(c_{max}^{(s)} - c^{(s)})c^{(s)}}, \quad (7.12)$$

The effective conductivities and diffusivity takes porosity into consideration as given by the following expressions

$$\begin{aligned} \sigma^{eff} &= \sigma \varepsilon^\gamma \\ \kappa^{eff} &= \kappa \varepsilon^\gamma \\ D_l^{eff} &= D_l \varepsilon^\gamma \end{aligned} \quad (7.13)$$

### 3. Input parameters

TABLE 7.1:  
Parameters for the electrodes

Parameter	$\text{Li}_x \text{C}_6$	$\text{Li}_y \text{Mn}_2 \text{O}_4$
$D^{(s)}$ ( $\text{m}^2/\text{s}$ )	$3.9 \times 10^{-14}$	$1.0 \times 10^{-13}$
$\sigma$ (S/m)	100	3.8
$c_{\max}^{(s)}$ ( $\text{mol}/\text{m}^3$ )	26390	22860

TABLE 7.2:  
Design adjustable other parameters & operating conditions

Parameter	$\text{Li}_x \text{C}_6$	Separator	$\text{Li}_y \text{Mn}_2 \text{O}_4$
Thickness $\delta, \delta_s, \delta_+$ (m)	$100 \times 10^{-6}$	$52 \times 10^{-6}$	$174 \times 10^{-6}$
$R_s$ (m)	$12.5 \times 10^{-6}$	-	$8.5 \times 10^{-6}$
$c^{(s)0}$ ( $\text{mol}/\text{m}^3$ )	14870	-	3900
$c^{(l)0}$ ( $\text{mol}/\text{m}^3$ )		2000	
$\varepsilon^{(p)}$	0.146	-	0.186
$\varepsilon^{(l)}$	0.357	-	0.444
$\varepsilon^{(f)}$	0.026	-	0.073
$T$ (K)		298	

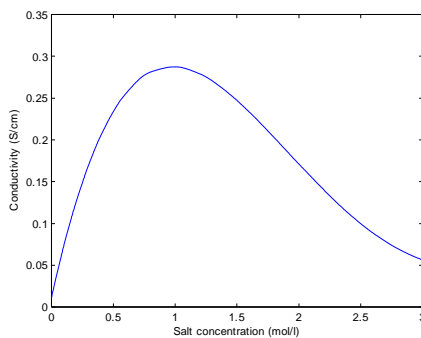


Figure 7.3. Ionic conductivity of electrolyte

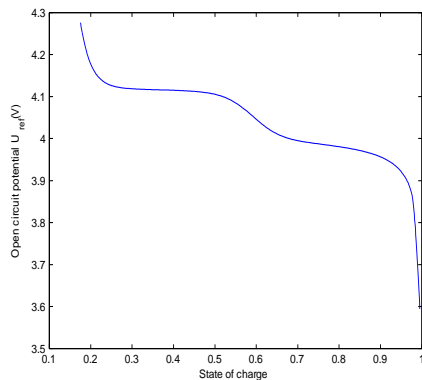


Figure 7.4. OCV of Lithium Manganese Oxide electrode

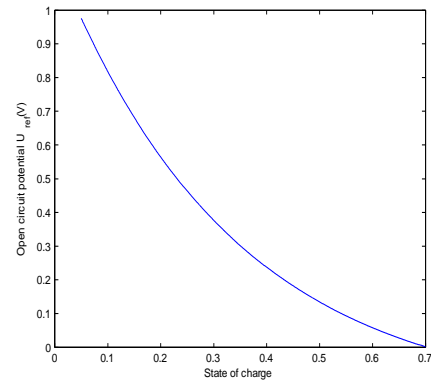


Figure 7.5. OCV of  $\text{Li}_x \text{C}_6$  electrode

The electrolyte is based on 1:2 EC:DMC as the solvent mixture and LiPF<sub>6</sub> as the salt. The electrolyte conductivity is measured experimentally and the dependency on the composition is as shown in figure 7.3. The model specifies the electrolyte conductivity according to this function.

$$\kappa = 1.0793 \times 10^{-4} + 6.7461 \times 10^{-3} c^{(l)} - 5.2245 \times 10^{-3} c^{(l)^2} + 1.3605 \times 10^{-3} c^{(l)^3} - 1.1724 \times 10^{-4} c^{(l)^4} \quad (7.14)$$

The electrode materials are graphite ( $\text{Li}_x \text{C}_6$ ) for the negative electrode and lithium manganese oxide spinel ( $\text{Li}_y \text{Mn}_2 \text{O}_4$ ) for the positive electrode. The open circuit potential of the negative and positive electrodes are dependent on composition and measured experimentally. The variations are as shown in figure 7.4 and 7.5 which gives the open circuit potential of  $\text{Li}_x \text{C}_6$  and  $\text{Li}_y \text{Mn}_2 \text{O}_4$  relative to solid lithium respectively.

The open circuit potential for the two electrodes are fit to the functions given below. For the manganese dioxide [1]

$$U_{ref} = 4.19829 + 0.0565661 \tanh[-14.5546\lambda + 8.60942] - 0.157123 \exp(-0.04735\lambda^8) \\ - 0.0275479 \left[ \frac{1}{(0.998432 - \lambda)^{0.492465}} - 1.90111 \right] + 0.810239 \exp[-40(\lambda - 0.133875)] \quad (7.15)$$

electrode, where  $\lambda$  is the amount of lithium inserted in  $\text{Li}_y \text{Mn}_2 \text{O}_4$ . For the lithiated carbon electrode [1]

$$U_{ref} = -0.16 + 1.32 \exp(-3.0\zeta) + 10.0 \exp(-2000.0\zeta) \quad (7.16)$$

where  $\zeta$  is the amount of lithium in the carbon electrode  $\text{Li}_x \text{C}_6$ .

#### 4. Results and discussion

Figure 7.6 gives the variation of cell potential with respect to the cell capacity at 25 °C. The discharge time for 17.5 A/m<sup>2</sup> is 1 hour (1C rate). The discharge curves are given at 1.75 A/m<sup>2</sup> (0.1C rate), 17.5 A/m<sup>2</sup> (1C rate) and 35 A/m<sup>2</sup> (2C rate). The cell attains a maximum capacity at 0.1C rate as shown by the figure.

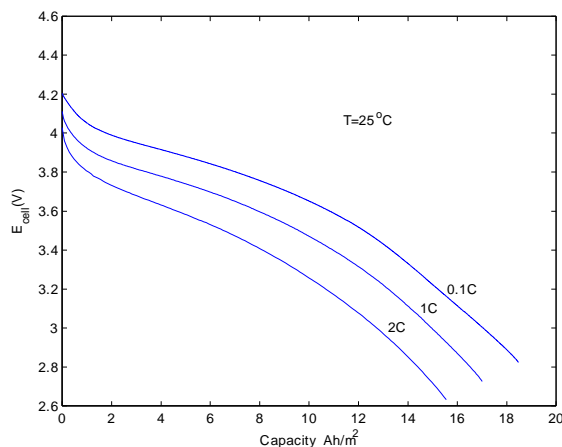


Figure 7.6. Cell capacity vs cell voltage

Figure 7.7 gives the salt concentration profile across the full cell during a constant current discharge at a rate of 1C. The separator region is shown within the dotted lines and the time is given from the start of discharge. The separator has a nearly constant concentration gradient unlike the two electrodes.

Figure 7.8 shows the concentration profiles of lithium inside a solid carbon particle at the negative electrode ( $\text{LiC}_6$ )-electrolyte interface at a time near the end of discharge. At higher discharge rates, most of the Li ions are not accessible at the end of discharge which is shown by the higher concentration for 35 A/m<sup>2</sup> when compared with 17.5 A/m<sup>2</sup> and 8.75 A/m<sup>2</sup>.

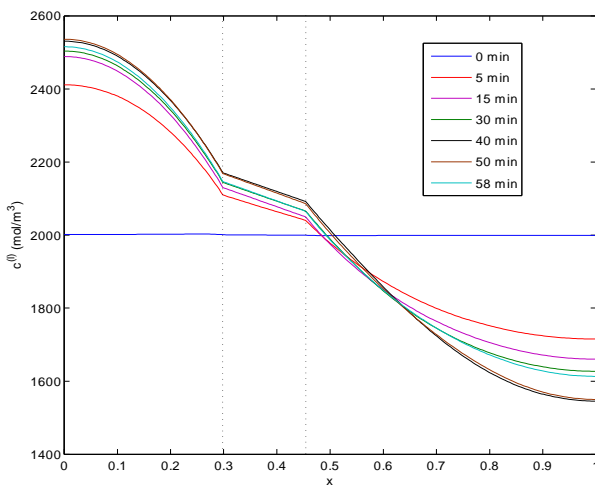


Figure 7.7. Salt concentration profile at a discharge rate of 1C from the start of discharge

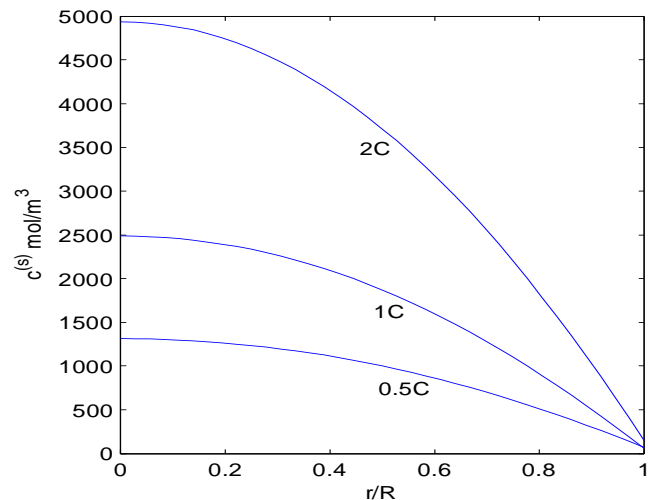


Figure 7.8. Concentration of Lithium inside a solid carbon particle near the electrode electrolyte interface near the end of discharge.

Also the solid phase concentration varies along with the distance across the electrode which is indicated in Figure 7.11. Figure 7.9 shows the charge discharge profile applied. The cycle applies 3500 s of discharge at current density of  $17.5 \text{ A/m}^2$  (1C), 200 s at open circuit, then 3500s of charge at the same current density, and finally open circuit conditions.

Figure 7.10 depicts the voltage of the cell ( $E_{cell} = \phi^{(s)}$  at  $x = L - \phi^{(s)}$  at  $x = 0$ ) predicted by the model. The voltage drops during discharge due to the ohmic loss and concentration overpotential. During the open circuit conditions, the ohmic losses can be seen clearly as shown by a sudden increase in voltage for around 150mV and then a gradual increase in voltage during charging.

Figure 7.11 and 7.12 shows the concentration distribution of solid lithium in the negative and positive electrodes respectively before the end of discharge ( $t = 3400 \text{ s}$ )

The concentration of lithium in the negative electrode near the end of discharge shows that there is less variation along the electrode but whereas the concentration varies from  $600 \text{ mol/m}^3$  to  $3450 \text{ mol/m}^3$  from the centre to the surface of the active electrode particle and in the case of positive electrode, the variation is just the opposite case of the negative electrode where the variation along the width of the electrode is greater than along the radius.

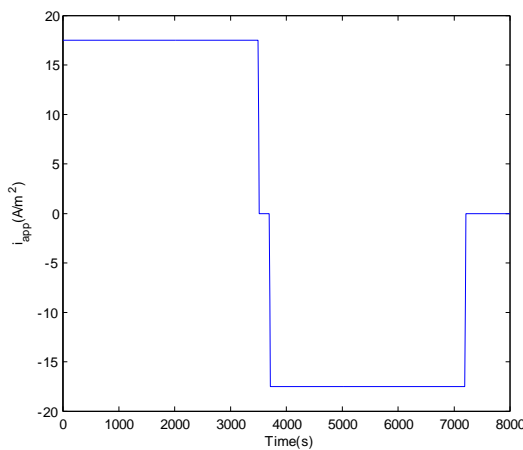


Figure 7.9. Applied charge – discharge profile

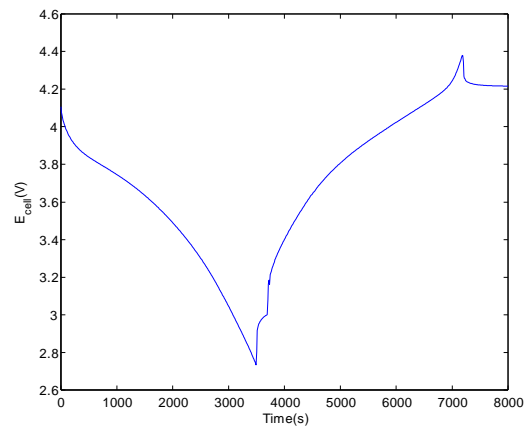


Figure 7.10. Predicted cell voltage vs time

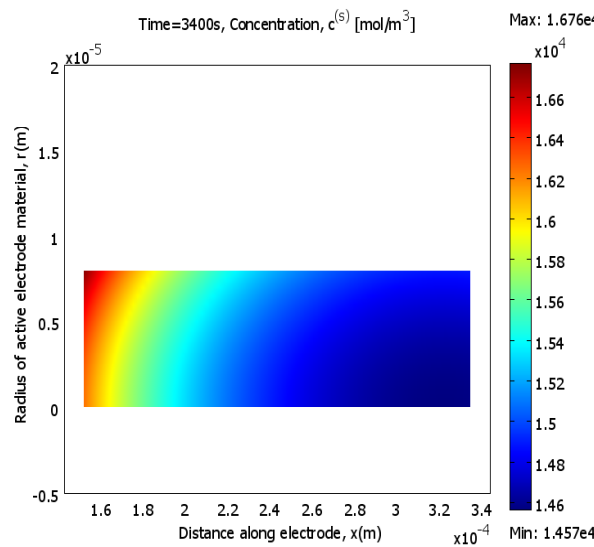


Figure 7.11. Concentration distribution of Li in the negative electrode particles near the end of discharge

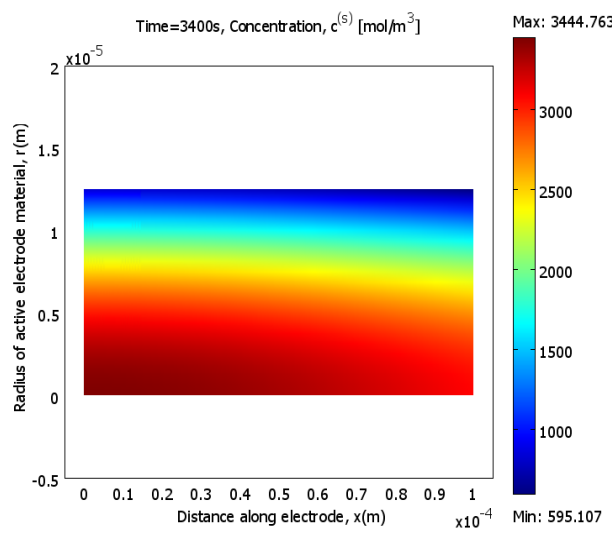


Figure 7.12. Concentration distribution of Li in the positive electrode particles near the end of discharge

## 5. Notation

$c^{(l)}$	salt concentration, mol/m <sup>3</sup>
$c^{(l)0}$	initial salt concentration, mol/m <sup>3</sup>
$c_{\max}^{(s)}$	maximum concentration of lithium in intercalation material, mol/m <sup>3</sup>
$c^{(s)0}$	initial concentration of lithium in intercalation material, mol/m <sup>3</sup>
$c^{(s)}$	concentration of lithium in solid, mol/m <sup>3</sup>
$\delta_-, \delta_+$	respective widths of negative and positive electrode, m
$\delta_s$	width of separator, m
$D^{(l)}$	salt diffusion co-efficient, m <sup>2</sup> /s
$D^{(s)}$	diffusion co-efficient of lithium in solid electrode particles, m <sup>2</sup> /s
$f$	mean molar activity co-efficient of salt
$F$	Faraday's constant, 96487 C/mol
$\mathbf{i}^{(l)}$	liquid/solution phase current density, A/m <sup>2</sup>
$\mathbf{i}^{(s)}$	solid phase current density, A/m <sup>2</sup>
$j$	local charge transfer current density, A/m <sup>2</sup>
$k_0$	reaction rate constant = $2 \times 10^{-6}$
$L$	width of the cell, m
$R$	gas constant, 8.314 J/molK
$R_s$	radius of electrode particle, m
$S_a$	specific interfacial area, m <sup>2</sup> /m <sup>3</sup>
$T$	temperature, K

$t$	time, s
$t_+$	transference number of cation = 0.363
$U_{ref}$	open circuit potential, V
$\gamma$	Bruggemann constant = 1.5
$\alpha_a$	anodic transfer coefficient = 0.5
$\alpha_c$	cathodic transfer coefficient = 0.5
$\varepsilon^{(l)}$	volume fraction of liquid phase of electrolyte
$\varepsilon^{(f)}$	volume fraction of conductive filler additive
$\varepsilon^{(p)}$	volume fraction of polymer phase
$\kappa$	ionic conductivity of electrolyte, S/m
$\sigma$	electronic conductivity of solid matrix, S/m
$\phi^{(l)}$	liquid phase potential, V
$\phi^{(s)}$	solid phase potential, V

## 6. References

1. Marc Doyle and John Newman, Comparison of Modeling Predictions with Experimental Data from Plastic Lithium Ion cells, *Journal of The Electrochemical Society*, **1996**, Vol.143,No.6, 1890-1903.
2. John Newman and Karen E.Thomas Alyea, *Electrochemical Systems Third Edition*, Wiley Inter Science, **2004**.
3. David Linden, *Handbook of Batteries Second edition*, Mc-Graw Hill, Inc, **1994**.
4. COMSOL model library documentation on Li battery.

## ►[ MODELING PEMFC AND NEW DESIGNS VIA THE CFD APPROACH]

### [Chapter 8]

**'Hee Joo POH and <sup>2</sup>Arun S. Mujumdar**

► [<sup>1</sup>Institute of High Performance Computing, A-STAR. <sup>2</sup>Mechanical Department, NUS]

Mathematical modeling plays an important role to understand the fluid mechanics, thermal, mass, ionic and electronic transport phenomena inside the Proton Exchange Membrane Fuel Cell (PEMFC), as this data is hardly accessible and measureable by the standard experimental apparatus. In this Computational Fuel Cell Dynamics (CFCD) analysis, the model is first validated with close agreement with the relevant experimental data for both cathode forced and free convection PEMFC. For forced convection fuel cell, a flow structure which delivers the reactant transversely to the MEA using an impinging jet configuration at cathode side is proposed and modeled to examine its effectiveness for enhanced PEMFC performance, especially at high current densities. For free convection air breathing PEM fuel cell (ABFC), the effect of geometry factors (e.g. channel length and width), device orientation (horizontal placement, alignment with gravity or at an inclined angle), and O<sub>2</sub> transfer configuration (channel vs. planar) were investigated. Based on the simulation results, an optimum design for the enhanced performance for self air breathing PEM Fuel Cells is derived.

## Modeling PEMFC and new designs via the CFD approach

### 1. Introduction

Increasing costs associated with fossil fuels, along with an increasing concern of the environmental impact of pollutants and greenhouse gases, results in a need to search for and develop new energy sources. Fuel cells have in recent years emerged as one of the more promising solutions. It is an electrochemical device in which the energy of the chemical reaction is converted directly into electricity. For instance, in the polymer electrolyte membrane fuel cell (PEMFC), when hydrogen fuel is combined with oxygen from air, electricity is formed without combustion of any form. Water and heat are the only byproducts when hydrogen is used as the fuel source.

Fuel cells are in fact a nineteenth-century invention. Its principle was discovered by the German scientist Christian Friedrich Schonbein in 1838. Based on his work, the first fuel cell was developed by the Welsh scientist Sir William Grove in 1843. This cell used similar materials to the modern phosphoric acid fuel cell. Since then, there has been no major developmental work on the fuel cell due to its high manufacturing and material costs. However, due to the recent rising costs of fossil fuels and the increasing concern with the environmental impact of pollutants and greenhouse gases, fuel cells have emerged as a more promising and viable solution. There are several different types of classification for fuel cells, each based on different criteria: type of fuel used, operating temperature, type of electrolytes etc. Table I shows the distinct characteristics for the six types of fuel cells commonly available in the market today.

Table I: Distinct characteristics for the six different types of fuel cell

Fuel Cell type	Electrolyte	Mobile Ions	Anode Gas	Cathode Gas	Temperature	Efficiency
Polymer Electrolyte Membrane (PEM)	Solid polymer membrane	H <sup>+</sup>	Hydrogen	Pure or atmospheric oxygen	75°C	35-60%
Alkaline (AFC)	Potassium hydroxide	OH <sup>-</sup>	Hydrogen	Pure oxygen	Below 80°C	50-70%
Direct Methanol (DMFC)	Solid polymer membrane	H <sup>+</sup>	Methanol solution in water	Atmospheric oxygen	75°C	35-40%
Phosphoric Acid (PAFC)	Phosphorous	H <sup>+</sup>	Hydrogen	Atmospheric oxygen	210°C	35-40%
Molten Carbonate (MCFC)	Alkali-Carbonates	CO <sub>3</sub> <sup>2-</sup>	Hydrogen, methane	Atmospheric oxygen	650°C	40-55%
Solid Oxide (SOFC)	Ceramic Oxide	O <sup>2-</sup>	Hydrogen, methane	Atmospheric oxygen	800-1000°C	45-60%

Generally, fuel cell applications have the unique advantage of being quiet (no moving parts) and clean (reduced air pollution and green house emissions such as NO<sub>x</sub> and SO<sub>x</sub>). They also enable improved efficiency for transportation, allow independent scaling between power (determined by fuel cell size) and capacity (determined by fuel storage size), and have a low temperature start-up (e.g. 60°C for PEMFC). However, certain disadvantage of fuel cells lies in making it commercially available for consumer usage. These include high cost of fuel cell, low volumetric power density compared to I.C. engines and batteries, and the various issues regarding safety, availability, storage and distribution of pure hydrogen fuel.

One of these fuel cells is the Proton Exchange Membrane Fuel Cell (PEMFC), which is a low temperature fuel cell. It is highly versatile as it can be used for portable devices, vehicles, as well as stationary power plants. Figure 1.2 shows a 2D schematic diagram to illustrate various components and operating principles of a single PEMFC.

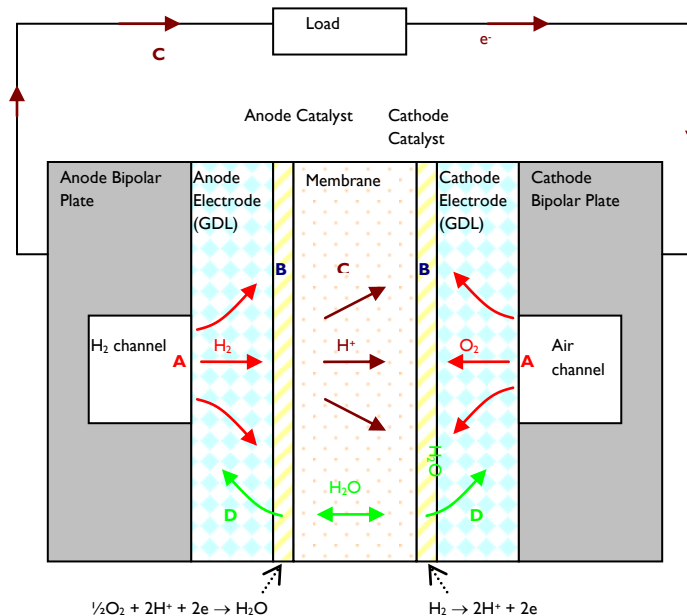


Figure I: 2D schematic diagram of a single fuel cell

As shown in Figure I, a single PEMFC cell consists of the following components:

#### 1. Polymer Electrolyte Membrane

The membrane in PEMFC is where the protons travel through from anode to cathode in order to combine with oxygen (and electrons) and form water. It is made of perfluoro-sulfonic acid proton conducting polymer (e.g. Nafion from Dupont). The performance is characterized by high ionic conductivity (and low electronic conductivity) and the adequate strength needed to prevent the reactants from crossing over. The membrane-electrolyte is hydrophilic. The presence of water content is essential for its conductivity because protons shuttle from anode to cathode by means of the hydronium (H<sub>3</sub>O<sup>+</sup>) ion. For all operations, temperature is limited to 100°C because of the loss of water by evaporation from the membrane. Membrane thickness is also important as a thinner membrane minimizes ohmic resistance losses but risks hydrogen cross-over to cathode, producing parasitic currents. Typical membrane thickness is in the range of 5 – 200μm (Kolde et al, 1995). The role for membrane in PEMFC is to provide ionic conduction, reactant separation and water transport.

#### 2. Catalyst Layer

The catalyst layer is a thin agglomerate-type structure where electrochemical reactions occur. The catalyst in PEMFC is usually made of platinum and its alloys. Fine particles of catalyst are dispersed on a high-surface area carbon in the active layer of the electrode in order to minimize platinum loading. Its performance is characterized by surface area of platinum by mass of carbon support and the typical Pt loading used is about 0.4 mg/cm<sup>2</sup>. Most of the catalyst layer thickness reported in the literature is about 10 μm (Ticianeli et al, 1988). The catalyst layer initiates electrochemical reaction associated with the relevant reactant consumption and product generation, ad also facilitates ionic and electronic conduction.

#### 3. Gas Diffusion Layer (GDL)

The gas diffusion layer (GDL) provides electrical and ionic contact between electrodes and bipolar plate, and distributes reactants to the catalyst layers. Besides, they also allow the water produced to exit the electrode structure and permit passage of water between electrodes and flow channels. The layer is made of porous carbon cloth or carbon paper, impregnated with a proton-conducting membrane to maximize the 3D reaction zone. It contains about 30% Teflon to make it hydrophobic and prevent water from blocking ready access of reactants to the active layer. The thicknesses of various GDL materials vary between 170 to 400 μm (Spiegel, 2008), with porosity of about 0.4 (O'Hare et al, 2006).

#### 4. Bipolar plates and flow channels

The bipolar plate is used to separate different cells in a fuel cell stack and it is made of graphite containing a resin to reduce porosity. Flow channels (parallel, serpentine, inter-digitated and etc) are machined in graphite plates to feed the reactant gases to the GDL. Optimum flow channel area can be determined, as in some cases a larger channel area is required for minimal gas transport pressure loss. However, a larger land area contact between bipolar plate and GDL is necessary for minimum electrical contact resistance and ohmic losses (Larminie and Dirks, 2003). Practically, in a portable PEMFC, the thickness of bipolar plate is about 3mm, while the footprints that sandwiching MEA is approximately 5cm x 5cm.

From Figure 1, the basic operating principle involves four physical transport phenomena described as follow. Many illustrations can be found in Larminie and Dicks (2003), Barbir (2005), O'Hare et al (2006), Li (2006) and Spiegel (2007a,b).

#### A. Reactant transport

Fuel and oxidizer streams enter through the flow channels that are carved into the bipolar plate. Reactants are transported by diffusion and/or convection to the catalyst layer through an electrically conductive GDL. The GDL serves the dual purpose of transporting firstly, reactants and products to and from the electrode, and secondly, electrons to and from the bipolar plates to the reaction site. Efficient delivery of reactants is accomplished by using flow field plates in combination with porous electrode structures. This is an important research area for fuel cell thermo-fluids and component design.

#### B. Electrochemical reaction

An electrochemical oxidation reaction at the anode produces electrons that flow through the bipolar plate/cell interconnect to the external circuit, while ions pass through the electrolyte to the opposing electrode. The electrons return from the external circuit to participate in the electrochemical reduction reaction at the cathode. Choosing the right catalyst and carefully designing reaction zones is an important task for fuel cell catalysis and electrochemistry research.

#### C. Ionic and electronic conduction

During operation of the hydrogen fuel cell, hydrogen is ionized (oxidation) into protons and electrons at the anode. The protons are then transported through the electrolyte to the cathode, and the electrons moved to the cathode, through the external circuit (the load). A thin electrolyte layer for ionic conduction without fuel cross over is crucial in the fuel cell membrane science.

#### D. Product Removal

At the cathode, oxygen (in most cases from air) combines with the protons and electrons (reduction) to produce water. "Flooding" by product water can be major issue in PEMFC and requires research in fuel cell modeling and system integration.

Sufficient water content in polymer membrane is required to sustain membrane protonic conductivity. However, excess water in the fuel cell system can cause flooding and blockage of the pores in GDL. These two competing phenomena pose a great challenge to achieve optimum operating humidity. Figure 2 shows the various water transport phenomena existing within the PEMFC.

For electro-osmotic drag, 1 to 2½ water molecules are dragged for every proton moving from anode to cathode. Water molecules can also diffuse back from cathode to anode, if the water concentration at the cathode is higher. Besides, externally humidifying fuel/oxidant also constitutes to water transport in PEMFC. In general, keeping the PEMFC at right humidity level for optimum membrane humidification is a complex and delicate task. The modeling tool is useful in carrying out the simulation, optimization and prediction for the enhanced fuel cell performance.

The mass transport resistances practically exist in all the components of PEMFC. These include the mass convection and diffusion resistance for neutral gas species ( $H_2$ ,  $O_2$  and  $H_2O$ ), liquid water transport resistance arising from electrical potential and pressure gradient and electrical resistance due to ion migration, convection and diffusion for charged species ( $H^+$  and electrons). Therefore, increasing the mass transport rate for gas, liquid and ions in the various components of PEMFC can yield enhanced cell performance.

Generally, the key components affecting PEM fuel cell performance are:

1. Slow kinetic rate of  $O_2$  reduction reactions in the cathode.
2. Slow oxygen transport rate due to cathode flooding (excess liquid water).
3. Mass transfer limitations due to nitrogen barrier layer effects in the porous layer.

Table 2 summarizes the mass transport implications and limitations in the various components of PEMFC.

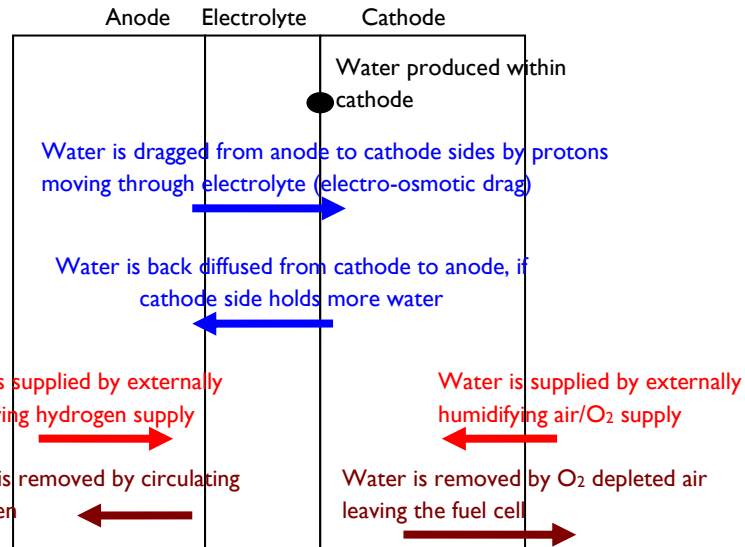


Figure 2: Various water transport phenomena in PEMFC

Table 2: Mass Transport Limitation in PEMFC

Component	Mass Transport Implication	Where mass transport limitation exists
Air/H <sub>2</sub> channel	To provide homogenous distribution of reactants across an electrode surface while minimizing pressure drop and maximizing water removal capability	Reactant depletion for downstream channel Impurity contamination, e.g. N <sub>2</sub>
Cathode/Anode GDL	Porous electrode support to reinforce catalyst, allow easy gas access to catalyst layer, and enhances electrical conductivity	Liquid water flooding block the pores for gas diffusion into catalyst layer
Cathode/Anode Catalyst	Electrochemical reaction takes place at the catalyst layer, consume reactant (H <sub>2</sub> and O <sub>2</sub> ) and generate product (H <sub>2</sub> O)	Poor total reaction surface area (catalyst loading) for optimal electrochemical performance
Membrane	To separate the air and H <sub>2</sub> while allowing liquid water and ionic transport across membrane	Membrane dry-out at high temperature, and loss of its proton conducting capability

The objectives of this paper are:

1. To develop and validate the 3D, non-isothermal, multiphase Computational Fuel Cell Dynamics (CFCD) models with the experimental data for both forced convection and self air breathing fuel cell (ABFC).
2. To explore new design concepts for enhancing the mass transport process in both forced convection PEMFC and ABFC and to further extend the fuel cell performance at high current densities.

## 2. Literature Review

This section explores the literature on PEMFC modeling. It includes: (1) the review of modeling work; (2) a 1D analytical analysis; and (3) 2D/3D numerical simulations, which is often termed Computational Fuel Cell Dynamics (CFCD). Literature on the mass transport enhancement techniques and self air-breathing design for PEMFC will also be discussed

## 2.1 Computational Fuel Cell Dynamics

### 2.1.1 Review of Prior Publications on PEMFC Models

Ma et al (2005) have reviewed the numerous Computational Fuel Cell Dynamics (CFCD) work and concluded that most of the advanced fuel cell models developed by several research groups and CFD vendors still lack of comprehensive modeling capability. A model must account for the detailed processes involving chemistry, electrochemistry, ion and charge transport, heat generation and development of stresses in a fuel cell. A number of fundamental issues, such as species diffusion in porous electrodes, catalytic electrochemical reactions, water management in a hydrolyte polymer membrane, fuel internal reforming and transient processes modeling have yet to be understood well.

Sousa et al. (2005) mentioned that modeling allows detail studies on the electro-catalysis of the reactions involved, as well as the design of water management schemes to avoid membrane dehydration. They concluded that both water transport through the membranes and oxygen diffusion effects in the gas diffusion electrode can be the limiting factors to fuel cell performance. A two-phase modeling of PEMFC was advocated, as the inclusion of liquid water formation and transport can improve model fidelity.

Cheddie et al (2005) categorized fuel cell models as analytical, semi-empirical or mechanistic. They further sub-divided the mechanistic model based on solution strategy, single domain or multi-domain. Single domain is highly recommended for CFD codes, as no internal boundary conditions and conditions of continuity need to be specified.

Biyikoglu (2005) carried out a detailed literature survey on both PEMFC models and experimental tests. For the modeling part, he tabulated the various aspects associated with numerical simulations such as objectives, transport phenomena included in the models, the limitations incurred, solution techniques used, assumptions made, commercial software employed as well as comparison with relevant experimental data from different groups of researchers. He also noted that a comprehensive fuel cell model should be able to describe the key physical processes such as homogenous current density distribution, stable cell operation by controlling water flow within the cell and keeping membrane hydration, avoiding porous electrode flooding and ensuring uniform cell temperature through efficient heat removal capability.

Recently, Siegel (2008) presented a literature review of PEMFC models ranging from 1D single component to 3D multiphase models. These models focus mainly on heat and mass transfer aspects. Siegel (2008) summarized the various modeling strategies, assumptions, computational techniques, numerical algorithms, model accuracy and convergence problems encountered in the modeling. He also presented an overview of the commonly used simulation software for fuel cell modeling e.g. FLUENT, COMSOL Multi-physics, STAR-CD, CFD-ACE+, NADigest FDEM and OpenFoam. He postulated that such PEMFC CFCD tools may not necessarily provide precise values for every computed quantity over the computational domain, but rather would provide trends over a wide range of operating conditions.

### 2.1.2 Computational Fuel Cell Dynamics (CFCD)

The local transport phenomena of flow, energy, chemical species and ionic transfer in PEM fuel cells are difficult to observe and measure by experiment. Computational modeling is an alternative approach to understand fuel cell performance related to the transport processes and electrochemical relations. Numerous researchers have focused on different aspects of the PEM fuel cell, and it is difficult to categorize the different fuel cell models since they vary in terms of the number of dimensions analyzed, modeling domains and complexity. However, a general trend can be established. In the early 1990s, most models were exclusively one dimensional, isothermal and often focused only on the electrode, catalyst layer and membrane. Towards late 1990s, the models became more elaborate and included multi-dimensionality (2D or 3D) and multiphase flow. Since then, researchers have begun to apply Computational Fuel Cell Dynamics (CFCD) method for fuel cell modeling. Some of the important modeling approaches will be mentioned in the following sections.

Bernardi and Verbrugge (1991, 1992) are considered pioneers in fuel cell modeling. They published a one-dimensional, isothermal model for the gas diffusion electrodes, the catalyst layer and the membrane. These provide valuable information on the physics of the electrochemical reactions and transport phenomena in these regions in general. In 1991, they developed a model addressing water management and species transport in the gas diffusion layer. This one-dimensional (1-D) computational domain consists of a cathode gas channel and a gas diffusion layer attached to the membrane. The analysis of this model focuses on polarization characteristics, water transport, and catalyst utilization. As an extension to the

previous model, in 1992, Bernardi and Verbrugge published a complete model with both anode and cathode sides. In this model, the authors focus on the calculations of the activation overpotential, membrane resistance loss and ohmic loss in the gas diffusion layers due to electron transport. Anode activation is also accounted for in this model. Overall, the electrochemical treatments in this model are very comprehensive. However, the drawbacks of this model are its one dimensionality and isothermal assumption.

Springer et al. (1991, 1993) are also pioneers in fuel cell modeling. They presented an isothermal, one-dimensional, steady state model for a PEM fuel cell with a hydrated Nafion-117 membrane. The unique feature of this model is the empirical relation for calculating membrane conductivity based on water content in the membrane. Also, membrane water content at the interface was determined by the activity of water vapor at the electrode/membrane interface. The electro-osmotic drag coefficient, i.e. the ratio of the number of water molecules transported across the membrane per proton, is also calculated based on the membrane water content. These correlations are widely used in FLUENT PEMFC models, and are shown in constitutive Equations 3.42 to 3.48.

Fuller and Newman (1993) were the first to publish a quasi two-dimensional model of the MEA, which is based on the concentration solution theory for the membranes and accounts for thermal effects. However, details of that model were not given. This makes it difficult to compare it with other experimental results. Quasi two-dimensionality is obtained by solving a one-dimensional through-the-membrane problem and integrating the solutions at various points in the down-the-channel direction.

Nguyen and White (1993) presented a steady, two-dimensional heat and mass transfer model. The computational domain consisted of all essential components such as gas flow channels, gas diffusion layers, catalyst layers, and membrane. This model takes into consideration water transport across the membrane by electro-osmosis and diffusion, - the net water flux across the membrane is calculated based on the difference between the electro-osmotic drag and back diffusion from the cathode to the anode. It also accounts for varying activation overpotential as a function of local current density and oxygen partial pressure.

Yi and Nguyen (1998) further extended the Nguyen and White (1993) model to develop an along-the-channel model. This model includes the convective water transport across the membrane caused by pressure gradient, temperature distribution in the solid phase along the flow channel and heat removal through natural convection, co-flow; and counter-flow heat exchangers. Effectiveness of various humidification design, higher cathode gas pressure and heat removal schemes can be evaluated using this model.

Gurau et al. (1998) also applied computational fluid dynamics to PEMFC. They began with a two-dimensional model consisting of both the anode and cathode sides. This model fully accounted for mass transport of reactant species which were simplified in earlier models. The application of CFD to fuel cell modeling has resulted in several advanced models that are three-dimensional (Berning, Lu and Djilali, 2002) and two phase (Z.H. Wang, C.Y. Wang and Chen, 2001).

Wöhr et al. (1998) developed a one-dimensional model that is capable of simulating the performance of a fuel cell stack. It allows for the simulation of the transient effects due to changes of electrical load or gas flow rate and humidification. The modeling domain consists of the diffusion layers, the catalyst layers and the membrane. The “dusty gas model” was applied to the diffusion layer, and the transport of liquid water occurs by surface diffusion or capillary transport. From their model results, various ways to reduce membrane dehumidification at high current densities have been suggested.

He, Yi and Nguyen (2000) published the detailed two-phase model of a PEM Fuel Cell. It is two-dimensional in nature and employs the inter-digitated flow field design proposed by Yi and Nguyen (1999).

Berning, Lu and Djilali (2002) developed a mathematical model for both single phase and multiphase flows in a straight channel. In particular, the single-phase model accounts for many important transport phenomena in a complete assembly of gas channels, porous gas diffusion electrodes, and thin catalyst layers. Heat transfer is also considered in this model. The electrode kinetic is modeled by a simplified version of the Butler-Volmer equation. This equation only accounts for the dependence of current density on oxygen concentrations and is thus one of the major limitations of this approach.

Another research group to apply the methods of CFD for fuel cell modeling is one from Pennsylvania State University. Um et al. (2000) developed a two-dimensional model of a whole fuel cell, similar to the one by Gurau et al. (1998). The

difference is that transient effects were included as well to allow modeling of fuel cell responses to a dynamic load change. This model is used to investigate the effect of hydrogen dilution on fuel cell performance. Since the model is isothermal, the interaction between the liquid water and the water-vapor is not accounted for. To further extend this work for multiphase model inclusion, Wang et al (2001) investigated the phase change at the cathode side of a PEM fuel cell with a two-dimensional model. A multiphase mixture model is applied here which solves for the saturation of liquid water, i.e. the degree of flooding.

Baschuk and Li (2005) presented a two-dimensional, isothermal and steady state mathematical model that can be used as a general formulation for simulation and analysis of PEMFC. They used their in-house finite volume computer code to solve for the governing equations that accounted for gas transport in flow channel, GDL and catalyst layer, water and proton transport in catalyst layer and membrane, as well as electrical current transport in the bipolar plate. The generalized Stefan-Maxwell equation is used to model the water and proton transport. Martínez et al (2008) compared the predictions of PEMFC model using the Stefan-Maxwell equations with the Approximated Multi-Component (AMC) model. They found that the maximum error between the two models is less than 5%. He further concluded that as compared to the Stefan-Maxwell equations which require more computation time and storage capacity, the simplified AMC model is sufficiently accurate for PEMFC prediction.

Djilali (2007) presented a new rational model for coupled proton and water transport in the polymer membrane and removed the limitations associated with empirical model used to date, e.g. membrane water content model proposed by Springer et al (1991). This approach combines pore network modeling and direct numerical simulations of two-phase flow in porous GDL. Le and Zhou (2008) developed a general model for PEMFC by implementing the necessary user defined functions (UDFs) into the commercial CFD software package, FLUENT® 6.2. This model is a three-dimensional, unsteady, multi-phase, multi-component one with Volume of Fluid (VOF) interface tracking technique.

## 2.2 Mass Transport Enhancement

In the past, several techniques for mass transport enhancement in PEMFC have been proposed and evaluated e.g. interdigitated, serpentine and parallel channels. The interdigitated flow field was first described by Ledjeff et al. (1993) and subsequently advocated by Nguyen (1996) and Yan et al (2006). The channel in an interdigitated flow field differs from the conventional parallel and serpentine channel as it is discontinuous between the inlet and outlet manifolds. In this way, the gas and oxidant are forced to flow through the electrodes porous layers from the inlet channels to the outlet channels and creates an additional forced convection mechanism with a much reduced gas diffusion boundary layer over the catalyst sites.

Wang et al (2005) proposed depositing small permanent magnetic particles into cathode catalyst layer. The magnetic particles can induce a Kelvin (magnetic) repulsive force against liquid water and an attractive force towards oxygen gas. They have numerically shown that the magnetic particle could promote liquid water removal from catalyst layer, as well as allow more oxygen diffusion to improve the PEMFC performance. No experimental data are available to test this novel idea.

Liu et al (2005) investigated the application of baffle-blocked flow channel. Their two dimensional numerical simulation shows that mass transport enhancement becomes significant at high current density. The beneficial effect becomes increasingly significant with increasing baffle width and number of baffles in tandem array.

Wang et al (2008) also worked on this baffle wall flow field effect, but extended the numerical simulation work to three dimensional for the newly proposed serpentine-baffle flow field - an added geometry complexity comparing to the previous straight channel baffle flow field by Liu et al (2005). Their results indicated that baffled design induces larger pressure differences between adjacent flow channels over the MEA surface than the conventional design. This enhances under-rib convection through the porous electrode, and therefore increases mass transport rates of the gas reactants and liquid products. Since it is a miniature PEMFC, the compressor power needed to overcome pressure drop is far smaller than the FC output power. This justifies the superior performance of baffled design compared to the conventional type.

Karvonen et al (2006) performed both experimental and simulation (3D; isothermal) analysis to improve the parallel channel design and achieve uniform flow distribution. This improvement can provide a promising alternative as the parallel

channel is typified by small pressure losses and hence low power requirement. However, one major drawback of this modeling approach is the exclusion of temperature, chemical species and electrochemical simulation.

Yan et al (2006) carried out experimental studies to investigate the effect of five different flow field designs (three conventional designs of serpentine, parallel and Z-type and two interdigitated designs of parallel with baffle and Z-type with baffle) on fuel cell performance. The optimal operating conditions (including humidification temperature, cell temperature and cathode gas flow rate) for these five different flow fields were derived. It was reported that the shearing stress generated in the corner areas of serpentine and Z-type flow fields can help enhance the liquid water removal efficiency and improve the mass transport of reactant gas. Under the optimal fuel flow rate conditions, parallel flow field with baffle provides the best performance.

Yan et al (2008) extended the research on the serpentine flow field by numerically investigating the effect of modified heights and lengths on the serpentine channel outlet. The predictions show that reductions of outlet channel areas increase reactant velocities and hence improve the reactant utilization and water removal capability. Increment in the length of reduced flow area also yields better FC performance. Optimal performance is obtained when the height and length contraction ratio is 0.4. However, this improvement comes at the expense of higher pressure drop across the channel. This was not taken into consideration in their work.

Feng and Su (2007) compared the parallel and serpentine flow fields with a stepwise depth flow channel, and postulated that the parallel flow design with stepwise depth is superior to the uniform depth design. However, they showed that the serpentine flow channel is insensitive to step-wise depth design, which is contradictory to the results from Yan et al (2008).

Jeon et al (2008) investigated the effect of the serpentine flow field with a single, double, cyclic-single and symmetric single configurations. They found that the double serpentine design yields better performance at high inlet humidity, while the cyclic and symmetric single serpentine with lower pressure drop would be advantageous for large scale systems and low inlet humidity operation.

Wang et al (2008) employed a three dimensional modeling technique to study the effect of flow channel bends, numbers and width ratio in the serpentine flow field design. Their results show that single serpentine is more superior to double and triple serpentines. FC performance for single serpentine also improves when the numbers of bends increase. Increasing channel width could yield only marginal improvement.

Kuo et al (2008) proposed the wave-like channel and carried out three dimensional simulations to compare its performance characteristics with the conventional straight flow channel. Their numerical results reveal that a wave-like structure can enhance reactant gas transport through porous GDL, improve convective heat transfer, increase gas flow velocity and yield more uniform temperature distribution. Consequently, this design can produce higher output voltage and power density.

### 2.3 Air Breathing Fuel Cells

In this literature survey of Air Breathing Fuel Cell (ABFC), the review begins with general remarks, followed by separate discussions into three main categories, namely analytical, computational and experimental studies on ABFC.

Dyer (2002) reported that despite the keen competition between batteries and fuel cells for portable applications, the opportunity in terms of market size and growth rate for small fuel cell is commercially compelling. Han et al (2007) designed and built probably the world's first commercialized self-hydrating air-breathing PEM fuel cell stack. It is done by adding silica into the anode side of a membrane electrode assembly (MEA).

#### 2.3.1 Analytical Studies

Li et al (2003) used the analogous phenomenon of free convection heat and mass transport to analyze the feasibility and restriction of feeding oxygen to planar ABFC. They verified the results through experimental testing. They found that orientation of the cathode surface can affect the performance of the ABFC, as free convection mass transfer coefficient depends on the orientation of the mass transfer surface. This is analogous to free convection heat transfer. The upward orientation can generate maximum 10% more power as compared to the downward orientation.

Litster and Djilali (2006) derived a 1D semi-analytical model of the MEA to elucidate the transport of ions, heat and mass in ABFC. They found that membrane dry out is the primary limitation on current density. Therefore, it was proposed that enhanced performance of ABFC can be achieved by increasing the heat removal rate, thus promoting higher relative humidity levels in the GDL.

O'Hayre et al (2007) developed a 1D, combined heat and mass transfer analytical model to study the coupling of cathode water generation, oxygen consumption, self-heating and natural convection for ABFC operated on dry hydrogen in dead end anode mode. They also included latent heat released during condensation process, whereas the earlier work by Litster and Djilali (2006) missed out this part. However, a similar finding to Litster and Djilali (2006) has been found, confirming the strong coupling effects between self-heating and water balance. Therefore the issue of matching the heat rejection with water rejection requirement is one of the most important considerations in optimizing ABFC performance.

### 2.3.2 Computational Modeling Studies

Schmitz et al (2004), Wang et al (2005a,b, 2007) and Hwang and Chao (2007) among others have carried out computational study of an air-breathing PEM fuel cell for the planar, open-tube and printed-circuit-based (PCB) cathode design, respectively. All of them used commercially available CFD software and incorporated their own subroutines to account for the electrochemical simulation module. Schmitz et al (2004) used FEMLAB 2.3 (now known as COMSOL), Wang et al (2005a,b, 2007) utilized STAR-CD 3.15 while Hwang and Chao (2007) made use of COMSOL.

Schmitz et al (2004) claimed to be the first to carry out computational modeling for ABFC. However, the model is not comprehensive as they only performed the simulation based on 2D, isothermal, single phase water vapor and simplified electrochemical reaction using the Tafel equation. They discovered an increase in water vapor concentration under the ribs, and hence proposed minimizing the width of the rib so as to avoid liquid water condensation. Consequently, the cathode opening ratio should be made as large as possible, in order to improve the oxygen supply. However, this large cathode open ratio compromises the structural integrity which impacts ABFC performance. This was not taken into consideration in their finding.

Wang et al (2005a,b, 2007) used STAR-CD V3.15 to develop a 3D model of ABFC which accounts for the natural convection on the cathode side, electrochemical reactions at the catalyst layer, as well as water transport across the membrane. The phase change of water was neglected. Model results compared reasonably well with the experimentally measured polarization curves. Their discovery suggested that ambient relative humidity (RH) has significant effect on ABFC

performance. However, the calculation of the limiting current density using the formula  $I_{\text{limit}} = \frac{4FD_{O_2}c_{O_2}^\infty Sh}{L}$  was applied incorrectly. According to O'Hayre et al, 2006,  $L$  and  $D_{O_2}$  are GDL thickness and effective mass diffusivity in GDL, respectively, not the characteristic length and mass diffusivity of the gas channel. This error could greatly affect their conclusions.

Using the same methodology, Wang et al (2005b) carried out CFCD to investigate the effects of three different channel widths of the ABFC, and found that the best performance was obtained with a cathode channel width of 3mm. Subsequently, Wang et al (2007) derived the dimensionless mass transfer coefficient Sherwood number as the function of

the sum of thermal Grashof number  $Gr_T = \frac{g\beta^T \rho^2 (T_{\text{catalyst}} - T_{\text{amb}})^3}{\mu^2}$  and oxygen diffusion Grashof number

$Gr_{O_2} = \frac{g\beta^{O_2} \rho^2 (c_{O_2,\text{catalyst}} - c_{O_2,\text{amb}})^3}{\mu^2}$ . This derivation provides some insight into the nature of the oxygen transport

limitation coupled with heat and mass transfer.

Huang et al. (2007) used COMSOL 3.3 to study the mass transport phenomena in an ABFC. They discovered that the optimal breathing hole diameter is about  $d = 2.1\text{mm}$ , considering the trade-off between the enhancement effect of gas diffusion with the increased of Ohmic resistance when the hole size is varied. Further, they found that the gas mixture flows predominantly outward from the porous cathode to the ambient, rather than inwards from the ambient.

### 2.3.3 Experimental Studies

Fabian et. al. (2006) performed an experimental investigation of the effects of varying ambient temperature ( $10 - 40^{\circ}\text{C}$ ) and relative humidity (20 – 80%) on the operation of a dry hydrogen dead-end mode of a planar ABFC. The average free convection air velocity in horizontal and vertical orientation was 9.1 cm/s and 11.2 cm/s, respectively. The critical membrane transition temperature (from the fully hydrated state to the dry out regime) at which the water removal due to evaporation balances the water generation rate due to reaction is approximately  $60^{\circ}\text{C}$ , irrespective of the ambient temperature and humidity conditions. Mass transport limitation becomes important when the current density exceeds about  $400 \text{ mA/cm}^2$ . The continuous polarization scans fail to capture the rapid membrane drying at high current densities as measured by the point-by-point scan. The performance is limited by membrane dry-out at temperatures above  $30^{\circ}\text{C}$ , and by flooding below  $20^{\circ}\text{C}$ . At high current densities, high temperature and low humidity can result in a membrane dry out. On the other hand, low temperature and high humidity can cause excess flooding. Maximum power density of  $356 \text{ mW/cm}^2$  was measured at ambient temperature of  $20^{\circ}\text{C}$  and relative humidity of 40%. They concluded that the ABFC performance is dependent on MEA water content, and it is governed by the transfer of heat and water vapor to the ambient.

## 2.4 Remarks

The review on PEMFC modeling shows that the goal of utilizing CFCD tools to make precise predictions for local distribution of variable is yet to be accomplished. This is because the fundamental physics and chemistry (e.g. research by Prof. Gerhard Ertl on modern surface chemistry for fuel cells, artificial fertilizers and clean exhaust which earned him the Nobel Prize in Chemistry for 2007) involved still needs further R & D. Nonetheless, the CFCD techniques have evolved much and have established fidelity in terms of coupling the basic flow, thermal and mass transport equations with the electrochemical processes, ionic/electronic transfer, membrane water uptake and multiphase issues. These factors are needed to understand the 3D physical aspects in PEMFC operation. This allows researchers to employ the CFCD tool to determine the overall integrated characteristics (e.g. polarization curves) and help make further improvements to enhance PEMFC performance.

For mass transport enhancement techniques, it is observed that there has been no research carried out on delivering the reactant transversely to the MEA with an impinging jet (IJ) configuration to improve mass transport in PEMFC. Hence, we propose and model this new IJ configuration in PEMFC. Modeling of ABFC remains a challenging task. Thus an attempt is made to extend the mathematical model to an ABFC. It includes a more realistic time-dependent simulation approach, which helps to understand the effects of various factors that can enhance ABFC performance.

## 3. PEMFC Modeling

### 3.1 Model Assumptions

Any model is as good as the assumptions that it is built upon. It is imperative to understand the assumptions made explicitly or implicitly to comprehend the model limitations and accurately interpret the results obtained. A complete fuel cell is an extremely complex system as it involves both micro-scale and macro-scale geometric features (membrane and catalyst layer of  $10 \sim 100 \mu\text{m}$ , gas diffusion layer of  $100 \sim 500 \mu\text{m}$ , and gas channel of 0.5mm to 3mm). It also requires a highly non-linear and coupled equations describing the mass, momentum, heat and electrochemical transport. Therefore, it is necessary to make out a number of simplifying but justifiable assumptions to devise a physically realistic yet numerically tractable model. The main model assumptions made in this study are:

1. Fuel cell operates under steady state condition
2. Ideal gas mixture
3. Laminar flow due to small and Reynolds number ( $<200$ )
4. Isotropic and homogenous membrane and electrode
5. Volume-averaged conservation equations (porosity  $\varepsilon$ ) can model the porous layer adequately

- 
6. In the multiphase flow model (gas and water liquid), “mist flow” assumption in the gas channel is made as water liquid velocity is equivalent to mixture gas velocity
  7. No interaction between gases and liquid water in the pores of the Gas Diffusion Layer (GDL)
  8. Electro-neutrality prevails; hence proton concentration is constant and equal to the concentration of fixed sulfonic acid groups in the membrane
  9. Phase equilibrium exists between water and the electrolyte. This allows for the use of membrane sorption isotherm using the water activity at the membrane boundaries
  10. No deformation occurs in all parts of the cell (no swelling/shrinking of the membrane, no deformation of GDL under land area due to compression)

In modeling the fuel cell transport processes, apart from the governing equations of mass, momentum, energy, species, there are four more phenomenological equations customized to account for PEMFC modeling (Bernardi and Verbrugge, 1991). These are listed below:

1. Butler-Volmer equations for electrochemical kinetics (Bard and Faulkner, 1980):

$$j = j_o \left\{ \exp \left[ \alpha_a \left( \frac{F}{RT} \right) \eta_{act} \right] - \exp \left[ -\alpha_c \left( \frac{F}{RT} \right) \eta_{act} \right] \right\} \quad (3.1)$$

2. Stefan-Maxwell equation for multi-species diffusion (Cussler, 1997):

$$\nabla x_i = RT \sum_j \left( \frac{x_i N_j - x_j N_i}{p D_{ij}} \right) \quad (3.2)$$

3. Nernst-Planck equation for proton transport through membrane (Nernst, 1889; Planck 1890):

$$N_f = -z_f \frac{F}{RT} D_f c_f \nabla \phi_{mem} - D_f \nabla c_f + \vec{v}_l c_f \quad (3.3)$$

4. Schlogl equation for transport of liquid water through membrane (Schloegl, 1955):

$$\vec{u}_l = \frac{K_\phi}{\mu_l} z_f c_f F \nabla \phi_{mem} - \frac{K_p}{\mu_l} \nabla p \quad (3.4)$$

Among the above four phenomenological equations, only the Butler-Volmer equation is associated with the governing equations in PEMFC modeling. The other three mass transport phenomenological equations have been modified or simplified as follows:

1. The Stefan-Maxwell equation is modified where by the effective mass diffusion coefficient in a porous medium is expressed in terms of reference pressure temperature, porosity, liquid water saturation factor and tortuosity (equation 3.21), using the so-called Bruggemann correction of effective medium theory (Um et al, 2000). The recent paper by Martínez et al., 2008 also confirmed that the simplified Approximated Multi-Component (AMC) model is sufficiently accurate for PEMFC modeling, as compared to as the Stefan-Maxwell equations which require more computation time and storage capacity.
2. The Nernst-Planck equation is simplified such that proton diffusion flux due to concentration gradient ( $D_i \nabla c_i$ ) and convection flux ( $\vec{v}_l c_i$ ) are eliminated. Only the proton migration flux due to membrane potential gradient terms is retained. Thus, the ionic transport across the membrane is governed by Ohm's Law (Spiegel, 2007)
3. The Schlogl equation is modified by replacing the membrane potential gradient term with water content concentration gradient term in order to form the phenomenological membrane water transport equation (equation 3.40). This equation describes the liquid water balance between electro-osmotic drag (EOD) and back diffusion. Water velocity across the membrane is dropped off in this equation (Spiegel, 2007).

With the aforementioned physical assumptions and mass transport model simplifications, the PEMFC model equations are developed as shown in the following section.

### 3.2 Governing and Constitutive Equations

The mathematical framework used in the simulation is a comprehensive three dimensional, multi-components, multiphase, non-isothermal, time-dependent transport computation model performed using a computational fuel cell dynamics code (FLUENT 6.3.16) with the add-on Polymer Electrolyte Membrane (PEM) fuel cell module. Essentially, the mathematical model provides a detailed description of the following transport phenomena (Berning et al, 2002):

- Multi-species ( $O_2$ ,  $H_2$  and  $H_2O$ ) flow;
- Convective heat and mass transport in the flow channels;
- Diffusion of reactants through porous electrodes;
- Electrochemical reactions;
- Migration of  $H^+$  protons through the membrane;
- Transport of water through the membrane;
- Transport of electrons through solid matrix;
- Conjugate heat transfer

A numerical solution of time-dependent conservation equations of mass, momentum, energy, species and charge transport is performed for the single computational domain. The domain comprises bipolar plate, gas channel, GDL, catalyst layer and membrane in PEMFC. The governing equations are shown in physical velocity formulation for porous media (Vafai, 2000).

#### 3.2.1 Conservation of Mass:

$$\frac{\partial(\varepsilon\rho)}{\partial t} + \nabla \cdot (\varepsilon\rho\vec{v}) = S_i \quad (3.5)$$

Mass continuity must hold for all the processes inside fuel cell such as fluid flow, diffusion, phase change, and electrochemical reactions. Source term,  $S_i$  is generally nonzero as a result of water phase changes ( $-r_w$ ) and electrochemical reactions. The mixture density is not constant, attributed to the variable gas composition. It is calculated from the ideal gas law for multi-component gases:

$$\rho = \frac{P}{RT \sum_{i=1}^n y_i / M_i} \quad (3.6)$$

#### 3.2.2 Conservation of Momentum:

$$\frac{\partial(\varepsilon\rho\vec{v})}{\partial t} + \nabla \cdot (\varepsilon\rho\vec{v}\vec{v}) = -\varepsilon\nabla p + \nabla \cdot (\varepsilon\mu^{eff}\nabla\vec{v}) + S_m \quad (3.7)$$

$S_m$  is different for different regions of the fuel cell. For gas channel,  $S_m = 0$ . Darcy's equation for fluid flow in porous media is used at GDL and catalyst layer:

$$S_m = -\frac{\mu^{eff}}{K} \varepsilon^2 \vec{v} \quad (3.8)$$

in which  $K$  and  $\varepsilon$  is the porous media permeability ( $m^2$ ) and porosity, respectively.

#### 3.2.3 Conservation of Energy:

$$(\rho c_p)^{eff} \frac{\partial(T)}{\partial t} + (\rho c_p)^{eff} \nabla \cdot (\vec{v}T) = \nabla \cdot (k^{eff} \nabla T) + S_h \quad (3.9)$$

The effective material properties in porous media take into account the bulk properties of both solid matrix and fluid phases for flow. Effective heat capacity  $(\rho c_p)^{eff}$  and thermal conductivity  $k^{eff}$  are adapted from Dagan (1989) and Vafai (2000), respectively:

$$(\rho c_p)^{eff} = (1 - \varepsilon) \rho_s c_{p,s} + \varepsilon (\rho c_p)_f \quad (3.10)$$

$$k^{eff} = (1 - \varepsilon) k_s + \varepsilon k_f \quad (3.11)$$

In the default FLUENT PEM Add On Module, the volumetric heat source term,  $S_h$  takes into account local heat production due to Ohmic heating, heat formation (reaction) of water, activation over-potential (electric work) and latent heat released by liquid water condensation (for multiphase flow), as shown Equation 3.12:

$$S_h = \frac{i^2}{\sigma} + h_{reaction} + |\eta| j_{anodecathode} + r_w h_{fg} \quad (3.12)$$

$\sigma$  ( $\Omega^{-1}\text{m}$ ) is the effective electrical conductivity in the respective zone (GDL, catalyst layer or bipolar plate).  $\eta$  (V) is the local surface over-potential (also known as activation loss) and it is the driving force for the reaction kinetics.  $j_{anodecathode}$  ( $\text{A/m}^2$ ) is the exchange current density at anode/cathode and the formulation is given in the subsequent Butler-Volmer equation.  $h_{fg}$  (kJ/kg) is the latent heat of vaporization.  $r_w$  ( $\text{kg/m}^3\text{s}$ ) is the condensation rate that is modeled as:

$$r_w = c_r \max \left( \left[ (1-s) \frac{P_{wv} - P_{sat}}{RT} M_{w,H_2O} \right], [-s\rho_l] \right) \quad (3.13)$$

The condensation rate constant,  $c_r$  is hardwired to  $100\text{s}^{-1}$ .

As the mathematical formula for heat formation of water,  $h_{reaction}$  ( $\text{W/m}^3$ ), is hidden from the user in the FLUENT code, it is removed and replaced by a more appropriate heat generation term that is related to the reversible cell potential. In the UDF customization developed in this work, the  $h_{reaction}$  term is dropped off by changing the default value for a fraction of the energy released in the chemical reaction for the formation of water as heat energy from 0.2 to 0.0. Instead, it is replaced by the heat generation term related to the reversible cell potential in the cathode catalyst layer. These are described in equations 3.9 and 3.10, respectively (Lampinen and Fomino, 1993):

$$S_h = \frac{i^2}{\sigma} + T \frac{dE^{rev}}{dT} j_{anodecathode} + |\eta| j_{anodecathode} + r_w h_{fg} \quad (3.14)$$

$$E_{rev} = 1.229 - 0.83 \times 10^{-3} (T - 298) + \frac{RT}{4F} \ln x_{O_2} \quad (3.15)$$

Physically, there should be a heat source or a sink in the gas channel due to phase change; that is, condensation of water vapor present in the saturated gas reactant as a heat source or evaporation of liquid water present in the unsaturated gas reactant as a heat sink. However, the current multiphase liquid saturation model used in FLUENT 6.3 has this limitation to model the phase change in the gas channel, as it is using the mist approximation; assuming the liquid velocity is similar to gas mixture velocity in the channel. Therefore, heat source terms do not appear in the energy equation for the gas channel.

In the (GDL), the heat sources are due to Ohmic resistance through solid and latent heat of liquid water condensation (only if the multiphase model is used):

$$S_h = \frac{i^2}{\sigma_{elec,GDL}} + r_w h_{fg} \quad (3.16)$$

In the catalyst layer, the heat sources include the heat generated due to ionic and electronic resistance, the heat released by electrochemical reaction and electric work and the latent heat of water.

$$S_h = \left( \frac{i^2}{\sigma_{elec,cat}} + \frac{i^2}{\sigma_{pro,cat}} \right) + T \frac{dE^{rev}}{dT} j_{anodecathode} + |\eta| j_{anodecathode} + r_w h_{fg} \quad (3.17)$$

In the membrane and bipolar plate, the heat source is mainly due to ohmic resistance, as shown in equation 3.18 and 3.19, respectively:

$$\text{Membrane: } S_h = \frac{i^2}{\sigma_{pro,mem}} \quad (3.18)$$

$$\text{Bipolar plate: } S_h = \frac{i^2}{\sigma_{elec,sol}} \quad (3.19)$$

### 3.2.4 Conservation of Non-Charged Species

Mass conservation for individual gas phase species is given by equation 3.20:

$$\frac{\partial(\varepsilon\rho y_i)}{\partial t} + \nabla \bullet (\varepsilon\rho \vec{v} y_i) = \nabla \bullet (\rho D_i^{eff} \nabla y_i) + S_{s,i} \quad (3.20)$$

$y_i$  = mass fraction of gas species,  $i = 1, 2, \dots, N$  (e.g.  $i = 1$  for hydrogen,  $i = 2$  for oxygen,  $i = 3$  for water vapor,  $i = 4$  for liquid water and etc...) and  $S_{s,i}$  = source or sink term for the species.

The mass diffusivities of individual gas species is given in equation 3.21 (Um et al 2000):

$$D_i = (1-s)^{2.5} D_i^o \left( \frac{p^o}{p} \right) \left( \frac{T}{T^o} \right)^{1.5} \quad (3.21)$$

and Bruggemann model ( $D_i^{eff} = D_i \varepsilon^\tau$ ,  $\tau$  = tortuosity) is incorporated to calculate the effective diffusion coefficient in porous medium.  $D_i^o$  is the mass diffusivity at reference pressure and temperature ( $p^o, T^o$ ).

$S_{s,i}$  is equal to zero everywhere except in the catalyst layer. For the  $H_2$  and  $O_2$  source term in the catalyst layer, the following forms can be obtained:

$$S_{s,H_2,anode} = -j_{anode} \frac{M_{H_2}}{2F} \quad (3.22)$$

$$S_{s,O_2,cathode} = -j_{cathode} \frac{M_{O_2}}{4F} \quad (3.23)$$

Water vapor generation at the cathode catalyst layer is given by  $S_{s,H_2O} = +j_{cathode} \frac{M_{H_2O}}{2F}$ . Molar flux of water due to electro-osmotic drag from anode to cathode is  $S_{s,H_2O} = +M_{H_2O}\alpha$ .  $\alpha$  is the electro-osmotic drag coefficient and will be elaborated in the phenomenological water transport equation across the membrane later. For multiphase flow,  $-r_w$  is added to water vapor equation. Therefore, water vapor source term in cathode catalyst layer is given in equation 3.24 (Bernardi and Verbrugge, 1991):

$$S_{s,H_2O,cathode} = M_{H_2O}\alpha + j_{cathode} \frac{M_{H_2O}}{2F} - r_w \quad (3.24)$$

Water vapor source term in anode catalyst layer is given by equation 3.25 (Bernardi and Verbrugge, 1991):

$$S_{s,H_2O,anode} = -M_{H_2O}\alpha - r_w \quad (3.25)$$

### 3.2.5 Conservation of Charge Species

$$\nabla \bullet (\sigma_{elec} \nabla \phi_{sol}) = S_{\phi,sol} \text{ for electrical current} \quad (3.26)$$

$$\nabla \bullet (\sigma_{pro} \nabla \phi_{mem}) = S_{\phi,mem} \text{ for ionic current} \quad (3.27)$$

$\phi_{sol}$  (V) and  $\phi_{mem}$  (V) is the solid phase and membrane phase potential, respectively.  $\sigma_{elec}$  and  $\sigma_{mem}$  ( $1/\Omega \cdot m$ ) is the solid phase electrical conductivity and membrane protonic conductivity, respectively.  $S_\phi$  ( $A/m^3$ ) is the source term representing volumetric transfer current.

$$\text{At anode catalyst layer: } S_{\phi,mem} = -j_{anode} \quad (3.28)$$

$$\text{At cathode catalyst layer: } S_{\phi,sol} = -j_{cathode}, S_{\phi,mem} = +j_{cathode} \quad (3.29)$$

The conservation of charge law requires the total current generated in the anode catalyst layer to equal the total current consumed in the cathode catalyst layer (and this must also be equal to the total current passing through the membrane):

$$\int_{V_{anode,catalyst}} j_{anode} dV = \int_{V_{cathode,catalyst}} j_{cathode} dV \quad (3.30)$$

The volumetric transfer current can be reflected in the Butler-Volmer equation, which describes how current and voltage are related in electrochemical systems (O' Hayre et al, 2006).

At the anode catalyst layer:

$$j_{anode} = j_{o,anode}^{ref} \left( \frac{c_{H_2}}{c_{H_2}^{ref}} \right)^{\gamma_a} \left[ \exp\left(\frac{\alpha_a F}{RT} \eta_{act,a}\right) - \exp\left(-\frac{\alpha_c F}{RT} \eta_{act,a}\right) \right] \quad (3.31)$$

$$\text{Anode activation over-potential } \eta_{act,a} = \phi_{sol} - \phi_{mem} \quad (3.32)$$

At the cathode catalyst layer:

$$j_{cathode} = j_{o,cathode}^{ref} \left( \frac{c_{O_2}}{c_{O_2}^{ref}} \right)^{\gamma_c} \left[ -\exp\left(\frac{\alpha_a F}{RT} \eta_{act,c}\right) + \exp\left(-\frac{\alpha_c F}{RT} \eta_{act,c}\right) \right] \quad (3.33)$$

$$\text{Cathode activation over-potential } \eta_{act,c} = \phi_{sol} - \phi_{mem} - V_{OC} \quad (3.34)$$

The electrochemical reactions are treated as heterogeneous reactions which take place on the catalyst surface in the porous media. Therefore, the species concentrations in the above Butler-Volmer equations are the surface value. The reaction-diffusion balance equation relates the transfer current density to the gas species concentration by

$$\frac{\rho D_i^{eff}}{\delta} (y_{i,surf} - y_{i,centroid}) \eta = \frac{M_{w,i}}{nF} j_{anodecathode} \quad (3.35)$$

$\eta$  (1/m) is the specific reacting surface area of the catalyst layer, or surface to volume ratio; and  $\delta$  is the average distance between reaction surface and cell center.

The average current density is the total current generated in a fuel cell divided by the MEA area:

$$i_{avg} = \frac{1}{A_{MEA}} \int_{V_{anode,catalyst}} j_{anode} dV = \frac{1}{A} \int_{V_{cathode,catalyst}} j_{cathode} dV \quad (3.36)$$

### 3.2.6 Conservation of Liquid Water Saturation

Water saturation in the gas channel:

$$\frac{\partial(\epsilon \rho_l s)}{\partial t} + \nabla \bullet (\rho_l \vec{v}_l s) = r_w \quad (3.37)$$

Water saturation in the porous GDL and catalyst (Wang and Cheng, 1997):

$$\frac{\partial(\epsilon \rho_l s)}{\partial t} + \nabla \bullet \left( \rho_l \frac{Ks^3}{\mu_l} \frac{dp_c}{ds} \nabla s \right) = r_w \quad (3.38)$$

The source term in the liquid water saturation model,  $r_w$ , has been elaborated in equation 3.13. In the gas channel, fine mist approximation is assumed for the liquid water formation, hence  $\vec{v}_l = \vec{v}$ .

In the porous zone, convection term is replaced with capillary diffusion term. Capillary pressure is computed as the Leverett function of  $s$  (Leverett, 1941 and Udell, 1985):

$$p_c = \begin{cases} \frac{\sigma \cos \theta_c}{\left(\frac{K}{\epsilon}\right)^{0.5}} (1.417(1-s) - 2.12(1-s)^2 + 1.263(1-s)^3) \theta_c & \theta_c < 90^\circ \\ \frac{\sigma \cos \theta_c}{\left(\frac{K}{\epsilon}\right)^{0.5}} (1.417s - 2.12s^2 + 1.263s^3) \theta_c & \theta_c > 90^\circ \end{cases} \quad (3.39)$$

### 3.2.7 Phenomenological Membrane Water Transport Equation

Water content physically refers to the number of water molecules adsorbed per sulphonic acid site. Water transport model through the membrane is described by the balance of water movement due to electro-osmotic drag and back diffusion. It is governed by equation 3.40 (Bernardi and Verbrugge, 1991):

$$\nabla \bullet \left( \frac{n_d}{F} \vec{i} - \frac{\rho_{mem}}{M_{mem}} D_l \nabla \lambda \right) = 0 \quad (3.40)$$

$\vec{i}$  ( $A/cm^2$ ) is the vector from of current flux. Both the electro-osmotic drag coefficient ( $n_d$ ) and membrane water content diffusivity ( $D_l$ ) are the functions of water content ( $\lambda$ ) and temperature ( $T$ ). The membrane density  $\rho_{mem} = 1980 \text{ kg/m}^3$  and equivalent weight  $M_w = 1100 \text{ kg/kmol}$  are used in the numerical simulation. The relevant derivation for electro-osmotic drag, membrane water content, water content diffusivity, water activity and protonic conductivity are given as follows:

Molar flux of water ( $\text{mol/m}^2\text{s}$ ) due to electro-osmotic drag (Bernardi and Verbrugge, 1991):

$$\alpha = \frac{n_d \vec{i}}{F} \quad (3.41)$$

Electro-osmotic drag coefficient (Springer et al, 1991):

$$n_d = 2.5 \frac{\lambda}{22} \quad (3.42)$$

Molar flux of water ( $\text{mol/m}^2\text{s}$ ) due to back diffusion (Bernardi and Verbrugge, 1991):

$$J_w^{diff} = -\frac{\rho_{mem}}{M_{mem}} D_l \nabla \lambda \quad (3.43)$$

Membrane water content (Springer et al, 1991):

$$\lambda = \begin{cases} 0.043 + 17.18a - 39.85a^2 + 36.0a^3 & \text{for } 0 < a \leq 1 \\ 14 + 1.4(a-1) & \text{for } 1 < a \leq 3 \end{cases} \quad (3.44)$$

Membrane water activity (Springer et al, 1991):

$$a = \frac{x_{H_2O} P}{P_{sat}} + 2s \quad (3.45)$$

Saturation pressure (Springer et al, 1991):

$$\log_{10} p^{sat} = -2.1794 + 0.02953(T - 273.15) - 9.1837 * 10^{-5}(T - 273.15)^2 + 1.4454 * 10^{-7}(T - 273.15)^3 \quad (3.46)$$

Membrane proton conductivity (Springer et al, 1991):

$$\sigma_{mem} = \beta \epsilon (0.514 \lambda - 0.326)^\omega e^{1268 \frac{1}{303} - \frac{1}{T}} \quad (3.47)$$

Membrane water content diffusivity (Springer et al, 1991):

$$D_l = f(\lambda) e^{2416 \frac{1}{303} - \frac{1}{T}} \quad f(\lambda) = \begin{cases} 1.00e-10 & \text{for } \lambda \leq 2 \\ 1.00e-10x(1+2(\lambda-2)) & \text{for } 2 < \lambda \leq 3 \\ 1.00e-10x(3-1.167(\lambda-3)) & \text{for } 3 < \lambda \leq 4.5 \\ 1.25e-10 & \text{for } \lambda > 4.5 \end{cases} \quad (3.48)$$

Both the membrane proton conductivity and membrane water diffusivity are the default membrane properties settings for NAFION®. In order to account for the GORE-SELECT membrane, adaptation for the above two parameters is necessary. Ju et al (2005) proposed a modification based on multiplying the constitutive relations with membrane coefficient ( $\beta_{mem}$ ).

$$\text{Adapted membrane proton conductivity } \sigma_{mem}^{adapted} = \beta_{mem} \sigma_{mem} \quad (3.49)$$

$$\text{Adapted membrane water content diffusivity } D_l^{adapted} = \beta_{mem} D_l \quad (3.50)$$

### 3.3 Boundary Conditions

The typical boundary conditions used for this PEMFC model are summarized as below:

1. Electrical potential ( $\phi_{sol}$ ) and membrane potential ( $\phi_{mem}$ ) boundary conditions
  - a. Cathode current collector terminal – Galvanostatic (constant electric potential flux,  $\frac{\partial \phi_{sol}}{\partial n} = constant$ ) boundary conditions are applied to maintain the same stoichiometric ratio at each polarization point. The sign should be negative as the current is drawn out of the computational domain at the cathode side
  - b. Anode current collector terminal - Constant electric potential,  $\phi_{sol} = 0$
  - c. Zero flux boundary condition for the membrane phase potential,  $\frac{\partial \phi_{mem}}{\partial n} = 0$  on all outside boundaries
  - d. Zero flux boundary condition for the solid phase potential,  $\frac{\partial \phi_{sol}}{\partial n} = 0$  on all outside boundaries, except cathode and anode current collector terminal
2. Velocity/Mass flow rate boundary conditions
  - a. Mass flow rate at both anode and cathode are determined by stoichiometric ratio ( $\lambda$ ) and current density ( $i_{ave}$ ) applied at cathode terminal for each polarization point.  $m_{anode\_inlet} = \lambda_a \frac{i_{ave} A_{MEA} M_{H_2}}{2F} \frac{1}{y_{H_2}}$  and  $m_{cathode\_inlet} = \lambda_c \frac{i_{ave} A_{MEA} M_{O_2}}{4F} \frac{1}{y_{O_2}}$ .
3. Species boundary conditions
  - a. Relative Humidity is the partial pressure of water vapor to the saturation pressure,  $RH = \frac{x_{H_2O} P}{P_{sat}(T)}$ . Mass fraction of water vapor ( $y_{H_2O}$ ) at both anode and cathode is determined by  $RH$ , temperature, and pressure at the inlet. A computer algorithm has been developed to determine the water vapor mass fraction through the iterative process.
  - b. As an illustration, at anode inlet, for 60°C and 100% RH, typical mass fraction for H<sub>2</sub>O and H<sub>2</sub> is 0.69 and 0.31, respectively. At cathode inlet, mass fraction of O<sub>2</sub> is 0.23. For 60°C and 100% RH, typical mass fraction for H<sub>2</sub>O is 0.13
4. Temperature boundary conditions
  - a. At anode/cathode inlet and current collector terminal, constant temperature (e.g. 60°C) is applied
  - b. Zero heat flux boundary condition on all outside boundaries

### 3.4 Remarks

The complexity involved in mathematical modeling of PEMFC performance is evident from the number and nature of the equations presented here. The main output parameters which are useful in explaining the transport phenomena at the micro-level are: (i) velocity ( $v$ ), (ii) species concentration ( $c_{H_2}, c_{H_2O}, c_{O_2}$ ), (iii) temperature ( $T$ ), (iv) water content ( $\lambda$ ), (v) liquid saturation factor ( $s$ ) and (vi) local current density ( $i$ ). At the global scale, the plot of intent is the integrated current density ( $i_{ave}$ ) versus electric potential ( $\phi_{sol}$ ) curve which is most commonly used to characterize fuel cell performance.

## 4. Results and Discussion

### 4.1 Model Validation

Figure 3 shows the schematic diagram of the computational domain used in the 2D simulation work for the necessary validation study.

Table 3 shows the various geometrical parameters used in the validation model.

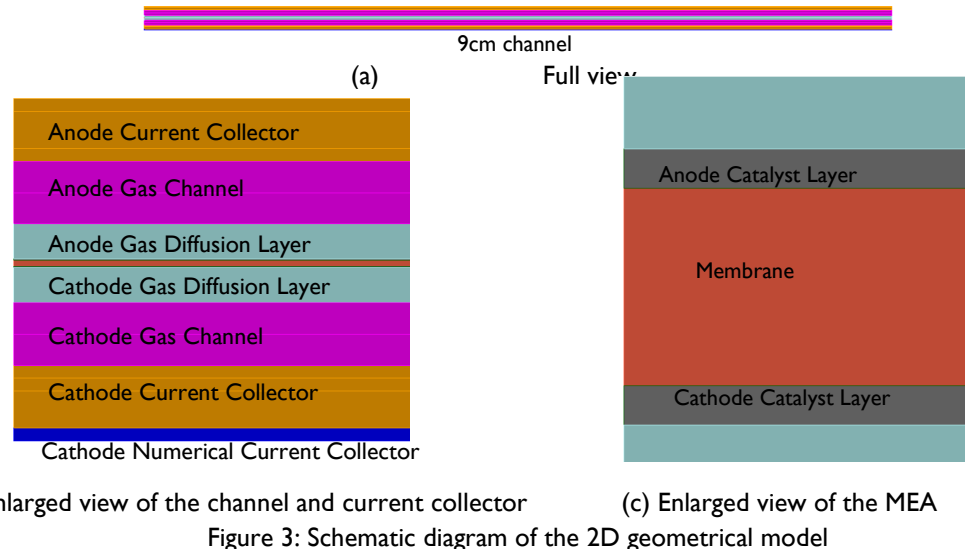


Figure 3: Schematic diagram of the 2D geometrical model

Table 3: Geometrical Parameters Used in the Validation Model

Geometry	Value	Ref.
Dimension	2D	Noponen et al. (2004)
anode distributor	straight channel	Noponen et al. (2004)
anode gas channel length	90mm	Noponen et al. (2004)
anode gas channel height	0.5mm	Noponen et al. (2004)
anode current collector thickness	0.5mm	Assumed
anode GDL thickness	0.28mm	Noponen et al. (2004)
anode catalyst thickness	10µm	Noponen et al. (2004)
cathode distributor	straight channel	Noponen et al. (2004)
cathode gas channel length	90mm	Noponen et al. (2004)
cathode gas channel height	0.5mm	Noponen et al. (2004)
cathode current collector thickness	0.5mm	Assumed
cathode GDL thickness	0.28mm	Noponen et al. (2004)
cathode catalyst thickness	10µm	Noponen et al. (2004)
cathode numerical current collector thickness	0.1mm	Assumed
membrane thickness	50µm	Noponen et al. (2004)
MEA area	90mm x 1m	

---

#### 4.1.1 Model Parameters

Tables 4 to 6 summarize the electrochemical parameters, gas diffusivities and multiphase model parameters used in the validation case.

Table 7 and 8 tabulates the anode and cathode component properties, whereas Table 9 shows the membrane properties used in the simulation.

Table 4: Electrochemistry Parameters

Electrochemistry parameters	Value	Ref.
anode reference current density, $j_{o,anode}^{ref}$ , A/m <sup>3</sup>	1.00e+09	Ju et al (2005)
anode reference concentration, $c_{H_2}^{ref}$ , kmol/m <sup>3</sup>	0.04088	Ju et al (2005)
anode concentration exponent, $\gamma_a$	0.5	Ju et al (2005)
anode exchange coefficient, $\alpha_a$	1	adapted
cathode reference current density, $j_{o,cathode}^{ref}$ , A/m <sup>3</sup>	4.00e+06	adapted
cathode reference concentration, $c_{O_2}^{ref}$ , kmol/m <sup>3</sup>	0.04088	Ju et al (2005)
cathode concentration exponent, $\gamma_c$	1	Ju et al (2005)
cathode exchange coefficient, $\alpha_c$	1.7	adapted

Table 5: Gas Diffusivity Parameters

Reference Diffusivity parameters	Value	Ref.
H <sub>2</sub> , m <sup>2</sup> /s	1.10e-04	Ju et al (2005)
O <sub>2</sub> , m <sup>2</sup> /s	3.23e-05	Ju et al (2005)
H <sub>2</sub> O, m <sup>2</sup> /s	7.35e-05	Ju et al (2005)

Table 6: Multiphase Parameters

Multiphase parameters	Value	Ref.
Saturation exponent for pore blockages	2.5	Um et al (2000)

Table 7: Anode Component Properties

	Value	Ref.
<b>Anode current collector</b>		
Electrical conductivity, $\sigma_{sol}$ (1/Ohm-m)	2.00e+04	Noponen et al. (2004)
Thermal conductivity, $k_{sol}$ (W/mK)	20	Wang et al. (2006)
<b>Anode Gas Diffusion Layer</b>		
Porosity, $\varepsilon_{GDL}$	0.4	Birgersson et al (2006)
Permeability, $\kappa_{GDL}$ ( $m^2$ ) [1/viscous resistance]	7.30e-13	Noponen et al. (2004)
Electrical conductivity, $\sigma_{GDL}$ (1/Ohm-m)	5.00e+02	Noponen et al. (2004)
Thermal conductivity, $k_{GDL}$ (W/mK)	0.333 (Effective = 0.2)	Wang et al. (2006)
Contact angle, $\theta_c$	0	Birgersson et al (2006)
<b>Anode gas channel</b>		
Water content, $\lambda$	0	Physical assumption
Net-flow electrical conductivity, $\sigma_{net}$ (1/Ohm-m)	1.00e+05	Noponen et al. (2004)
Net-flow thermal conductivity, $k_{net}$ (W/mK)	71 (Effective = 5)	Wang et al. (2006)
Net type Porosity, $\varepsilon_{net}$	0.93	Jeng et al. (2005)
Net type Permeability, $\kappa_{net}$ ( $m^2$ ) [1/viscous resistance]	1.00e-10	Noponen et al. (2004)
<b>Anode Catalyst Layer</b>		
Porosity, $\varepsilon_{CAT}$	0.4	Birgersson et al (2006)
Permeability, $\kappa_{CAT}$ ( $m^2$ ) [1/viscous resistance]	7.30e-13	Noponen et al. (2004)
Electrical conductivity, $\sigma_{CAT}$ (1/Ohm-m)	5.00e+02	Noponen et al. (2004)
Thermal conductivity, $k_{CAT}$ (W/mK)	0.333 (Effective = 0.2)	Wang et al. (2006)
Surface to volume ratio, $\eta$ , (1/m)	1.00e+05	Calculated
Contact angle, $\theta_c$	0	Birgersson et al (2006)

Table 8: Cathode Component Properties

	Value	Ref.
<b>Cathode current collector</b>		
Electrical conductivity, $\sigma_{sol}$ (1/Ohm-m)	2.00e+04	Noponen et al. (2004)
Thermal conductivity, $k_{sol}$ (W/mK)	20	Wang et al. (2006)
<b>Cathode Gas Diffusion Layer</b>		
Porosity, $\varepsilon_{GDL}$	0.4	Birgersson et al (2006)
Permeability, $\kappa_{GDL}$ ( $m^2$ ) [1/viscous resistance]	7.30e-13	Noponen et al. (2004)
Electrical conductivity, $\sigma_{GDL}$ (1/Ohm-m)	5.00E+02	Noponen et al. (2004)
Thermal conductivity, $k_{GDL}$ (W/mK)	0.333 (Effective = 0.2)	Wang et al. (2006)
Contact angle	0	Birgersson et al (2006)
<b>Cathode gas channel</b>		
Water content, $\lambda$	0	Physical assumption
Net-flow electrical conductivity, $\sigma_{net}$ (1/Ohm-m)	1.00e+05	Noponen et al. (2004)
Net-flow thermal conductivity, $k_{net}$ (W/mK)	71 (Effective = 5)	Wang et al. (2006)
Net type Porosity, $\varepsilon_{net}$	0.99	Birgersson et al (2006)
Net type Permeability, $\kappa_{net}$ ( $m^2$ ) [1/viscous resistance]	1.00e-10	Noponen et al. (2004)
<b>Cathode Catalyst Layer</b>		
Porosity, $\varepsilon_{CAT}$	0.4	Birgersson et al (2006)
Permeability, $\kappa_{CAT}$ ( $m^2$ ) [1/viscous resistance]	7.30e-13	Noponen et al. (2004)
Electrical conductivity, $\sigma_{CAT}$ (1/Ohm-m)	5.00E+02	Noponen et al. (2004)
Thermal conductivity, $k_{CAT}$ (W/mK)	0.333 (Effective = 0.2)	Wang et al. (2006)
Surface to volume ratio, $\eta$ , (1/m)	1.00e+05	Calculated
Contact angle	0	Birgersson et al (2006)

Table 9: Membrane Properties

Material	GORE membrane	Ref.
Equivalent weight, (kg/kmol)	1100	Springer et al (1991)
Protonic conduction coefficient, $\beta$	1	Springer et al (1991)
Protonic conduction exponent, $\omega$	1	Springer et al (1991)
Membrane porosity, $\varepsilon_{mem}$	0.28	Birgersson et al (2006)
Electrical conductivity, $\sigma_{mem}$ (1/Ohm-m)	$f(\beta, \varepsilon, \lambda, \omega, T)$	Springer et al (1991)
Thermal conductivity, $k_{mem}$ (W/mK)	0.95	Wang et al. (2006)
Membrane coefficient (adapted for GORE membrane)	0.65	adapted

#### 4.1.2 Boundary Conditions

Table 10 shows the boundary conditions for the anode and cathode used in the validation exercise. These values correspond to the actual operating condition.

Table 10: Operating Conditions in the Validation Case

Anode inlet	Value
Anode mass flow rate ( $H_2$ ), (kg/s)	$\lambda_a = 3.35$
Mass fraction of $H_2$ , $y_{H_2}$	1 - $y_{H_2O}$
Mass fraction of $H_2O$ , $y_{H_2O}$	100% RH at 60°C
Temperature, °C	60
Operating Pressure, Atm	1
Cathode inlet	
Cathode mass flow rate ( $O_2 + H_2O + N_2$ ), (kg/s)	$\lambda_c = 2.3$
Mass fraction of $O_2$ , $y_{O_2}$	0.23
Mass fraction of $H_2O$ , $y_{H_2O}$	100% RH at 60°C
Mass fraction of $N_2$ , $y_{N_2}$	1 - $y_{H_2O} - y_{O_2}$
Temperature, °C	60
Operating Pressure, Atm	1

#### 4.1.3 Mesh Independence Study

A mesh independence study was carried out to establish model fidelity. Simulations were carried out using a grid size of 7,920 cells, in which the computer CPU time is about 15 minutes using a single Intel processor 1.6GHz, 1GB RAM. To assess mesh independence, a much denser mesh with a grid size of 273,600 cells was generated and the computation was carried out using 4 parallel AMD Dual Core-Duo Processors, 2.6Ghz, 4GB RAM. As these were much more intensive simulations, they required about 2 hours of CPU time to obtain converged solutions after about 1000 iterations. Table 11 summarizes the grid size distribution for the 7,920 and 273,600 computational cells.

Table 11: Grid size distribution for mesh numbers of 7,920 and 273,600

Component	Thickness (mm)	Mesh density = 7,920 cells		Mesh density = 273,600 cells	
		Number of cells along transverse (thickness) direction	Number of cells along stream-wise direction (90mm)	Number of cells along transverse (thickness) direction	Number of cells along stream-wise direction (90mm)
Membrane	0.05	4	120	10	1800
Catalyst	0.01	3	120	6	1800
GDL	0.28	7	120	25	1800
Gas Channel	0.5	10	120	20	1800
Current collector	0.5	10	120	18	1800
Numerical current collector	0.1	2	120	4	1800

Figure 4 shows enlarged views of the graphical mesh size distribution for the 7,920 and 273,600 computational cells models.

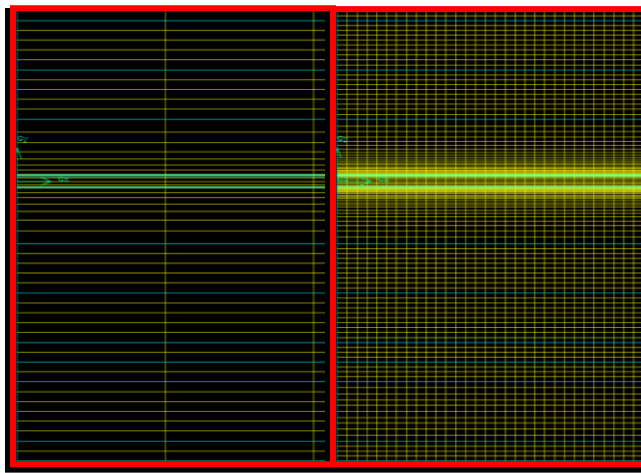


Figure 4: Mesh size distribution for two different mesh densities tested

Table 12 summarizes the global results obtained using these two different mesh densities. Figures 5 to 7 compare the local values obtained from the simulation.

Table 12: Comparison between mesh densities of 7,920 and 273,600 cell calculations

Cells	Current density (A/cm <sup>2</sup> )	Voltage (V)	Temperature rise at the catalyst layer (°C)	Liquid saturation at the catalyst layer	Pressure drop across cathode channel (Pa)
7,920	1	0.623	4.47	0.126	20,900
273,600	1	0.625	4.52	0.095	21,100

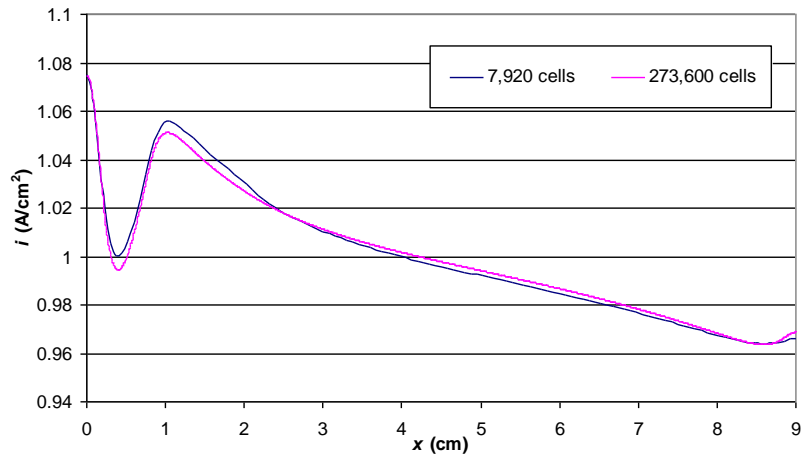


Figure 5: Comparison of the predicted local current density along the anode bipolar plate,  $i = 1\text{A}/\text{cm}^2$ , for two different mesh densities

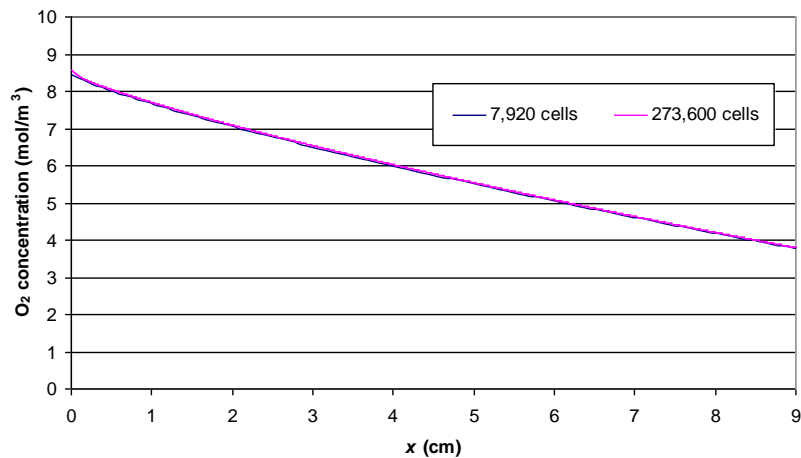


Figure 6: Comparison of the local  $\text{O}_2$  concentration along the cathode gas channel/GDL,  $i = 1\text{A}/\text{cm}^2$ , for two different mesh densities

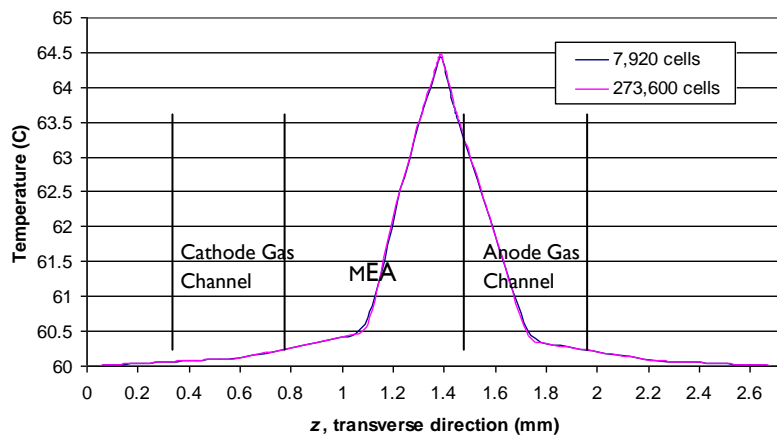


Figure 7: Comparison of the local temperature along the center line,  $i = 1\text{A}/\text{cm}^2$ , for two different mesh densities

From Table 12 and Figures 5 to 7, it can be seen that both global and local values from these two different mesh densities match reasonably well; only a slight deviation (0.1%) occurs for the predicted voltage. A larger number of meshes generally have a smoothing effect on the simulation output. However, both meshes eventually produce residual values about 1e-05 and are hence considered converged results. In view of the computing time and also the massive computer resources required for the higher mesh density case, it was not deemed necessary to carry out such intensive simulations with a 273,600 cell grid. The smaller mesh of 7,920 cells is considered sufficiently accurate to capture the multi-physics and transport phenomena involved in this fuel cell simulation.

#### 4.1.4 Validation Results

##### 4.1.4.1 Global Polarization Curves

Figure 8 shows a comparison of the polarization curve obtained using the 2D simulation model with the experimental data from Noponen et al (2004). Good agreement is evident up to a current density of  $1.3\text{A}/\text{cm}^2$ .

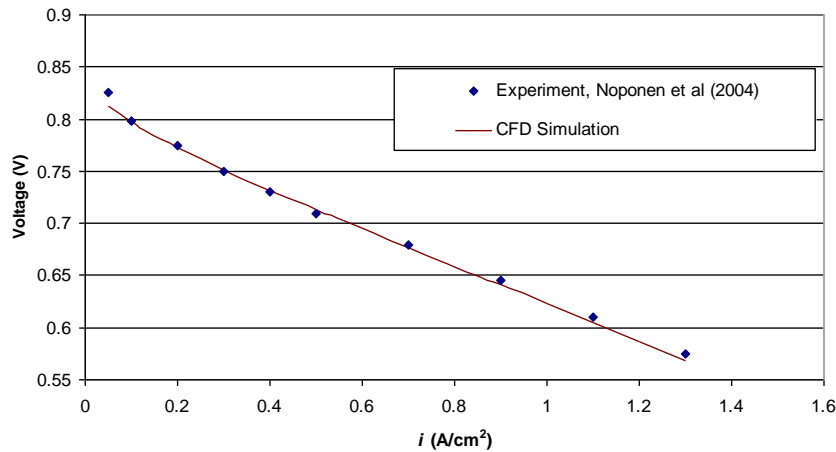


Figure 8: Comparison of global polarization curve between 2D simulations with experimental data (Noponen et al (2004))

Further simulation with both potentiostatic and galvanostatic boundary conditions were performed (see Figure 9). This is to ascertain that a numerical current collector of sufficiently high electrical conductivity ( $1\text{e}6 \text{ S/m}$ ) is able to produce accurate results for both cases. If the electrical conductivity of the actual bipolar plate is low (e.g.  $7,500 \text{ S/m}$ ), then a “numerical” bipolar plate with a fictitiously high value of electrical conductivity is required to recover the galvanostatic simulation results from its potentiostatic counterpart. In this simulation, the numerical bipolar plate of  $1\text{e}06 \text{ S/m}$  is found to be sufficiently large to match both galvanostatic and potentiostatic simulation results.

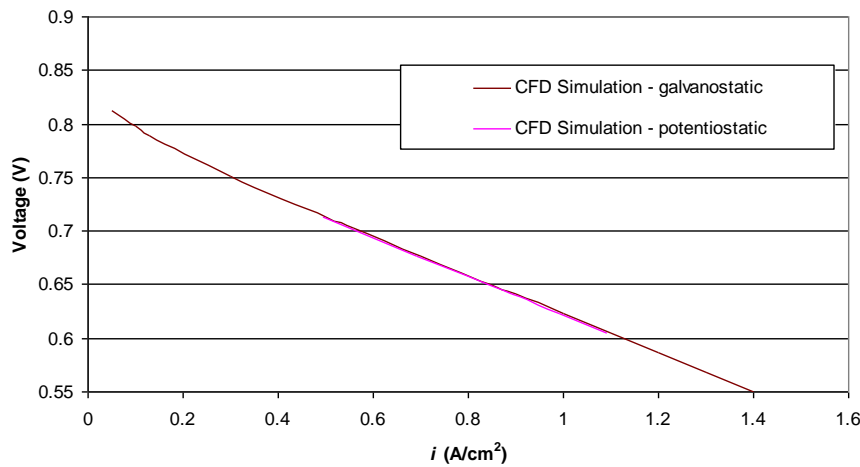


Figure 9: Comparison between potentiostatic and galvanostatic boundary conditions

Experimental results from Noponen et al (2004) are available only up to  $1.3 \text{ A/cm}^2$ , and therefore validation of polarization curve is valid only up to  $1.3 \text{ A/cm}^2$ . However, simulations for higher current density values have been carried out in order to assess the limiting current density (see Figure 10). It shows that the current model is capable of predicting the sharp drop of the limiting current density in the vicinity of  $2.2 \text{ A/cm}^2$ .

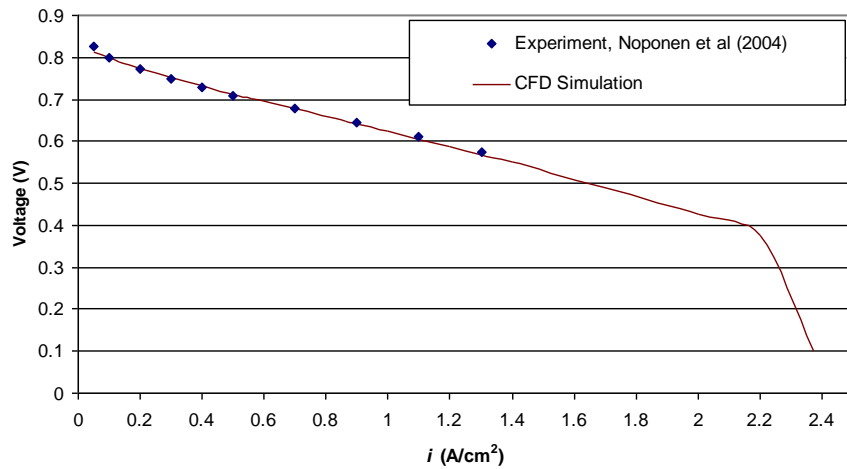


Figure 10: Global polarization curve of the 2D simulations results

#### 4.1.4.2 Local Current Density Variations and Drop at Entrance Region

Figure 11 compares the local current density distribution between the 2D simulation model with the experimental data from Noponen et al (2004). Near the entry region of the channel, there is about a 40% difference in the local current density obtained by simulation and the experimental data. Our simulation overestimates the current density relative to the experimental data over the first 1/3 of the channel length. This difference can be attributed to the 3D geometry of the experimental setup which uses manifold to deliver the gas/oxidant transversely to the MEA. This 3D transverse effect is not considered in our current 2D simulation model, as the flow is directly delivered to MEA in the stream-wise direction. However, the general trend of the local maximum current density produced from the experimental data is well captured by the simulation model, as the local maximum of  $1.16 \text{ A/cm}^2$  obtained from computer simulation is close to the experimental result of  $1.24 \text{ A/cm}^2$ , with 6% uncertainty.

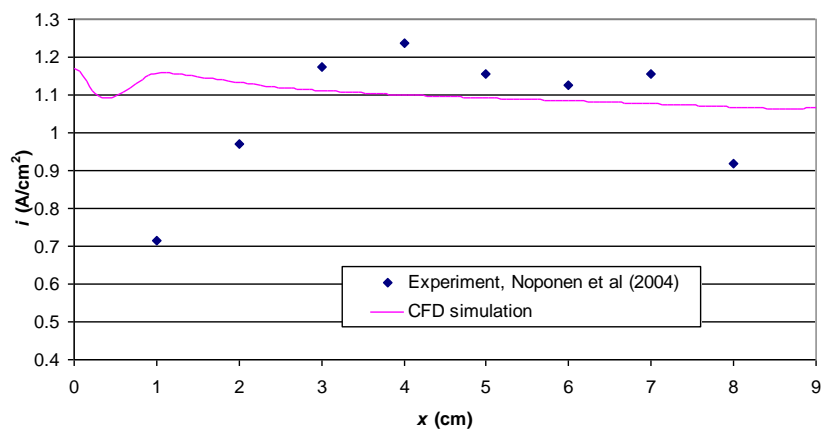


Figure 11: Comparison of local current density between 2D simulations with experimental data from Noponen et al (2004),  $i = 1.1 \text{ A}/\text{cm}^2$

From Figures 5 and 11, it is observed that there is a drastic drop in the local current density at the entry of the channel flow. One related phenomena to the above observation is the excess liquid water saturation in the channel entry region.

This is caused by the low value of net porous channel permeability ( $1e-10 m^2$ ), which generates a higher pressure at the gas channel in the entry region and drives high humidity (100% RH) air towards the catalyst layer. When the net permeability is increased from  $1e-10$  to  $1e-05 m^2$ , the high pressure region shifts towards the catalyst layer (Figure 12), hence displacing the liquid water generated in the catalyst layer.

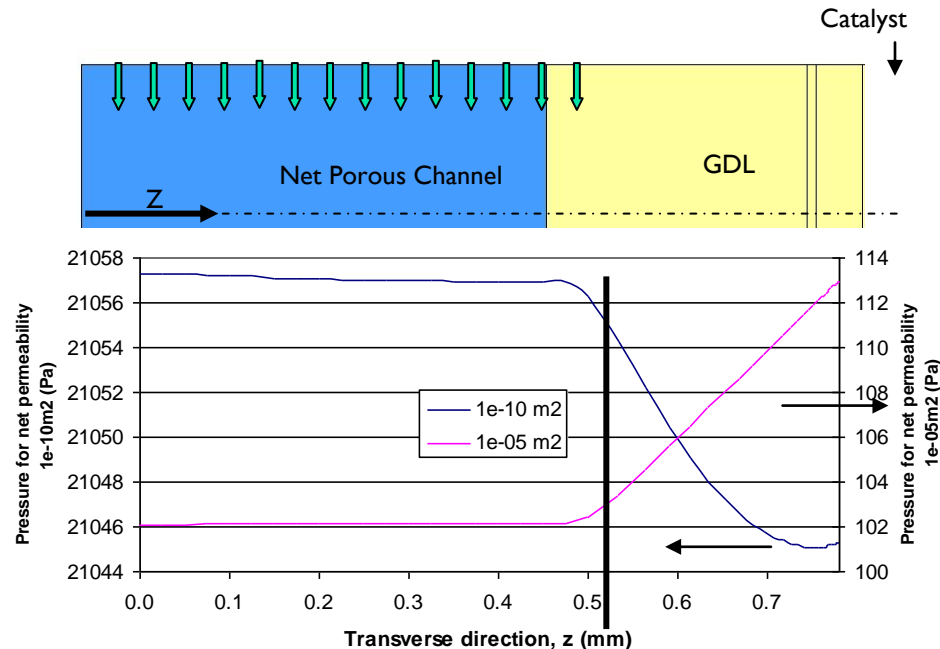


Figure 12: Comparison of predicted static pressure profile along gas channel and GDL near the channel entry at two different net porous channel permeability values

The plot of the velocity flow field around the cathode GDL near the channel entry region (c.f. Figure 13) for two different values of the net permeability shows that the flow around GDL moves away from catalyst layer when net channel permeability is increased from  $1e-10 m^2$  to  $1e-05 m^2$ . Therefore, when the net permeability is increased, excess liquid water is removed from the cathode catalyst layer.

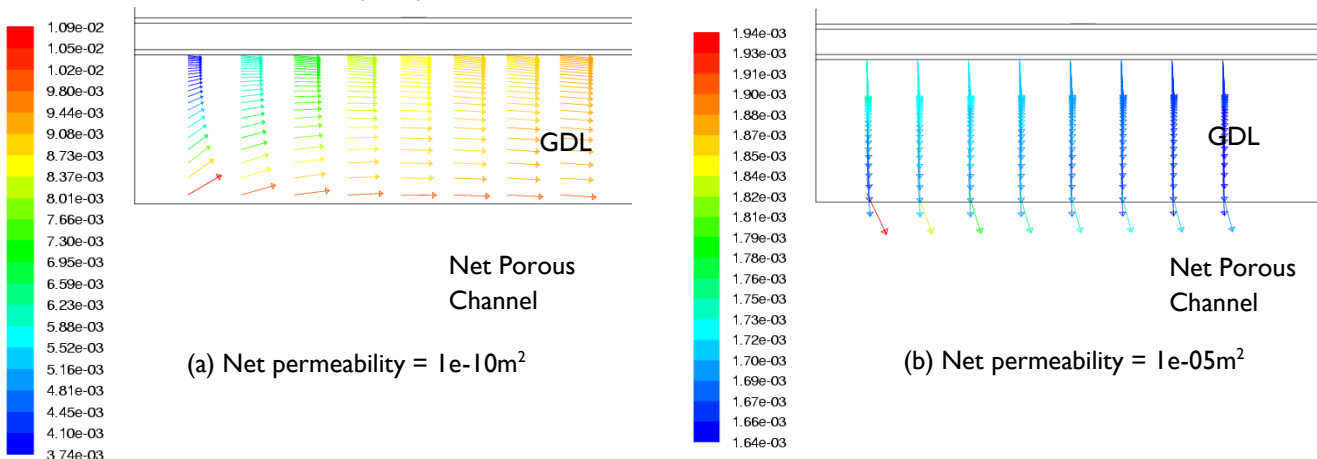


Figure 13: Flow field around the GDL in the channel entry region for two different net porous channel permeability values

The plot in Figure 14 shows that the liquid saturation factor for  $1e-05 m^2$  vanishes (Fig. 14(b)) compared to 17% at the lower permeability value of  $1e-10 m^2$  (Fig. 14(a)). This implies that lower net permeability is favorable to reduce water

content but not necessarily advantageous to fuel cell performance as it can reduce the membrane proton conductivity and thus current density (see Figure 4.30).

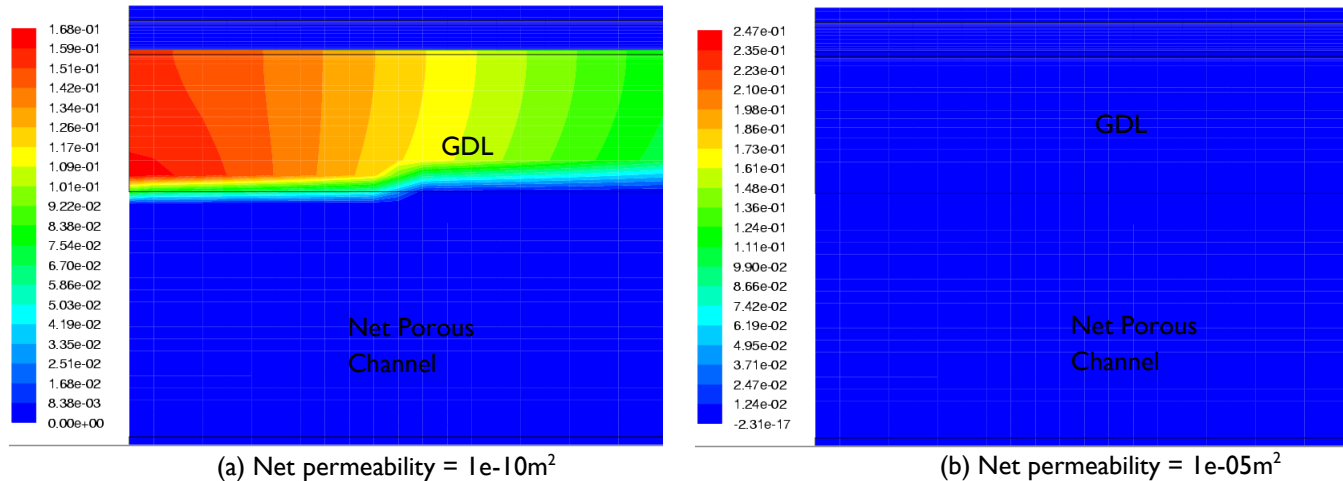


Figure 14: Liquid water saturation in the channel entry region for two different net porous channel permeability values

When the net permeability is increased, the velocity along the net flow distributor changes from a flat profile towards a parabolic profile (c.f. Figure 15). This further facilitates water suction from the catalyst layer, and hence enhances the water removal capability near the channel entrance. Therefore, the liquid water saturation factor disappears at this higher net permeability of  $1\text{e-}05\text{m}^2$  (see Figure 14(b)).

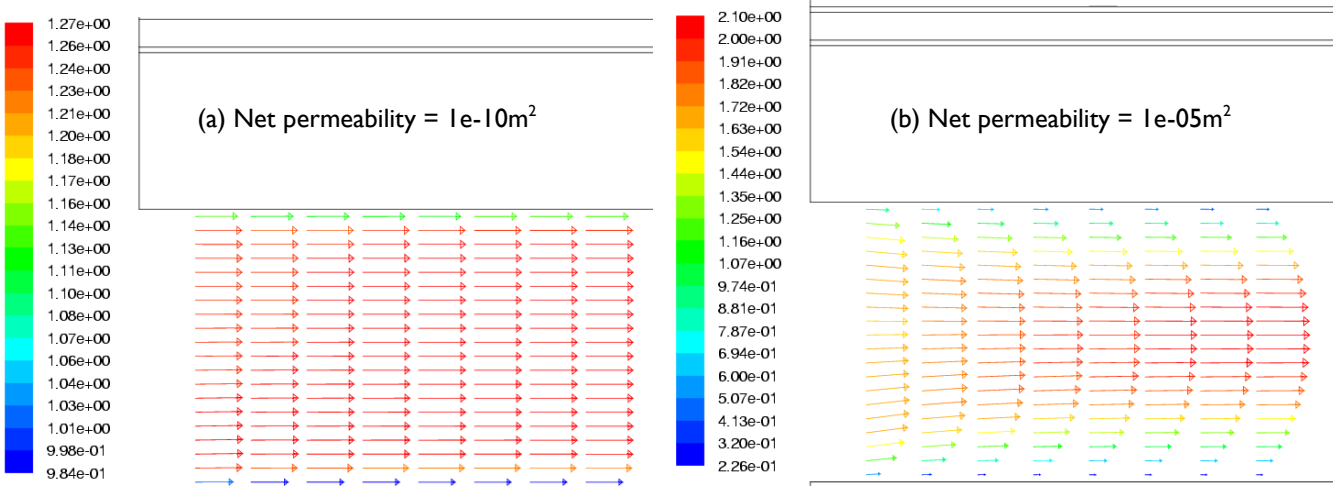


Figure 15: Flow field around net flow distributor at the channel entry region for two different net porous channel permeability values

Figure 16 shows the computed local current density distribution for two different values of net porous channel permeability. Generally, the lower permeability value ( $1\text{e-}10\text{m}^2$ ) can produce a higher current density at the upstream regime (about 2cm from entrance) as it keeps the membrane hydrated with the associated higher liquid saturation factor (c.f. Figure 14(a)). However, a drastic drop in current density (about 0.5cm from the entry region) is observed for this lower permeability value, attributed to the adverse effect of liquid water accumulation. Nevertheless, when the net flow distributor permeability value is increased from  $1\text{e-}10\text{m}^2$  to  $1\text{e-}05\text{m}^2$ , the drastic drop in the local current density at channel entry region disappears.

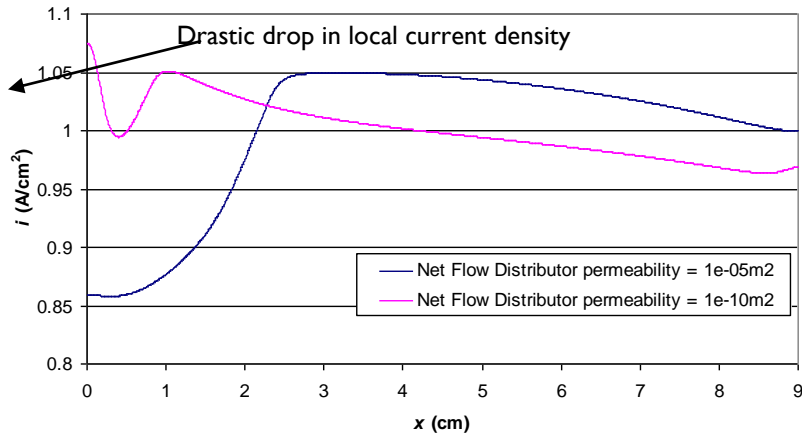


Figure 16: Comparison of local current density along anode bipolar plate for two different net porous channel permeability values

The plot of transverse velocity along the centerline of GDL in Figure 17 shows that at higher net permeability ( $1e-05\text{m}^2$ ), the flow within the first half of the channel length (4.5cm) is mainly moving away from the catalyst layer. For lower net permeability ( $1e-10\text{m}^2$ ), the saturated air from the cathode inlet is directed towards the catalyst layer only near the channel entry (about 0.05cm from the inlet), but afterwards the flow is directed away from the catalyst layer. At the second half of channel length ( $> 4.5\text{cm}$ ), both cases have the flow in the GDL directed towards catalyst layer. This phenomenon reflects the way water vapor and  $\text{O}_2$  are carried towards or away from the catalyst layer by convection velocity with different net porous channel permeability values.

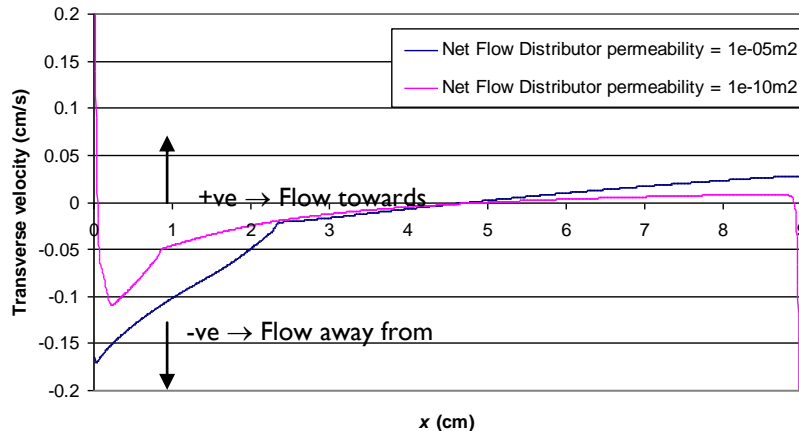


Figure 17: Predicted transverse velocity along cathode GDL centerline for two different net porous channel permeability values

Figure 18 shows the corresponding mapping between current density and transverse velocity for net flow distributor permeability value of  $1e-05\text{m}^2$ . It shows that when the flow within the cathode GDL is directed away from cathode catalyst layer, the local current density improves and vice versa. This is due to the capability of removing the excess liquid water when the flow is directed away from catalyst layer.

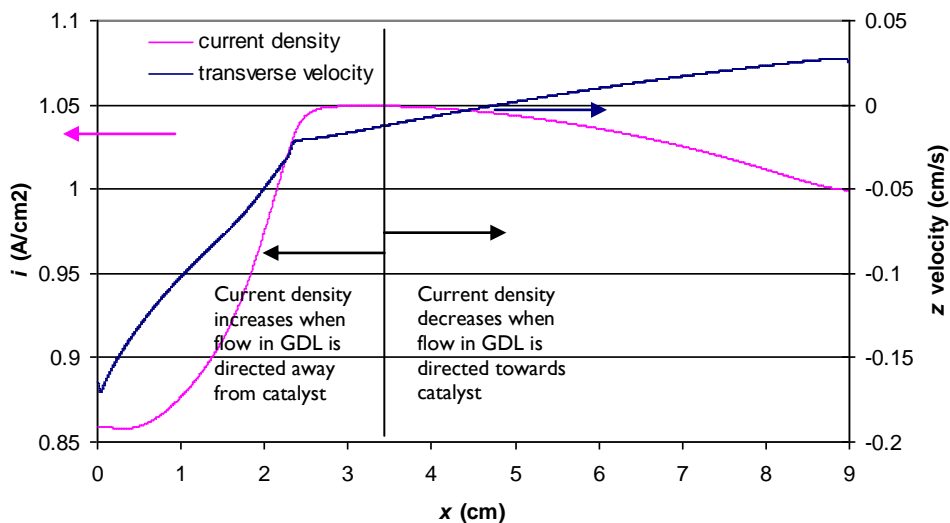


Figure 18: Current density along anode bipolar plate and transverse velocity along cathode GDL centerline for net porous channel permeability of  $1e-05\text{m}^2$

#### 4.1.4.3 Comparison of Local Temperature Distributions and Liquid Saturation Factor

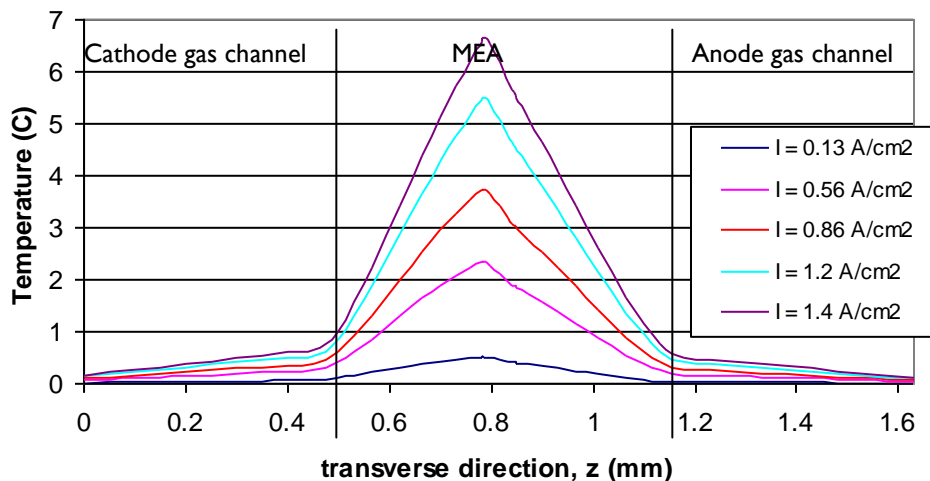


Figure 19: Temperature profile across MEA at different current densities

Figure 19 depicts the temperature profile in the transverse direction from the cathode flow channel to the anode gas channel, passing across the MEA at different current densities. It is observed that at  $1 \text{ A/cm}^2$ , a temperature difference of about  $4.5^\circ\text{C}$  is obtained for the cathode catalyst layer, after incorporating heat generation in the cathode catalyst layers (related to the reversible cell potential) and deactivating the heat energy released in the chemical reaction in the formation of water. This is within the temperature range of  $4-6^\circ\text{C}$  measured by Vie and Kjelstrup (2004).

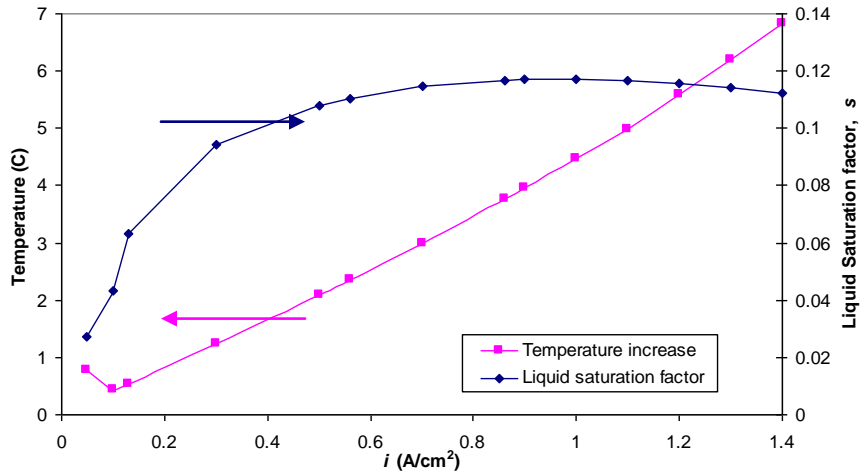


Figure 20: Temperature increase and liquid saturation factor at the cathode catalyst layer

Figure 20 shows the temperature rise and liquid saturation factor predicted by the model. The temperature rise is slightly lower than the model results from Noponen et al (2004) - our maximum is  $7^\circ\text{C}$  as compared to Noponen et al's (2004) value of  $10^\circ\text{C}$ . The liquid saturation factor obtained from this simulation result, 12%, is higher than that from the model of Noponen et al (2004), about 6%.

#### 4.1.4.4 Multiphase Model Results

To further explain the drastic drop of local current density in the channel entry region, additional simulations without multiphase capability (hence the liquid saturation factor is zero) were performed. The resulting comparison is shown in Figure 21.

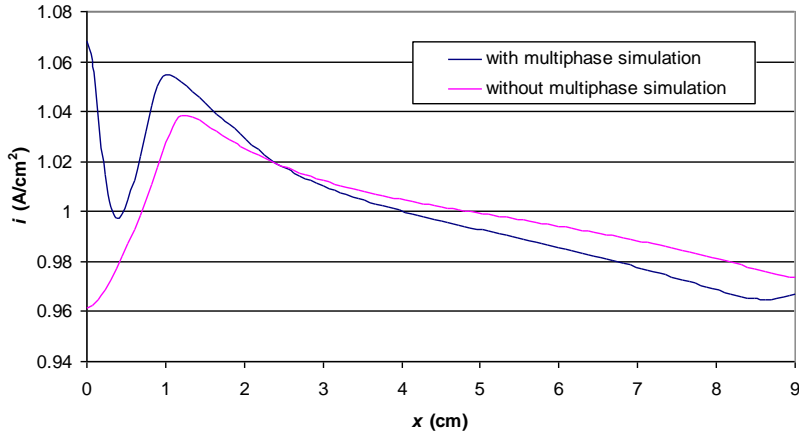


Figure 21: Comparison of local current density along the anode bipolar plate, with and without accounting for multiphase physics

It is observed that the sudden drop in current density near the channel entry disappears when the multiphase model is not adopted. Therefore, the sudden decrease in the current density is due to the high liquid water saturation at the channel entry (c.f. Figure 22). This high liquid water saturation factor is caused by firstly, the high local pressure at the net flow distributor nears the channel entry that pushes the saturated flow towards the catalyst layer and secondly, the thinner boundary layer at the entrance regions which allows more diffusion of water vapor into the GDL upstream.

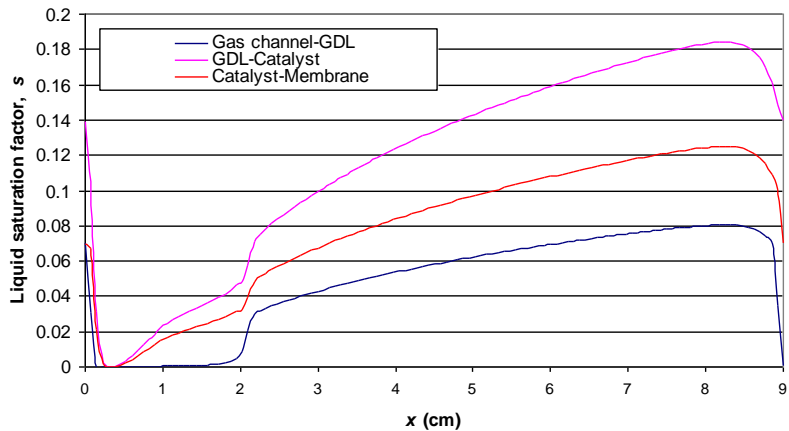


Figure 22: Liquid saturation at the cathode accounting for multiphase physics

As for air breathing fuel cell, Hottinen et al. (2004), Wang et al (2005), Schmitz et al (2006), and Singapore A-STAR researchers in Temasek Poly [TP] (2008) have carried out experimental studies for the ABFC. Table 13 summarizes the operating characteristics of their experimental work.

Table 13: Operating Characteristics of Prior ABFC Experimental Work

Exp.	Cell orientation	H <sub>2</sub> operation	T <sub>amb</sub>	T <sub>cell</sub>
T. Hottinen et al (2004)	6 cm <sup>2</sup> horizontal –GORE® MEA, 100% open cathode, single cell	open	Finland ambient condition	27-30°C
Y. Wang et al (2005)	34 cm <sup>2</sup> vertical, 4.9 cm channel length, single cell	Stoich=1	26°C, 63% RH	38°C at 250 mA cm <sup>-2</sup>
A. Schmitz, et al (2006)	10 cm <sup>2</sup> horizontal –GORE® MEA 80% open, single Cell	open	German ambient condition	43°C at 250 mA cm <sup>-2</sup>
TP exp. (2008)	TP MEA, 10 cm <sup>2</sup> , 40% open area, 2 series MEAs	open	22°C, 60% RH air-con	48-26°C at 200 mA cm <sup>-2</sup>

It is noteworthy to mention that out of the four experimental works carried out, only the setup by Wang et al (2005) follows the cathode channel design, while the other three ABFC experimental works utilized the cathode planar design. This is shown in Figure 23, which depicts the schematic diagram of the experimental setup.

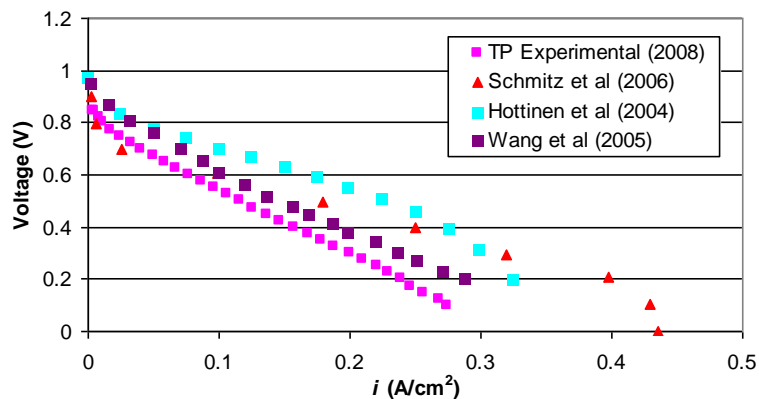


Figure 24: Polarization Curves of Prior Experimental Work on ABFC (from TP, 2008)

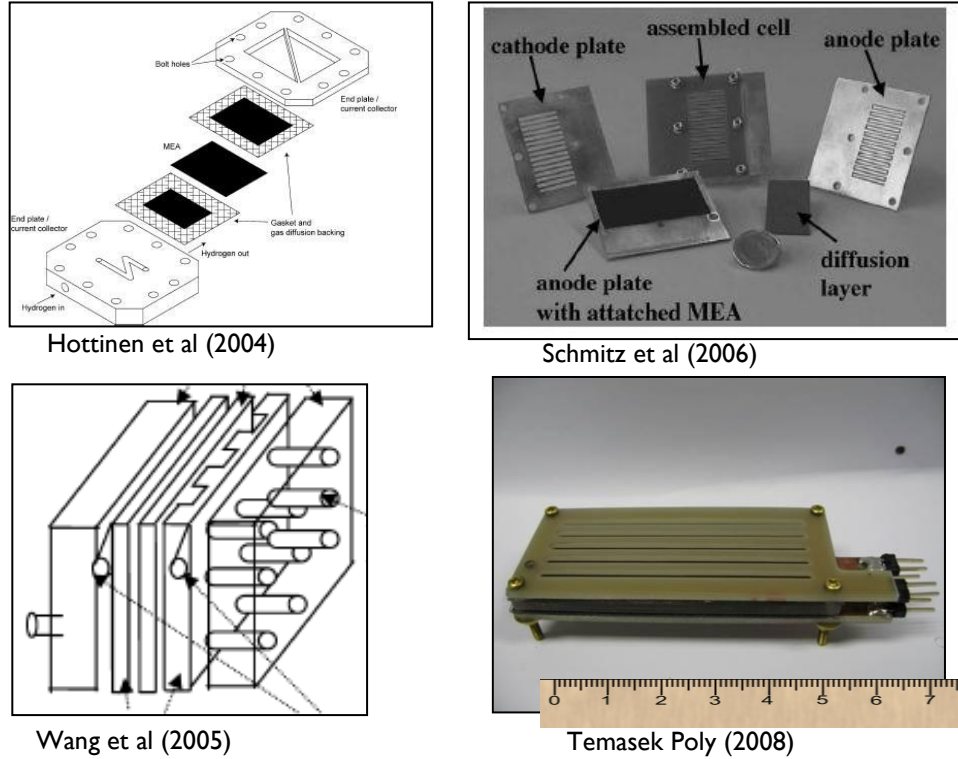


Figure 23: Schematic Diagram of the Prior Experimental Work on ABFC

Figure 24 shows the polarization curves obtained from the ABFC experimental work. The results further confirmed the earlier literature data from Fabian et al (2006), which stated that mass transport limitation for air breathing fuel cell could reach as low as  $0.4\text{A}/\text{cm}^2$ , unlike the forced air convection fuel cell which could extend beyond  $2\text{ A}/\text{cm}^2$  (see later impinging jet PEMFC section).

Figures 25 and 26 show the geometric description for the both the experimental setup from Wang et al (2005) and the 3D simulation model developed in this work. The computational model uses the periodic boundary condition to simulate one channel configuration. This is because the prior result from Wang et al (2005) shows that hydrogen supply to the serpentine channel produces uniform flow and species distribution at the anode side, and therefore yields almost negligible variation of  $\text{O}_2$  and water content between each cathode channel. In this case, the repetitive segmented cathode flow channel can be simulated and represented on the global scale.

Table 14: Operating Condition for ABFC Model Validation

Anode Inlet	
Anode mass flow rate ( $\text{H}_2$ ), ( $\text{kg}/\text{s}$ )	$\lambda = 3.35$
Mass fraction of $\text{H}_2$ , $y_{\text{H}_2}$	0.31
Mass fraction of $\text{H}_2\text{O}$ , $y_{\text{H}_2\text{O}}$	0.69 (100% RH)
Temperature, $^{\circ}\text{C}$	33
Operating Pressure, Atm	1
Cathode Inlet	
Cathode ambient	Pressure outlet (ABFC)
Mass fraction of $\text{O}_2$ , $y_{\text{O}_2}$	0.23
Mass fraction of $\text{H}_2\text{O}$ , $y_{\text{H}_2\text{O}}$	0.03 (100% RH)
Temperature, $^{\circ}\text{C}$	33
Operating Pressure, Atm	1

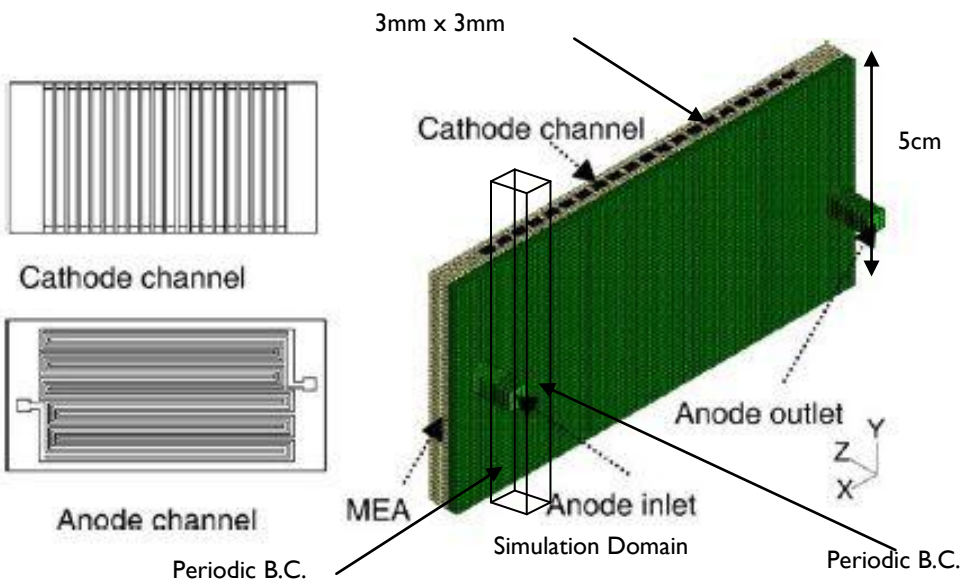


Figure 25: Geometric description of experimental setup from Wang et al (2005)

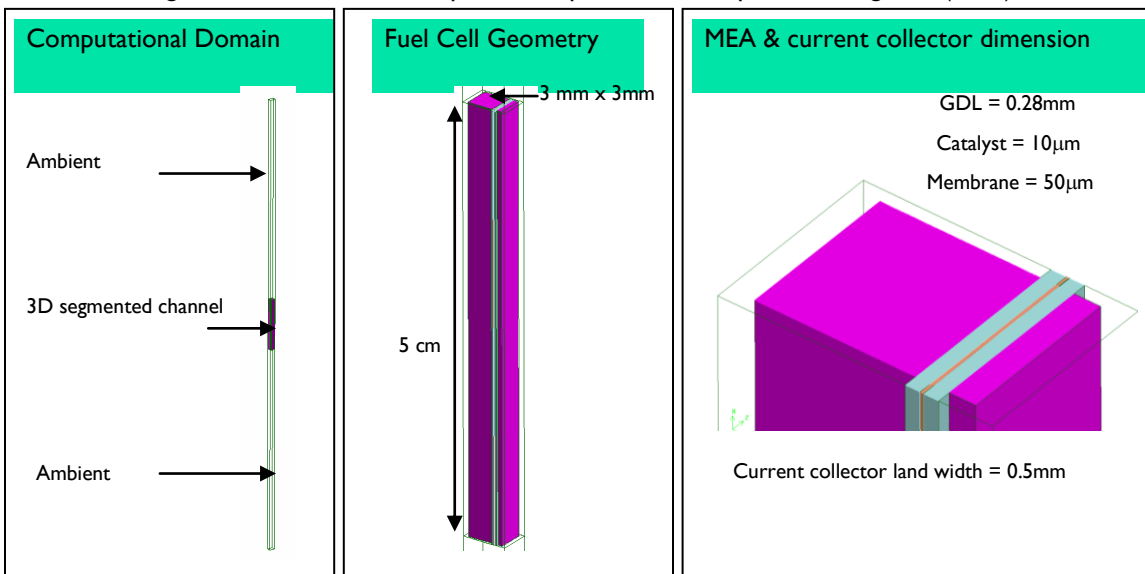


Figure 26: Geometric description of 3D validation model

The model is first validated by benchmarking the simulation results with experimental data from Wang et al (2005). Table 14 shows the operating conditions used for this model validation study.

As shown in Figure 27, reasonable agreement (about 10% uncertainty) has been obtained when comparing the simulation data to the experimental work. The difference gets larger at higher current density. This is because the O<sub>2</sub> consumption is higher at the onset of mass transport limitation and hence necessitates a larger reservoir size to supply O<sub>2</sub>. However, this larger size is not achievable in the current simulation model as it conflicts with the periodic boundary conditions.

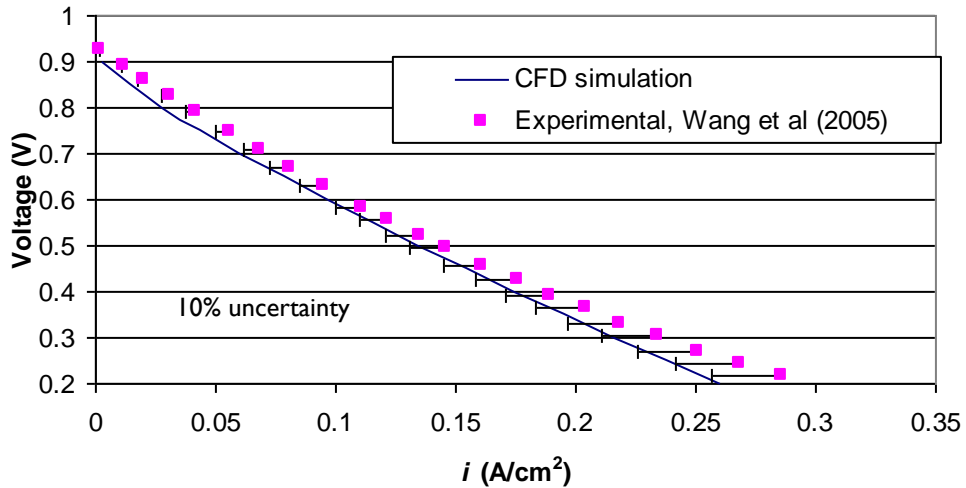
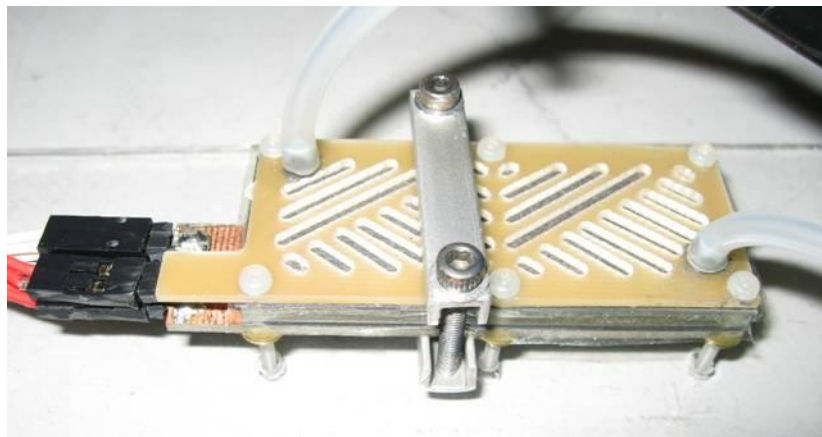


Figure 27: Comparison of global polarization curve between simulation results with experimental data

One important consideration in model validation is the thermal issue, as highlighted by the experimental counterpart in Temasek Poly (2008). A temperature difference as high as  $18^\circ\text{C}$  can be obtained at the GDL when the two stack cells of ABFC are operating at ambient temperature. In the current simulation, the temperature difference of  $10^\circ\text{C}$  is achieved for a single cell. Figures 28(a) and 28(b) show the temperature difference obtained from the ABFC operation in the experimental work using slot planar and modeling results for the channel cathode, respectively. Although the model did not reproduce the experimental setup correctly (there are unknown parameters associated with it, such as hydrogen flow rate etc), it shows that the simulation model is able to capture the necessary heat generation phenomena in ABFC, thus negating isothermal assumption in ABFC simulation, for example, paper by Hwang and Chao (2007).



Temperature Distribution ( $^\circ\text{C}$ ) for two stack cell at GDL @  $0.2\text{A}/\text{cm}^2$

38	43	42	42	40
33	33	39	37	H <sub>2</sub> out 36
24	25	27	26	24

Figure 28(a): Temperature distribution for ABFC slot planar experimental data

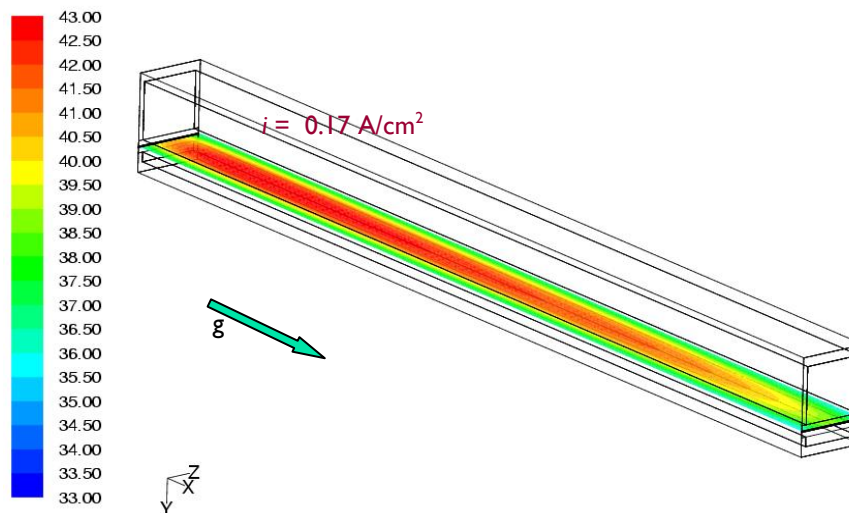


Figure 28(b): Temperature distribution for channel ABFC model results

As can be seen, the current simulation compares reasonably well with the measured global current density, as well as the local temperature value obtained in the experiments. Next, this modeling tool is used to characterize various important factors affecting ABFC performance such as channel geometric design and device orientation, as well as investigating the fuel cell durability and stability. Finally, the enhanced performance criteria for ABFC are established based on this computational analysis.

#### 4.2 Enhanced Performance with Impinging Jet Configurations

Figure 29 shows a schematic diagram of a single impinging jet on the cathode side of a PEMFC. It is implemented on the cathode side (rather than the anode) due to the slower reaction kinetics there governing the overall fuel cell performance. Here, the reactant is supplied through a vertical opening created within the bipolar plate and connected perpendicularly to the gas channel. This impinging jet fluid delivery system supplies the fresh reactant transversely towards the catalyst region. This is different from the conventional serpentine or channel flow delivering the reactant along the stream-wise direction. In our proposed design, the jet of  $O_2$  impinges on the porous gas diffusion layer. The reduced  $O_2$  concentration boundary layer thickness is expected to enhance the mass transport rate to the catalyst region and further alleviate reactant depletion in the flow downstream.

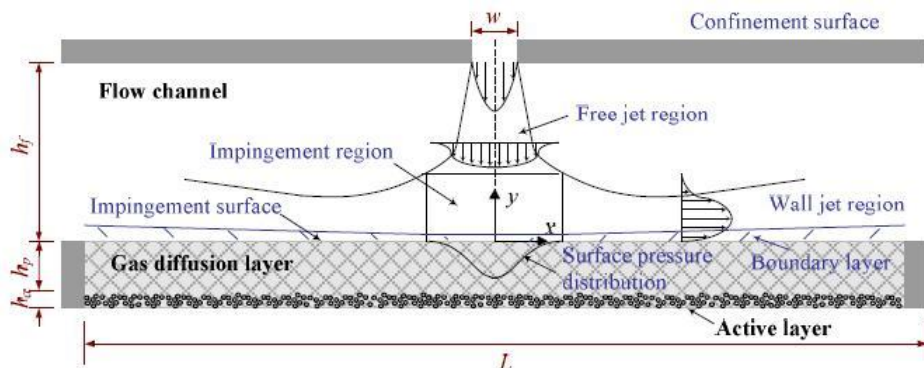


Figure 29: Impinging Jet in PEMFC

Figure 30 describes the practical and feasible design of using the impinging jet configuration in PEMFC (hereafter referred as IJ-PEMFC) for both the single and stack cell, respectively. This is the multiple jet design, but it can be easily

reduced to a single jet by closing up the other unused jets. The IJ-PEMFC in comparison to the conventional parallel and serpentine channel simply requires extra thickness of the bipolar plate (e.g. 3mm thickness comparing to normal 1.5mm). This gives provision for the chamber on top of the impinging jet and the fabrication of the perforated bipolar plate. Apart from this modification, the manifold gas channel and flow pumping requirement remain similar. Therefore, a simple yet innovative design for flow distributors in PEMFC is proposed.

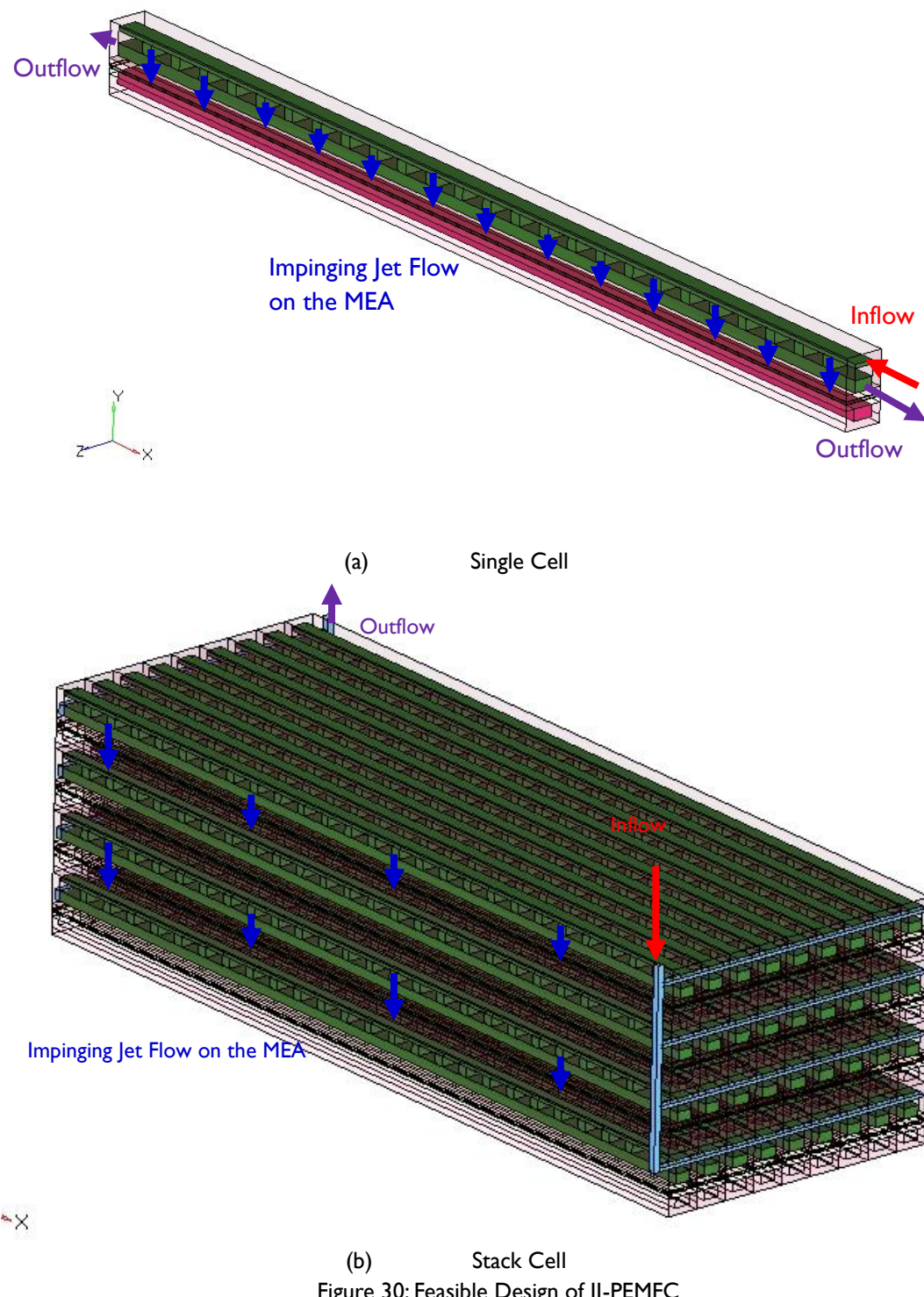


Figure 30: Feasible Design of IJ-PEMFC

The objective of this work is to examine via simulations the concept of utilizing single/multiple impinging jets to supply the reactant gases to the catalyst layer. Parametric studies with different net types and GDL permeability values have also been performed. From the author's review of literature, no researchers have discussed the impinging jet concept in PEMFC. It was first proposed by Mujumdar (2004) when this research was defined.

#### 4.2.1 2D Cathode Side Single Impinging Jet Design

Simulation of the single central impinging jet in the cathode channel and a conventional straight anode channel was carried out. The results were compared with the equivalent straight channel flow case. In this IJ-PEMFC simulation, given that the jet opening is created in the bipolar plate, it takes out a small fraction of the current collector area that is available for current conduction. As such, when the galvanostatic BC is applied at the cathode current collector, one has to make sure that the total current applied to the simulation model matches the required current density. For example, in this typical case of MEA area of 90mm (per unit meter depth), with the impinging jet width of 0.5mm, the total area for current conduction is reduced to  $89.5\text{mm}^2$ . For a current density of  $1\text{A}/\text{cm}^2$ , the current flux applied at the cathode current collector has to be increased to  $90/89.5*\text{I} = 1.005586 \text{ A}/\text{cm}^2$ . This correction factor contributes to a significant difference if the impinging jet width is increased to a large value, e.g. 30mm, as done in our subsequent study.

Figure 5.3 shows the geometry used in the simulation for a 2D single IJ-PEMFC design.

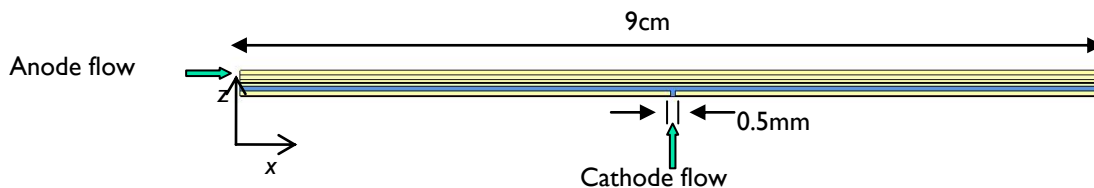


Figure 31: 2D Geometry for Cathode Side Single IJ-PEMFC

For this 2D simulation, flow along  $x$ - $z$  direction is referred as stream-wise and transverse direction, respectively. The channel length is 9cm, channel height is 0.5mm and the dimension of the jet inlet on the cathode side is 0.5mm. Anode channel is maintained as channel flow. All other electrochemical, reference diffusivities and multiphase model parameters, the anode/cathode electrodes and membrane properties as well as the operating conditions used in the previous chapter for model validation are implemented correspondingly in this IJ-PEMFC scenario.

##### 4.2.1.1 Effect of net flow distributor and GDL permeability

The performance of impinging jet configuration with porous gas channel (or net flow distributor, hereafter referred as NFD) depends on the ideal combination of GDL and NFD permeability values. A total of 8 polarization curve predictions (120 simulation cases) with a combination of two different values of cathode GDL permeability ( $1\text{e}-09$  and  $1\text{e}-12 \text{ m}^2$ ) and two different values of cathode NFD permeability ( $1\text{e}-10$  and  $1\text{e}-08 \text{ m}^2$ ) for both straight channel (hereafter referred as SC) and single IJ-PEMFC (hereafter referred as SIJ-PEMFC) have been carried out to evaluate these characteristics.

Normal NFD and GDL permeability ( $\kappa$ ) values are  $1\text{e}-10 \text{ m}^2$  and  $1\text{e}-12 \text{ m}^2$ , respectively. Simulations were also carried out with marco-porous GDL (Shimpalee et al, 2005) of higher permeability values ( $1\text{e}-10 \text{ m}^2$  &  $1\text{e}-09 \text{ m}^2$ ) and aluminium foam NFD (Jeng and Tzeng, 2005) of much greater permeability value ( $1\text{e}-08 \text{ m}^2$ ) for both SC-PEMFC and SIJ-PEMFC designs. This allows more of the jet flow to penetrate deeper into the catalyst site.

For brevity, the simulation cases studies are renamed as follows:

- Case 1: GDL permeability of  $1\text{e}-12 \text{ m}^2$  and NFD permeability of  $1\text{e}-10 \text{ m}^2$
- Case 2: GDL permeability of  $1\text{e}-09 \text{ m}^2$  and NFD permeability of  $1\text{e}-10 \text{ m}^2$
- Case 3: GDL permeability of  $1\text{e}-09 \text{ m}^2$  and NFD permeability of  $1\text{e}-08 \text{ m}^2$
- Case 4: GDL permeability of  $1\text{e}-12 \text{ m}^2$  and NFD permeability of  $1\text{e}-08 \text{ m}^2$

Table 15 shows the results of voltage and pressure drop across the NFD at a current density of 1 and 2 A/cm<sup>2</sup> for Cases 1 to 4.

Table 15: Comparisons between SC-PEMFC and SIJ-PEMFC designs computed with 2D multiphase model

Case	$\kappa_{NFD}$ (m <sup>2</sup> )	$\kappa_{GDL}$ (m <sup>2</sup> )	$i$ (A/cm <sup>2</sup> )	Voltage (V)		Pressure drop(Pa) across NFD	
				SC- PEMFC	SIJ-PEMFC	SC- PEMFC	SIJ-PEMFC
1	1.00e-10	1.00e-12	1	0.623	0.622	20,834	5,739
2	1.00e-10	1.00e-09	1	0.611	0.620	4,072	1,239
3	1.00e-08	1.00e-09	1	0.609	0.619	310	79
4	1.00e-08	1.00e-12	1	0.609	0.620	351	89
1	1.00e-10	1.00e-12	2	0.426	0.421	38,919	11,425
2	1.00e-10	1.00e-09	2	0.136	0.357	8,221	2,536
3	1.00e-08	1.00e-09	2	0.205	0.379	632	162
4	1.00e-08	1.00e-12	2	0.246	0.379	713	182

From Table 15, it is seen that for Case 1, both SC-PEMFC and SIJ-PEMFC designs have similar performance, viz. 0.623V and 0.426V at 1 and 2A/cm<sup>2</sup>, respectively. As GDL permeability increases from 1e-12 to 1e-09 m<sup>2</sup> (Case 2), the SIJ-PEMFC outperforms SC-PEMFC, especially at a higher current density of 2A/cm<sup>2</sup>, as 0.357V is obtained for SIJ-PEMFC design whereas only 0.136V is attained by SC-PEMFC design.

However, as the GDL permeability is increased in Case 2, fuel cell performance for both SC-PEMFC and SIJ-PEMFC deteriorate. This is because as the GDL permeability is increased, pressure drop across NFD reduces. Lower pressure at cathode NFD causes fuel cell performance to drop, as depicted in Nernst's equation 1.3. SC-PEMFC's performance drop is more significant, as compared to SIJ-PEMFC. For Case 2, at current densities of 1 and 2 A/cm<sup>2</sup>, the SIJ-PEMFC outperforms the SC-PEMFC design, only marginally for the former by 1.4% (from 0.620 to 0.611V) and more significantly for the latter by 162% (from 0.136 to 0.356V).

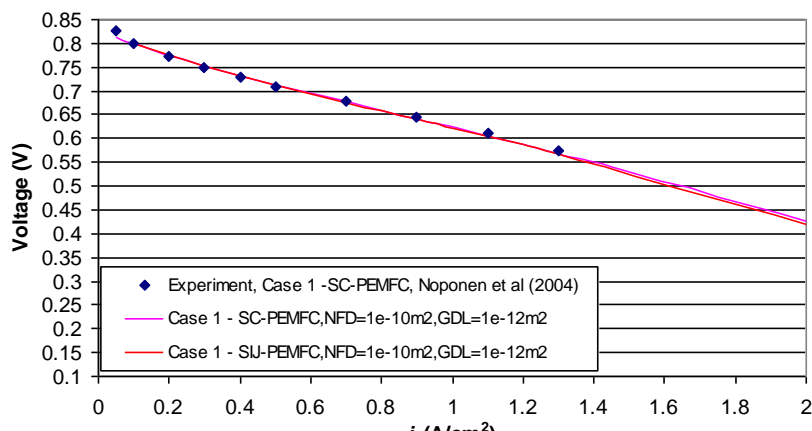
When the NFD permeability is increased to 1e-08m<sup>2</sup> (Case 3), variation of GDL permeability has a negligible effect on fuel cell performance for SIJ-PEMFC. However, for the SC-PEMFC at a higher current density of 2 A/cm<sup>2</sup>, reducing GDL permeability results in enhanced fuel cell performance. The voltage increases from 0.205V to 0.246V if GDL permeability is reduced from 1e-09m<sup>2</sup> to 1e-12m<sup>2</sup>. Nevertheless, the SIJ-PEMFC still has superior performance to that of a SC-PEMFC at NFD permeability of 1e-08m<sup>2</sup>.

Figure 32 compares the global polarization curves between SC-PEMFC and SIJ-PEMFC for Case 1, 2, 3 and 4. For completeness, corresponding experimental result from Noponen et al (2004) for Case 1 SC-PEMFC is also included for comparison. It is obvious that except Case 1, all other three cases show enhanced performance using SIJ-PEMFC when  $i$  is larger than 1 A/cm<sup>2</sup>. This also implied that the impinging jet can augment the cell performance, especially near the straight channel limiting current density.

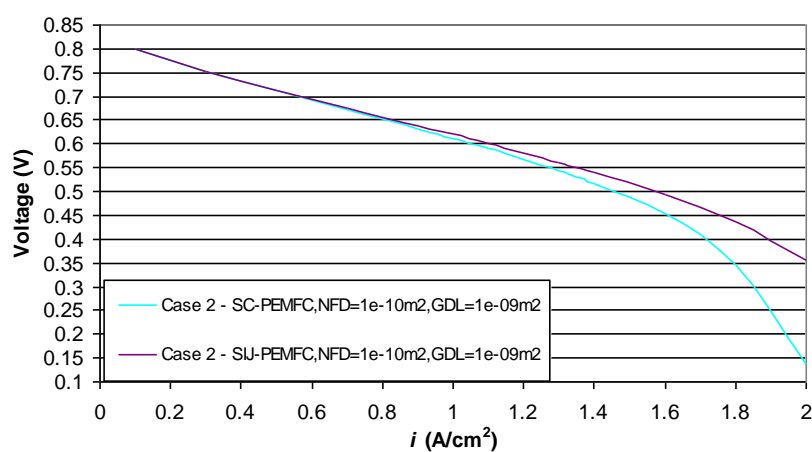
For Case 1, no significant difference is obtained for the global current density, including over the range beyond experimental value from 1.3 to 2.0 A/cm<sup>2</sup>. This is caused mainly by the low GDL permeability (1e-12 m<sup>2</sup>) which dampens the jet penetration effect and reduces the forced convection flow in the porous gas channel, leading to weaker diffusion in the GDL area under the impinging jet. Thus, the effect of impingement is apparently damped fully by the low permeability.

From Figure 32(b), using the macro-porous GDL with permeability of 1e-09 m<sup>2</sup> in Case 2, the SIJ-PEMFC could enhance the PEMFC performance, especially at high current densities, by about 4% at 1.4 A/cm<sup>2</sup> and reaching about 160% at 2 A/cm<sup>2</sup>. However, this combination of NFD and GDL permeability value is not desirable because they nullify the NFD functionality. Detailed explanation will be given in the later section.

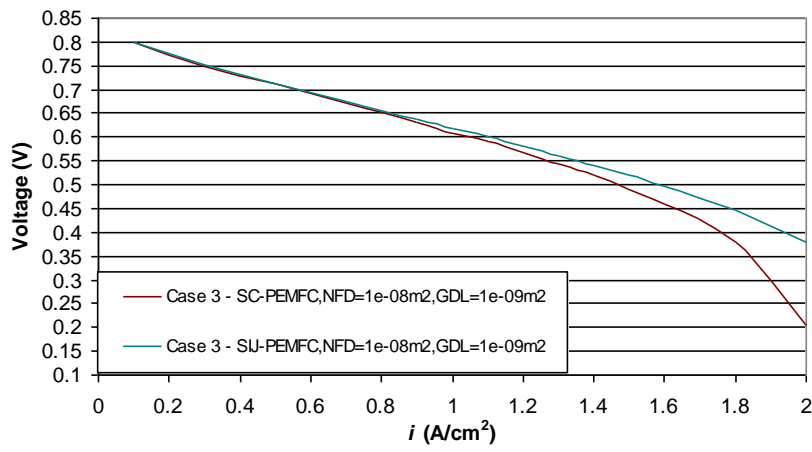
Figure 32(c) shows that by increasing both NFD and GDL permeability in Case 3, the SIJ-PEMFC can still yield 84% performance enhancement over SC-PEMFC at 2.0 A/cm<sup>2</sup>. Case 3 is considered as the ideal permeability combination between NFD and GDL for enhanced SIJ-PEMFC performance.



(a) Case 1 and Experimental data



(b) Case 2



(c) Case 3

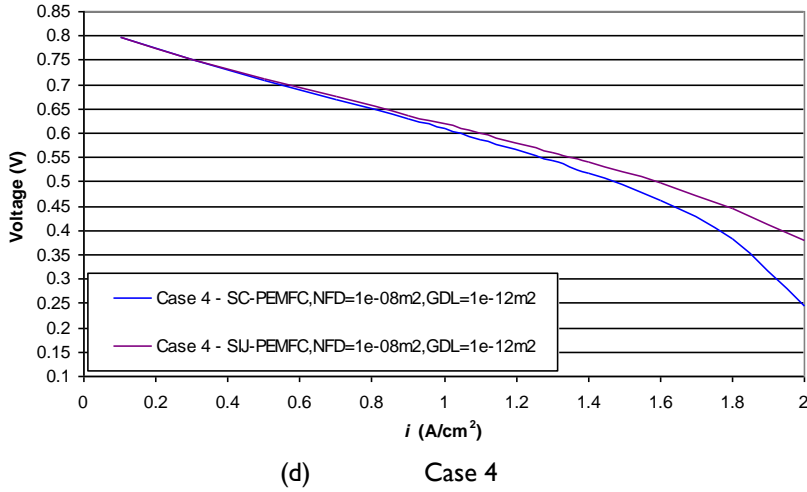


Figure 32: Polarization curve comparison between SC-PEMFC and SIJ-PEMFC

From Figure 32(d), although using higher value of NFD permeability gives 54% enhanced performance for SIJ-PEMFC at  $2.0 \text{ A}/\text{cm}^2$ , it is still regarded as a poor choice as flow reversal from GDL to the porous gas channel can happen and counteract the  $\text{O}_2$  distribution. A detailed explanation will be given in the later section.

It is noteworthy to mention that the simulation result at the current density of  $2\text{A}/\text{cm}^2$  is physically justifiable. Experimental data from Gerteisen et al (2008) and Ferng et al (2007) has confirmed that using a perforated GDL and single serpentine channel can yield current density up to  $1.8\text{A}/\text{cm}^2$  and  $2.5\text{A}/\text{cm}^2$ , respectively.

Figure 33 and 34 compares  $\text{O}_2$  concentration and water content profiles, respectively, along the cathode GDL/catalyst at  $2 \text{ A}/\text{cm}^2$  for the four different cases of SIJ-PEMFC.

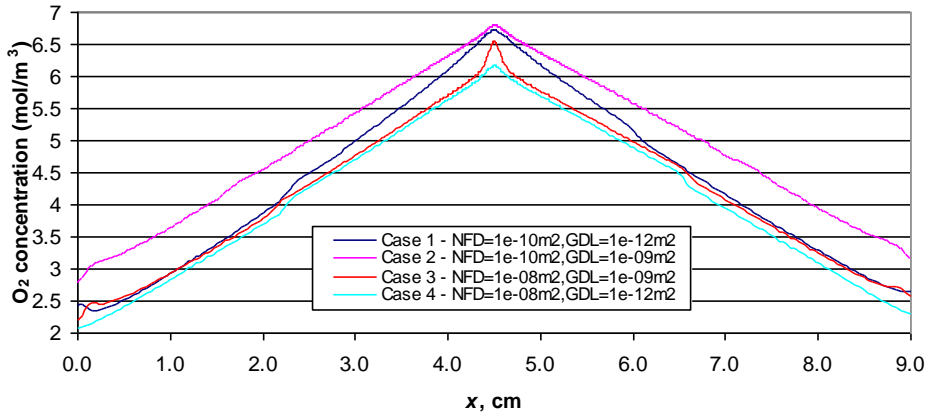


Figure 33: Comparison of  $\text{O}_2$  profile for SIJ-PEMFC, at  $2 \text{ A}/\text{cm}^2$

From Figure 33, it is found that Case 2 yields the highest  $\text{O}_2$  profile along the GDL/catalyst. However, this combination of NFD ( $1\text{e}-10\text{m}^2$ ) and GDL ( $1\text{e}-09\text{m}^2$ ) permeability values does not produce the highest voltage but gives the lowest fuel cell performance. The reason being that: besides  $\text{O}_2$  content at the cathode, membrane water content constitutes another important factor to determine the fuel cell performance (c.f. Figure 34). In this circumstance, Case 2 gives the lowest water content value at the cathode catalyst/GDL. It can be seen from Figure 34 that Case 1 (NFD  $1\text{e}-10\text{m}^2$  and GDL  $1\text{e}-12\text{m}^2$ ) has the capability to maintain water content within the vicinity of the impingement region higher than the Case 2 (NFD  $1\text{e}-10\text{m}^2$  and GDL  $1\text{e}-09\text{m}^2$ ). This is because the  $\text{O}_2$  reactant bypasses the porous gas channel (c.f. Figure 5.9, will be explained later) in Case 2, and flows predominantly along the GDL layer. This constitutes the lower water content along the GDL layer, as the inlet carries zero membrane water content.

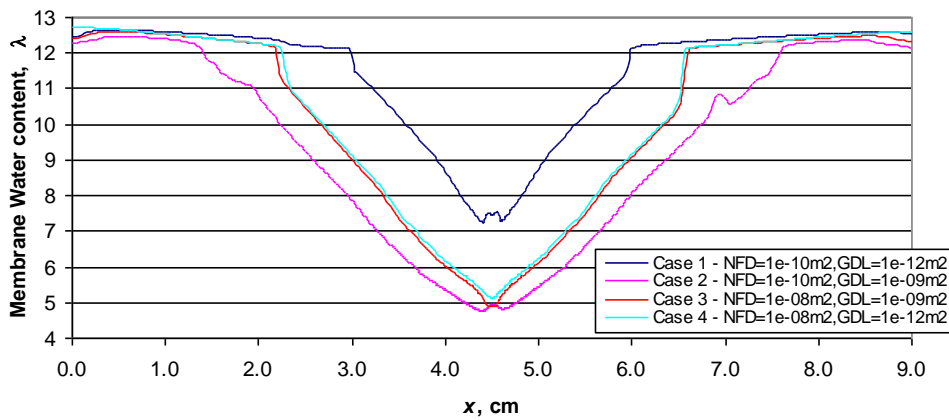


Figure 34: Comparison of water content profile for SIJ-PEMFC, at  $2 \text{ A}/\text{cm}^2$

Figure 35 compares the local current density variation along the anode bipolar plate for the four different cases of SIJ-PEMFC. The voltage result is also included in the legend for clarity.

It is well understood that for the impinging jet case, the stagnation point has the highest mass transfer rate and hence  $\text{O}_2$  concentration is maximum at that impingement point (c.f. Figure 33). However, this is not replicated in the current density output, as Figure 35 shows the minimum current density otherwise. This implies that  $\text{O}_2$  concentration profile cannot be used as the sole criterion to gauge fuel cell performance. Other factors such as water management (membrane water content profile (c.f. Figure 34) also affects the membrane proton conductivity and determines the fuel cell performance.

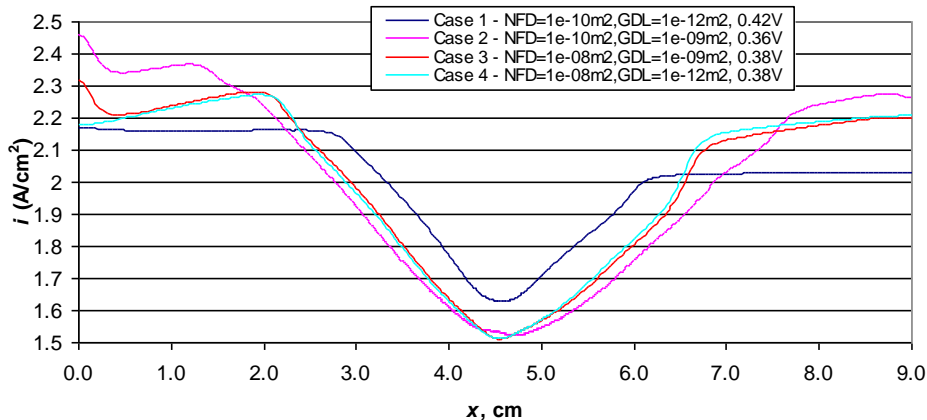


Figure 35: Comparison of local current density profile for SIJ-PEMFC, at  $2 \text{ A}/\text{cm}^2$

From Figure 35, it is also observed that the local minimum current density for Case 2 and 3 with a macro-porous GDL of  $1\text{e}-09 \text{ m}^2$  is larger compared to Case 1 with a normal GDL of  $1\text{e}-12 \text{ m}^2$ . This implies that the localized area affected by the jet penetration is larger for macro porous GDL, as the depression of local minimum helps broaden the bandwidth of current density spread, making the effective coverage area larger. Further, the macro-porous GDL also allows more water vapor to diffuse out of the catalyst layer, hence reducing the liquid saturation factor. Simulation results show that for the impinging jet case, when the GDL permeability is increased from  $1\text{e}-12$  to  $1\text{e}-09 \text{ m}^2$ , the liquid saturation factor is reduced from 13.3% to 11.4%.

Table 16 summarizes the average water content,  $\text{O}_2$  concentration and resultant voltage for various combinations of GDL and net permeability values at  $2 \text{ A}/\text{cm}^2$ . From Table 5.2, Case 1 (GDL  $1\text{e}-12 \text{ m}^2$  and NFD  $1\text{e}-10 \text{ m}^2$ ) gives the highest

water content (10.54). Although the O<sub>2</sub> content is the second highest (5.03 mol/m<sup>3</sup>) among all, it can still give the best fuel cell performance. Conversely, even though Case 2 (GDL 1e-09m<sup>2</sup> and net 1e-10m<sup>2</sup>) gives the highest oxygen content (5.43 mol/m<sup>3</sup>), the water content is the lowest (8.02) and hence the fuel cell performance is still the worst case among all.

Table 16: Average water content, O<sub>2</sub> concentration and resultant voltage for different combination of NFD and GDL permeability values, at 2A/cm<sup>2</sup>

Case	1	2	3	4
NFD permeability (m <sup>2</sup> )	1e-10	1e-10	1e-08	1e-08
GDL permeability (m <sup>2</sup> )	1e-12	1e-09	1e-09	1e-12
Average membrane water content along cathode GDL/catalyst	10.54	8.02	8.78	8.90
Average O <sub>2</sub> concentration along cathode GDL/catalyst (mol/m <sup>3</sup> )	5.03	5.43	4.81	4.69
Voltage	0.421	0.357	0.379	0.379

In general, impinging jet design coupled with the porous gas channel in PEMFC necessitates optimal combination between GDL and NFD permeability values for enhanced fuel cell performance. As a rule of thumb, the impinging jet design is suited for PEMFC only with a highly permeable GDL (e.g. 1e-09 m<sup>2</sup>).

#### 4.2.1.2 Results for Net Flow Distributor permeability 1e-10m<sup>2</sup> (Case 1 and 2)

Figure 36 compares the velocity flow field in the cathode GDL between SC-PEMFC and SIJ-PEMFC for GDL permeability of 1e-12 m<sup>2</sup> (Case 1). This figure shows that a low permeability GDL practically behaves like an “impermeable solid wall” to the jet flow, as the reactant in the cathode GDL beneath SIJ-PEMFC flows mainly along a stream-wise direction, and at a velocity lower than that in the SC-PEMFC.

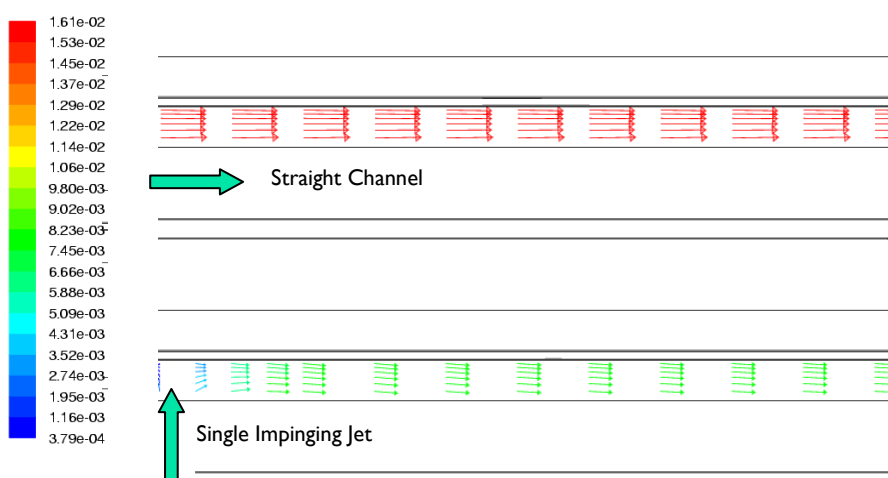


Figure 36: Comparison of flow field in cathode GDL between SC-PEMFC and SIJ-PEMFC for Case 1, at  $i = 1.1\text{A}/\text{cm}^2$

Figure 37 confirmed that a lower velocity value is obtained throughout the cathode GDL for the SIJ-PEMFC, as compared to the SC-PEMFC. Even at the centerline of the impinging jet ( $x = 4.5\text{cm}$ ), the flow is restricted by the low GDL permeability ( $1\text{e-12m}^2$ ), causing a sharp drop in the local velocity. This nullifies the jet momentum and inhibits intimate contact between the reactant gas and the catalyst. The low GDL permeability value is the reason for the identical global

current density between SC-PEMFC and SIJ-PEMFC. No advantage is gained by using a more complex design for the PEMFC.

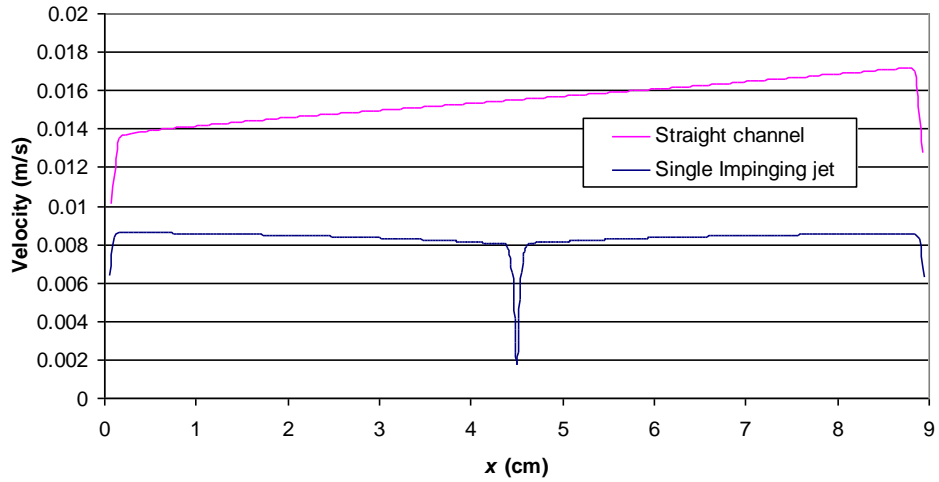


Figure 37: Comparison of velocity profiles along cathode GDL centerline between SC-PEMFC and SIJ-PEMFC for Case I, at  $i = 1.1\text{A}/\text{cm}^2$

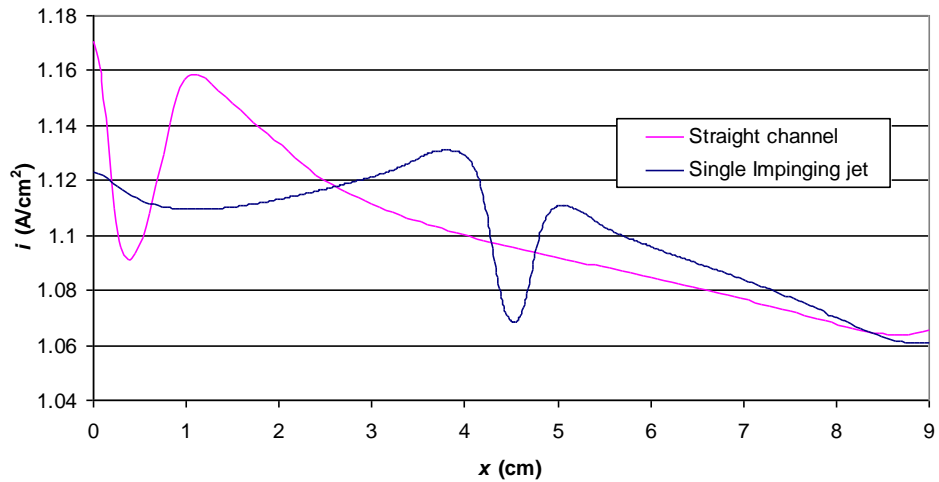


Figure 38: Comparison of local current density between SC-PEMFC and SIJ-PEMFC for Case I, at  $i = 1.1\text{A}/\text{cm}^2$

Although the global values for both SC-PEMFC and SIJ-PEMFC are almost identical (c.f. Figure 32(a)), a detailed investigation of the local current density maps shows a substantial variation for these two cases (c.f. Fig. 38). For the SC-PEMFC, the local current density drops abruptly in the entrance region, but immediately increases to a local maximum at about 1cm downstream. Subsequently, the current density decreases monotonically along the stream-wise direction. This is mainly caused by high liquid water saturation. Low NFD permeability ( $1\text{e}-10 \text{ m}^2$ ) tends to hinder the main flow as it enters the flow channel. This deflects the humidified air towards the catalyst layer and subsequently causing excess liquid water saturation factor near the channel entrance. As for the SIJ-PEMFC, the current density directly below the impinging jet is at a minimum, and then increases to a local maximum at the two sides of the impinging jet (as explained earlier in Figure 35). The side adjacent to the upstream anode flow has a higher value compared to the downstream anode flow. It can be deduced that the local minimum current density for SC-PEMFC is attributed to possible flooding effect at the entrance, while the local minimum current density for SIJ-PEMFC is caused by initial membrane dehumidification at the central channel.

Figure 39 shows the flow distribution in the cathode GDL and porous gas channel beneath the impinging jet for Cases 1 and 2.

In Case 2, the impinging jet can penetrate into the GDL layer. For this macro porous GDL of  $1e-09\text{m}^2$ , the flow actually bypasses the porous gas channel and gets through the GDL. This provides better contact with the catalyst layer, as the flow velocity is higher in the GDL. It also allows a higher  $\text{O}_2$  concentration profile to be attained (c.f. Figure 40). It shows that in Case 1, the  $\text{O}_2$  mass fraction is immediately reduced when approaching the GDL layer under the impinging jet. However, in Case 2, the original oxygen content from the impinging jet can be delivered to the catalyst site at the impingement point, with minimum concentration drop across the GDL layer.

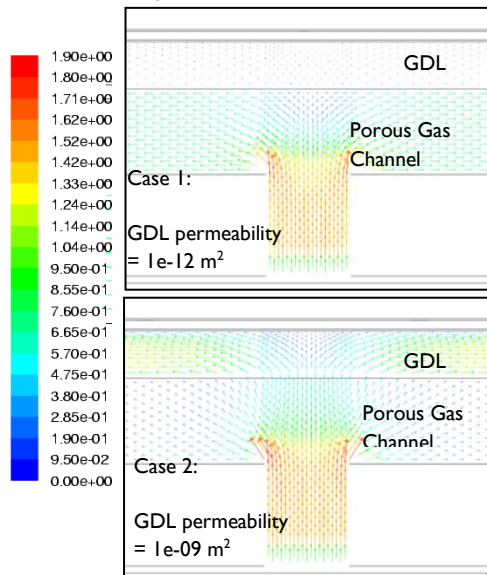


Figure 39: Comparison of flow field in cathode GDL and porous gas channel between Case 1 and Case 2

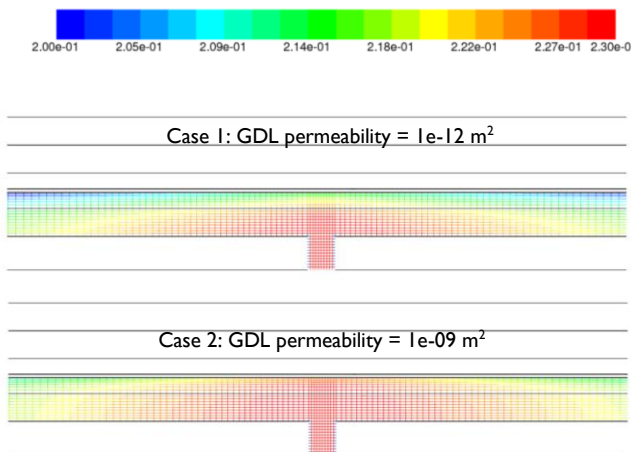


Figure 40: Comparison of  $\text{O}_2$  mass fraction distribution between Case 1 and Case 2

In Case 2, the macro-porous GDL with permeability of  $1e-09\text{ m}^2$  is higher than the NFD permeability of  $1e-10\text{m}^2$ . Therefore, the flow at the GDL is higher than that at NFD (c.f. Figure 41). The reactant gas bypasses the NFD and flows along the GDL. This negates the original function of NFD as fluid delivery channel because it can neither carry nor direct the bulk of reactant fluid flow. Further, pressure drop is reduced when GDL permeability is increased to  $1e-09\text{m}^2$ , and according to Nernst equation, the performance is dropping. Therefore, the Case 2 permeability combination of NFD and GDL is undesirable.

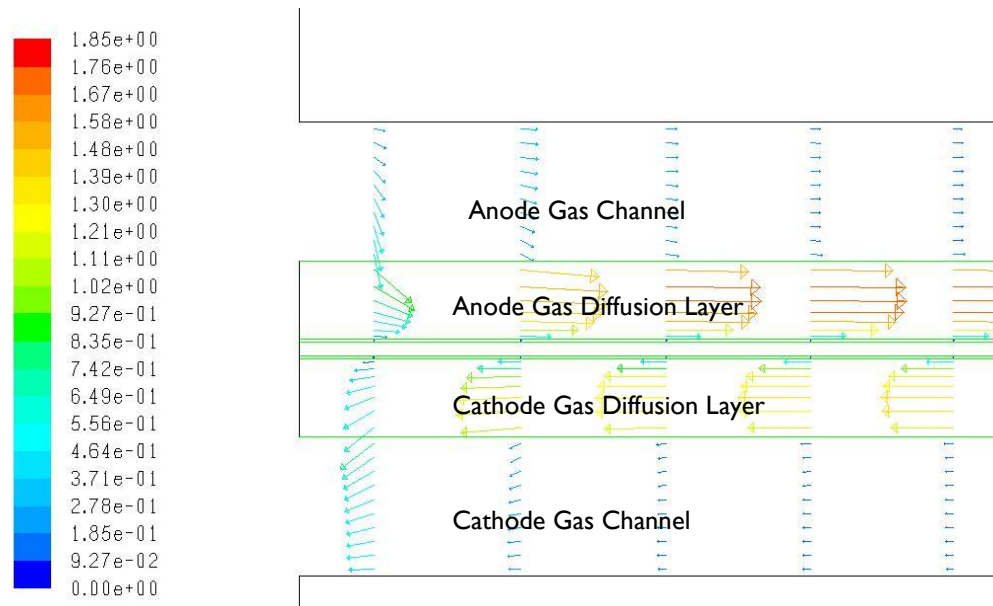


Figure 41: Pre-dominant flow at cathode/anode GDL in Case 2

#### 4.2.1.3 Results for net flow distributor permeability $1e-08\text{m}^2$ (Case 3 and 4)

Previous Case 2 results show that the bulk fluid flow along the macro porous GDL has nullified the porous gas channel function. In order to make the NFD perform effectively as the flow distributor in PEMFC, its permeability is increased to  $1e08\text{ m}^2$  (Jeng and Tzeng, 2005) when used together with a macro-porous GDL permeability of  $1e-09\text{m}^2$  (Case 3).

Figure 42 shows the flow distribution in the cathode GDL beneath the impinging jet for Case 3 and Case 4. The fluid velocity in the GDL within the vicinity of the jet impingement zone is negligible when the permeability is  $1e-12\text{ m}^2$ , whereas the flow for GDL permeability of  $1e-09\text{ m}^2$  shows significant penetration of the jet fluid at a velocity of about 0.3 m/s at the interface between gas channel and GDL.

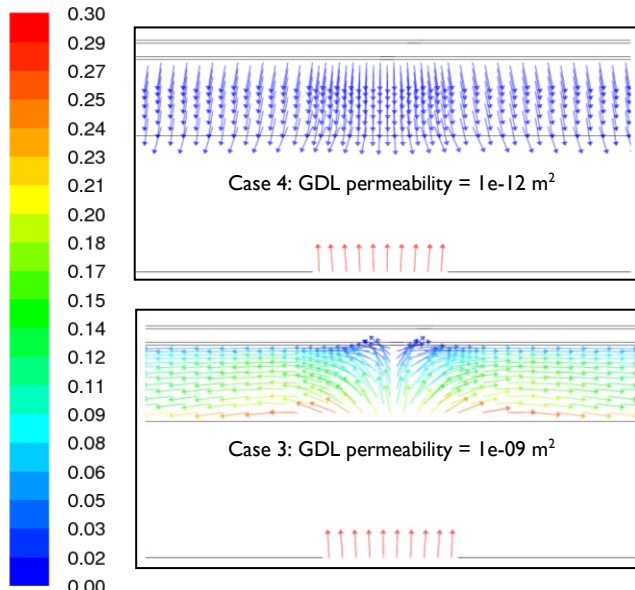


Figure 42: Comparison of flow field in cathode GDL between Case 3 and Case 4

The flow reversal for GDL permeability  $1e-12 \text{ m}^2$  can be explained from the pressure contours and centerline profiles, depicted in Figures 43 and 44, respectively.

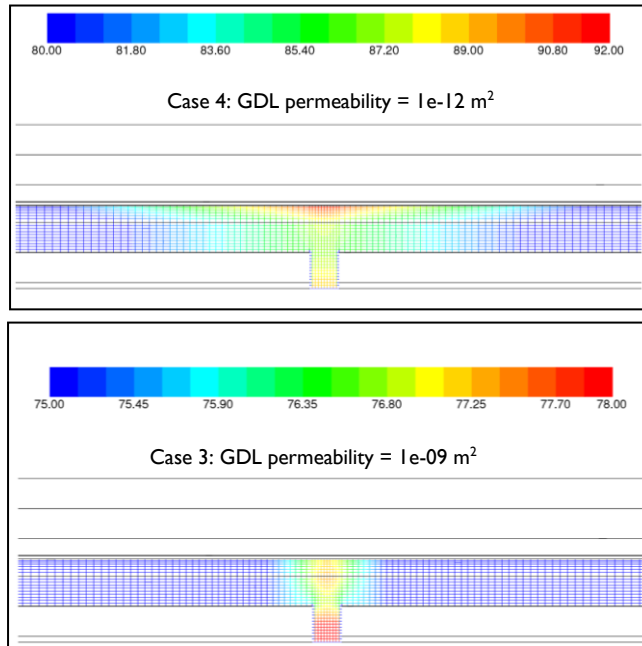


Figure 43: Comparison of pressure field in cathode GDL and gas channel for two values of GDL permeability, with NFD permeability of  $1e-08 \text{ m}^2$

Figure 43 show that when the normal GDL permeability (Case 4) is used with impinging jet design, it results in higher stagnation pressure at the end of the porous GDL. This explains the flow reversal away from catalyst layer and it is detrimental to the fuel delivery process. Conversely, when macro-porous GDL permeability of  $1e-09 \text{ m}^2$  is used (Case 3), it displaces the high stagnation pressure towards the interface between GDL and gas channel. This will be favorable in distributing reactants towards the catalyst layer.

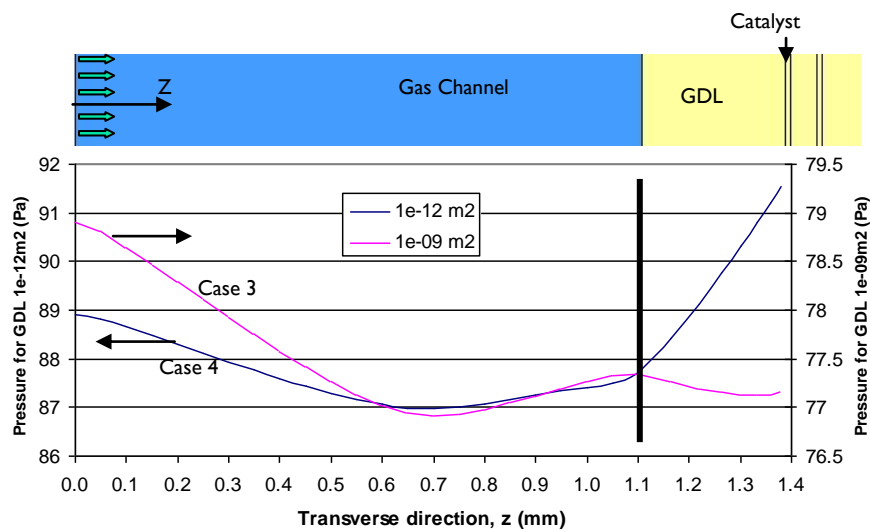


Figure 44: Comparison of pressure profile along jet impingement centerline in gas channel and GDL between Case 3 and Case 4

Figure 44 shows that the pressure profile in the GDL increases nearly linearly from channel/GDL to GDL/catalyst for Case 4, whereas Case 3 exhibits local maximum pressure at channel/GDL and a subsequent pressure drop towards the catalyst layer.

Figure 45 compares the oxygen concentration at the catalyst layer in the vicinity of the impingement zone. It is apparent that in the impinging jet design, a lower GDL permeability results in higher O<sub>2</sub> concentration.

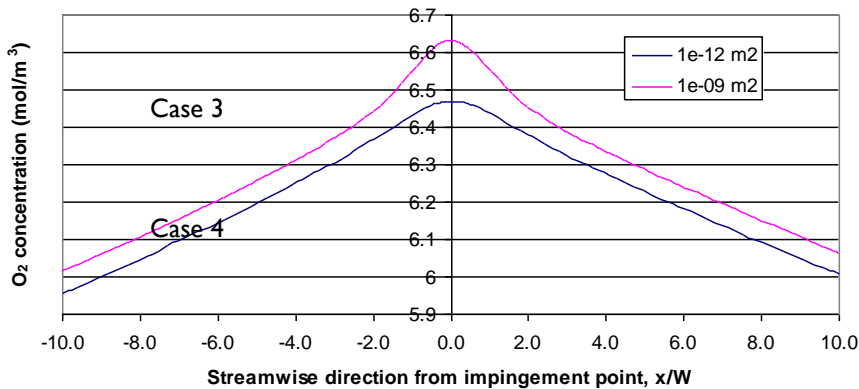


Figure 45: Comparison of O<sub>2</sub> concentration along cathode GDL between Case 3 and Case 4

The effect of GDL and NFD permeability for SJJ-PEMFC design is summarized below:

- 1 For GDL 1e-12m<sup>2</sup> and NFD 1e-10m<sup>2</sup> permeability values, while it yields the highest fuel cell performance within the impinging jet cases, it gives no improvement as compared to the straight channel case. Moreover, pressure drop for this case is the highest and thus consumes the largest pumping cost.
- 2 For GDL 1e-09m<sup>2</sup> and NFD 1e-10m<sup>2</sup> permeability values, the flow bypasses the net flow distributor. Flow predominantly occurs along the GDL layer and hence negates the functionality of net flow distributor. It yields the largest O<sub>2</sub> concentration, but also has lowest water content at the catalyst layer. Therefore, the fuel cell performance is considered one of the worst among impinging jet cases (albeit an improvement over the corresponding straight channel case, approximately 160%).
- 3 For GDL 1e-12m<sup>2</sup> and NFD 1e-08m<sup>2</sup> permeability values, an unusual flow reversal away from catalyst layer within impingement region is observed. This makes GDL impermeable to the impinging jet penetration. It also reduces O<sub>2</sub> concentration to the lowest value among impinging jet cases and is unfavorable to the reactant delivery system (though improvement over corresponding straight channel case is about 54%).
- 4 For GDL 1e-09m<sup>2</sup> and NFD 1e-08m<sup>2</sup> permeability values, it allows the jet penetration towards the catalyst layer with a minimum pressure drop. Yet, it is able to maintain water content from the direct dehumidification effect by impinging jet. It is considered the optimum combination among the four cases and produces 84% improvement over the straight channel case. Therefore, this value would be used in the subsequent simulations to carry out the parametric studies for single and multiple impinging jets.

### 4.3 Enhanced Performance for Self Air-Breathing Fuel Cell

#### 4.2.2 2D CFCD Simulation

A two-dimensional time-dependent CFCD analysis was carried out for the channel ABFC, with conditioned air (60°C and 100%RH) in the surrounding environment at the cathode and operating at ambient pressure (1 Atm).

##### 4.2.2.1 Geometry and Computational Model

Figure 46 describes the three different cases of geometry parameters variation (length and width of cathode channel) and Figure 47 shows grid resolution for the 2D simulation model. Flow along x-z direction is referred to stream-wise and transverse direction, respectively. The number of computational grids used is about 70,000 cells. Table 17 summarizes the various dimensions used for the parametric study.

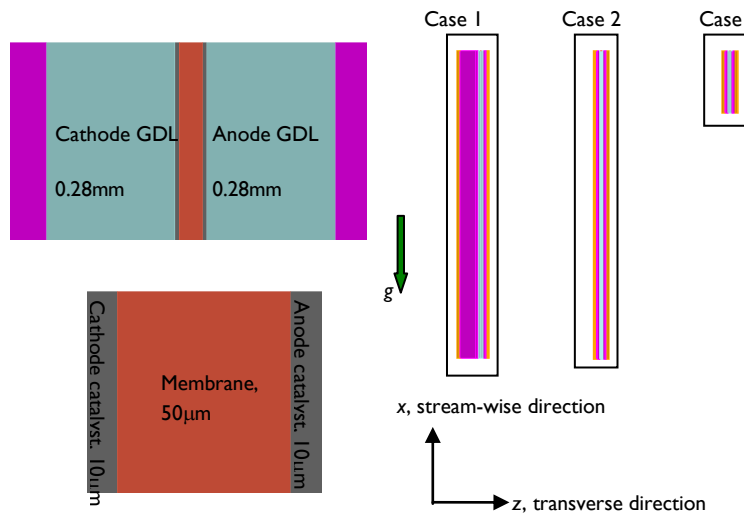


Figure 46: Geometry description of 2D simulation model

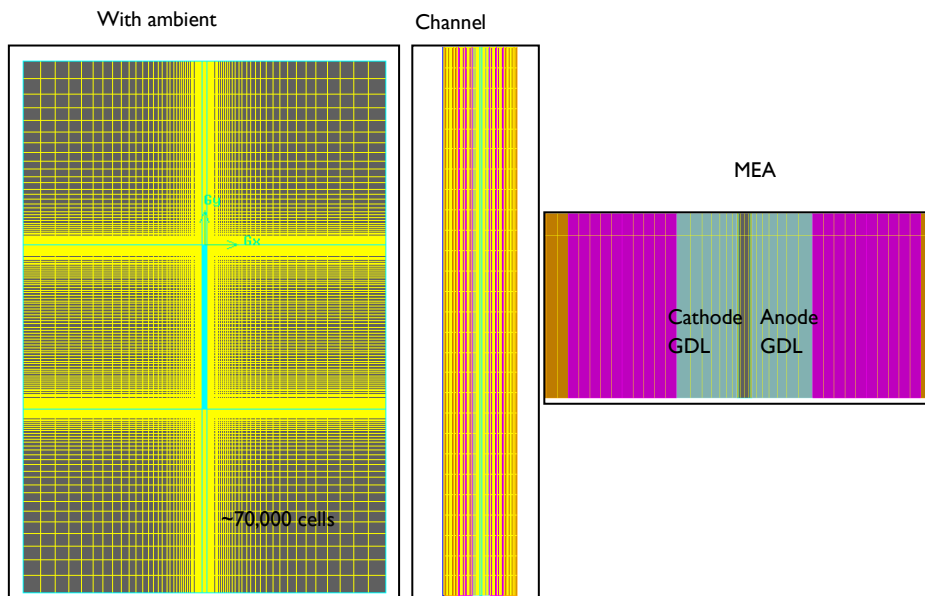


Figure 47: Grid resolution of 2D simulation model

Table 17: Cathode gas channel dimension used in 2D simulation model

Case	Cathode Gas channel dimension
1	5cm x 3.0mm
2	5cm x 0.5mm
3	1cm x 0.5mm

#### 4.2.2.2 Results and Discussion - Global and Local Results

This section presents the global current density and local results of flow, species ( $O_2$ ,  $H_2$ ,  $H_2O$ ) concentration and temperature distribution for Case 1 configuration (5cm length x 3mm height), which is also the geometry used in the experimental setup from Wang et al (2005). Figure 48 shows the 2D simulation result of the global polarization curve and power density result. These results show that maximum power density ( $P_{max}$ ) of  $94 \text{ mW/cm}^2$  is obtained at  $i = 0.24 \text{ A/cm}^2$ . This is consistent with the experimental findings from Wang et al (2005), which produced  $P_{max}$  of  $74 \text{ mW/cm}^2$  at current

density  $0.2 \text{ A/cm}^2$ . The simulation model used an operating temperature of  $60^\circ\text{C}$ , while experimental data from Wang et al (2005) used an ambient temperature of  $33^\circ\text{C}$  (refer to the validation model). Therefore, a higher result is obtained from the modeling data. Nevertheless, reasonable qualitative comparison can be derived from this model in comparison with experimental data.

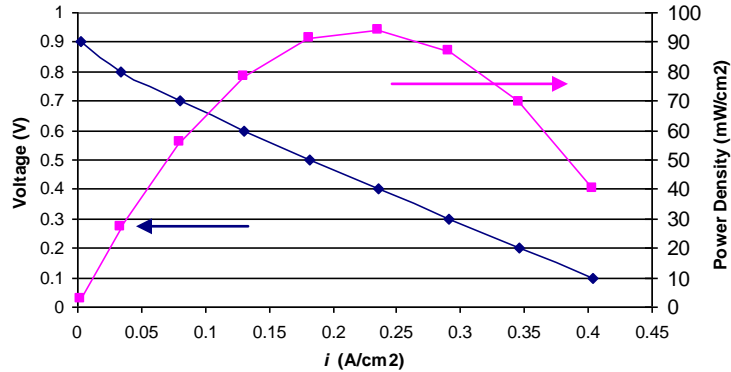


Figure 48: Polarization curve and power density of the 2D simulation result

In terms of the velocity profile across the gas channel, Figure 49 shows that this 2D ABFC simulation predicts an average flow velocity of about  $32 \text{ cm/s}$  within the cathode gas channel. This is much higher than the experimental measurement from Fabian et al (2006) as their measurement for average free convection air speed was  $11.2 \text{ cm/s}$  in vertical cell orientations. This can be explained by the nature of 2D simulation here which excludes the span-wise wall shear effect, whereas the actual experimental setup is 3D and is thus subjected to higher wall shear stress.

The flow direction in cathode channel ABFC is predominantly unidirectional. It enters from the bottom channel and exits through the top channel, flowing against the  $g$  direction. This prediction also makes amendments to the widespread incorrect assumption that the flow in the vertical ABFC is supposedly flowing into the cathode gas channel through both the top and bottom openings. Indeed, it will be shown later that this flow phenomenon strongly depends on the geometric factors. Figure 49 also reveals that a parabolic velocity profile is established in the downstream fully developed flow region. In this scenario, very fine grid (at least 20 cells along transverse direction in the cathode gas channel) is necessary in order to capture this detailed velocity profile.

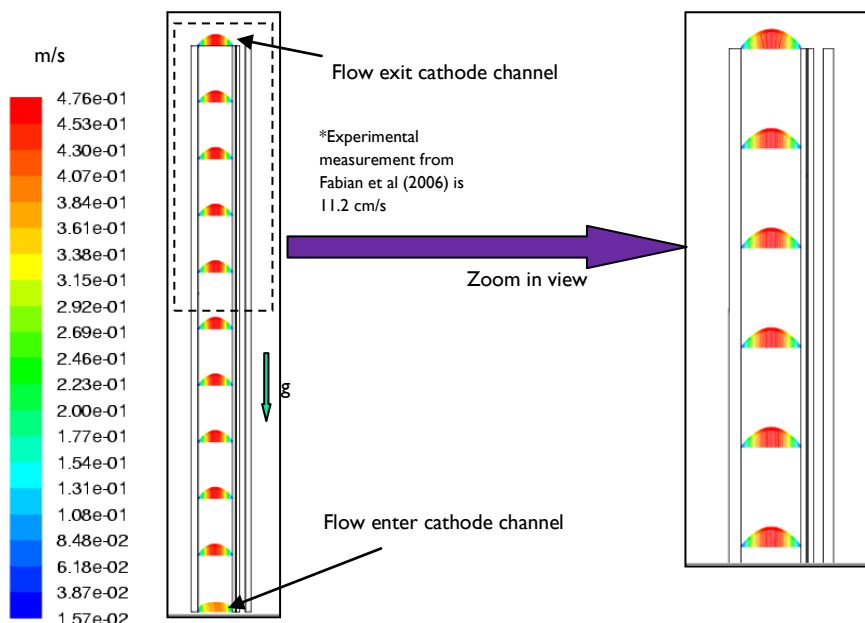


Figure 49: Velocity profile across cathode gas channel at  $i = 0.24 \text{ A}/\text{cm}^2$

The centerline velocity along the stream-wise direction of cathode gas channel in Figure 50 shows that the entrance flow developing region in the cathode gas channel is about 1 cm from the bottom opening. Further downstream, the centerline velocity achieves a constant profile of about 0.46 m/s. For mass transport enhancement, it is important to reduce this flow entrance region; as opposed to the heat transfer improvement to extend the flow developing region. This is because this flow entrance phenomena has a lower mass transport coefficient (by virtue of its smaller velocity), and it is therefore unfavorable to reactant transport and fuel cell performance. As shown later, this entrance region would result in a larger O<sub>2</sub> concentration loss.

Besides, it is also noted that the flow velocity at the cathode gas channel is gaining its strength along flow direction. This is due to water transport across the membrane from anode to cathode, attributed to the electro-osmotic drag (EOD) and the adding of extra water vapor mass to the cathode gas channel. As the mass flow rate in the cathode gas channel is increased due to water migration from the anode side, so is the flow velocity. In return, the flow velocity along anode gas channel is reduced along the stream-wise flow direction (c.f. Figure 51).

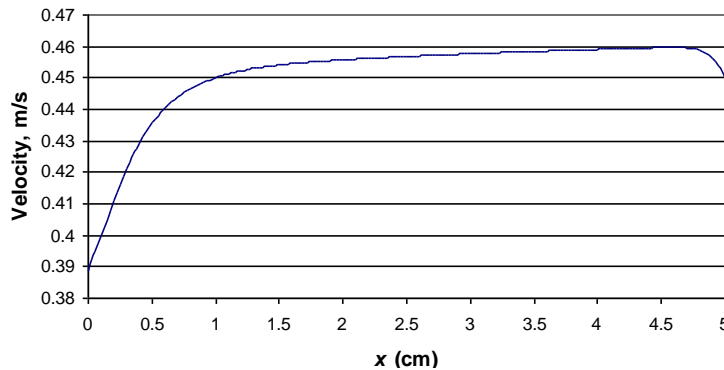


Figure 50: Centerline velocity along cathode gas channel

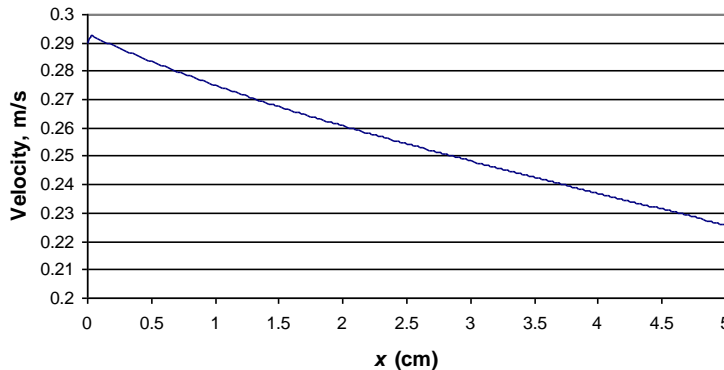


Figure 51: Centerline velocity along anode gas channel

Figures 52 (a) and (b) show the O<sub>2</sub> concentration distribution and profile at the cathode gas channel, GDL and catalyst layer. As can be seen, the O<sub>2</sub> concentration is decreasing exponentially near to the entrance regime (about 1 cm from bottom opening), compared to linear drop at downstream region. This high O<sub>2</sub> depreciation region also corresponds to the flow entrance regime (c.f. Figure 50), and is mainly associated with the lower airflow velocity and mass transport coefficient as compared to the downstream developed region.

The H<sub>2</sub> concentration distribution and profile in the anode gas channel, GDL and catalyst layer in Figure 53 shows that H<sub>2</sub> concentration actually increases along flow direction. This is due to the EOD that transports water from anode to cathode, causing a corresponding increase in the H<sub>2</sub> mole fraction. A similar finding has also been reported by Schwarz and Djilali (2007).

In this simulation, it is found that 1.2e-05 kg/s of water vapor is transported from the anode to the cathode by EOD, while opposing back diffusion transports only a negligible amount of 1.5e-17 kg/s of water vapor from the cathode to the

anode. Therefore, the resultant movement of water vapor across the membrane is mainly due to EOD. The relative humidity distribution in the cathode and anode gas channels in Figure 54 further explains the superiority of EOD source over back-diffusion in terms of water transport across the membrane. Both anode inlet ( $H_2 + H_2O$ ) and cathode channel inflow ( $O_2 + H_2O + N_2$ ) have a RH of 100%. However, at the anode outlet, RH is reduced to 54%, while at the cathode channel outflow, RH is increased and air becomes fully-saturated. This implies that water vapor concentration is reduced along the anode channel, but increased along the cathode channel. This phenomenon is attributed to the net effect of EOD (when protons are transferred across membrane,  $\alpha$ ) over back-diffusion (water is back diffused from cathode to anode due to water content gradient,  $J_w^{diff}$ ) which effectively migrates water vapor from the anode to the cathode. This can potentially cause anode membrane dehydration.

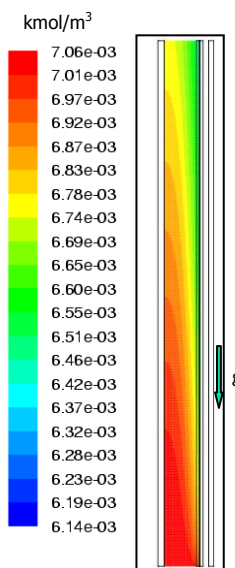


Figure 52(a)  $O_2$  concentration distribution in the cathode channel, GDL and catalyst

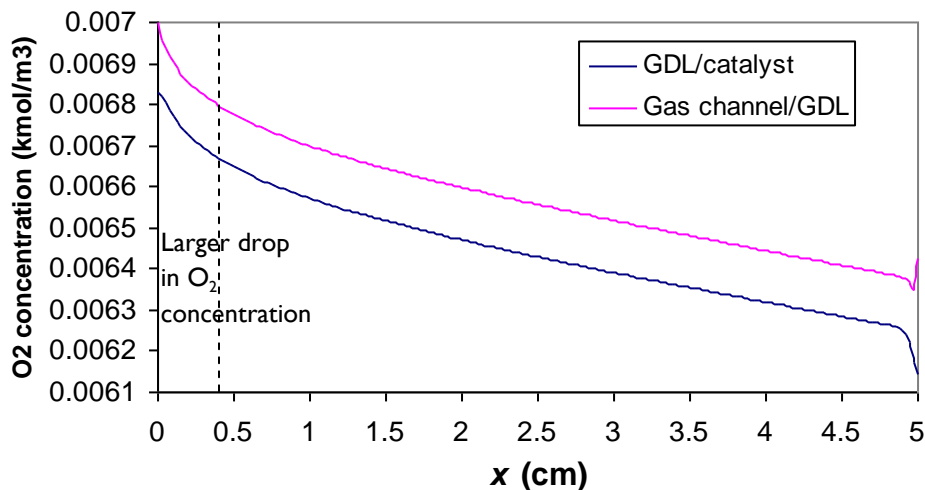


Figure 52(b): Computed  $O_2$  concentration profiles along cathode GDL

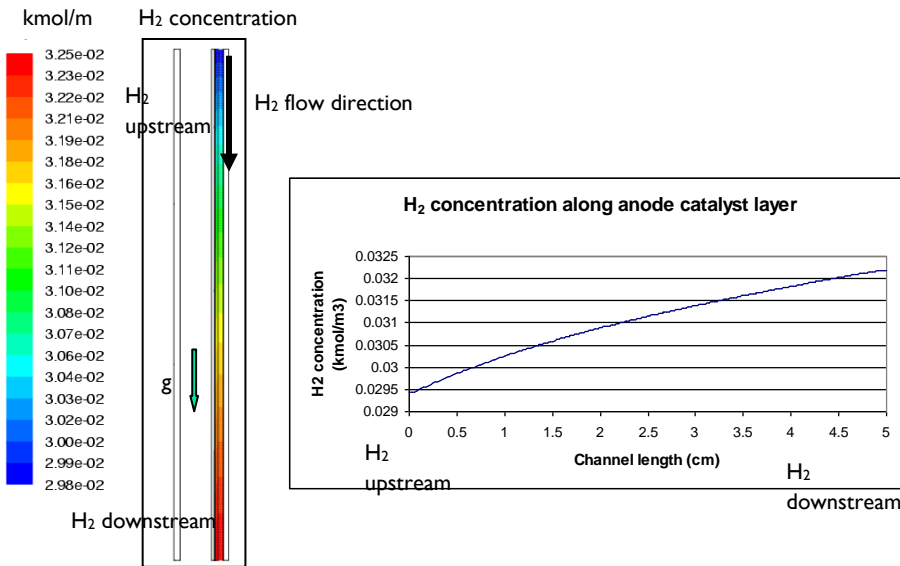
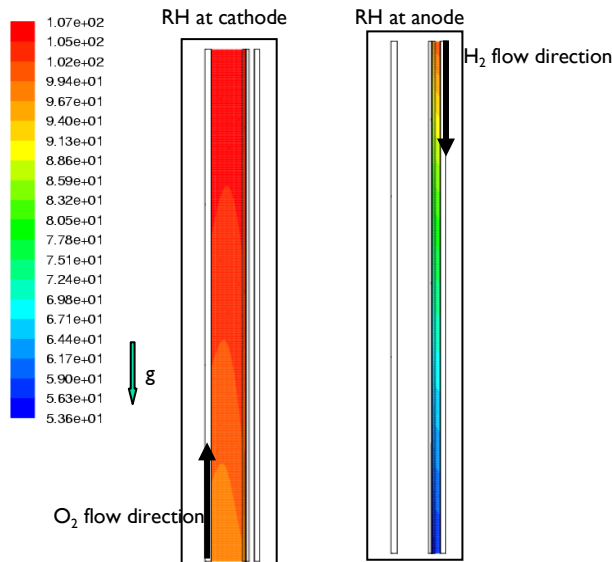
Figure 53:  $H_2$  concentration distribution and profile at anode channel, GDL and catalyst

Figure 54: RH distribution in cathode and anode gas channel

Table 18 shows mass balance for both the anode and cathode gas channels, including the various source terms such as EOD ( $\alpha M_{H_2O} \eta$ ), back-diffusion ( $J_w^{diff} M_{H_2O} \eta$ ) and phase change ( $r_w$ ) which internally transfers or produces or consumes mass flow rate within the ABFC model. From Table 6.14, it can be seen that the total mass flow rate is conserved for both the anode and cathode channels, within 5% of uncertainty. For the anode channel, the outlet flow rate is reduced by about 48% compared to that at the inlet, as this reduction is transferred by EOD to the cathode channel. For cathode channel, the outflow is 1% higher flow rate compared to inflow. This amount is offset by the net effect of mass increase due to EOD water transferred from the anode and the mass reduction due to liquid water condensation. The back-diffusion contribution to the overall mass balance is negligible, as the simulation result shows that the membrane water content diffusivity ( $D_l = 2.3e-8 \text{ l/s}$ ) is insignificant as compared to the osmotic drag coefficient ( $\lambda = 1.53$ ).

Table 18: Mass Balance of ABFC model

Anode	Inlet	Outlet	$\alpha M_{H_2O} \eta$	$J_w^{diff} M_{H_2O} \eta$	$r_w$	Total in	Total out
Mass in (kg/s)	2.80e-5	-	-	1.5e-17	-	2.80e-5	
Mass out (kg/s)	-	-1.47e-5	-1.20e-5	-	-		-2.67e-5
Cathode	Inflow	Outflow	$\alpha M_{H_2O} \eta$	$J_w^{diff} M_{H_2O} \eta$	$r_w$	Total in	Total out
Mass in (kg/s)	9.31e-4		0.12e-4			9.43e-4	
Mass out (kg/s)		-9.39e-4		-1.5e-17	-0.05e-4		-9.44e-4

The temperature increase along the stream-wise direction of the cathode catalyst layer is shown in Figure 55. The cathode catalyst layer is a hot spot as all the heat generated from enthalpy change, entropy irreversibility and latent heat of condensation occurs there. It is seen that a relatively uniform temperature difference can be maintained at the catalyst layer, only about a  $0.3^{\circ}\text{C}$  temperature increase. For this polarization point ( $i = 0.24 \text{ A/cm}^2$ ), the overall temperature increase is about  $2^{\circ}\text{C}$  when operating temperature is  $60^{\circ}\text{C}$ . It is smaller than the  $10^{\circ}\text{C}$  temperature difference when operating temperature is ambient  $33^{\circ}\text{C}$  (c.f. Figure 28(b) for validation case). This shows that elevating the operating temperature can help to maintain a more uniform temperature distribution within the MEA.

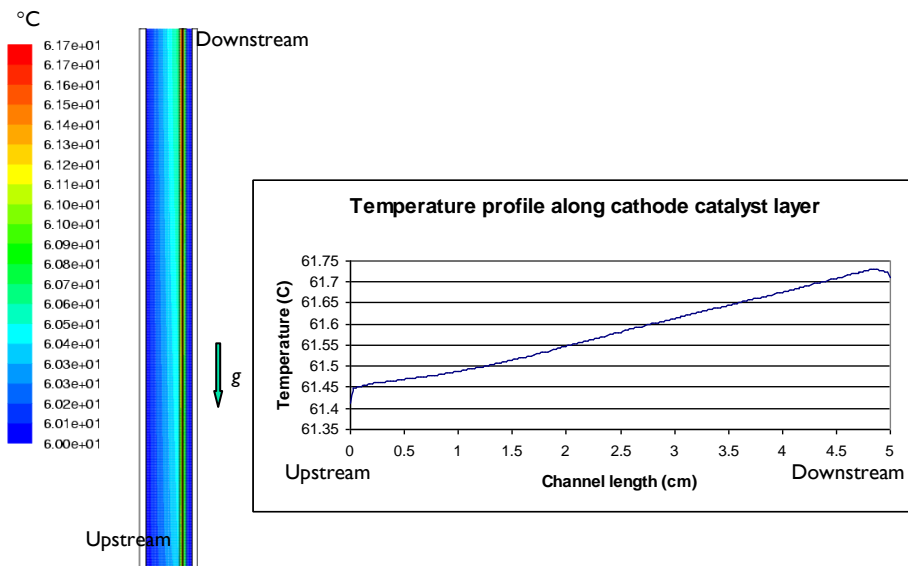


Figure 55: Calculated temperature distribution in ABFC

#### 4.2.2.3 Effect of Channel Height and Length

Figure 56 compares the polarization curve between two different channel heights (Case 1: 3mm and Case 2: 0.5mm) in the 2D ABFC simulations. The channel length is maintained at 5cm. As can be seen, reducing channel height from 3mm to 0.5mm greatly deteriorates fuel cell performance. The current density at 0.4V is reduced threefold, from  $0.24$  to  $0.08 \text{ A/cm}^2$ . This is attributed to  $\text{O}_2$  starvation, as reflected in Figure 57 of the  $\text{O}_2$  concentration distribution for cases 1 and 2. For case 1, the unidirectional convection flow (c.f. Figure 49) is able to supply sufficient  $\text{O}_2$  throughout the MEA region for the electrochemical reactant consumption. However, for case 2,  $\text{O}_2$  is only transported by the weak diffusion process

within the vicinity of the channel entrance and exit. This insufficient  $O_2$  mass transport results in most of the interior MEA region suffering from  $O_2$  depletion.

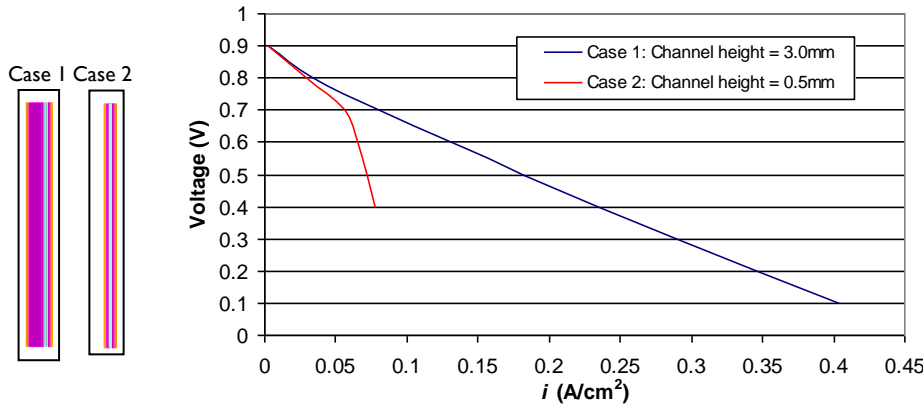


Figure 56: Comparison of polarization curves between two different ABFC channel heights

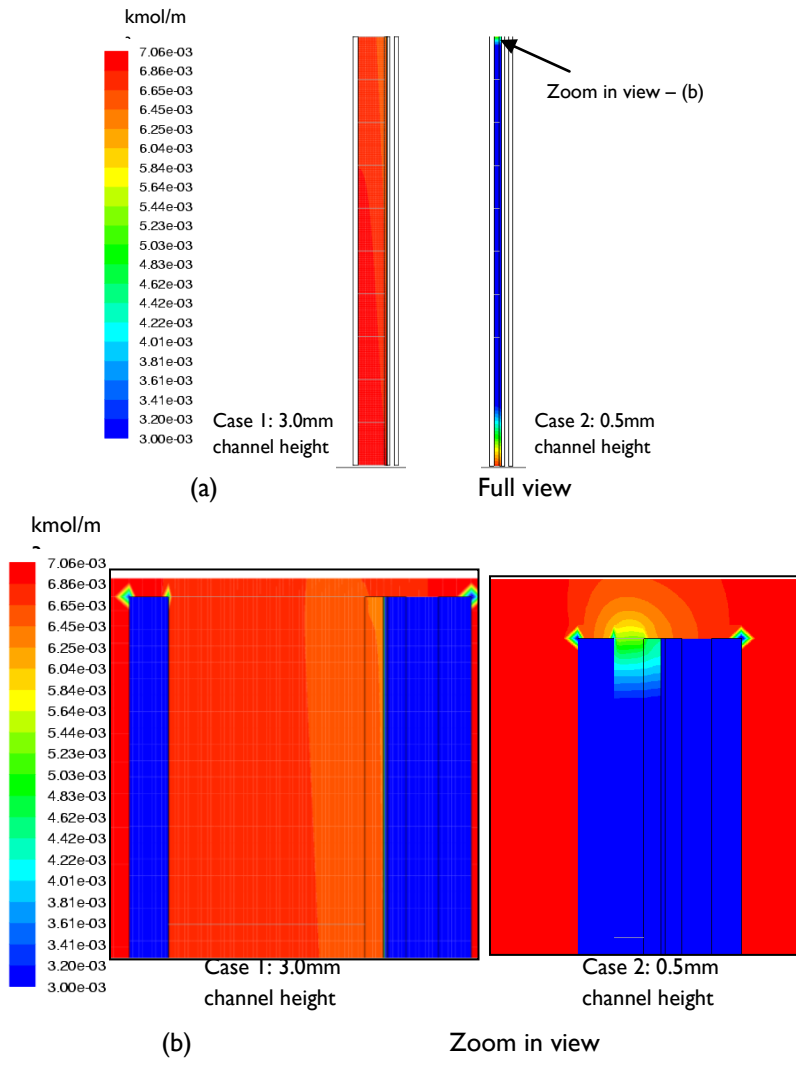


Figure 57: Comparison of  $O_2$  concentration between two different ABFC channel heights

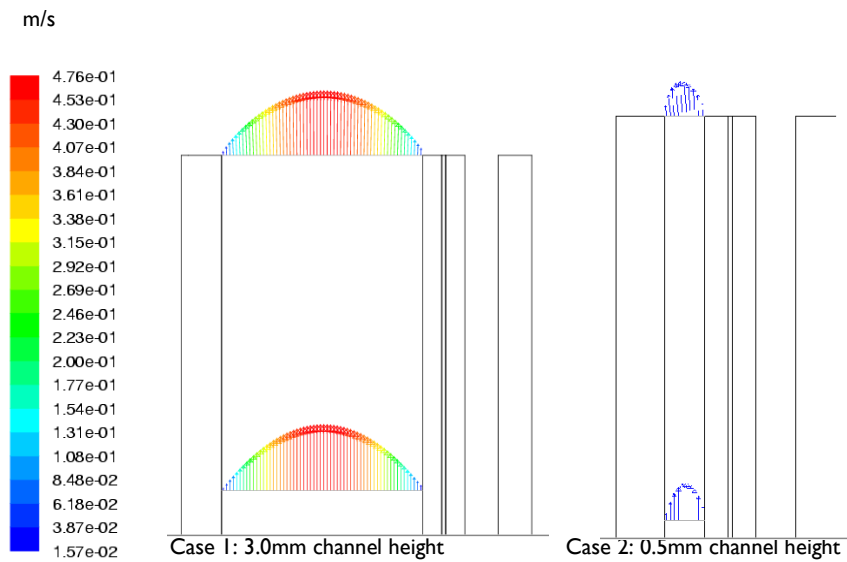


Figure 58: Comparison of cathode channel exit velocity between two different ABFC channel heights

Comparison of channel exit velocity in Figure 58 shows that the flow velocity in the cathode channel is reduced very significantly when channel height decreases from 3mm to 0.5mm. The average velocity for case 1 is 32cm/s, whereas for case 2, it is merely 1 cm/s.

It is also noteworthy to point out that although the exit flow velocity in case 2 is directed outwards away from the channel, the  $O_2$  concentration gradient (high value to low value) is formed in the opposite direction towards the channel (c.f. Figure 57(b)). This shows that in the event of geometry restriction, diffusion transport dominates over convection transport. Consequently, a concentration gradient is established based on the mass consumption process in the catalyst and forms a region with higher  $O_2$  at the ambient and lower  $O_2$  at the channel, even though the airflow is directed from the channel to ambient at the channel exit. This finding is important for the micro-ABFC design as the miniature geometry poses resistance to airflow along the channel. On the other hand, the electrochemical reaction can still generate sufficient concentration gradient to facilitate the mass transport process in the micro-device through diffusion transport.

Figure 59 compares the polarization performance at two different channel lengths (Case 2: 5cm and Case 3: 1cm) in the 2D simulations. The channel width is maintained at 0.5mm. Reducing channel length is seen to enhance fuel cell performance. This is again due to the obvious reason of increased  $O_2$  mass transport for a shorter channel.

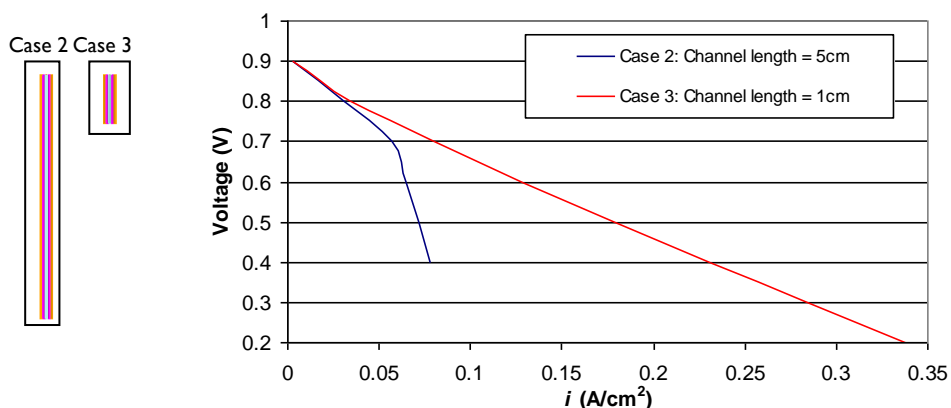


Figure 59: Comparison of polarization curves between two different ABFC channel lengths

#### 4.2.2.4 Effect of Device Orientations

Table 19 tabulates the case studies with three different device orientations. Figure 60 shows the relevant schematic layout.

Table 19: Three different device orientations for ABFC simulations

Case	Cathode Gas channel dimension	g direction
1	5cm x 3.0mm	90° w.r.t. horizontal
4	5cm x 3.0mm	45° w.r.t. horizontal
5	5cm x 3.0mm	horizontal

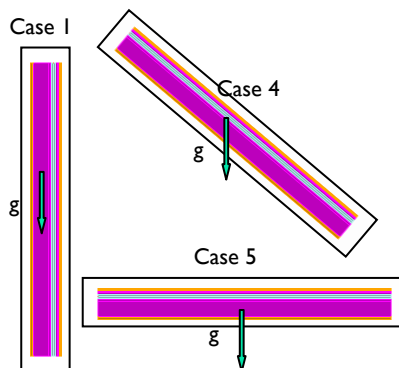


Figure 60: Schematic layout of three different device orientations for ABFC simulation

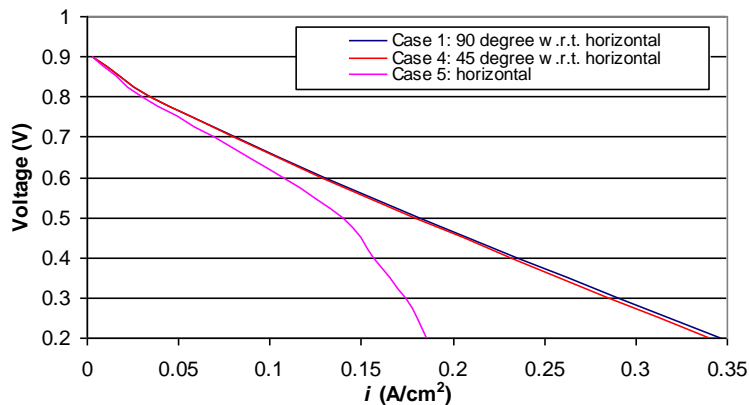


Figure 61: Comparison of polarization curves between three different ABFC device orientations

Figure 61 compares the polarization curve between three different device orientations (Case 1: 90°, Case 4: 45° and Case 5: 0°) in the 2D ABFC simulations. As compared to the vertical orientation in Case 1, only marginal performance deterioration is noted when orienting the ABFC at 45° in Case 4. However, when aligning the ABFC horizontally in Case 5, it drastically reduces the performance. This can be explained from the  $\text{O}_2$  concentration distribution in Figure 62 which shows that the  $\text{O}_2$  distribution is sufficient to sustain the electrochemical reaction throughout the MEA. The slight performance decrease in Case 4 is reflected by the relatively smaller amount of  $\text{O}_2$  presence in the cathode gas channel, especially in the exit region. However, aligning the ABFC in horizontal orientation completely depletes the central portion of MEA of  $\text{O}_2$ , thus limiting catalyst utilization to only the two channel ends. As such, performance is degraded.

In addition, Figure 63 shows that changing the ABFC orientation from vertical to horizontal reduces the convection velocity in the cathode gas channel, from 32 cm/s in Case 1 to 12 cm/s in Case 4, and finally reducing it to merely 0.2 cm/s in Case 5. This in turn also reduces the  $\text{O}_2$  mass transfer coefficient.

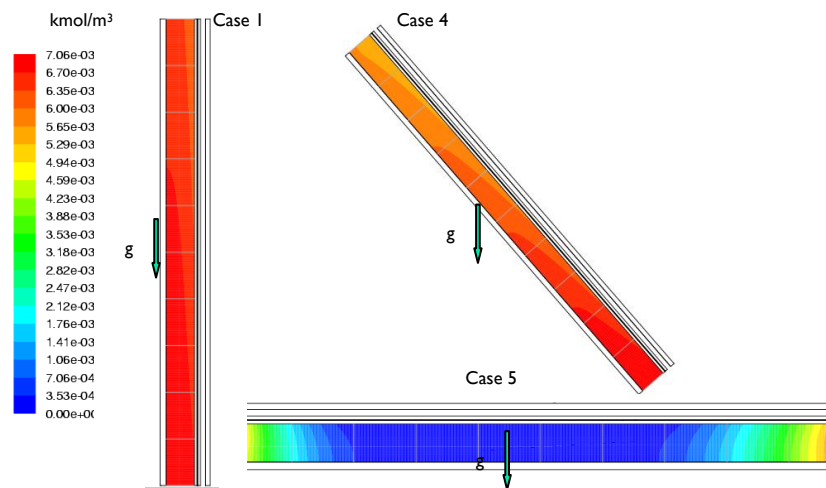
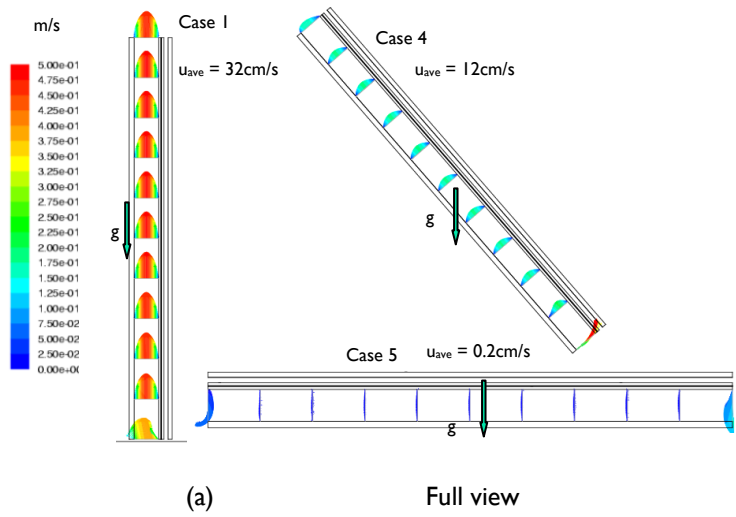
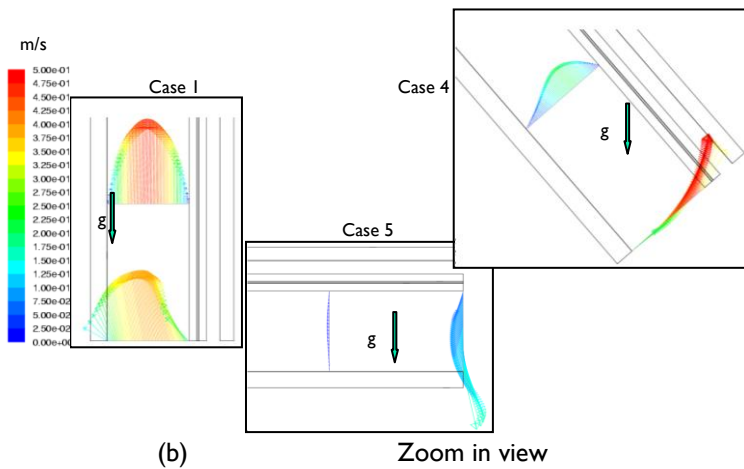


Figure 62: Comparison of  $\text{O}_2$  concentration between three different ABFC device orientations



(a)

Full view



(b)

Zoom in view

Figure 63: Comparison of velocity profile between three different ABFC device orientations

#### 4.2.3 3D CFCD Simulation

In this section, the results for three dimensional time-dependent CFCD simulation for two main designs of ABFC, namely channel and planar, are presented and discussed. For convenience, the following case studies with different ABFC geometry designs and operating conditions are renamed as follows:

Case 7: Channel; vertical orientation

Case 8: Full planar perforations with bipolar plate thickness 3.5mm, facing upwards

##### 4.2.3.1 Geometry and Computational Model

Figure 64 shows the geometry models for both channel and planar ABFC used in the 3D simulation analysis. The computational domain makes use of translational periodic boundary conditions to mimic the repeating units, as shown in Figure 65.

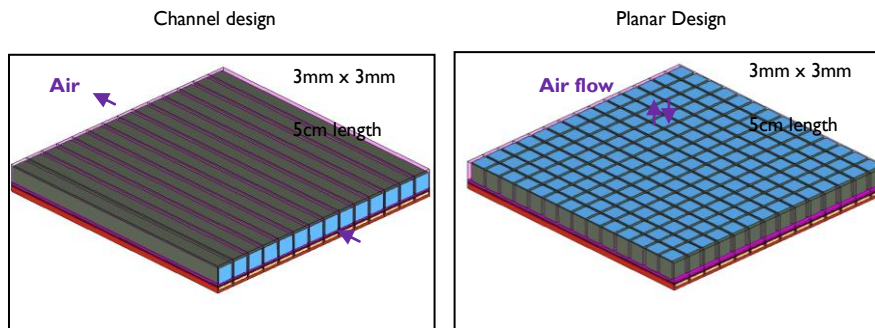


Figure 64: Geometry of physical model for 3D ABFC simulation

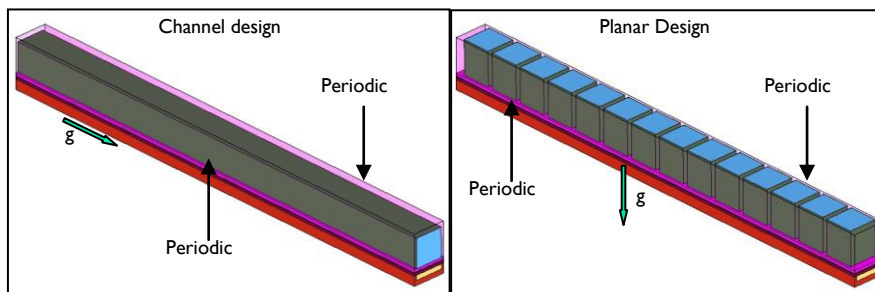


Figure 65: Computational model for 3D ABFC simulation

Figure 66 shows the typical grid resolution used for the channel ABFC. Generally, the number of meshes for this 3D ABFC simulation reaches about 150,000 cells. The number of cells has to be limited within this range as this is a time-dependent simulation and hence requires massive computer resources (minimum 20,000 iterations) in order to reach the pseudo steady state converged results.

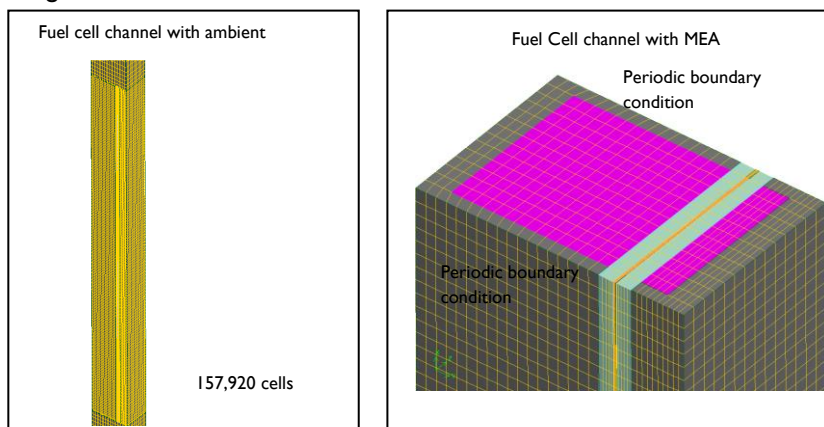


Figure 66: Grid resolution for 3D channel ABFC model

#### 4.2.3.2 Comparison between channel and planar ABFC with perforations

3D simulation for the planar ABFC with perforations (Case 8) has been carried out, and the results are compared with its channel counterpart (Case 7). The geometric description for these two models can be seen from Figure 65.

From the global current density comparison shown in Figure 67, it is noted that with everything else being equal (channel opening, MEA length, operating condition), planar ABFC with perforations yields performance enhancement of about 4-5% as compared to the channel ABFC. Higher improvement is achieved when current density is increased, as the mass transport limitation becomes more critical.

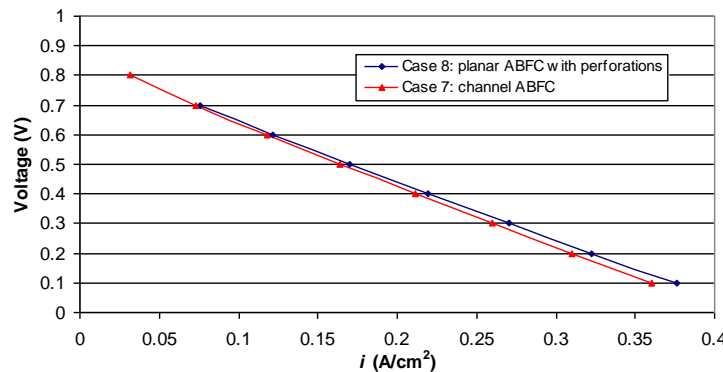


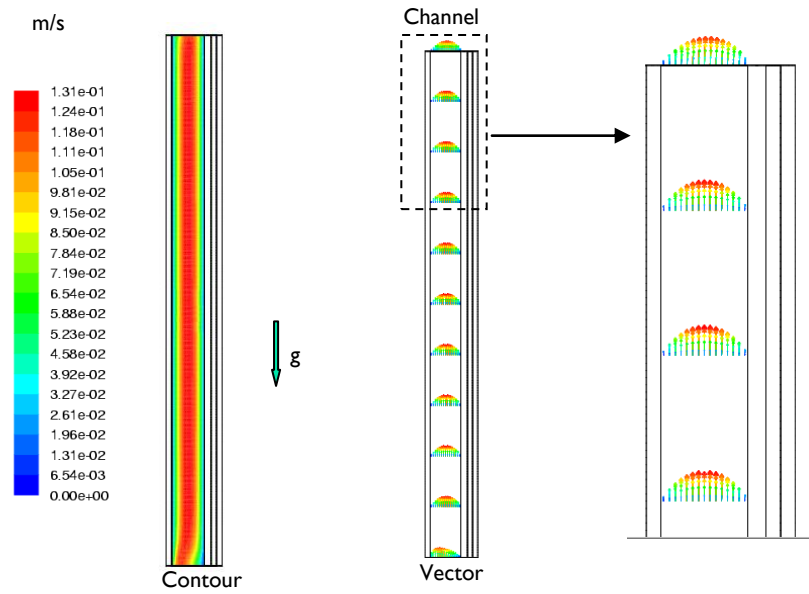
Figure 67: Comparison of polarization curves between Cases 7 and 8

Figures 68 to 73 describe the local distribution results for both channel and planar ABFC with perforations in terms of the flow (Fig. 68), reactant/product (Fig. 69 – 70) and temperature (Fig. 71) distribution, as well as the proton conductivity (Fig. 72) and liquid saturation factors (Fig. 73).

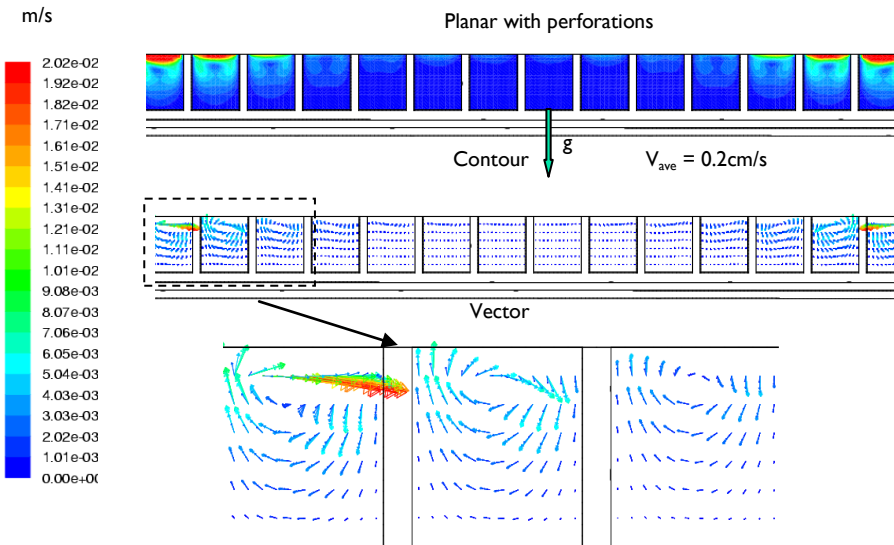
From Fig. 68, it can be seen that for channel ABFC, the flow in the cathode channel is mainly driven by natural convection; whereas for the planar ABFC with perforations, it is mainly driven by diffusion. This observation is in agreement with previous 2D simulation results which deduced that when cathode length scale in fuel cell is reduced, transport mechanism in the flow channel would change from reaction-convection dominated to reaction-diffusion dominated. In this comparative study, channel ABFC is considered to have a sufficiently large volume (3mm x 3mm x 5cm opening) for convection flow. However, the planar ABFC with perforations has a rather restrictive volume (3mm x 3mm x 3.5mm opening) and hence has higher tendency to be associated with diffusion transport. In addition, the geometric design for planar ABFC with perforations has no clear provision for single outflow, as the flow would enter and leave the channel through the same opening. This also promotes diffusion transport, especially with a small opening (3mm x 3mm) for planar ABFC with perforations.

In Figure 68, it is also noted that the average flow velocity in planar ABFC is much lower than that in the channel ABFC. Besides, the central portion displays flow stagnation. However, the overall fuel cell performance for planar ABFC is still higher than that of the channel. This is because the key issue for enhanced fuel cell performance is to achieve the optimal balance between reactant and water content. The flow in both gas channel and MEA regions is mainly reaction dominant. In this scenario, the planar ABFC design is able to provide favorable factors for reaction transport such as a larger opening with a smaller flow path between ambient and MEA to attain the optimum O<sub>2</sub> and water content, with an apparently lower air velocity. This shows that higher flow rate does not necessarily assure better fuel cell performance.

It is also important to note that our finding here of the flow circulation across the gas channel is more realistic as compared to the modeling results from Hwang and Chao (2007), which stated that the gas mixture in planar ABFC flows predominantly outwards from porous cathode to ambient. This is because in nature, self air-breathing process involves the intake of O<sub>2</sub> from ambient and rejection of excess water vapor to ambient. To accomplish this mass transport phenomenon, flow circulation is certainly required. Hence, our model results conforms more to reality as compared to Hwang and Chao (2007).



(a) Case 7: Channel ABFC



(b) Case 8: Planar ABFC with perforations

Figure 68: Comparison of velocity flow field between Cases 7 &amp; 8

In Figure 69, channel ABFC shows O<sub>2</sub> depletion at channel exit, while planar ABFC suffers from O<sub>2</sub> starvation at MEA center. This can be linked to the previous Figure 68(b) which shows the flow stagnation at the MEA center for planar ABFC design. It is worthwhile to note that this finding is different from the recent publication of Al-Baghdadi (2009), as their O<sub>2</sub> distribution is similar for each perforated opening. Their computational modeling carried out using FEMLAB 2.3 did not include O<sub>2</sub> reservoir as the boundary condition to simulate the air breathing process. In addition, it was conducted in the steady state simulation. This mathematical modeling's approach, in the author's opinion, does not actually represent the true physical operating condition for ABFC, and is hence unreliable.

From Figure 69, it is also discovered that the  $O_2$  concentration decrease along cathode GDL/catalyst for channel ABFC is a linear profile, but the  $O_2$  profile is relatively flat with slight dip in the center for planar ABFC. Therefore, for planar ABFC, there is a potential improvement by increasing the  $O_2$  mass transfer rate towards the MEA center, and as shown later, can be achieved by reversing device orientation (making planar ABFC facing downwards)

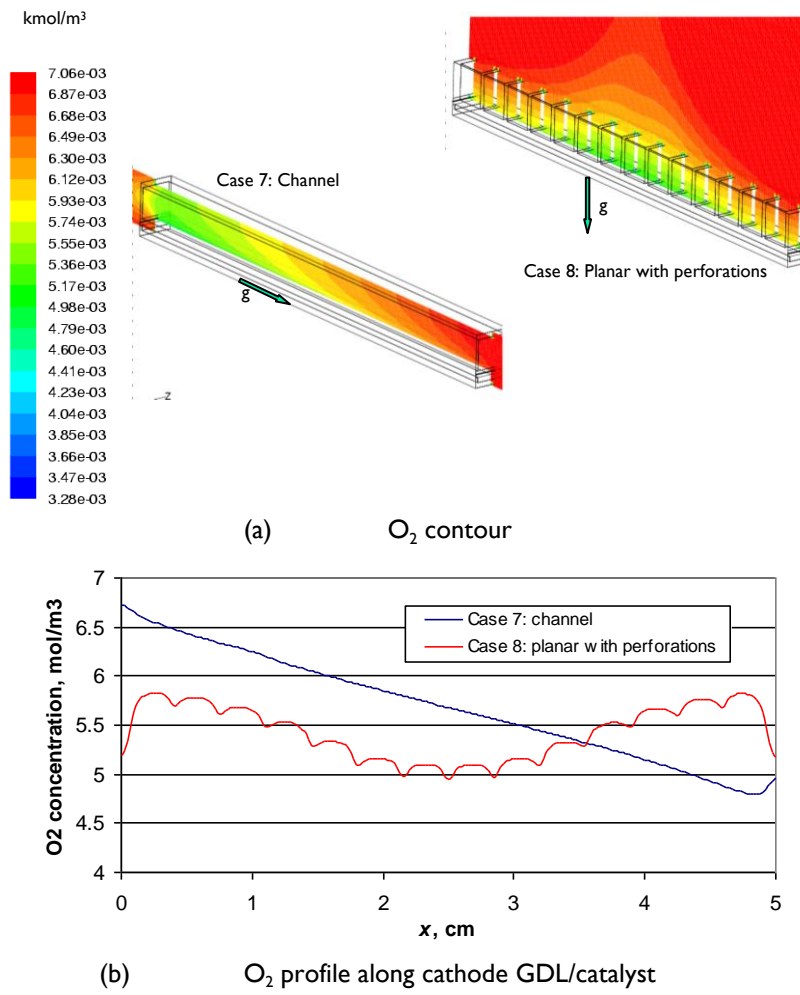


Figure 69: Comparison of  $O_2$  concentration between Cases 7 and 8

In Figure 70, it is observed that planar ABFC has less water vapor concentration than that in the channel design. This is because a more open area to the ambient is available for exchanging fresh unsaturated air with the saturated gas mixture in the cathode channel. This also implies that a superior performance for water removal capability can be obtained for planar ABFC with perforation.

Figure 71 reveals a more uniform temperature distribution obtained for the planar ABFC. Again, this is due to the fact that there are more openings to ambient for fresh air exchange with cathode gas channel.

Water content ( $\lambda$ ) is a direct measure to estimate proton conductivity ( $\sigma_{mem}$ ), as given by Springer et al (1991). Therefore, the plot of proton conductivity is a direct indicator for water content. As seen in Figure 72, a more uniform proton conductivity distribution for planar ABFC is achieved. Besides, in Figure 73, higher liquid water saturation factor is produced by channel ABFC. This results in the inferior performance of the channel ABFC, implying that planar ABFC has a higher water removal capability.

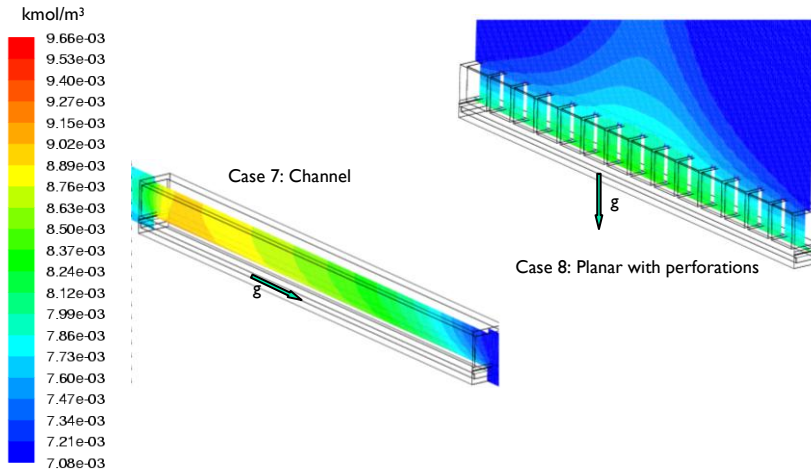


Figure 70: Comparison of water vapor concentration between Cases 7 and 8

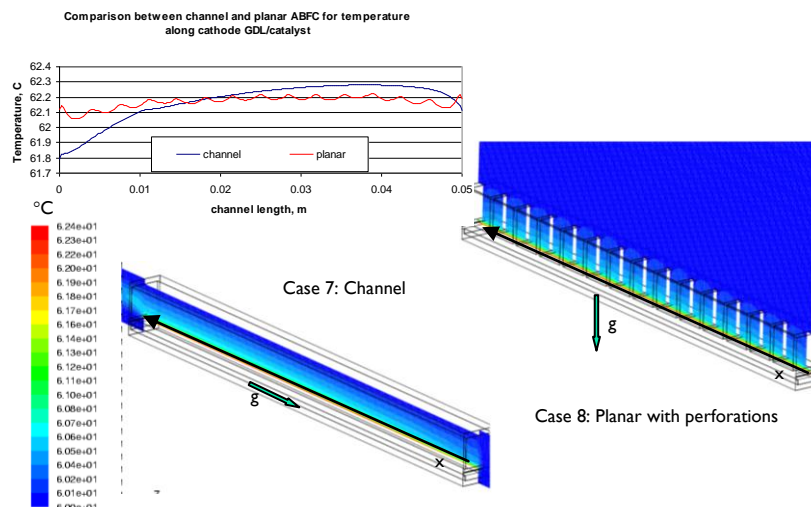


Figure 71: Comparison of temperature contour and profile along cathode GDL/catalyst between Cases 7 and 8

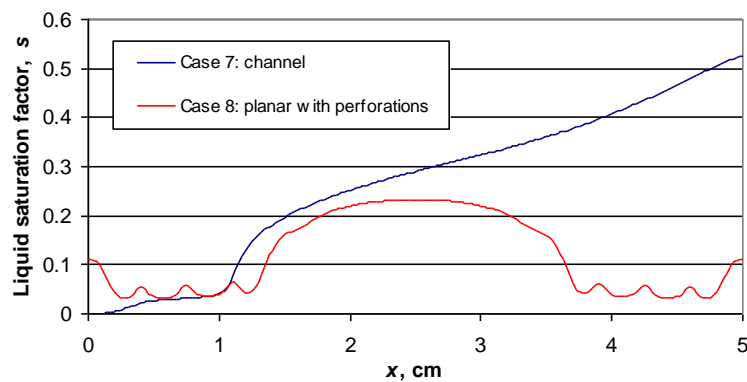


Figure 73: Comparison of liquid saturation factor between Cases 7 and 8

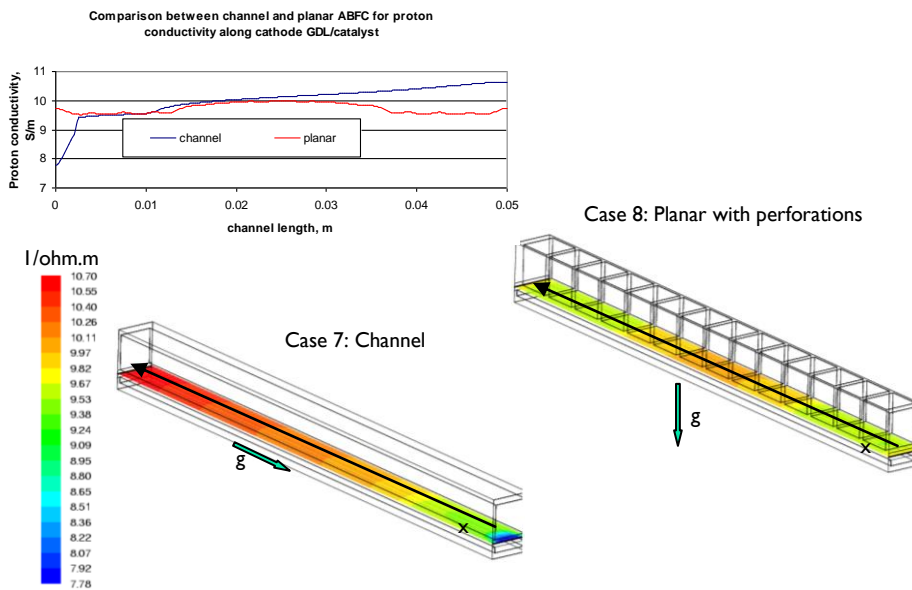


Figure 72: Comparison of proton conductivity contour and profile along cathode GDL/catalyst between Cases 7 and 8

## 5. Conclusions and Future Work

In this work on exploring PEMFC new designs viz. computational modeling, the CFCD model was first validated by demonstrating agreement with the relevant experimental data for both cathode side forced and free convection PEMFC. In the forced convection fuel cell, good agreement of the global polarization curve was obtained by comparing 2D simulation results with experimental data from Noponen et al (2004). Local current density comparison shows that a maximum value of  $1.16 \text{ A/cm}^2$  is predicted by computer simulation. This is close to the experimental result of  $1.24 \text{ A/cm}^2$ , with 6% uncertainty. In terms of the temperature profile comparison, an increase of  $4.5^\circ\text{C}$  is obtained for the cathode catalyst layer, and this is within the temperature range of  $4\text{-}6^\circ\text{C}$  measured by Vie and Kjelstrup (2004). In the ABFC, the model is validated through reasonable comparison with experimental data from Wang et al (2005), and a time dependent methodology is required to simulate the air breathing process.

Concerning mass transport enhancement for forced convection fuel cell, a flow structure which delivers the reactant transversely to the MEA using an impinging jet configuration at cathode side is proposed and modeled to examine its effectiveness, especially at high current densities. Comparative studies between straight channel and single impinging jet with different permeability values of net flow distributor ( $1\text{e-}10 \text{ m}^2$  and  $1\text{e-}08 \text{ m}^2$ ) and GDL ( $1\text{e-}12 \text{ m}^2$  and  $1\text{e-}09 \text{ m}^2$ ) was performed. For enhanced performance with a single impinging jet, a macro-porous GDL with permeability of  $1\text{e-}09 \text{ m}^2$  combined with lower net flow distributor permeability of  $1\text{e-}08 \text{ m}^2$  is required, as it allows the jet to penetrate the GDL towards catalyst layer with the minimum pressure drop and yet is able to maintain water content from direct dehumidification by the jet. Compared to the channel flow, a single impinging jet can improve fuel cell performance up to 80% at high current densities.

For free convection air breathing PEM fuel cell (ABFC), the effect of geometric factors (e.g. channel length and width), device orientation (horizontal placement, alignment with gravity or at an inclined angle), and  $\text{O}_2$  transfer configuration (channel vs. planar) are investigated. It is noteworthy to mention that when anode inlet is fully humidified, electro-osmotic drag (EOD) outweighs back-diffusion for water transport across the membrane, and consequently risks anode membrane dehydration. Planar ABFC can outperform the channel design by about 5%, and the performance enhancement is more significant at higher current densities (e.g.  $0.4 \text{ A/cm}^2$ ). It is noted that the transport phenomena in the cathode channel of ABFC is closely linked to the geometric design and length scale of the cell. For channel ABFC with an adequate opening size (e.g.  $3\text{mm} \times 3\text{mm} \times 5\text{cm}$ ), the flow is reaction-convection dominated; whereas for planar ABFC with perforations in which

cathode channel length scale is restrictive and small (e.g. 3mm x 3mm x 3.5mm), the flow is reaction-diffusion dominated. Therefore, it can be deduced that channel ABFC prefers large channels whereas the planar perforated ABFC prefers the opposite.

Finally, this work contributes to a better understanding of the design for enhanced performance of PEMFC (both forced convection and ABFC). This necessitates an optimal combination of improved reactant mass transport for electrochemical reaction and concurrently keeping the right membrane water content for ionic transfer without causing flooding of the GDL.

A few suggestions for R & D to enhance PEMFC performance are listed as follows:

1. To couple the impinging jet configuration with a baffle in the flow distributor to convert the diffusion transport to convection transport in the GDL.
2. To analyze round shaped MEA for ABFC, as it could provide higher peripheral area for fresh air entrainment during the air breathing process.
3. To implement flow pulsation for higher diffusion rate across GDL.
4. To use wavy walls for flow channel and/or GDL for mass transfer enhancement. The parametric study on the variation of wavy wall amplitude between parallel (geometrical constriction,  $\alpha = 1$ ) and inter-digitated ( $\alpha = 0$ ) can also be explored.
5. To vary the temperature along channel flow in order to alleviate the flooding problem. However, feasibility study from the operating point of view has to be carried out first in order to establish the proof of concept.
6. To design variable permeability GDL so that lower permeability is present at the higher reaction side. Manufacturing issues have to be addressed in order to see whether it is achievable.
7. To taper the parallel channel wall in order to suppress the species concentration boundary layer and improve mass transport process across porous GDL.
8. To use fractal flow channel as flow distributor. Earlier work on this design had been advocated by Bejan (2000) to solve for fluid flow and thermal management issues. However, the application of fractal channel in PEMFC for gas management is rarely seen in the open literature.
9. To investigate the effect of intermittent pulsation to flush out water. This will involve the study on the transient effect of the flooding phenomena in PEMFC, with sudden rise in flow rate for short durations to flush out accumulated moisture.

## Acknowledgments

The authors wish to thank Dr Erik Birgersson, Asst. Professor in NUS for valuable discussions in numerical simulation works

## References

1. Franco Barbir, PEM fuel cells: Theory and Practice, Amsterdam : Elsevier Academic, 2005
2. James Larminie and Andrew Dicks, Fuel cell Systems Explained, Chichester: New York : J. Wiley, 2<sup>nd</sup> ed., 2003
3. Ryan O'Hayre, Suk-Won Cha, Whitney Colella and Fritz B. Prinz, Fuel Cell Fundamentals, John Wiley & Sons, 2006
4. Colleen Spiegel., Designing and Building Fuel Cells, McGraw-Hill, 2007
5. Xianguo Li., Principle of Fuel Cells, Taylor & Francis, 2006
6. Colleen Spiegel., PEM Fuel Cell: Modeling and Simulation Using MATLAB, Elsevier Academic, 2007
7. B. Sundén, and M. Faghri., Transport phenomena in fuel cells, WIT Press, c2005
8. J.A. Klode, B. Bahar, M.S. Wilson, T.A. Zawodzinski, and S. Gottesfeld, Advanced Composite Polymer Electrolyte Fuel Cell Membranes, *Proc. Electrochem. Soc.*, 23:193-201, 1995
9. J. O'M Bockris and S.Srinivasan, Fuel Cells: Their Electrochemistry, McGraw-Hill, New York, 1969
10. J.S. Newman, Electrochemical Systems, Prentice Hall, Englewood Cliffs, New Jersey, 1991

11. Atilla Biyikoğlu, Review of proton exchange membrane fuel cell models, *International Journal of Hydrogen Energy*, Volume 30, Issue 11, September 2005, Pages 1181-1212
12. Denver Cheddie and Norman Munroe, Review and comparison of approaches to proton exchange membrane fuel cell modeling, *Journal of Power Sources*, Volume 147, Issues 1-2, 9 September 2005, Pages 72-84
13. Ruy Sousa, Jr and Ernesto R. Gonzalez, Review - Mathematical modeling of polymer electrolyte fuel cells, *Journal of Power Sources*, Volume 147, Issue 1-2, September 2005, Pages 32-45
14. L. Ma, D. B. Ingham, M. Pourkashanian, and E. Carcadea, Review of the Computational Fluid Dynamics Modeling of Fuel Cells, *Journal of Fuel Cell Science and Technology*, November 2005, Volume 2, Issue 4 pp. 246-257
15. C. Siegel, Review of computational heat and mass transfer modeling in polymer-electrolyte-membrane (PEM) fuel cells, *Energy*, 33 (2008) 1331– 1352
16. D. M. Bernardi and M. W. Verbrugge, Mathematical Model of a Gas Diffusion Electrode Bonded to a Polymer Electrolyte, *AIChE journal*, Vol. 37, No. 8, 1151 – 1163 (1991).
17. D. M. Bernardi and M. W. Verbrugge, A Mathematical Model of the Solid Polymer Electrolyte Fuel Cell, *J. Electrochem. Soc.*, Vol. 139, No. 9, 2477-2491,(1992)
18. T.E. Springer, T.A. Zawodzinski, and S. Gottesfeld. "Polymer Electrolyte Fuel Cell Model". *J. Electrochem. Soc.*, 138(8): 2334-2342, 1991.
19. Vladimir Gurau, Frano Barbir, and Hongtan Liu, An Analytical Solution of a Half-Cell Model for PEM Fuel Cells. *J. Electrochem. Soc.* 147, 2468 (2000)
20. T. V. Nguyen and R. E. White. "A Water and Heat Management Model for Proton-Exchange-Membrane Fuel Cells". *J. Electrochem. Soc.*, 140(8):2178–2186, 1993.
21. T. F. Fuller and J. Newman. Water and Thermal Managament in Solid- Polymer-Electrolyte Fuel Cells. *J. Electrochem. Soc.*, 140(5):1218–1225, 1993.
22. J. S. Yi and T. V. Nguyen., An Along-the-Channel Model for Proton Exchange Membrane Fuel Cells, *J. Electrochem. Soc.*, 145(4):1149–1159, 1998.
23. Vladimir Gurau, Hongtan Liu and Sadik Kakaç, Two-Dimensional Model for Proton Exchange Membrane Fuel Cells, *AIChE Journal*, Volume 44, Issue 11, (November 1998) Pages 2410-2422
24. M. Wöhr, K. Bolwin, W. Schnurnberger, M. Fischer, W. Neubrand and G. Eigenberger, Dynamic modeling and simulation of a polymer membrane fuel cell including mass transport limitation, *International Journal of Hydrogen Energy*, Volume 23, Issue 3, Pages 159-232 Pages 213-218, 1998
25. Wensheng He, Jung S. Yi and Trung Van Nguyen Two-Phase Flow Model of the Cathode of PEM Fuel Cells Using Interdigitated Flow Fields *AIChE Journal*, Volume 46, Issue 10, October 2000, Pages 2053-2064
26. T. Berning, D. M. Lu and N. Djilali "Three-dimensional computational analysis of transport phenomena in a PEM fuel cell" *Journal of Power Sources*, Volume 106, Issues 1-2, 1 April 2002, Pages 284-294
27. Sukkee Um, C. -Y. Wang, and K. S. Chen, "Computational Fluid Dynamics Modeling of Proton Exchange Membrane Fuel Cells" *J. Electrochem. Soc.* 147, 4485 (2000)
28. Michael J. Martínez, Sirivatch Shimparee, J.W. Van Zee, Comparing predictions of PEM fuel cell behavior using Maxwell-Stefan and CFD approximation equations, *Computers & Chemical Engineering*, Volume 32, Issue 12, 2008, Pages 2958-2965
29. N. Djilali, Computational modeling of polymer electrolyte membrane (PEM) fuel cells: Challenges and opportunities, *Energy*, Volume 32, Issue 4, April 2007, Pages 269-280
30. Anh Dinh Le, Biao Zhou, A general model of proton exchange membrane fuel cell, *Journal of Power Sources*,Volume 182, Issue 1, 15 July 2008, Pages 197-222
31. J.J. Baschuk and Xianguo Li, A general formulation for a mathematical PEM fuel cell model, *Journal of Power Sources*, Volume 142, Issues 1-2, 24 March 2005, Pages 134-153
32. Edson A. Ticianelli, Charles R. Derouin, Supramaniam Srinivasan, , *Journal of Electroanalytical Chemistry*, Volume 251, Issue 2, Pages 275-295, 1988

33. Lin Wang, Attila Husar, Tianhong Zhou and Hongtan Liu, "A parametric study of PEM fuel cell performances," *International Journal of Hydrogen Energy*, Volume 28, Issue 11, November 2003, Pages 1263-1272
34. David H. Schwarz and Nedjib Djilali, 3D Modeling of Catalyst Layers in PEM Fuel Cells, *J. Electrochem. Soc.* 154, B1167 (2007)
35. S. M. Senn and D. Poulikakos, "Polymer Electrolyte Fuel Cells With Porous Materials as Fluid Distributors and Comparisons With Traditional Channeled Systems" *J. Heat Transfer* 126, 410 (2004)
36. Sukkee Um, C. Y. Wang, and K. S. Chen, "Computational Fluid Dynamics Modeling of Proton Exchange Membrane Fuel Cells" *J. Electrochem. Soc.* 147, 4485 (2000)
37. M. Noponen, J. Ihonen, A. Lundblad and G. Lindbergh, Current distribution measurements in a PEFC with net flow geometry, *Journal of Applied Electrochemistry* 34: 255 – 262, 2004
38. M. Noponen, E. Birgersson, J. Ihonen, M. Vynnycky, A. Lundblad and G. Lindbergh, Two-Phase Non-Isothermal PEFC Model PEFC: Model and Validation, *Fuel Cell*, 4, No.4, pp 365 – 377, 2004
39. Hyunchul Ju and Chao-Yang Wang, Experimental Validation of a PEM Fuel Cell Model by Current Distribution Data, *J. Electrochem. Soc.* 151, A1954 (2004)
40. P.J.S. Vie and S.Kjelstrup, Thermal conductivities from temperature profiles in the polymer electrolyte fuel cell, *Electrochim Acta*, Volume 49, Issues 7, 2004, pp. 1069 - 1077
41. Hyunchul Ju, Chao-Yang Wang, Simon Cleghorn, and Uwe Beuscher, Nonisothermal Modeling of Polymer Electrolyte Fuel Cells, *J. Electrochem. Soc.* 152 (8), pp. A1645-A1653 (2005)
42. T. Berning and N. Djilali "A 3D, Multiphase, Multi component Model of the Cathode and Anode of a PEM Fuel Cell" *J. Electrochem. Soc.* 150, A1589 (2003)
43. P.C. Sui, S. Kumar, N. Djilali, Advanced computational tools for PEM fuel cell design: Part 1. Development and base case simulations, *Journal of Power Sources*, Volume 180, Issue 1, 15 May 2008, Pages 410-422
44. P.C. Sui, S. Kumar, N. Djilali, Advanced computational tools for PEM fuel cell design: Part 2. Detailed experimental validation and parametric study, *Journal of Power Sources*, Volume 180, Issue 1, 15 May 2008, Pages 423-432
45. Sukkee Um and C. Y. Wang, "Three-dimensional analysis of transport and electrochemical reactions in polymer electrolyte fuel cells", *Journal of Power Sources*, Volume 125, Issue 1, 2 January 2004, Pages 40-51
46. [http://www.bASF-fuelcellproducts.com/standard/product\\_MEAS.php?prodid=42](http://www.bASF-fuelcellproducts.com/standard/product_MEAS.php?prodid=42), accessed on 23 Feb 2009
47. K. Ledjeff, A. Heinzel, V. Peinecke, F. Mahlendorf, 1993, Die Reversible Membran-Brennstoffzelle, in *Elektrochemische Energiegewinnung*, Dechema Monographien, Vol. 128, , pp. 103.
48. Trung V. Nguyen, 1996, A Gas Distributor Design for Proton-Exchange-Membrane Fuel Cells, *J. Electrochem. Soc.* 143 L103.
49. Wei-Mon Yan, Sheng-Chin Mei, Chyi-Yeou Soong, Zhong-Sheng Liu and Datong Song, Experimental study on the performance of PEM fuel cells with interdigitated flow channels, *Journal of Power Sources*, Volume 160, Issue 1, 29 September 2006, Pages 116-122
50. Yuh Ming Ferg and Ay Su, 2007, A three-dimensional full-cell CFD model used to investigate the effects of different flow channel designs on PEMFC performance, *International Journal of Hydrogen Energy*, Volume 32, pp. 4466 – 4476.
51. D.H. Jeon, S. Greenway, S. Shimpalee, J.W. Van Zee, 2008, The effect of serpentine flow-field designs on PEM fuel cell performance, *International Journal of Hydrogen Energy*, Volume 33, Issue 3, , pp. 1052-1066.
52. Suvia Karvonen, Tero Hottinen a, Jaakkko Saarinen, Olli Himanena, Modeling of flow field in polymer electrolyte membrane fuel cell, *Journal of Power Sources* 161 (2006) 876–884
53. L.B. Wang, Nobuko I. Wakayama and Tatsuhiko Okada, Numerical simulation of enhancement of mass transfer in the cathode electrode of a PEM fuel cell by magnet particles deposited in the cathode-side catalyst layer, *Chemical Engineering Science*, Volume 60, Issue 16, August 2005, Pages 4453-4467
54. Wei-Mon Yan, Ching-Hung Yang, Chyi-Yeou Soong, Falin Chen, Sheng-Chin Mei, Experimental studies on optimal operating conditions for different flow field designs of PEM fuel cells, *Journal of Power Sources*, Volume 160, Issue 1, 29 September 2006, Pages 284-292

55. Wei-Mon Yan, Hung-Yi Li, Po-Chiao Chiu, Xiao-Dong Wang Effects of serpentine flow field with outlet channel contraction on cell performance of proton exchange membrane fuel cells, *Journal of Power Sources*, Volume 178, Issue 1, 15 March 2008, Pages 174-180
56. Hui-Chung Liu, Wei-Mon Yan, Chyi-Yeou Soong and Falin Chen, Effects of baffle-blocked flow channel on reactant transport and cell performance of a proton exchange membrane fuel cell, *Journal of Power Sources*, Volume 142, Issues 1-2, 24 March 2005, Pages 125-133
57. Xiao-Dong Wang, Yuan-Yuan Duan, Wei-Mon Yan, Xiao-Feng Peng, Effects of flow channel geometry on cell performance for PEM fuel cells with parallel and interdigitated flow fields, *Electrochimica Acta*, Volume 53, Issue 16, 30 June 2008, Pages 5334-5343
58. Xiao-Dong Wang, Yuan-Yuan Duan, Wei-Mon Yan, Novel serpentine-baffle flow field design for proton exchange membrane fuel cells, *Journal of Power Sources*, Volume 173, Issue 1, 8 November 2007, Pages 210-221
59. Jenn-Kun Kuo, Tzu-Hsiang Yen, Cha'o-Kuang Chen, Three-dimensional numerical analysis of PEM fuel cells with straight and wave-like gas flow fields channels, *Journal of Power Sources* 177 (2008) 96–103
60. C.K. Dyer, Fuel cells for portable applications, *Journal of Power Sources*, 106 (2002) 31–34
61. Ming Han, Avier Lim and Siew-Hwa Chan, Self-hydrating PEM fuel cell developed, *Membrane Technology*, Volume 2007, Issue 11, November 2007, Page 6
62. Pei-Wen Li, Tao Zhang, Qing-Ming Wang, Laura Schaefer, Minking K. Chyu, The performance of PEM fuel cells fed with oxygen through the free-convection mode, *Journal of Power Sources*, Volume 114, Issue 1, 25 February 2003, Pages 63-69
63. S. Litster, N. Djilali, Mathematical modelling of ambient air-breathing fuel cells for portable devices, *Electrochimica Acta*, Volume 52, Issue 11, 1 March 2007, Pages 3849-3862
64. Ryan O'Hayre, Tibor Fabian, Shawn Litster, Fritz B. Prinz, Juan G. Santiago, Engineering model of a passive planar air breathing fuel cell cathode, *Journal of Power Sources*, Volume 167, Issue 1, 1 May 2007, Pages 118-129
65. A. Schmitz, C. Ziegler, J. O. Schumacher, M. Tranitz, E. Fontes, C. Hebling, Modeling Approach for Planar Self-Breathing PEMFC and Comparison with Experimental Results, *Fuel Cells*, Volume 4, Issue 4, pp 358-364, 2004
66. Wang Ying, Tae-Hyun Yang, Won-Yong Lee, J. Ke and Chang-Soo Kim, Three-dimensional analysis for effect of channel configuration on the performance of a small air-breathing proton exchange membrane fuel cell (PEMFC) *Journal of Power Sources*, Volume 145, Issues 2, Aug 2005, Pages 572-581
67. Ryan O'Hayre, Tibor Fabian, Shawn Litster, Fritz B. Prinz, Juan G. Santiago, *Fuel Cell Fundamentals*, John Wiley & Sons, 2006
68. Wang Ying, Young-Jun Sohn, Won-Yong Lee, J. Ke and Chang-Soo Kim, Three-dimensional modeling and experimental investigation for an air-breathing polymer electrolyte membrane fuel cell (PEMFC), *Journal of Power Sources*, Volume 145, Issues 2, Aug 2005, Pages 563-571
69. Ying Wang and Minggao Ouyang, Three-dimensional heat and mass transfer analysis in an air-breathing proton exchange membrane fuel cell, *Journal of Power Sources*, Volume 164, Issue 2, 10 February 2007, Pages 721-729
70. J.J. Hwang and C.H. Chao, Species-electrochemical transports in a free-breathing cathode of a PCB-based fuel cell, *Electrochimica Acta*, Volume 52, Issue 5, 1 January 2007, Pages 1942-1950
71. Tibor Fabian, Jonathan D. Posner, Ryan O'Hayre, Suk-Won Cha, John K. Eaton, Fritz B. Prinz and Juan G. Santiago, The role of ambient conditions on the performance of a planar, air-breathing hydrogen PEM fuel cell, *Journal of Power Sources*, Volume 161, Issue 1, 20 October 2006, Pages 168-182
72. A. Schmitz, M. Tranitz, S. Wagner, R. Hahn and C. Hebling, Planar self-breathing fuel cells, *Journal of Power Sources*, Volume 118, Issues 1-2, 25 May 2003 Pages 162-171
73. A. Schmitz, S. Wagner, R. Hahn, H. Uzun, C. Hebling, Stability of planar PEMFC in Printed Circuit Board technology, *Journal of Power Sources*, 127 (2004) 197–205
74. Tero Hottinen, Mikko Mikkola, Peter Lund, Evaluation of planar free-breathing polymer electrolyte membrane fuel cell design, *Journal of Power Sources*, 129 (2004) 68–72
75. Tero Hottinen, Olli Himanen, Peter Lund, Performance of planar free-breathing PEMFC at temperatures below freezing, *Journal of Power Sources* 154 (2006), 86–94

76. Olli Himanen, Tero Hottinen, Saara Tuurala, Operation of a planar free-breathing PEMFC in a dead-end mode, *Electrochemistry Communications* 9 (2007) 891–894
77. Tero Hottinen, Olli Himanen, Peter Lund, Effect of cathode structure on planar free-breathing PEMFC, *Journal of Power Sources*, 138 (2004) 205–210
78. Yutaka Tabe, Sang-Kyun Park, Kazushige Kikuta, Takemi Chikahisa and Yukio Hishinuma, Effect of cathode separator structure on performance characteristics of free-breathing PEMFCs, *Journal of Power Sources*, Volume 162, Issue 1, 8 November 2006, Pages 58-65
79. S. U. Jeong, E. A. Cho, H.-J. Kim, T.-H. Lim, I.-H. Oh, and S. H. Kim, “Effects of cathode open area and relative humidity on the performance of air-breathing polymer electrolyte membrane fuel cells”, *J. Power Sources*, 158, 348-353, (2006)
80. C.S. Spiegel, R. Agarwal, S. Bhansali, Comparison of microchannel dimensions for air-breathing polymer exchange membrane microfuel cells, *Journal of Power Sources*, Volume 182, Issue 2, 1 August 2008, Pages 603-608
81. Maher A.R. Sadiq Al-Baghdadi, Performance comparison between airflow-channel and ambient air-breathing PEM fuel cells using three-dimensional computational fluid dynamics models, *Renewable Energy*, Volume 34, Issue 7, July 2009, Pages 1812-1824
82. Yun Ho Kim, Hun Sik Han, Seo Young Kim, Gwang Hoon Rhee, Influence of cathode flow pulsation on performance of proton-exchange membrane fuel cell, *Journal of Power Sources*, Vol. 185 (2008) pp. 112–117
83. S. Litster, J.G. Pharoah, G. McLean and N. Djilali Computational analysis of heat and mass transfer in a micro-structured PEMFC cathode, *Journal of Power Sources*, Volume 156, Issue 2, 1 June 2006, Pages 334-344
84. Wensheng He, Jung S. Yi and Trung Van Nguyen Two-Phase Flow Model of the Cathode of PEM Fuel Cells Using Interdigitated Flow Fields *AIChE Journal*, Volume 46, Issue 10, October 2000, Pages 2053-2064
85. Z. H. Wang, C. Y. Wang and K. S. Chen “Two-phase flow and transport in the air cathode of proton exchange membrane fuel cells” *Journal of Power Sources*, Volume 94, Issue 1, 15 February 2001, Pages 40-50
86. Jinliang Yuan and Bengt Sundén Two-phase flow analysis in a cathode duct of PEFCs *Electrochimica Acta*, Volume 50, Issues 2-3, 30 November 2004, Pages 673-679.
87. Mingruo Hu , Anzhong Gu , Minghua Wang , Xinjian Zhu and Lijun Yu Three dimensional, two phase flow mathematical model for PEM fuel cell: Part I. Model development *Energy Conversion and Management*, Volume 45, Issues 11-12, July 2004, Pages 1861-1882
88. Mingruo Hu , Xinjian Zhu , Minghua Wang , Anzhong Gu and Lijun Yu Three dimensional, two phase flow mathematical model for PEM fuel cell: Part II. Analysis and discussion of the internal transport mechanisms *Energy Conversion and Management*, Volume 45, Issues 11-12, July 2004, Pages 1883-1916
89. Cullen R. Buie, Jonathan D. Posner, Tibor Fabian, Suk-Won Cha, Daejoong Kim, Fritz B. Prinz, John K. Eaton and Juan G. Santiago, Water management in proton exchange membrane fuel cells using integrated electroosmotic pumping, *Journal of Power Sources*, Volume 161, Issue 1, 20 October 2006, Pages 191-202
90. Daniel G. Strickland, Shawn Litster and Juan G. Santiago, Current distribution in polymer electrolyte membrane fuel cell with active water management, *Journal of Power Sources*, Volume 174, Issue 1, 22 November 2007, Pages 272-281
91. Shawn Litster, Cullen R. Buie, Tibor Fabian, John K. Eaton, and Juan G. Santiago Active Water Management for PEM Fuel Cells, *J. Electrochem. Soc.* 154, B1049 (2007)
92. Peter Berg, Keith Promislow, Jean St. Pierre, Jürgen Stumper, and Brian Wetton, Water Management in PEM Fuel Cells, *J. Electrochem. Soc.* 151, A341 (2004)
93. G. Dagan,, *Flow and Transport in Porous Formation*, Springer-Verlag, Berlin, 1989
94. Kambiz Vafai, *Handbook of Porous Media*, Marcel Dekker, 2000
95. J.H. Nam and M. Karviany., Effective Diffusivity and Water-Saturation Distribution in Single and Two-layer PEMFC Diffusion Medium. *Int. J. Heat Mass Transfer*, 2003.
96. A.S. Mujumdar, Personal Communication, NUS Singapore, March 2004
97. E. Birgersson and M. Vynnycky, Quantitative study on the effect of flow distributor geometry in the cathode of PEM fuel cell, *J. Power Sources*, 153, 2006, pp. 76-88
98. S. Anantawaraskul and A. S. Mujumdar, Techniques for Enhancement of Impingement Heat and Mass Transfer Rates, *Proceedings of the First Asian-Australian Drying Conference (ADC'99)*, Indonesia, 1999, pp. 117-135

99. S. H. Chuang, M. H. Chen, S. W. Lii, and F. M. Tai, Numerical Simulation of Twin-jet Impingement on a Flat Plate Coupled with Cross-Flow, *Int. J. Numer. Methods Fluids*, 14, 1992, pp. 459-475
100. S. Shimpalee, U. Beuscher and J.W. Van Zee, Analysis of GDL flooding effects on PEMFC performance, *Electrochim. Acta*, 52, 2007, pp. 6748–6754
101. E. Birgersson, B. Fallenius, and M. Vynnycky, Heat and Mass transfer in the Cathode of a Polymer Electrolyte Fuel Cell with a Porous Flow Distributor, HEFAT 2005
102. M. Noponen, J. Ihonen, A. Lundblad, G. Lindbergh, Current Distribution Measurement in a PEFC with Net Flow Geometry”, *J. Appl. Electrochem.*, 34, 2004, pp. 255-262
103. T. M. Jeng and S. C. Tzeng, Numerical Study of Confined Slot Jet Impinging on Porous Metallic Foam Heat Sink, *Int. J. Heat Mass Transfer*, 48, 2005, pp. 4685-4694
104. Y. Wang and C.Y. Wang, Modeling Polymer Electrolyte Fuel Cells with Large Density and Velocity Changes, *J. Electrochem. Soc.*, 152 (2), 2005, pp. A445-A453
105. H. Ju, C.Y. Wang, S. Cleghorn, and U. Beuscher, Nonisothermal Modelling of Polymer Electrolyte Fuel Cell, I. Experimental Validation, *J. Electrochem. Soc.*, 152 (8), 2005, pp. A1645-A1653
106. Tzer-Ming Jeng, Sheng-Chung Tzeng, Numerical study of confined slot jet impinging on porous metallic foam heat sink, *International Journal of Heat and Mass Transfer* 48 (2005) 4685–4694
107. D. Gerteisen , T. Heilmann and C. Ziegler, Enhancing liquid water transport by laser perforation of a GDL in a PEM fuel cell, *Journal of Power Sources*, 177 (2008) 348–354
108. N. Djilali, Computational modelling of polymer electrolyte membrane (PEM) fuel cells: Challenges and opportunities, *Energy*, Vol. 32, 4, 2007, pp. 269-280
109. A. Bejan, *Shape and structure, from engineering to nature*, Cambridge University Press, 2000

# ► [ MODELING OF FLOW BEHAVIOR IN TUNDISHES: EFFECT OF GEOMETRIC MODIFICATIONS]

## [Chapter 9]

**Zhonghua Wu<sup>12</sup> and Arun S. Mujumdar<sup>1</sup>**

► [<sup>1</sup> Minerals, Metals, and Materials Technology Centre, National University of Singapore.

<sup>2</sup>College of Mechanical Engineering, Tianjin University of Science and Technology ]

Fluid dynamics in a lab-scale model tundish was simulated using computational fluid dynamics (CFD) incorporating the standard k- $\varepsilon$  turbulence model and the multiphase volume of fluid (VOF) model. A cold flow simulation was carried out using water to replace liquid steel, which has the same kinematic viscosity as molten metal. Numerical results show flow characteristics in the tundish and the corresponding residence time distribution. Several tundish configurations are proposed by modifying shape of tundish or by using interior dams. The hydrodynamics of liquid flow in these tundish were studied to reduce the fraction of dead volume zones and augment nonmetallic inclusions to float into the slag. Such explorations improve our understanding of the hydrodynamics of liquid flow in tundish and contribute to an optimized operation. Modeling can thus lead to improved tundish designs.

## Modeling of Flow behavior in Tundishes: Effect of Geometric Modifications

### 1. Introduction

A tundish is a shallow, rectangular refractory-lined metallurgical vessel through which molten metal flows before solidifying in the continuous casting mould. It is the most important link between the ladle, the batch vessel and the casting mould with a continuous flow of metal in a continuous casting operation and it serves both as a metal reservoir and as a distributor. Figure 1 shows the construction of a tundish in the steelmaking process. The tundish is divided into two sections, namely, the inlet section and the outlet section. The molten steel is fed from the ladle into the tundish at the inlet section, while the molten steel is fed into the molds from the tundish at the outlet section. At the bottom in the outlet section, the tundish has a nozzle with slide gates or stopper rods in order to control the metal flow into the mold. The tundish is an important component in the steel production processes with two main functions.

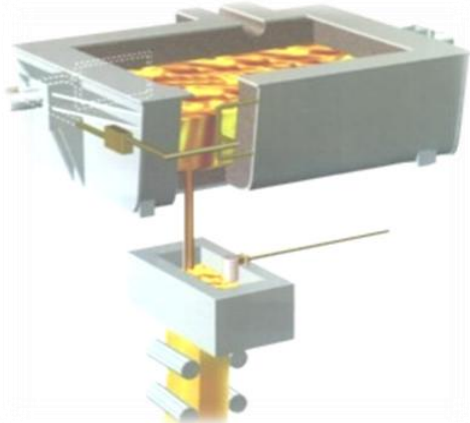


Figure 1: Tundish in steelmaking process

First, the tundish serves to deliver molten steel to the molds at a constant rate and at a constant temperature. The delivery rate into the mold is kept constant by maintaining a constant depth of molten steel in the tundish. When incoming supply of the molten steel is stopped during an exchange of the ladles, the tundish holds sufficient metal to provide a continuous flow to the mold. Moreover, the delivery rate is also controlled by the slide gates or stopper rods at the outlet section. In this manner, the tundish provides more stable stream patterns to the mould.

Second, the tundish serves as a refining vessel to float out detrimental inclusions into the slag layer. Inclusion formation and contamination of molten steel is caused by reoxidation of the melt by air, oxidizing ladle slag being carried over, entrainment of the tundish and ladle slag and also, emulsification of these slags into the molten steel. The slag layer which provides thermal insulation and protects the molten steel from air also absorbs inclusions. Thus, it should be removed as it would cause surface defects to form during subsequent rolling operations and cause local internal stress concentration, lowering the fatigue life of steel. A longer path flow is preferred to prolong the molten steel residence time in the tundish to promote flotation of macro-inclusions into the slag layer. These inclusions should be floated out of the molten steel during the flow through the tundish before being fed into the mold for the production of clean steel. In this manner, the tundish enhances oxide inclusion separation.

It is generally necessary to optimize the features of steel flow in the tundish. With the given outer shape of tundish it is possible to optimize by adjustments of the internal arrangement e.g. by installation of different elements (dams, weirs, baffles) <sup>[1-2]</sup>. Efforts are being made worldwide to obtain the most favorable shape of tundish interior by including dams, overfills and partitions, which favorite nonmetallic inclusions floating into the slag, and also reduce the share of dead zones, short-circuit flow <sup>[3-6]</sup>.

Some researchers in the past used the water model to evaluate the existing or new tundish design configurations. For example, Dainton used water model to develop a novel Tundish flow system incorporating a new turbulence suppresser design <sup>[3]</sup>. However, water model operations are expensive and time-consuming. More researchers uses numerous model to simulate the liquid behaviors in the tundish to explain the effect of tundish working space shape and steel flow conditions on the inclusion floating processes, or to evaluate the new designs of tundish geometries. Merder, et al (2007) developed a mathematical model to study the fluid flow phenomena taking place in continuous casting tundish-a six-strand tundish of a capacity of 30 Mg liquid steel <sup>[4]</sup>. Numerical results include spatial distribution of the velocity vectors, temperature of steel

flowing in the tundish, etc.

The primary purpose of this investigation was to develop a computational fluid dynamics (CFD) model to simulate the flow behaviors in the tundish. Different tundish configuration designs by modifying the tundish shape and using interior dams, baffles, etc are proposed and the flow behaviors in these tundishes are evaluated by numerical simulation. A water-model facility was also constructed and the experiments were carried out on some tundish configuration designs. Experimental data were compared with the numerical results. Numerical results improved our understanding of the flow dynamics in the tundish. Such process contribute to reduce the time and cost of novel tundish geometry.

## 2. Physical Modeling of Tundish Flow Behavior-Water Model Study

To assess the effectiveness of the devices and to optimize the tundish design, a water model study was conducted to simulate the melt flow. In the physical modeling, a full or reduced scale tundish model was designed based on appropriate similarity criteria (Froude similarity) in which the flow of molten metal was simulated by the flow of water. The flow of molten steel is simulated by the flow of water as it has similar kinematic viscosity. If water flow in the model is a realistic representation of the actual tundish melt flow, it may be used to study various aspects of the melt flow in a tundish, including the flow behavior in tundish steady state operation and vortex formation during the draining of the melt from the tundish.

Figure 2 shows the experimental set-up used to study the flow behavior in the tundish at steady state operation. A glass tank is used to represent the tundish. It was designed based on an industrial tundish, by scaling down by 1/3. It is 1520 mm in length, 320 mm in width and 600 mm in height. The inlet nozzle is 150mm away from the left side of the tundish while the outlet nozzle is 150mm away from the right side of the tundish. The inlet nozzle is submerged to a height of 200mm from the bottom of the tundish for the experiments conducted with an initial water level of 300mm. The tundish is filled to an initial water level of 300mm. A water pump is then switched on and the flow control valve knob at the outlet is fully opened. The water is pumped in via the pump and filter into the tundish inlet at a flow rate of 40L/min. Under this inflow rate, the water level in tundish remains constant, indicating a steady state operation. The water is drained away from the outlet nozzle.

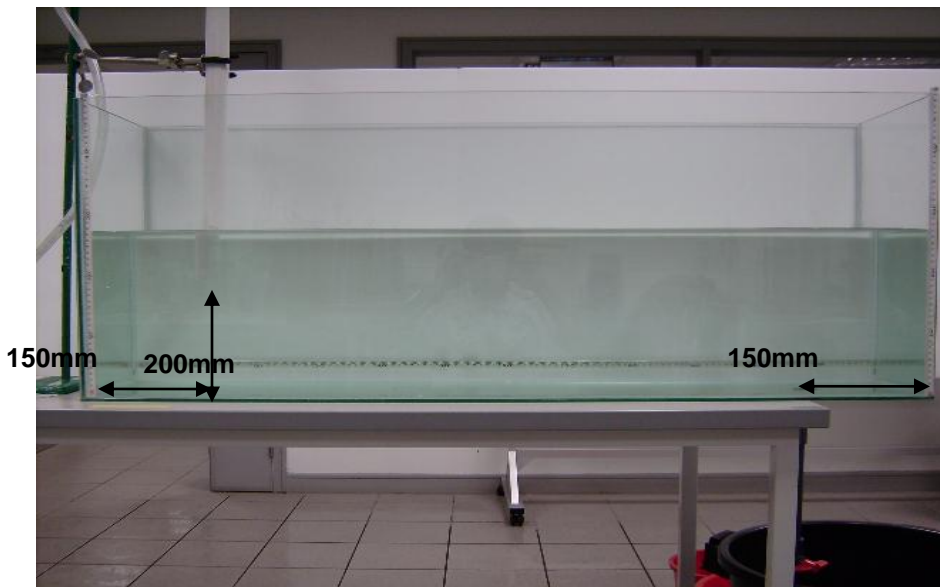


Figure 2 The experiment set-up to study the flow behavior in tundish)

The inlet water from the nozzle impinges on the tundish bottom. Then, the water jet separates into several streams. These streams travel through the middle part of the tundish and finally, reach to the outlet nozzle. The flow pattern of the water jet is very important; it provides information for inclusion flotation and steel quality control. To observe the fluid flow characteristics during steady state and unsteady state operations of the simulated tundish, a tracer (food dyes) was injected at a constant rate into the inlet water jet, to provide a good indication of the overall flow behavior. Some detail about the flow behavior was obtained by post-processing of photos and videos recorded by the digital video camera.

### 3. Mathematical Modeling

Water modeling is a very convenient and useful method to gain a good understanding of the overall flow behavior in the tundish. It can quickly indicate any abnormalities or undesired flow characteristics, such as short-circuiting. Effects of various flow control devices in improving the overall flow characteristics can also be easily studied. In addition, many aspects of the flow that can be simulated in a water model are difficult to simulate mathematically. But, mathematical modeling provides detailed information about velocity, turbulence and temperature fields as a function of location and time which is difficult to obtain via experiments. Mathematical modeling is also a very useful link between a water model and the actual tundish with molten steel as a liquid. In addition, certain configuration changes, such as location and size of the flow control devices, can also be incorporated into the mathematical model. Results can be obtained in a much shorter time compared to the corresponding water modeling experimental results. Thus, the two modeling techniques should be considered as complementary to each other, each with its own advantages and shortcomings.

#### 3.1 Governing Equations

The tundish, flow is two phase with presence of air and water. To catch the air-water interface, the volume of fraction (VOF) two phase model is applied in the CFD model. For the incompressible water –air flow, the continuity equation of the VOF model is

$$\frac{\partial a_w}{\partial t} + \vec{u}_i \cdot \frac{\partial}{\partial x_j} (a_w) = 0 \quad (1)$$

where  $a_w$  is the volume fraction of the water phase in the two-phase flow. The volume fraction of air in the tundish is computed based on the following constrain:

$$a_g = 1 - a_w \quad (2)$$

In the VOF model, only a single set of momentum equations (water phase) needs to be solved. Then, a common flow field is shared by the two-phase flow at each interface:

$$\frac{\partial(\rho_m \vec{u}_i)}{\partial t} + \frac{\partial}{\partial x_j} (\rho_m \vec{u}_i \cdot \vec{u}_j) = \frac{\partial P}{\partial x_i} + \frac{\partial}{\partial x_j} \left[ \mu_{eff} \left( \frac{\partial \vec{u}_i}{\partial x_j} + \frac{\partial \vec{u}_j}{\partial x_i} \right) \right] - \frac{\partial(\rho_m \vec{u}_i \vec{u}_j)}{\partial x_j} + \rho_m \vec{g} + F_{vol} \quad (3)$$

The surface tension can be written in terms of the pressure jump cross the surface. The force at the surface can be expressed as a volume force using the divergence theorem. It is this volume force that is the source term which is added to the momentum equation. It has the following form:

$$F_{vol} = \sigma_{i,j} \frac{\rho k_i \nabla a_i}{0.5(\rho_i + \rho_j)} \quad (4)$$

$\sigma_{i,j}$  is the surface tension coefficient between phase i and j.

Here the Reynolds decomposition is given by  $u_i = \bar{u}_i + u'_i$ . In this study, the standard k- $\varepsilon$  turbulence model was applied to simulate the flow turbulence. The turbulence kinetic energy, k, and its dissipation rate,  $\varepsilon$  are obtained from the following transport equations:

$$\frac{\partial \rho k}{\partial t} + \frac{\partial}{\partial x_i} (\rho k u_i) = \frac{\partial}{\partial x_j} \left( \mu + \frac{\mu_t}{\sigma_k} \right) \frac{\partial k}{\partial x_j} + G_k - \rho \varepsilon \quad (5)$$

$$\frac{\partial \rho \varepsilon}{\partial t} + \frac{\partial}{\partial x_i} (\rho \varepsilon u_i) = \frac{\partial}{\partial x_j} \left( \mu + \frac{\mu_t}{\sigma_\varepsilon} \right) \frac{\partial \varepsilon}{\partial x_j} + C_{1\varepsilon} \frac{\varepsilon}{k} (G_k + C_{3\varepsilon} G_b) - C_{2\varepsilon} \rho \frac{\varepsilon^2}{k} \quad (6)$$

In these equations,  $G_k$  represents the generation of turbulence kinetic energy due to the mean velocity gradients.  $G_b$  is the generation of turbulence kinetic energy due to buoyancy.  $C_{1\varepsilon}$ ,  $C_{2\varepsilon}$ ,  $C_{3\varepsilon}$ , are constants.  $\sigma_k$  and  $\sigma_\varepsilon$  are the turbulent Prandtl number for k and  $\varepsilon$ , respectively.

The properties of water and air used in this study are summarized in Table I

**Table 1 Properties of water and air**

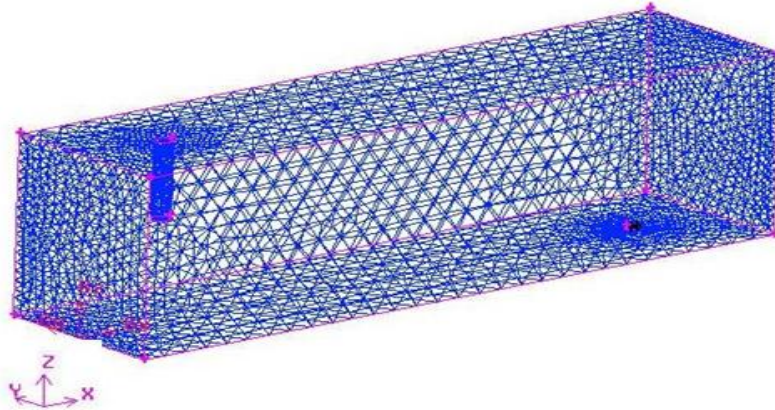
Properties	Water	Air
Density (kg/m <sup>3</sup> )	1000	1.225
Viscosity (kg/m·s)	0.07	01.7894e-05
Surface tension (N/m)	0.072	-

### 3.2 Computational Domain and Mesh

Several tundish designs are proposed and simulated in this study and their fluid flow behavior is evaluated by the physical and mathematical modeling. Figure 3 shows the computational domain and mesh used. These correspond to the tundish configuration described in Figure 2. In this design, no dams and interior baffles are used inside the tundish to regulate the melt flow. The computation domain consists of an inlet nozzle, the top surface which is open to ambient environment, the outlet nozzle. The domain is divided into a non-uniform three dimensional grid. In the inlet section, the jet flow from ladle is highly turbulent and thus a fine mesh is applied in this area, as shown in Figure 3. Also, near the outlet nozzle, a fine mesh is used due to the turbulent flow draining out from the outlet nozzle. Grid independence was tested by increasing the grid point numbers by 1/3 in all three dimensions. The mesh size shown in Figure 3 is about 8 M memory. Of course, a finer grid takes more computer time but generally results in a more accurate solution. Thus, a balance has to be struck between the accuracy of solution and computer time.



(a) Computation domain of the simulated tundish



(b) Computational Mesh of the simulated tundish

Figure 3 Computation domain and mesh for the simulated tundish

### 3.3 Initial and Boundary Conditions

Several tundish designs were proposed and tested in this paper. Boundary conditions depend upon the specific geometric design, but the most commonly used boundary conditions are presented here. The boundary conditions imposed are as follows:

- No-slip boundary conditions at the side and bottom of solid walls
- Normal velocity components and the normal gradients of all other variables (momentum and scalar transport properties) are assumed to be zero at the free surface and at symmetry planes.
- Top surface,  $P=0$
- At the jet entry, the jet flow rate was measured to be 40L/min. Generally, the jet flow is in the highly turbulent range, a flat velocity profile was assumed.
- Pressure out boundary condition is assumed at the Submerged Entry Nozzle (tundish outlet). That is,  $P=0$ .

The initial and boundary conditions are:

- Inlet mass flow rate (ladle shroud nozzle): 40 L/m
- Initial water level: 0.392 mm

### 3.2 Solution Procedure

The continuity, momentum equations were solved using the computational fluid dynamics package FLUENT 6.3. The numerical algorithm used is known as PISO [15] for the filling simulation. A criterion for convergence in all cases simulated here were established when the sum of all residuals for the dependent variables was less than  $10^{-4}$ . The time step size used is 0.01s. In this simulation, the ladle shroud nozzle is first open and water is filling into the tundish. An equilibrium state will be arrived after a certain time. When the equilibrium state arrives, the water level in the tundish is kept constant and it is tundish steady state operation. Then, the idle shroud nozzle is close and allows the water in the tundish drain out. The drainage process is called as tundish unsteady state operation. Under both steady and unsteady state operations, the flow behavior in tundish is simulated using the unsteady solver.

### 4. Liquid Flow Behavior in the Baseline Reference Case

Given an inlet jet flow rate and initial water level, the water level will drop due to the drainage of water from the outlet nozzle, resulting a decreasing outlet flow rate. At a certain water level, the inlet jet flow rate matches the outlet flow rate and then, a steady state is reached. Figure 4 shows the mass fraction distribution of water in the tundish under the steady state operation. The water level is kept constant during subsequent computation and calculated to be 0.38 m, corresponding to the value measured by the physical modeling. The average theoretical residence time of steel in the tundish is defined as a ratio of the steel volume in tundish and the steel flow rate from the tundish. In the equilibrium state, the corresponding average residence time is 8.9 Min.

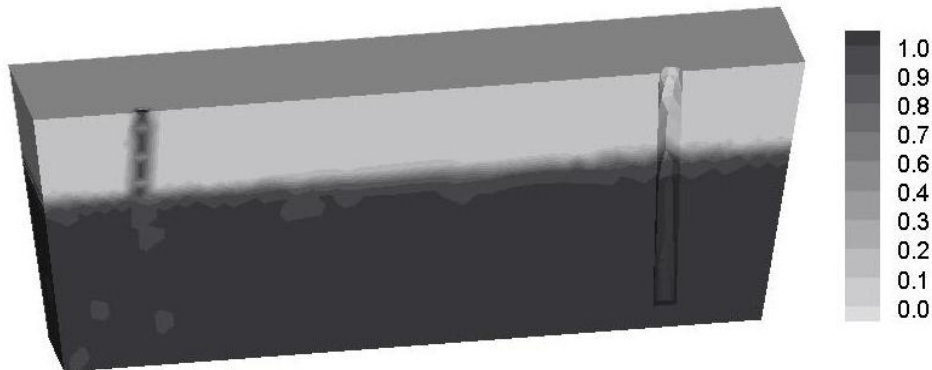


Figure 4 Volume fraction of water in the tundish without dams at steady state

Figure 5 shows the flow pathlines in the tundish without dams when the steady state is reached. From Figure 5, it was found that the flow of water from the ladle shroud nozzle divides itself into two separate flows after the fall on the bottom wall and heads in the horizontal direction. One of these two flows heads to the left side wall of the tundish, rises up along the wall and then descends. This cause a big circulation zone (CZ) observed on the left side of the shroud nozzle. The other flow heads in the horizontal direction on the right side of the shroud nozzle. However, the flow also divides itself into three separate flows at a distance of 100mm close to the nozzle. One stream flows back and forms a large circulation

zone on the left side of the shroud nozzle. The second flow deviates from the horizontal direction and forms the third circulation zone at the upstream of the casting nozzle. The third flow heads to the casting nozzle along the bottom wall. The residence time of this flow should be less than the average one. It can be called “short-circuit” flow. When the incoming liquid steel practically immediately gets into the outlet of the tundish, it is undesirable with regard to steel purity and thermal homogeneity of cast steel in individual strands. In Figure 5, three big circulation zones were observed inside which the residence time of flow is longer than the average one and can be called “dead volumes”. Dead volume is defined [3] as the volume where the liquid steel stays in tundish longer than the double of the average residence time. Existence of dead volume can substantially decrease the active volume of the tundish. It can also lead to the unsteady temperatures of steel cast in individual casting strands and so lead to the increase of breakout danger.

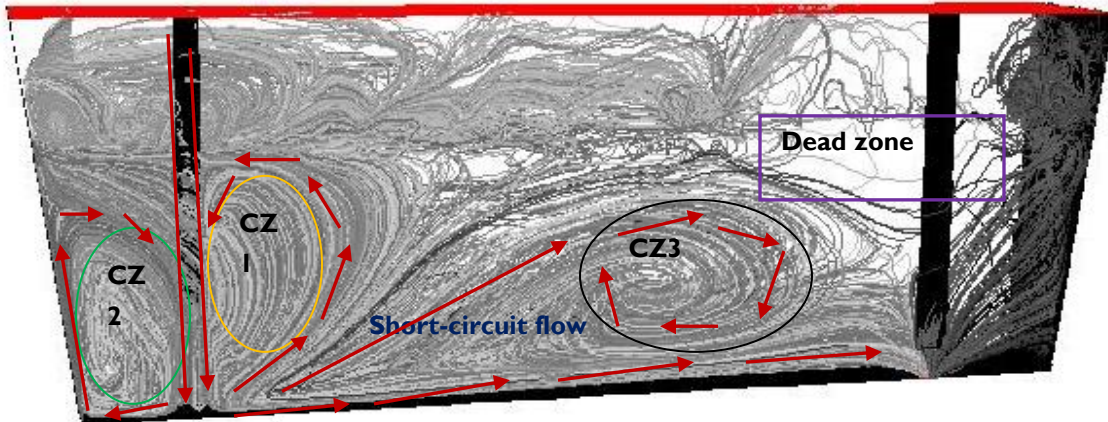


Figure 5 Flow pathlines in the tundish without dams at the steady state (without pads and dams, stop rod is included)

## 5. Liquid Flow Behavior in Several Tundish Configurations

### 5.1 Tundish Configuration (TC) II

Figure 6 shows other tundish configurations tested in this study. This tundish has a length of 1520 mm, width of 320 mm and height of 600 mm. The ladle shroud nozzle has a diameter of 52mm and the casting strand nozzle is 36 mm in diameter. At the bottom wall, there are two blocks: One is the impact pad of  $300 \times 300 \times 90$ mm and putted under the ladle shroud nozzle. Its function is to reduce the turbulence energy caused by the filling liquid steel jet from the ladle. Another is the stepping dam of  $300 \times 62 \times 62$ mm and putted at a location  $x=1088$  mm. Since the geometry is symmetry on the x-z plane, only half of the geometry is computed.



Figure 6 The proposed tundish configuration II

Figure 7 shows the corresponding flow pathlines in the tundish with dams when the steady state was reached. Compared with Figure 5, it was found that the flows in the tundish were redirected by the impact pad under the shroud nozzle and the dam located in front of the casting nozzle and a relative homogenous residence time of flows was achieved. The used impact pad fully inhibited the direct flow to the casting nozzle along the bottom wall—the “short-circuit” flow and increased

its residence time. Also, the impact pad reduced the sizes of the two circulation zones near to the shroud nozzle. The third circulation zone observed in Figure 5 almost diminished due to the stepping dam locating in the front of the casting nozzle. Present results show that the introduction of an impact pad, dams, etc can redirect the flow movement and reduce “short-circuit” flow and dead volumes in the tundish. A small dead zone is observed near the bottom dam. Compared with Figure 5, the flow movement is more gentle and homogenous in this new tundish configuration.

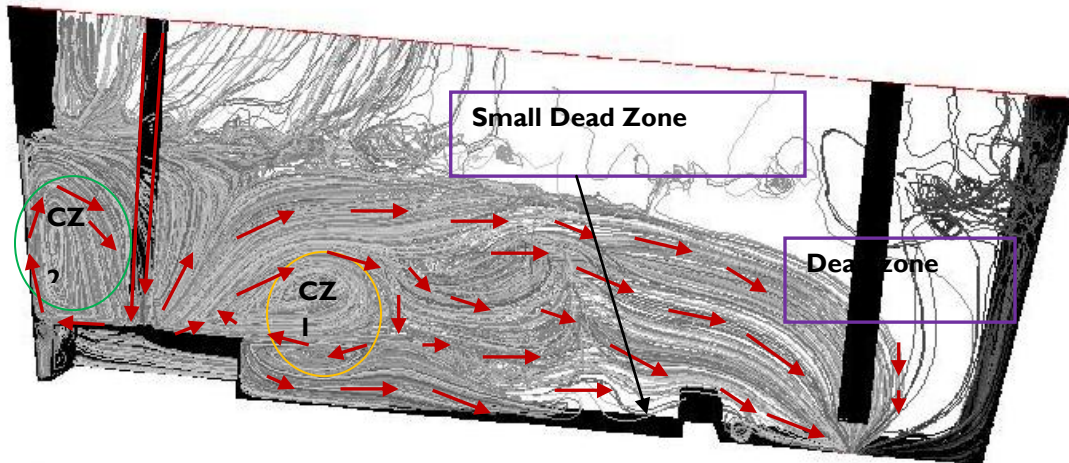


Figure 7 Flow pathlines in the tundish with configuration II at the steady state (with impacting pads and dams, stop rod is included)

## 5.2 Tundish Configuration (TC) III

Figure 8 shows the third tundish configuration proposed and modeled in this study. It has a length of 1200 mm, width of 300mm and height of 600 mm. The tundish is bit shorter than the first one. Near the inlet nozzle, a solid baffle with a dimension of  $5 \times 300 \times 150$  mm is installed at the position 300mm away from the left side of the tundish and 200mm above the bottom. This baffle severs to regulate the inlet flow. A dam with dimensions of  $5 \times 300 \times 100$ mm and four slots of length 15mm each is placed at a distance D, 900 mm from the left side of the tundish. This dam serves to regulate the flow near the bottom of the tundish and its structure is shown in Figure 11 (b). The distance D can be modified in physical or mathematical modeling. In this case, no stop rod is included. The outlet nozzle diameter is 20mm and when the water inflow rate is 40 L/m, the water level is kept at 290 mm above the tundish wall in early tests. The aim of this tundish configuration is to demonstrate the effect of the upper baffle and slotted bottom dam on the flow behavior in the tundish.

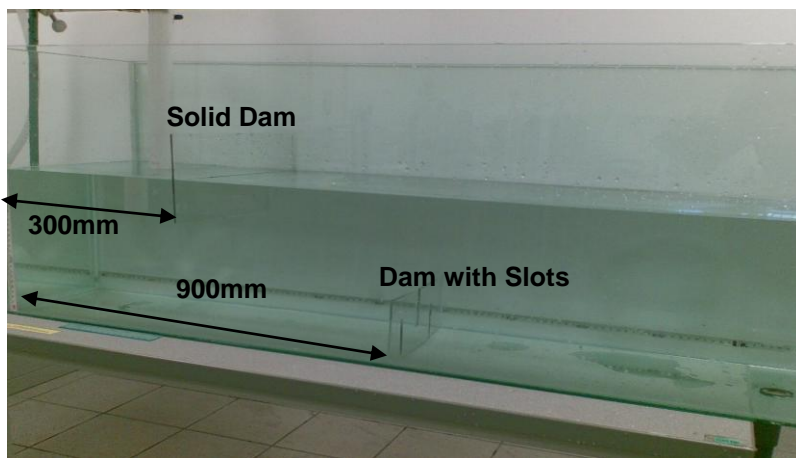


Figure 8 The proposed tundish configuration III

Figure 9 shows the simulated flow pathline in the third tundish design with an upper solid baffle and a slotted bottom dam. It was observed that the flow from the inlet nozzle impinges on the bottom wall of the tundish and then splits into two flows: one of the flows deflects upwards towards the left wall of the tundish, rises up and then descends down back into the incoming water jet, resulting in a recirculation zone located at the left side of inlet nozzle. The other flow deflects upwards towards the right of the inlet nozzle and also rises up. But, only a small part of this flow can drop down back into the inlet jet. Due to the block of the upper solid baffle, most of the flow cannot circulate back into the nozzle and was forced to move forward to the outlet section of the tundish. The flow pattern shown in Figure 9 demonstrates that the central region of the tundish exhibits smoother flow transition. Thus, the upper solid baffle contributes to stop the back flowing and regulate the flow in the tundish.

From Figure 9, it can be observed that the liquid flowing horizontally along the tundish bottom is blocked by the second slotted dam near the outlet and was lifted towards the surface layer. In this manner, the short-circuit passage observed in TC1 was diminished. In addition, the slots in the second dam permit the liquid to flow through the dam and thus, eliminate the small dead zone, which is caused by the solid dam and is observed in TC2. Thus, a slotted dam is better than the solid one because the slots are helpful to eliminate the small dead zone.

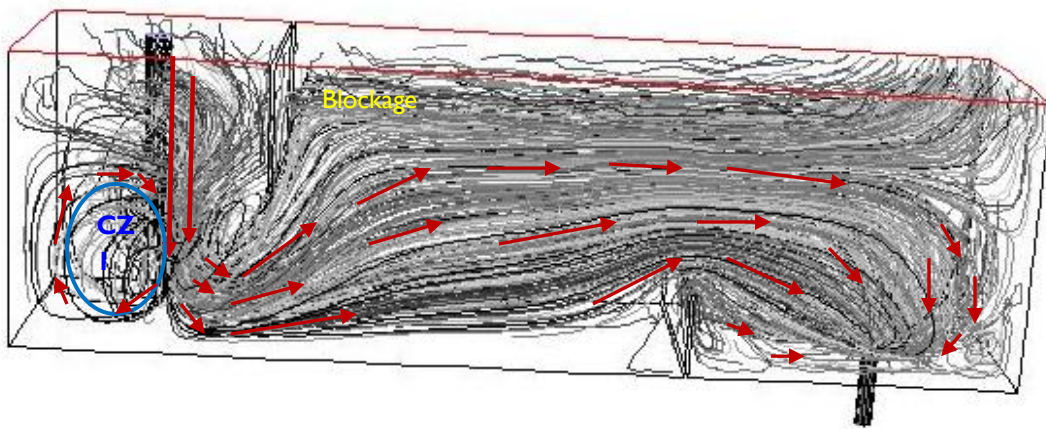


Figure 9 Flow pathlines in the tundish with configuration III at the steady state (with a upper solid baffle and bottom dam with slots, no stop rod is included)

### 5.3 Tundish Configuration (TC) IV

Figure 10 shows the fourth tundish configuration (TC 4) proposed in this study. It has a length of 1200 mm, width of 300mm and height of 600 mm. Near the inlet nozzle, a dam with a dimension of 5×300×300 mm is installed at the position 300mm away from the left side of the tundish and the distribution of holes in dam is shown in Figure 11(b). This baffle serves to regulate the inlet flow. A dam with a dimensions of 5×300×100mm and four slots of length 15mm each is placed at a distance D, 900 mm from the left side of the tundish. This dam serves to regulate the flow near the bottom of the tundish. Also, in this case, no stop rod is considered. The aim of this tundish configuration is to demonstrate the effect of the dam with holes on flow behaviors in tundish.

Figure 12 shows some results of the flow visualization experiment conducted with the aid of a dam with holes placed near the inlet nozzle replacing the solid dam in the experiment earlier and a dam with slots is placed near the outlet nozzle at D=80mm. It was observed that upon entering the inlet nozzle, the flow hits the bottom of the tundish and is split into two flows as mentioned earlier. However, the flow that circulates towards the right of the tundish is filtered by the dam with holes and as a result, very smooth clean flow enters the right of the tundish via the holes, thus smoothening out the turbulence entrancing from the inlet nozzle. In addition, the short-cut passage is crippled by the present of the dam with slots near the outlet nozzle and the dead zone is absent behind the dam due to the slots present.

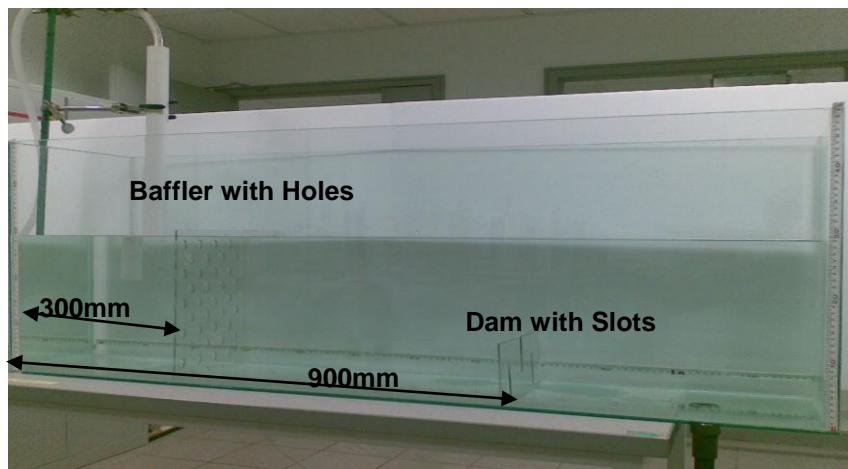
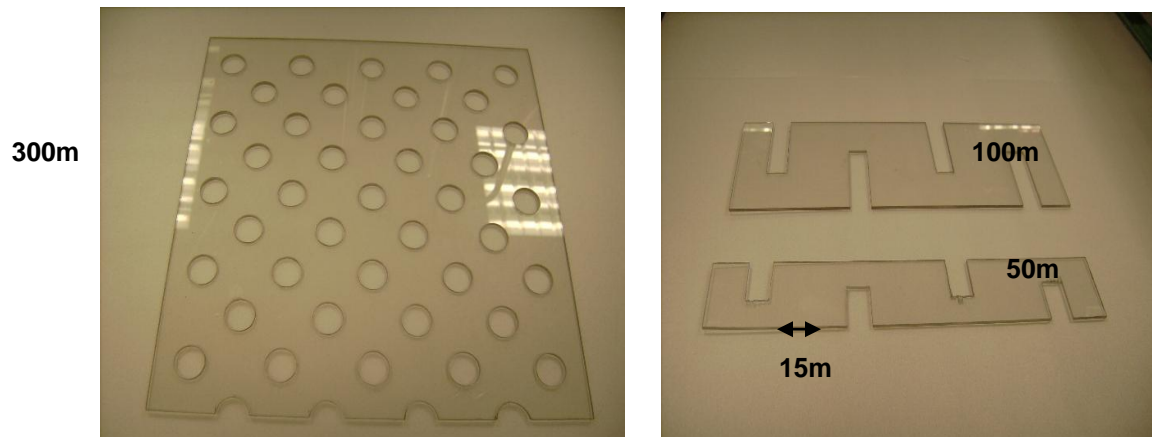


Figure 10 The proposed tundish configuration IV



(a) Dam with homogeneous distributed holes    (b) Dams with slots

Figure 11 The structure of dams with holes (a: diameter: 20 mm) and with slots (b)

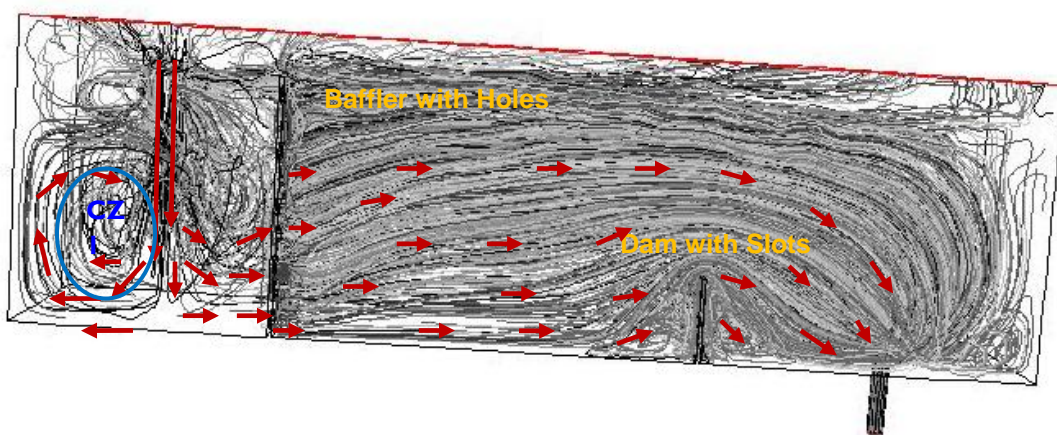


Figure 12 Flow pathlines in the tundish with configuration IV at the steady state (with a holed baffle and bottom dam with slots, no stop rod is included)

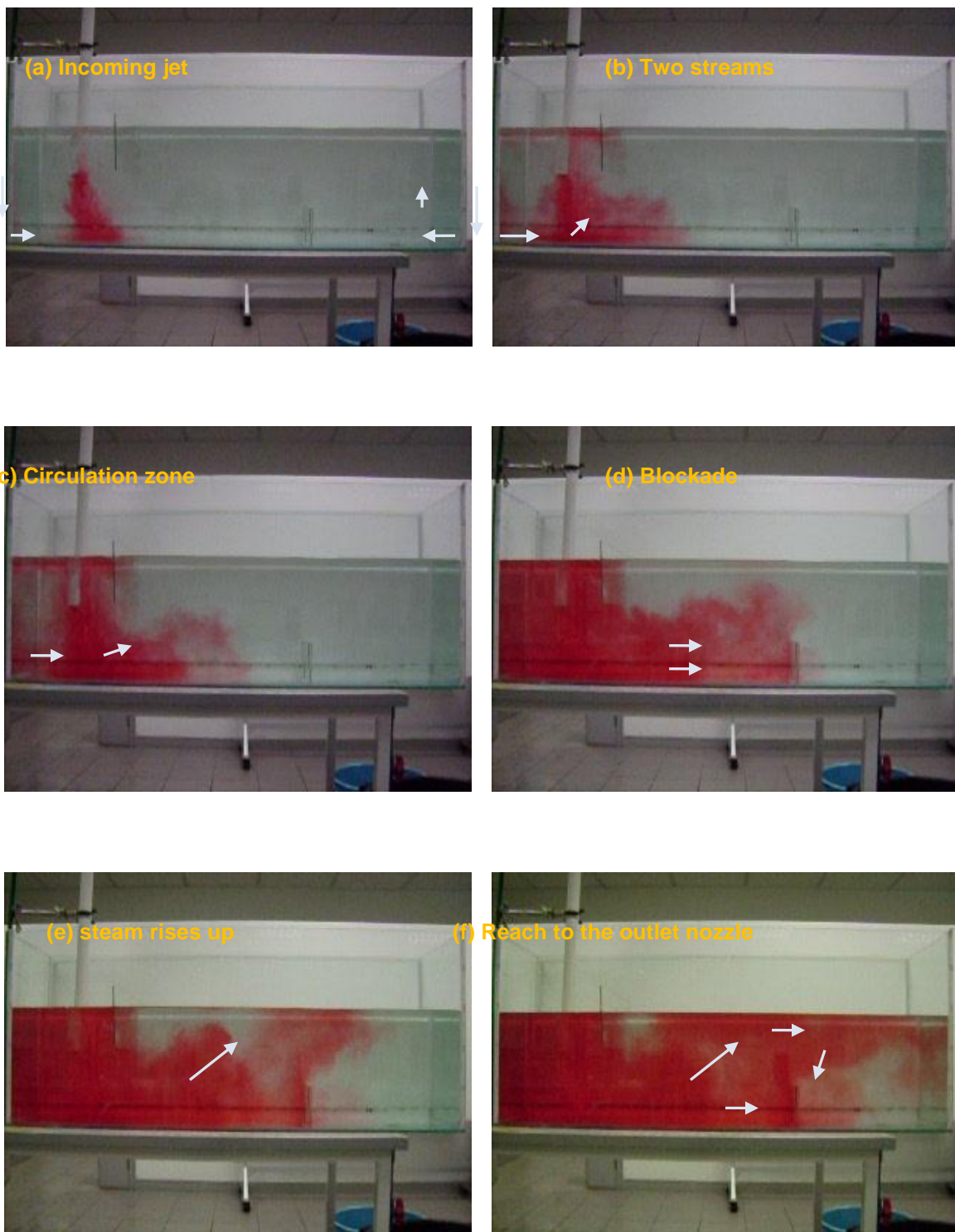


Figure 13 The transient flow behaviors in the tundish configuration III (Red food dye was used to show the liquid movement)

## 6. Comparison with the Physical Modeling Results

The physical modeling (water model study) was also carried out for the configurations TC III and TC IV. Food dyes were used to visualize the liquid movement in the tundish. Here, we make a qualitative comparison with numerical results with the experimental one. The detailed and quantitative comparison will be carried out later when the advanced flow visualization equipments are ready.

Figure 13 shows a sequential snapshot of liquid movement in the tundish, in which food dyes are added into the incoming jet and visualize how the liquid movement in tundish. Figure 13a shows that the incoming jet impinges on the bottom of the tundish. The incoming jet splits into two flows as shown in Figure 13 b: one of the flows deflects upwards towards the left wall of the tundish, rises up and then drops down back into the incoming water jet, resulting in a recirculation zone locating at the left side of inlet nozzle. This can be seen in Figure 13c. The other flow deflects upwards towards the right of the inlet nozzle and also rises up. Due to blockage due to the upper solid baffle, most of the flow cannot circulate back into the nozzle and was forced to move forward to the outlet section of the tundish, as shown in Figures 13 c~d. From Figures 13d~e, it can be observed that the liquid flowing horizontally is blocked at the second slotted dam near the outlet and was uplifted towards the surface layer. In this manner, the short-circuit passage observed in TCI was diminished. Figure 13 f shows the liquid from the incoming jet has reached to the outlet nozzle and also, some liquid was observed to flow through the slots in the second dam. Thus, no dead zone exists near the second dam. Compared with the predicted flow pathlines shown in Figure 9, the physical modeling results show a very similar liquid movement. Some important phenomena are predicted well such as the recirculation zone, flow rising up, etc.

## 7. Concluding Remarks

A three-dimensional numerical simulation has been carried out to study the flow behavior in an lab-scale model tundish. Tundish designs with/without interior dams are compared. It was found that undesirable short-circuit flow, dead volumes exist in the proposed tundish designs. The introduction of a impact pad and a stepping dam will modifies the flow in the tundish and inhibits the short-circuit and dead volumes. This can improve tundish performance and hence steel quality.

Furthermore, water model study of some tundish designs was also conducted. A qualitative comparison shows that both numerical simulation and physical modeling results demonstrate a similar flow movement in the tundish. In this preliminary study, only four basic tundish geometric designs are discussed. Additional designs and their steady /unsteady performance will be investigated in the next phase of this project.

## Acknowledgments

This work was jointly supported by M3TC at National University of Singapore.

## 8. References

- 1) Ghosh, A. Secondary steelmaking: principles and applications. New York: CRC Press, 2000: 285-295
- 2) Yogeshwar Sahai and Toshihiko Emi, "Tundish Technology for Clean Steel Production," World Scientific Publishing Company, USA, 2007, pp.94-97, 131-138.
- 3) Dainton, A.E. Development of a novel tundish flow system-the application and results in North American steel plants. 28<sup>th</sup> Seminar on Melting, Refining and Solidification of the ABM, Brazil, 12-14 May, 1997
- 4) Merder, T., Boguslawski, A., Warzecha, M. Modelling of flow behaviour in a six-strand continuous casting tundish. Metallurgical, 2007: 46(4): 245-249
- 5) Wu Z.H. and Mujumdar, A.S. , CFD Modeling of Liquid Steel Flow Behaviors in an Industrial Tundish, In: 3<sup>rd</sup> Baosteel Biennial Academic Conference, 26-28 September, Shanghai, China (2008).
- 6) Don Zacharias, The Integrated Tundish: A Comprehensive Approach to Tundish Flow Control Design, Foseco International Limited, In: XXXIV Seminario de fusao, refine e Solidificacao dos Metais, 19-21 March, Brazil (2003)

# ► [ MATHEMATICAL MODELING OF BREAD BAKING IN AN IMPINGEMENT OVEN]

## [Chapter 10]

**Salem Banooni<sup>1</sup> and Arun S. Mujumdar<sup>2</sup>**

►<sup>1</sup> Mechanical Engineering Department, Engineering Faculty, Shahid Chamran University of Ahwaz, Iran. <sup>2</sup> Mechanical Engineering Department, Engineering Faculty, National University of Singapore, Singapore]

Baking is a complex process that brings about a series of physical, chemical and biochemical changes in a product such as volume expansion, evaporation of water, formation of a porous structure, denaturation of protein, gelatinization of starch, crust formation and browning reaction. Four quality attributes -i.e., bread crumb temperature, moisture content, volume increase and surface color represent bread acceptability in terms of various aspects. The objective of this study is to develop a model that predicts these attributes as a function of the baking conditions continuously. An artificial neural network (ANN) was used to obtain such a model of bread quality attributes during baking. Using hot air impinging jets for baking of bread can provide a good compromise between texture and appearance. As the hot air impinging jets were employed for baking, the baking control parameters were the jet temperature, the jet velocity, and the time elapsed from the beginning of the baking. The data used in the training of the network were acquired experimentally. In addition, using the data provided by ANN, a multi-objective optimization algorithm was employed to achieve the optimum baking control parameters that satisfy all of the quality indexes. Also Impingement heat transfer distribution effects on bread baking was investigated by numerical simulation and related to the bread color. Considerable effect of local variations in impingement heat transfer and nonuniform nozzle exit velocity distribution on the color of baked bread was observed.

## Mathematical Modeling of Bread Baking in an Impingement Oven

### 1. Introduction

Bread texture is chiefly developed by starch gelatinization. Starch gelatinization is the most important quality attribute of the bread, which contributes to the sensory acceptability. On the other hand, Zanoni et al.<sup>[1]</sup> indicated that starch gelatinization completes at crumb temperature of about 100°C. Thus, crumb temperature was chosen as the first parameter representing the bread quality. Another parameter considered is bread moisture content (ratio of bread water mass to total mass), which not only influences the bread texture but is a significant factor from a staling viewpoint; i.e., lower water content downgrades the bread quality, whereas higher water content postpones the staling of the bread<sup>[2]</sup>. In addition, for bread producers, the lower the weight loss, the higher the profit margin. Bread thickness is another factor contributing to bread acceptability. The maximum increase in bread volume is desirable, particularly in bread. None of these three parameters are directly related to bread appearance. The key factor that contributes to consumer preference, of course, is its surface color.

As the physicochemical principles governing the bread baking process (e.g., surface color and volume change during baking) are not completely illuminated and understood, the ANN modeling is an appropriate method to relate the oven condition with bread quality attributes without requiring prior knowledge on the mechanisms involved in the process<sup>[3]</sup>. Further information about the state of the art in mathematical modeling of the baking process can be found elsewhere (Sablani et al., 1998; Mondal and Datta, 2008)<sup>[4, 5]</sup>.

Thus, in this study, ANN was used to obtain such a model of bread quality attributes during baking. In all of earlier works (also the studies which did not use ANN for modeling); various models were developed to describe one of the quality attributes individually as a function of baking control parameters. If two or more quality attributes were to be predicted, two or more separate ANN models were developed, respectively. Although these models are not pointless, the second aim of this study is acquiring the specific baking condition which causes all of the quality attributes to lie in the acceptable range. Therefore, there must be a model which calculates four quality attributes simultaneously from the input variables. This model provides the required data for optimization algorithm.

Here, in this study, multi-objective Genetic Algorithm (GA) was employed to find the optimum baking control parameters which satisfy all the quality indexes. The GA uses ANN model to produce its required data. Multi-objective optimization means that two or more objectives (here, four baking parameters) are optimized simultaneously. Otherwise, that is, if a multi-objective optimization was not applied, one of the quality indexes should be optimized using a single objective optimization algorithm while the other quality attributes have to be constrained to some predefined limits. Indeed, this method was resulted in one of the solutions rather than the best solution. However, using multi-objective optimization algorithms, a set of different solutions are provided from which the best one is selected due to the designer preference.

In the domestic forced convection oven ("hot air oven") the temperature distribution in the cavity is much more even than in a traditional static ("top-bottom" heated) oven. However, the surface browning of food cooked in hot air ovens can be uneven. This is an effect of the inherent non-uniformity of the air velocity distribution, resulting in different local heat fluxes.<sup>[6]</sup> The hot air oven is one type of forced convection oven where the air flow is largely parallel to the bread surface (Fig. 1); another is the impingement oven (Fig. 2), in which the hot air jets impinge normally on the baking surface. Air jet impingement units are used in various industrial processes for efficient heat and mass transfer operations such as in textile and paper drying, electronics cooling, metal annealing, glass tempering, etc., because of the high heat and mass transfer rates attainable with such convection designs. Mujumdar<sup>[7]</sup> has given a concise but comprehensive summary of impingement drying.

These systems have found many applications in industrial food processing in the last two decades. Li et al.<sup>[8]</sup> compared large impingement ovens and the combination of impingement and microwaves and found large differences to industrial hot air ovens. Walker et al.<sup>[9]</sup> and Henke et al.<sup>[10]</sup> in general describe impingement ovens. Considerable reduction in process time and improvement in product quality can be obtained using this technique.<sup>[11-13]</sup>

In impingement oven design, it is important to select the jet configuration very carefully since a two- or fourfold decrease can occur due to errors in the selection of nozzle geometry, spacing, etc. Polat [14] provided an excellent review of impinging jet heat transfer. Several recent papers also deal with impinging jet heat transfer with a variety of jet designs and include important effects such as those of jet multiplicity,<sup>[15]</sup> complex geometries such as noncircular nozzles,<sup>[16]</sup> effects of cross-flow,<sup>[17]</sup> effect of large temperature differences,<sup>[18]</sup> etc. The jet configuration used in this study cannot be considered truly optimal but is a reasonable design based on literature recommendation.<sup>[19, 20]</sup>

A point of concern when using air impingement systems is the wide variation of heat transfer coefficient on the surface of a product. This can cause undesirable variation in certain quality attributes. Previous studies have indicated that air impingement systems can result in localized hot and cold spots on the surface of a food.<sup>[21]</sup> Practically, two sources of non-uniformity exist: local convection heat transfer coefficient variation and non-uniformity of jet temperature and velocity in oven cavity. Computational fluid dynamics simulations were carried out in our laboratory to examine the impingement heat transfer characteristics.<sup>[22–25]</sup> Improvement is done by implementation of a proper turbulence model ( $v^2 - f$ ) in these simulations for accurate prediction of the oven heat transfer uniformity effects on bread during baking.

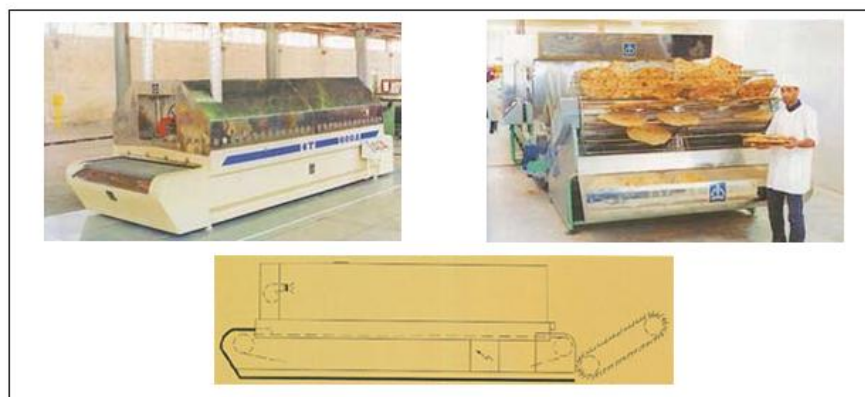


Figure 1: Forced convection oven used for bread baking ( Technopokht Company, Iran, 2007)

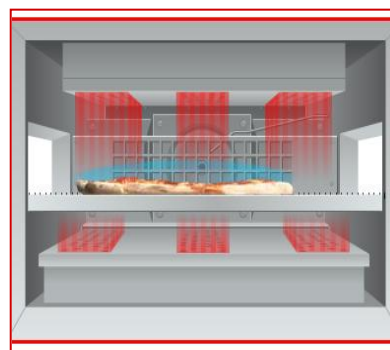


Figure 2: Schematic of bread baking in an Impingement Oven

## 2. Experiments and Mathematical Models

### 2.1 Experiments

An experimental oven was custom designed and constructed to study the bread baking. It is equipped with electrical heaters and PID controllers to facilitate oven temperature control. The belt width is 72 cm, and the total active length for baking is 1m. In this oven, jets of high-velocity hot air impinge perpendicularly onto the dough surface. The air jets are directed onto the product from above and below through “fingers” faced with sets of plates perforated with jet holes or nozzles, each 1.2 cm in diameter. There are four top and four bottom fingers within baking zone. Each finger is 16 cm wide

and reaches across the entire width of the conveyor. The four bottom jet plates are located 6 cm below the conveyor belt. The top fingers, available in different heights to accommodate different baking products, contain five rows of 13 holes arranged in a staggered pattern. For our study it is fixed at H/D=7. The jet holes are punched in the form of dimpled nozzles, the design of which helps to increase the effective air velocity and reduce the friction loss between the finger and the air. The air propelled by the centrifugal fan enters the baking chamber by passing through holes in both the top and bottom fingers and is recycled by passing between the fingers back into the fan inlet. The air jet exits the nozzles at 1–10 m/s. A schematic of the oven is presented in Fig. 3.

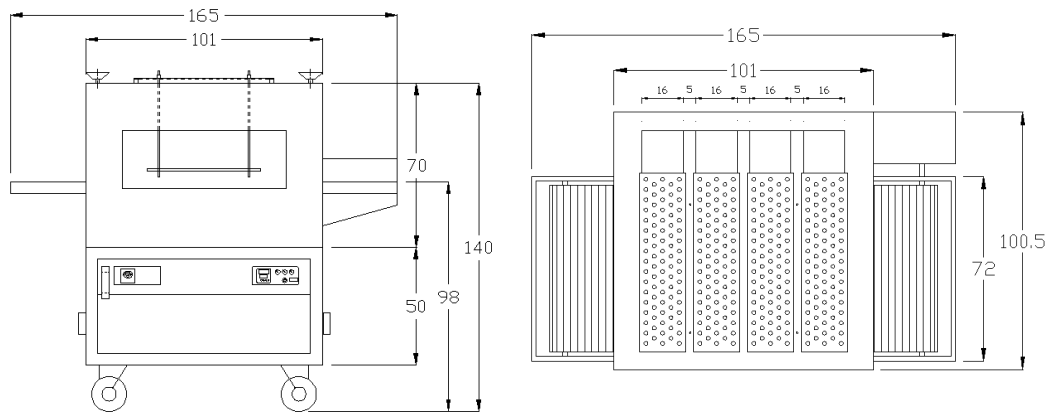


Figure 3: Front and top view of experimental set up (all dimensions in cm)

Using suitable sensors, a measurement and recording system was implemented. Pt-100 probes were used for temperature measurement. A new measurement system was developed for an on-line measurement and recording of bread weight. Thickness and color of the bread surface were measured using an image processing technique with two digital cameras (Fig. 4). The change of the front side of the bread was used to determine the change in bread thickness. For volume change, a Sony Cyber-shot 7.2 MP digital camera was placed horizontally and photos were taken every 30 s for 25 minutes of baking time. Bread cross-sectional area was calculated from the pixel numbers that are counted using the well-known MATLAB software.

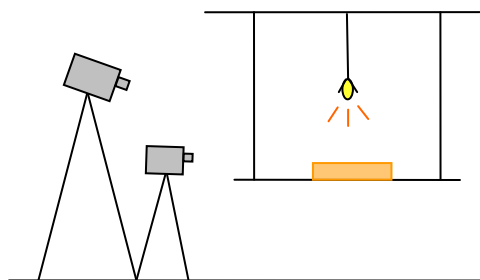


Figure 4: measuring of thickness and color of the bread surface during baking using image processing method

The surface color was first calculated using our MATLAB software in the RGB system from photos taken every 30 seconds with a digital camera (Samsung 4 MP) and then converted to the  $l^*a^*b^*$  space. CIE 1976 ( $l^*a^*b^*$ ) color space was selected to measure the color values not influenced by illumination and also the fine differences in color can be recognized well in comparison to other color spaces. The  $l^*$  parameter represents the lightness of the color which ranges from 0 to 100 (black to white). The  $a^*$  parameter is between -120 and +120 (green and red) and the  $b^*$  parameter is between -120 and +120 (blue and yellow). To acquire the parameters  $l^*a^*b^*$  space, first the color space must be converted from RGB to XYZ and then to  $l^*a^*b^*$ . Conversion between color spaces must be done using a white reference. In this study, white

photographic paper was taken as the true white reference. The correlations for color space conversion from RGB to XYZ are as follows [26]:

$$X = 0.4124 g\left(\frac{R}{255}\right) + 0.3576 g\left(\frac{G}{255}\right) + 0.1805 g\left(\frac{B}{255}\right) \quad (1)$$

$$Y = 0.2126 g\left(\frac{R}{255}\right) + 0.7152 g\left(\frac{G}{255}\right) + 0.0722 g\left(\frac{B}{255}\right) \quad (2)$$

$$Z = 0.0193 g\left(\frac{R}{255}\right) + 0.1192 g\left(\frac{G}{255}\right) + 0.9505 g\left(\frac{B}{255}\right) \quad (3)$$

Where:

$$g(p) = \begin{cases} p > 0.04045 \rightarrow 100 \left[ \left( \frac{p+0.055}{1.055} \right)^{2.4} \right] \\ p \leq 0.04045 \rightarrow 100 \left[ \frac{p}{12.92} \right] \end{cases} \quad (4)$$

It should be mentioned that the values of R, G and B in RGB color space are between 0 and 255. To convert the color space from XYZ to  $l^*a^*b^*$  the following correlations were used:

$$l^* = 116h\left(\frac{Y}{Y_w}\right) - 16 \quad (5)$$

$$a^* = 500 \left[ h\left(\frac{X}{X_w}\right) - h\left(\frac{Y}{Y_w}\right) \right] \quad (6)$$

$$b^* = 200 \left[ h\left(\frac{Y}{Y_w}\right) - h\left(\frac{Z}{Z_w}\right) \right] \quad (7)$$

Where:

$$h(q) = \begin{cases} q > 0.008856 \rightarrow \sqrt[3]{q} \\ q \leq 0.008856 \rightarrow 7.787q + 16/116 \end{cases} \quad (8)$$

Where  $X_w$ ,  $Y_w$  and  $Z_w$  are the reference white values in XYZ space. The image of the reference white should be taken at the same illumination as for the other images. In this study, the values of  $X_w$ ,  $Y_w$  and  $Z_w$  were obtained as 0.9705, 1 and 0.7441, respectively. The total color change of the bread is defined as follows:

$$\Delta E = \left( (l^* - l^*_{\text{0}})^2 + (a^* - a^*_{\text{0}})^2 + (b^* - b^*_{\text{0}})^2 \right)^{\frac{1}{2}} \quad (9)$$

Where  $l^*_{\text{0}}$ ,  $a^*_{\text{0}}$ ,  $b^*_{\text{0}}$  were the initial values of bread before baking. These were obtained as 92, -2 and 31, respectively.

## 2.2 Sample Preparation

After complete mixing of the dough, it was divided into 250g pieces and kept for 15 minutes. Then, the dough was shaped, punched with the fingers (to obtain small and spatially uniform gas distribution) and placed into an incubator for 35

minutes at a relative humidity of 80% at  $35^{\circ}\text{C}$  until its thickness reached 2 cm. Each loaf of bread was composed of 135g (54%) wheat flour, 100g (40%) water and 15g (6%) salt, sugar, dry yeast and flavors.

### 2.3 ANN Model

As explained earlier, an ANN was developed to model the quality attributes of the bread after baking. The four attributes were bread crumb temperature, moisture content, surface color change, and volume change. The independent variables were baking time, oven jet temperature, and oven jet velocity. The acquired datasets were divided into three subsets. Sixty percent of data sets were used in training, 20% in validation process, and 20% in testing.

A multi-layer perceptron feed forward (MLPFF) network was used to model the quality attributes of the baked bread. These types of networks are one of the most popular and successful neural network architectures that are suited to a wide range of applications such as prediction and process modeling [27, 28]. An MLPFF network comprises a number of identical units named neurons organized in layers, with those on one layer connected to those on the next layer so that the outputs of one layer are fed forward as inputs to the next layer. Any input is multiplied by the connection weight and then a bias (a constant number) is added to the product before introducing to the next layer. The output of each neuron is calculated through a transfer function.

Fig. 5 shows a typical multi layer perceptron (MLP) model which involves 3 layers (input layer, hidden layer and output layer). In presented model the input and output layer had 3 neurons (baking time, oven jet temperature and oven jet velocity) and 4 neurons (bread crumb temperature, moisture content, surface color change and relative volume) respectively.

After investigating various ANN structures, the best case containing one hidden layer with 18 neurons was obtained. A Levenberg-Marquardt algorithm was used in network training. Mean absolute error (MAE) was selected to evaluate the ANN performance during the training process. A hyperbolic tangent sigmoid transfer function was used in the hidden layer and linear transfer function for the output layer.

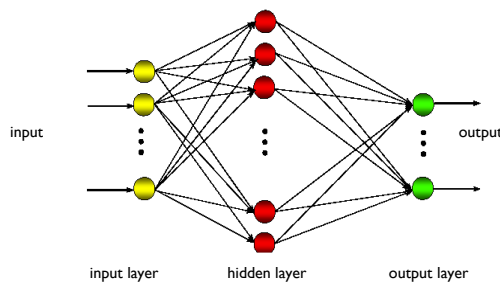


Figure 5: Multi layer perceptron model (MLP)

#### 2.3.1 ANN Data

All of the baking experiences lasted deliberately for 25 minutes which provided investigators with the comprehensive information to investigate the baking process until full burning. Other oven control variables, i.e. jet temperature and velocity, were changed such that different baking conditions were experienced. Jet temperature was increased from 150 to  $250^{\circ}\text{C}$  with  $25^{\circ}\text{C}$  increments. Jet velocity was adjusted at 1, 2.5, 5, 7.5 and 10 m/s. Preliminary experiments had shown that the required input variables which result in acceptable values for quality attributes lies in these chosen ranges. Also, the color and thickness of the bread were recorded 51 times during 25 minutes (every 30 s). Therefore, in total 1275 (5 jet temperatures  $\times$  5 jet velocities  $\times$  51 recording times) sets of data were acquired experimentally, each of them containing three input variables and four output quality parameters.

### 2.4 Optimization

Using the trained neural network model, the quality attributes of the bread during baking can be calculated using any arbitrary values for the inputs, i.e. oven jet temperature and velocity and baking time. However, the objective here is to obtain the input values for which the quality attributes lie in the acceptable range. In other words, to provide the appropriate condition for the optimum baking, all of the four quality parameters must be as close as possible to the desired values; that is, the following objective functions should be minimized:

$$\begin{aligned} g_1(x) &= |f_1(x) - d_1| \\ g_2(x) &= |f_2(x) - d_2| \\ g_3(x) &= |f_3(x) - d_3| \\ g_4(x) &= |f_4(x) - d_4| \end{aligned} \quad (10)$$

Where  $f_1, f_2, f_3$  &  $f_4$  are the bread crumb temperature, moisture content, color change and relative volume, respectively and  $x = \{x_1, x_2, x_3\}$  is a vector comprised of input variables, i.e. time, oven jet temperature and velocity.  $d_1, d_2, d_3$  &  $d_4$  are the desired values for the quality attributes of the bread after baking. Therefore the optimization problem was formulated as follows:

$$\text{Minimize } g(x) = \{g_1(x), g_2(x), g_3(x), g_4(x)\}$$

$$\begin{aligned} \text{While: } & \quad 0 < x_1 < 25 \quad (\text{min.}) \\ & \quad 150 < x_2 < 250 \quad (^{\circ}\text{C}) \\ & \quad 1 < x_3 < 10 \quad (\text{m/s}) \end{aligned} \quad (11)$$

This is an unconstrained and bounded multi-objective optimization problem. Most optimization problems naturally have several objectives to be achieved normally conflicting with each other. It is rarely the case that there is a single point that simultaneously optimizes all the objective functions. Therefore, we normally look for “trade-offs”, rather than single solutions when dealing with multi-objective optimization problems. These sets of solutions are called Pareto optimal sets [29]. So far, different methods have been used to solve the multi-objective optimization problem.

Here in this study, Genetic Algorithm was employed to find the Pareto set. This GA uses the previously developed ANN model to calculate the quality attributes from the randomly selected input variables. After processing and refining the data, a new generation of input variables is provided by GA; that is, applying these values of input variables will give a better quality of the bread at the end of the baking. This process continues until the optimum solution is acquired. NSGA-II is a very famous multi-objective optimization algorithm that used in this study. Details on NSGA-II can be found in Sarkar et al. (2002) [29].

## 2.5 Numerical Simulation

Usually, wall functions or the so-called low Reynolds number models are introduced to model the region near a wall. Wall functions are used to bridge the viscous wall region. However, the usual wall function approach is based on the assumption that the near-wall flow satisfies a universal behavior, which is not valid in most applications of industrial interest. Low Reynolds number models are usually derived with the use of damping functions or extra nonlinear terms to account for the wall effects in the viscous region. Both are based on the assumption of quasi-homogeneity. These assumptions are not valid in the wall region [30].

In particular, kinematic effects of the wall, such as the blocking of the normal velocity component, are fundamentally nonlocal and cannot be modeled without introducing an explicit or implicit dependence on the distance to the wall. Durbin [31] introduced the elliptic relaxation method, which allows the derivation of the wall-proximity models that do not suffer from the above-mentioned shortcomings. The quasi-homogeneity assumption is not used and the terms involving the pressure are solved using a differential equation, the so-called elliptic relaxation equation, which enables the reproduction of the nonlocal effect. The application of this approach to an eddy-viscosity model leads to the so-called  $v^2 - f$  model. It uses  $v^2$  as a velocity scale,  $f$  as an elliptic relaxation parameter, which accounts for non-viscous wall blockage effects and a switch of the scales from energy-containing to the Kolmogorov range, to account for viscosity effects very close to a wall.

Therefore, it solves two additional equations in comparison with the  $k-\varepsilon$  model; i.e., a transport equation for  $v^2$  and an elliptic equation for the elliptic relaxation parameter  $f$ .

$$\partial_t(\rho k) + \frac{\partial}{\partial X_j}(\rho U_j k) = \frac{\partial}{\partial X_j} \left[ (\mu + \frac{\mu_t}{\sigma_k}) \frac{\partial k}{\partial X_j} \right] + 2\mu_t S_{ij} S_{ij} - \rho \epsilon \quad (12)$$

$$\frac{\partial}{\partial t}(\rho \epsilon) + \frac{\partial}{\partial X_j}(\rho \epsilon U_j) = \frac{\partial}{\partial X_j} \left[ (\mu + \frac{\mu_t}{\sigma_\epsilon}) \frac{\partial \epsilon}{\partial X_j} \right] + \frac{C_{\epsilon_1} P - C_{\epsilon_2} \rho \epsilon}{T} \quad (13)$$

$$\frac{\partial}{\partial t}(\rho \bar{v}^2) + \frac{\partial}{\partial X_j}(\rho U_j \bar{v}^2) = \frac{\partial}{\partial X_j} \left[ (\mu + \frac{\mu_t}{\sigma_k}) \frac{\partial \bar{v}^2}{\partial X_j} \right] - 6\bar{v}^2 \rho \frac{\epsilon}{K} + \rho K f \quad (14)$$

$$f - L^2 \nabla^2 f = \frac{C_1}{T} \left[ \frac{2}{3} - \frac{\bar{v}^2}{k} \right] + \frac{C_2 p}{k} + 5 \frac{\bar{v}^2}{k T} \quad (15)$$

$$\mu_t = C_\mu \bar{v}^2 T \quad (16)$$

**Model constants :**

$$C_\mu = .22, C_L = .23, C_\eta = 85$$

$$C_1 = .4, C_2 = .3, C_{\epsilon_2} = 1.9$$

$$\sigma_\epsilon = 1.3, \sigma_k = 1, C_T = 6$$

$$C_{\epsilon_1} = 1.4 \left[ 1 + .045 \sqrt{\frac{k}{\bar{v}^2}} \right]$$

**Stagnation time scale :**

$$T = \text{Min} \left[ \text{Max} \left[ \frac{k}{\epsilon}, \sigma \sqrt{\frac{\mu}{\epsilon}}, \frac{.6k}{\sqrt{6} C_\mu \bar{v}^2 S} \right] \right] \quad (17)$$

**Stagnation Length scale:**

$$L = C_L \text{Max} \left[ \text{Min} \left[ \frac{k^{3/2}}{\epsilon}, \frac{k^{3/2}}{\sqrt{6} C_\mu \bar{v}^2 S}, C_\eta \left( \frac{\mu}{\epsilon} \right)^{3/4} \right] \right] \quad (18)$$

**Boundary conditions on wall :**

$$k_w = 0, \bar{v}^2_w = 0, f_w = 0, \epsilon_w = \frac{2\bar{v}k}{y_1^2} \quad (19)$$

Also those constraints are used to improve the convergenc<sup>[32]</sup>:

$$f = \text{Min} \{ f, \frac{1}{T} [(C_1 - 6) \frac{\bar{v}^2}{k} - \frac{2}{3} (C_1 - 1)] + \frac{C_2 P_k}{k} \}$$

$$\frac{\bar{v}^2}{k} = \text{Min} \left( \frac{\bar{v}^2}{k}, \frac{0.6}{\sqrt{6} C_\mu T S}, 2 \right) \quad (20)$$

The code is a finite volume computer code that uses collocated variable arrangement and Cartesian velocity components for prediction of mass, heat, and momentum. A schematic representation of the impinging jet configuration is

shown in Fig. 6. Due to geometric and physical symmetry, only the flow field within the domain shown in Fig. 6 was solved numerically. The following boundary conditions were used: the impinging surface was specified as an isothermal wall; constant temperature equal to that of the jet was set to the top confinement wall; the uniform velocity, temperature, turbulent kinetic energy and energy dissipation rate profiles were assumed at the nozzle exit; symmetry and outflow boundary conditions were assumed at symmetry and outlet planes; without special statement, turbulence intensity and length scale at the nozzle exit were set to be 2% and 0.05D,<sup>[22]</sup> respectively.

In the interest of accuracy, the governing equations were discretized using a second-order upwind interpolation scheme. The convergence criteria were specified as follows: the normalized residuals of all dependent variables must be less than  $10^{-5}$ . To resolve the near-wall region with large gradients satisfactorily, finer computational grids were set near the wall such that  $y^+$  was always kept below unity for all cases.

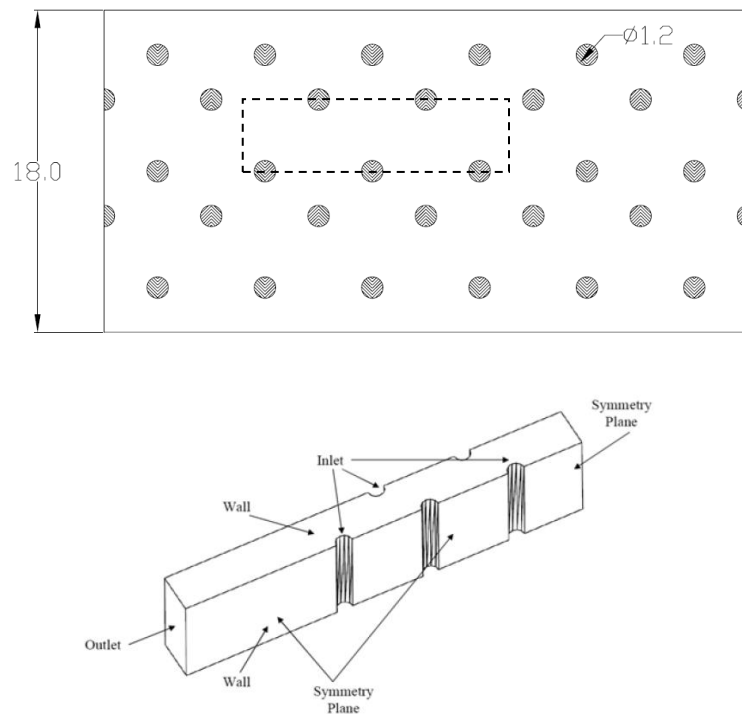


Figure 6: Solution domain and boundary conditions for numerical simulation (all dimensions in cm)

To ensure the attainment of grid-independent results, the sensitivities of both grid numbers and grid distributions were tested for each case. Typically, a grid density of  $210 \times 21 \times 90$  provides a satisfactory solution for the example shown at  $H/D=7$ .

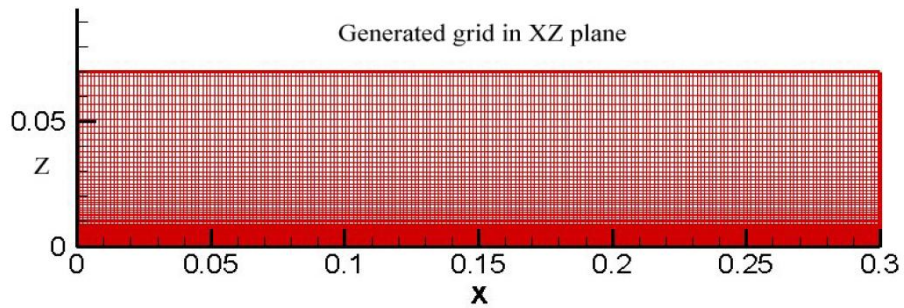


Figure 7: Generated grid in XZ plane (expansion factor = 1.05)

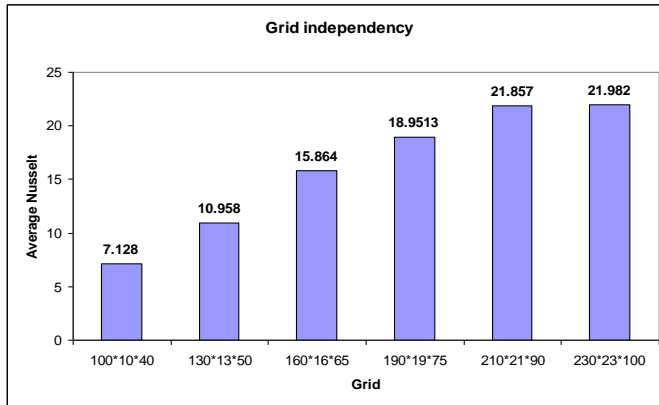


Figure 8: Grid independency of numerical solution

### 3. Results and Discussion

#### 3.1 ANN-GA Models Results

Table I, shows the ANN model performance for training and testing datasets. Fig. 9 shows the performance of the neural network for prediction of the quality attributes using the experimental data (banooni et al.)<sup>[33]</sup>. As it is clear, the network predicts these parameters with a high accuracy. Experimental results provide investigators information but in discrete values of input variables. Therefore, using the modeling results rather than experimental ones, the trade-off between quality attributes was studied more accurately and comprehensively.

As it is clear from the foregoing discussions, finding an optimum combination of jet temperature, jet velocity and time which provides all the quality attributes may not be achieved intuitively. For this reason, genetic algorithm, as an optimization tool, was employed to find the optimum solution. Based on the experimental results, the objective functions can be rewritten as follows:

$$\begin{aligned} g_1(x) &= |f_1(x) - 100| \\ g_2(x) &= |f_2(x) - 0.35| \\ g_3(x) &= |f_3(x) - 17.5| \\ g_4(x) &= -f_4(x) \end{aligned} \quad (21)$$

**TABLE 1**  
ANN model performance

	Performance	Crumb Temperature	Moisture Content	Color Change	Relative Volume
Training dataset	R	0.9983	0.9975	0.9959	0.9924
	MAE	1.481	0.002339	0.8464	0.01529
Testing dataset	R	0.9979	0.9973	0.9956	0.9922
	MAE	1.510	0.002342	0.8926	0.01571

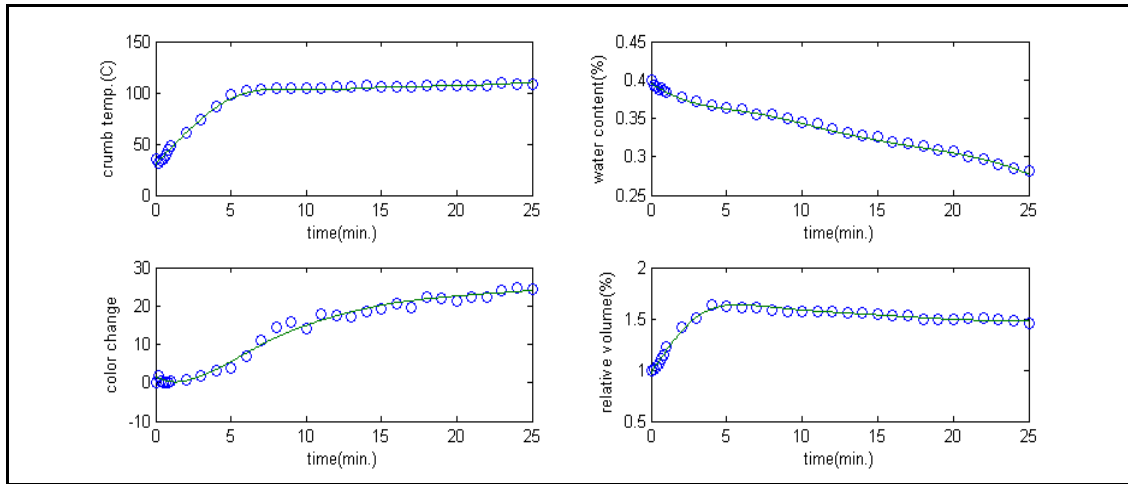


Figure 9: Correlation between experimental value and ANN model output for crumb temperature, moisture content, color and relative volume at jet temperature 200 °C and jet velocity 7.5m/s

However, the acceptable range of quality attributes should be specified experimentally. The crumb temperature, as stated before, must reach to 100 °C in order for the process of starch gelatinization to be completed. For the moisture content, the acceptable range differs for different types of the bread, but a range of 30 to 35 percent seems appropriate for the samples used in this study. Therefore, a moisture content of 35% was taken as target. For the crust color, the acceptable color ranges from 15 to 20. Therefore color equal to 17.5 was taken as the most desired for this case. The relative volume is needed to be maximized, so the negative value of the thickness should be minimized.

**TABLE 2**  
Optimization solutions (the Pareto optimal set)<sup>[34]</sup>

No.	Independent Variables			Quality Attributes			
	Jet Temperature (°C)	Jet Velocity (m/s)	Baking Time (min)	Crumb Temperature (°C)	Moisture Content (%)	Color Change (ΔE)	Relative volume
1	186.43	8.33	8.53	106.39	34.39	19.91	1.45
2	185.94	9.32	7.06	107.9	35.43	17.44	1.51
.	.	.	.	.	.	.	.
.	.	.	.	.	.	.	.
.	.	.	.	.	.	.	.
8	<b>190.08</b>	<b>8.46</b>	<b>5.52</b>	<b>103.86</b>	<b>35.75</b>	<b>16.51</b>	<b>1.48</b>
.	.	.	.	.	.	.	.
.	.	.	.	.	.	.	.
11	180.97	8.91	7.44	105.98	35.26	15.59	1.53
.	.	.	.	.	.	.	.

Using GA, the Pareto optimal set was finally acquired as shown in table 2 (more details can be found in banooni et al.)<sup>[34]</sup>. All of 13 solutions in table 2 are equivalent from the mathematical point of view. Looking practically, however, the solutions may differ. As can be seen, the jet temperature varies from 177.8 to 190.08 °C, jet velocity from 8.33 to 9.80 m/s and baking time from 4.85 to 8.53 minutes. For the mass production purposes, reducing 2 minutes from the baking time (out of 7.44 min.) through an increase of 9 °C in jet temperature and a little increase in jet velocity seems desirable (comparing the

solutions No. 8 and 11 in table 2). As gaining the lower baking time by means of impinging jets is one of the aims of this study, solution No. 8 was taken as the best answer, i.e. jet temperature of  $190.08^{\circ}\text{C}$ , jet velocity of 8.46 m/s and baking time of 5.52 min. In addition, this solution is of the best ones based on the acquired values for quality attributes. The crumb temperature of  $103^{\circ}\text{C}$  guarantees the starch gelatinization. The moisture content is so close to the desired value, that is 35%. Color change is in the acceptable range and the volume is increased by about 50% which is good enough.

### 3.2 Numerical Simulation Results

#### 3.2.1 Impingement Heat Transfer Distribution

With a single jet, very high heat transfer can be achieved in the stagnation region, but further away from the stagnation point the heat transfer rate decreases rapidly. As a result, the total heat transfer field is highly non-uniform as shown in Fig. 10. Therefore, industrial applications must use multiple impinging jets, which enhances the heat transfer over the desired area and also improves its uniformity. The optimum performance of the multiple impinging jets depends primarily on the jet nozzle distance from the targeted wall ( $H/D$ ), geometrical arrangement of the jets, viz. the distance between the jets ( $S/D$ ), and the relative positioning (staggered, hexagonal, rectangular arrangement, etc.). If the spacing is too large, one ends up with many single jets, obviously with poor heat flux uniformity. If they are too close, the jets start to influence each other and may reduce the heat transfer significantly.

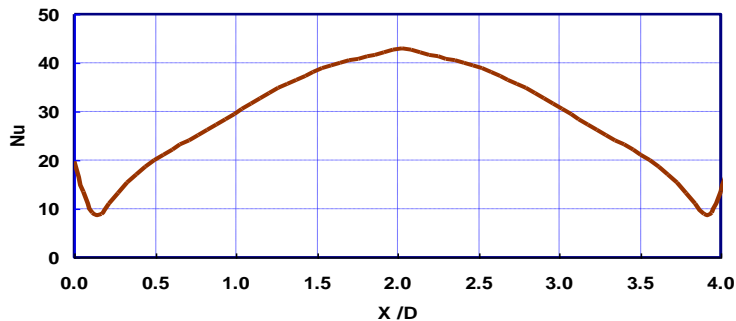


Figure 10: Single jet Nu distribution at  $H/D=5$ ,  $T_j= 200^{\circ}\text{C}$  and  $V_j= 10 \text{ m/s}$

Multiple jet arrangement increases uniformity across the total target area but each jet has a sharp peak that results in increased non-uniformity of the local heat transfer distribution. According to the oven air circulation in solution domain, from left symmetry plane to the outlet, the right jets are affected by cross flow as is shown in Fig. 11. In the south plane, the cross-flow effect is negligible for the middle jet but heat transfer coefficient in the stagnation region decreased about 16% for the third jet<sup>[35]</sup>.

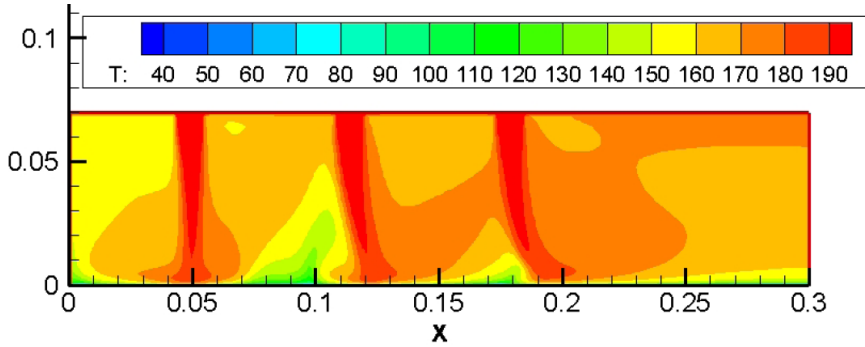


Figure 11: Nu distribution for a middle finger row of jets in XZ plane at  $H/D=7$ ,  $T_j= 200^{\circ}\text{C}$  and  $V_j= 10 \text{ m/s}$

More uniformity is also produced by the staggered arrangement. According to Figs 12 and 13, the valleys between the peaks are well compensated with staggered side jet rows.

Jet temperature variation does not affect the Nu distribution as shown in table 3. Also, bread surface temperature rise had a negligible effect on jet Nu value. Against the jet temperature, jet velocity had a much greater effect on jet Nu number, as shown in table 4.

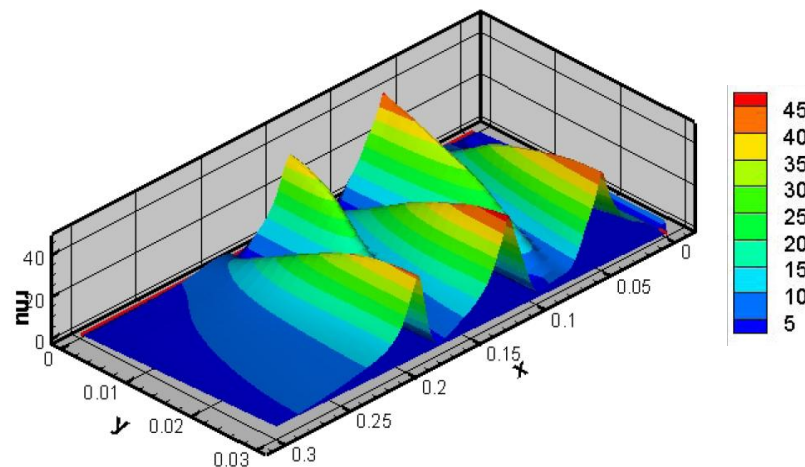


Figure12: 3D Nu distribution for two jet rows of a middle finger at  $H/D=7$ ,  $T_j= 200^\circ\text{C}$  and  $V_j= 10 \text{ m/s}$

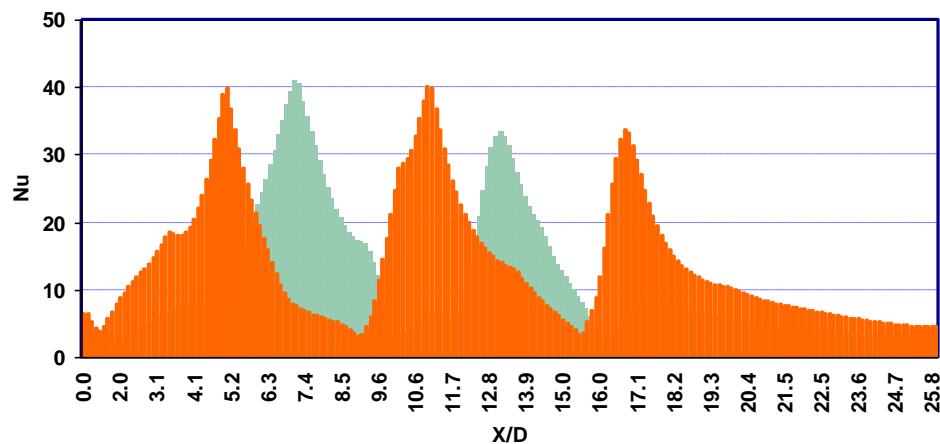


Figure13: Nu distribution for two jet rows of a middle finger in XZ plane at  $H/D=7$ ,  $T_j= 200^\circ\text{C}$  and  $V_j= 10 \text{ m/s}$

TABLE 3  
Effect of jet temperature on  $\text{Nu}_{\max}$  and  $\text{Nu}_{\text{Ave}}$

$T_j (\text{ }^\circ\text{C})$	$\text{Nu}_{\max}$	$\text{Nu}_{\text{Ave}}$
150	41.28	15.46
175	41.08	15.53
200	40.87	15.47
225	40.46	15.71
250	40.25	15.78

**TABLE 4**  
Effect of jet velocity on  $Nu_{max}$  and  $Nu_{Ave}$

$V_j$ (m/s)	$Nu_{max}$	$Nu_{Ave}$
2	8.88	3.04
4	15.54	5.33
6	24.43	8.38
8	33.98	12.83
10	40.87	15.47

### 3.2.2 Even/Uneven Bread Baking

Apart from the consideration of impingement heat transfer uniformity, in bread baking, because of the large surface area, more consideration is required to produce even bread loaves. According to our comprehensive investigation, the sample bread is baked for 5 minutes at 175–200°C and 10 m/s jet temperature and velocity. At this condition and H/D = 7, top surface temperature and average color changes were in the range 115–130°C and 15–20, respectively<sup>[33]</sup>.

Bread color is an important characteristic of baked products dictating consumer preference. In bread baking, crust browning reactions or surface color change occurs at temperatures exceeding 110°C and are complete when the temperature reaches 150°C. According to Fig. 14, the main color changes occur in the last few minutes of baking when the bread surface temperature reaches 110°C. Small differences in surface temperature in this period of baking cause extreme local surface color change.

Figure 15 shows non-uniform bread surface color (dark point) under two jet rows. The variation in surface color is the consequence of the heat transfer distribution on the bread surface.

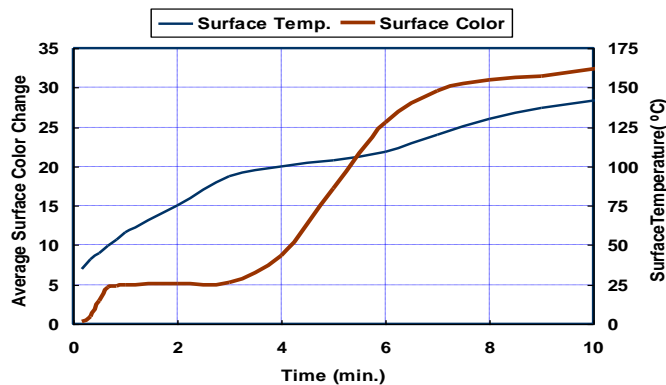


Figure 14: Surface color change and surface temperature at  $T_j = 200^\circ\text{C}$  and  $V_j = 10 \text{ m/s}$



Figure 15: Nu distribution in XZ plane for two jet rows of a middle finger in oven

### 3.2.3 Effect of H/D on Even/Uneven Surface Color

According to our experiments, uneven bread surface color was observed at  $H/D=4$ . Fig. 16 shows maximum surface color values at different  $H/D$ s ( $T_j=180^\circ C$ ,  $V_j= 10 \text{ m/s}$ , baking time= 5 minutes). As observed in Fig. 16, at  $H/D$  greater than 4, the maximum values of surface color decreased and acceptable even baking was achieved. The optimal  $H/D$  was observed to be around 6–7 at the beginning of baking for the thin bread examined here (2 cm).

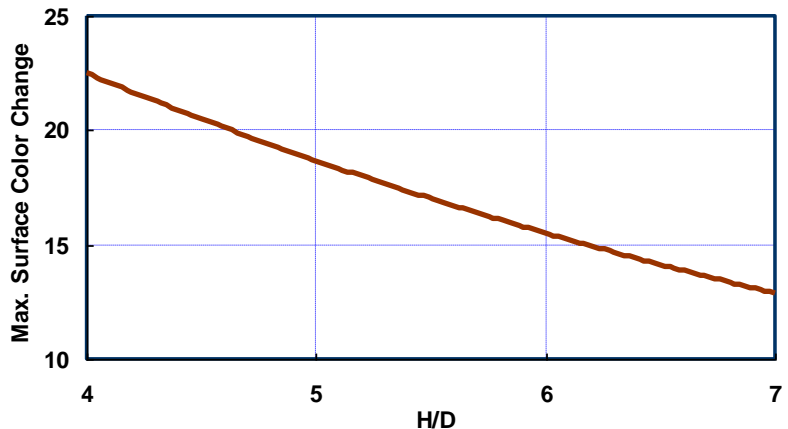


Figure 16: Max. surface color Changes vs.  $H/D$  at  $T_j=180^\circ C$ ,  $V_j= 10 \text{ m/s}$  and baking time= 5 minutes

### 3.2.4 Effect of Jet Velocity on Even/Uneven Surface Color

Fig. 17 shows the effect of jet velocity variation on final baking condition. Surface color change at  $V_j > 6 \text{ m/s}$  was more visible. For jet temperatures between  $175$  and  $200^\circ C$ , the velocity variation in finger nozzles up to 20% assures evenly baked loaves, as was seen in experiments. This required great consideration in finger design in impingement ovens.

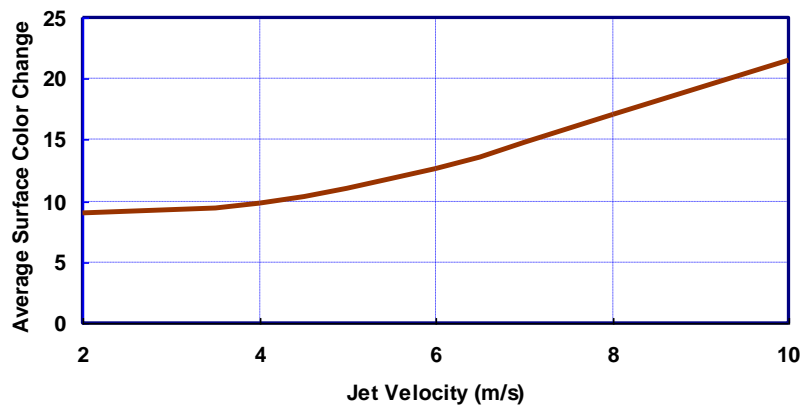


Figure 17: Average surface color change vs. jet velocity at  $T_j= 200^\circ C$ , baking time= 5 minutes

### 3.2.5 Effect of Jet temperature on Even/Uneven Surface Color

At high jet temperatures ( $T_j > 200^\circ C$ ), uneven baking appears as dark spots directly under the nozzles (dark surface obtained when  $\Delta E > 30$ ). Fig. 18 shows the average surface color at baking temperatures in the range  $170$ – $250^\circ C$ . Setting  $T_j < 200^\circ C$  can assure even baking conditions. Because of temperature uniformity in an impingement oven, only localized uneven conditions caused by temperature beyond  $200^\circ C$  for this jet temperature effect was negligible.

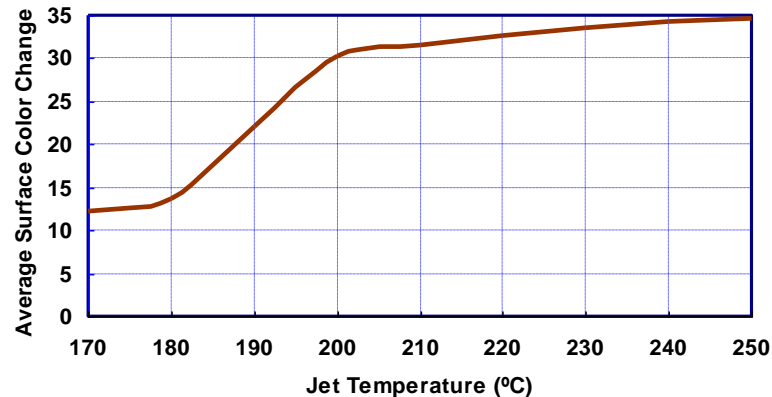


Figure18: Average surface color changes vs. jet temperature at  $V_j = 10 \text{ m/s}$ , baking time= 5 minutes

#### 4. Concluding Remarks

This study shows that inductive modeling techniques using ANN models make it possible to obtain relatively accurate predictions of product qualities variations. The ANN modeling approach is nevertheless of considerable technological interest since a functional form of the relationship between process data and product quality data can be estimated without a priori putting forward hypotheses on the underlying physico-chemical mechanisms involved. This is why a wide range of experimental conditions were tested. Hence, the ANN modeling technique seems to be a promising tool for predicting product quality changes during baking or dehydration processes.

Considerable reduction in process time and improvement in product quality can be obtained using impingement ovens. A point of concern when using air impingement systems is the wide variation of heat transfer coefficient on the surface of a product. This can cause undesirable variation in certain quality attributes. Two types of uneven baking may occur in impingement baking: uneven surface color for each loaf and uneven loaf color related to each other. The first occurs due to local heat transfer distribution resulting from the nozzle arrangement and the second due to non-uniform jet exit velocity distribution in oven cavity. At  $H/D > 4$  and jet temperatures  $<200^\circ\text{C}$  and jet velocity of 10 m/s, local heat transfer distribution and surface darkening was negligible and an even surface color was obtained.

#### References

1. Zanoni, B.; Peri, C. A study of the bread baking process I: A phenomenological model, *Journal of Food Engineering*, **1993**, 19, 389–398.
2. Therdthai, N., Zhou, W., Adamczak, T., “Optimisation of the temperature profile in bread baking”, *Journal of Food Engineering*, **2002**, 55, 41–48.
3. Broyart, B., Trystram, G., “Modeling of heat and mass transfer phenomena and quality changes during continuous biscuit baking using both deductive and inductive (neural network) modeling principles,” *Institution of chemical engineers, Trans IChemE*, **2003**, 81, 316–326.
4. Sablani, S.S., Marcotte, M., Baik, O.D., Castaigne, F. Modeling of simultaneous heat and water transport in the baking process. *Lebensmittel-Wissenschaft und-Tech.*, **1998**, 31, 201–209.
5. Mondal, A., Datta, A.K. Bread baking – a review. *Journal of Food Engineering*, **2008**, 86, 465–474.
6. Wahlby U.; Skjoldebrand Ch.; Junker E. Impact of impingement on cooking time and food quality, *Journal of Food Engineering* **2000**, 43, 179–187
7. Mujumdar, A.S. Impingement drying. In *handbook of Industrial drying*, 3rd edition, CRC press, Boca Raton, FL, USA, **2007**, pp1426
8. Li, A.; Walker, C.E. Cake baking in conventional impingement and hybrid ovens, *Journal of Food Science*, **1996**, 61 (I), 188–197.

9. Walker, C.E. Impingement oven technology: Part II. Applications and future, Technical Bulletin of American Institute of Baking **1989**, 9 (11), 1-11.
10. Henke, M.C. Air impingement technology. In G. Glew, Advances in Catering Technology **1984**, 107-113, barking: Elsevier applied science
11. Millsap, S.; Marks, B.P. Condensing-convective boundary conditions in moist air impingement ovens, Journal of Food Engineering **2004**, 68, 2310-2316
12. Xue, J.; Walker, C.E. Humidity change and its effects on baking in an electrically heated air jet impingement oven, Food Research International, **2002**, 36, 561–569
13. Kokko, T.; Lautala, P.; Huhtelin, T. Advanced Control Strategy for Impingement Drying, Drying Technology, **2003**, 21(10), 1969–1990
14. Polat, S. Heat and mass transfer in impingement drying, Drying Technology **1993**, 11 (6), 1147–1176.
15. Lou, Z.Q.; Mujumdar, A.S.; Yap, C. Effects of geometric parameters on confined impinging jet heat transfer, Applied Thermal Engineering **2005**, 25(17-18), 2687-2697
16. Zhao, W.; Kumar, K.; Mujumdar, A.S. Flow and heat transfer under confined noncircular turbulent impinging jets, Drying Technology, **2004**, 22(9), pp. 2027-2049
17. Shi Y.L.; Mujumdar, A.S.; Ray, M.B. Numerical study on the effect of cross-flow on turbulent flow and heat transfer characteristics under normal and oblique semi-confined impinging slot jets, Drying Technology **2003**, 21(10), 1909-1923
18. Shi, Y.L.; Mujumdar, A.S.; Ray, M.B. Effect of large temperature difference on impingement heat transfer under a round turbulent jet, International Communications in Heat and Mass Transfer **2004**, 31(2), 251-260
19. Moriera R.G. Impingement drying of food using hot air and superheated steam, Journal of Food Engineering **2001**, 49, 291-295
20. Thielen, T.; Jonker, J. Numerical study of the flow in multiple impinging jets, Technical Report APTF-R/01-06, Technical University, Delft, **2001**
21. Baughn J.W.; Shimizu S. Heat transfer measurements from a surface with uniform heat flux and an impinging jet. ASME J. Heat Transfer **1989**, 111:1096–1098
22. Wang S.J.; Mujumdar A.S., A comparative study of five low Reynolds number k–epsilon models for impingement heat transfer, Applied Thermal Engineering, **2005**, 31-44
23. Hosseinalipour, S.M.; Mujumdar, A.S.. Comparative evaluation of different turbulence models for confined impinging and opposing jet flows, Numerical Heat Transfer **1995**, Part A, 28, pp. 647-666
24. Hosseinalipour, S.M., Mujumdar, A.S., Flow and thermal characteristics of steady two-dimensional confined laminar opposing jets, Part I: Equal Jets; Part II: Unequal Jets, International Communications in Heat and Mass Transfer **1997**, 24, pp. 27-38; pp. 39-50
25. Shiravi, A. H; Mujumdar, A. S.; Kubes, G. J. Numerical Study of Heat Transfer and Fluid Flow in Multiple turbulent Impinging Jets, Drying Technology **1995**, 13(5-7), 1359-1375
26. Macdougall, D.B., “Colour in Food Improving Quality”; Woodhead Publishing Limited, CRC Press: Cambridge, England, **2002**.
27. network to predict industrial drying performance,” Drying Technology, **1993**, 11(3), 525-541.
28. Sablani, S.S., Baik, O.D., Marcotte, M., “Neural networks for predicting thermal conductivity of bakery products”, Journal of Food Engineering, **2002**, 52, 299-304.
29. Sarkar, R., Mohammadian, M., Yao, X., “Evolutionary Optimization”, KLUWER ACADEMIC PUBLISHERS, **2002**.
30. Geers, L. Multiple impinging jets: an experimental study of flow and heat transfer. PhD thesis, Delft University of Technology, **2003**
31. Durbin, P.A. Near-wall turbulence closure modeling without damping functions. Theoretical and Computational Fluid Dynamics **1991**, 3:1–13
32. Moran, A.G. Prediction of the Axsymmetric Impinging Jet with Different k-epsilon Turbulence Models, MS thesis, Department of Thermo and Fluid Dynamics, Chalmers university of technology, Goteborg, Sweden **2004**
33. Banooni, S., Hosseinalipour, S. M., Mujumdar, A. S., Taheran, E., Bahiraei, M., Taherkhani, P., “Baking of Flat Bread in an Impingement Oven: An Experimental Study of Heat Transfer and Quality Aspects”, Drying Technology, **2008**, 26(7), 910 – 919
34. Banooni S., Hosseinalipour S., Mujumdar A. S., Taherkhani P., Bahiraei M. Baking of flat bread in an impingement oven: Modeling and optimization, Drying Technology, **2009**, vol. 27, 1-10
35. Banooni S., Hosseinalipour S. M., Mujumdar A. S., Taheran E., Mashaiekhi M. Impingement heat transfer effects on flat bread, Drying Technology, **2008**, vol. 26( 7), 910-919



## TPR GROUP

Transport Processes Research (TPR) group's current research effort is directed towards experimental and modeling studies of heat, mass and momentum transport problems of industrial interest. They are motivated by the need to conserve energy and enhance productivity. Among projects recently completed or on-going are: studies of pulse combustion and novel dryers based on pulse combustor exhaust as drying medium, convective heat transfer using nanofluids, heat transfer characteristics of constructal channels; phase change material (PCM) based cooling systems for electronic components, modeling of PEM fuel cells etc. Basic fluid and thermal characterization of impinging and opposing jets has also been carried out in a series of studies. A number of international collaborative projects are under way with institutions around the world.



**Professor  
Arun S. Mujumdar**

Dr. Arun S. Mujumdar is currently a Professor of Mechanical Engineering at National University of Singapore (Singapore). Earlier, he was Professor of Chemical Engineering at McGill University in Montreal (Canada). He earned his B.Chem.Eng. (with distinction) from UDCT, University of Mumbai (India) and his M.Eng. and Ph.D., both in Chemical Engineering, from McGill University. He has published over 300 refereed publications in heat-mass transfer and drying. Founder of the International Drying Symposium series, he is a frequent keynote speaker at major International conferences and consultant in drying technology for numerous multi-national companies. He serves as an Editor-in-Chief of the archival journal and is also the Editor of over 50 books including the widely acclaimed Handbook of Industrial Drying (Marcel Dekker, New York). Winner of many prestigious international awards, the Technical University of Lodz conferred upon him the award of Doctor Honoris Causa in June 2008. Recently, he was awarded its Platinum Award by Institute of Chemical Technology, Mumbai.

**URL:** <http://serve.me.nus.edu.sg/arun/>